Author:
Linares Vallejo, Erick

Title:
Analysis of Optoelectronic Device for QKD applications

University of BRISTOL

Analysis of Optoelectronic Devices for QKD applications

Erick Eugenio Linares Vallejo

Supervisors: Professor John Rarity and Dr Naim Dahnoun

A dissertation submitted to the University of Bristol in accordance with the requirements for the degree of ***Doctor of Philosophy*** *in the Faculty of Engineering,*

Department of Electrical and Electronic Engineering.

Department of Electrical and Electronic Engineering

University of Bristol

February 2019

Counter word = 46,644

“Regardless of the size of the city or town where men or women are born, they are eventually the size of their work, the size of their will to magnify and enrich their brothers and sisters”

Lt. Gen. Ignacio Allende (1769 – 1811)

“Will and constancy create determination, but it is the will that finally builds that bridge between our dreams and reality”.

Author's Declaration

Hereby I, Erick Eugenio Linares Vallejo declare: That the content of this thesis is original and only the parts that are specified by reference marks contain parts of other research work, and no part of this thesis has been submitted by me to obtain an external academic award. Thereby the thesis work accomplishes the requirements of the University of Bristol for dissertation, such as the regulations and code of practice for a research degree.

All the possible views expressed are completely mine and the University of Bristol is excluded from any responsibility.

_____

Erick Eugenio Linares Vallejo

Date: _____

Abstract

This thesis work contributes to the analysis of the optoelectronic devices that are used for QKD systems. Chapter one discusses and introduces light sources and single photon avalanche diodes (SPADs), their advantages and issues. Then finally it analyses commercial QKD systems in order to know the performance requirements for SPADs in QKD systems.

The light emitting diodes (LEDs) has for many years been ubiquitous in a wide range of applications. Chapter two analyses the way in which an approximate single photon source can be constructed from an LED without an excessive multi-photon production and with short pulse operation achieved by a reverse bias voltage after the LED excitation, to shorten the pulse tail associated with slow carrier recombination. The electronic circuits used for this task are the following two: one with an operational amplifier and the other with discrete electronic components.

The single photons are detected with special photodiodes (single-photon avalanche diodes), because the capabilities of most commercial photodiodes means they cannot detect low light intensities. Chapter three analyses and characterises a relatively new single-photon avalanche diode type, which can detect single photons and reduce some undesired features such as a dead-time after each detection. It is based on a detector chip coupled with an on-chip quenching resistor which minimises stray capacitance effects commercially known as a negative feedback avalanche diode (NFAD).

Another way to reduce the undesired features in the single-photon avalanche diode is through electronic gating circuits. Chapter four uses a sine wave gating method to characterise the single-photon avalanche photodiode using a sine wave interference cancellation method to suppress the gating signal while retaining the breakdown pulses.

The scheme works well up to 100MHz gating showing good efficiency and reduced dead time. Preliminary tests using a gating signal is beyond 1GHz reveals a the non-linear nature of the single-photon avalanche diode (or related amplifier and combiner components) that prevents adequate cancellation and ruling out GHz single photon detection within the timeframe of this thesis.

Acknowledgements

There are many people to acknowledge but not enough space, hence I apologize if I forgot anyone. First I want to regard to the National Council of Science and Technology in Mexico (CONACyT) for the opportunity of a scholarship to study in this great country. Also I want to acknowledge to Study across the Pond for all the paperwork management to enter to the University of Bristol.

To the Prof. John Rarity and Dr. Naim Dahnoun for advice, patience and support after accepting me as a PhD student, thank you so much. To the friends I made during my PhD course such as Dr. Xiao Ai, Dr. Richard Nock, Dr. Ying-Lung Ho, Dr. Mike Taverne, Agustin Gaxiola, Dr. David Lowndes and Stefan Frick for their support and motivation.

To my English family: Ray “Papa” Dawson, my wife Lora Linares and son Lorenzo “cheeky” Linares for being my main strut when I arrived to the United Kingdom and giving me the warmth and support of a family. To my Mexican family like my mother, Maria del Carmen Vallejo Espindola because she was my first motivation to start the academic adventure that brought me to Bristol, to my sister Teresa Linares Vallejo and her family (Pedro and Souji) for supporting me economically and giving motivation from a long distance…

To all of them my infinite gratitude for helping me and crossing in my life…

Table of Contents

List of Figures

Chapter 1. Optoelectronic devices used in QKD systems

Chapter 2. Fast Optical Pulse Circuit for Alice

Chapter 3. Single photon detection using a Negative Feedback Avalanche Diode

Chapter 4. Sine Wave Gating and Subtractive Cancellation

Chapter 5. Conclusions

Appendix A. From Classic optics to Quantum optics

Appendix B. Quantum Optics Application

Appendix C. Photo-electric effect and Photodiodes

List of Tables

Chapter 1. Optoelectronic devices used in QKD systems

Chapter 2. Fast Optical Pulse Circuit for Alice

Chapter 3. Single photon detection using a Negative Feedback Avalanche Diode

Appendix A. From Classic optics to Quantum optics

Appendix B. Quantum optics applications

List of Abbreviations

AC: Alternating Current

APD: Avalanche photodiode

ATM: Automatic Teller Machine

BB84: Bennett-Brassard 1984

BJT: Bipolar Junction Transistor

BS: Beam Splitter

C_0: Speed of light at vacuum

CNOT: Controlled-NOT

CPS: Count Per Second

CW: Continuous Wave

DC: Direct Current

FET: Field Effect Transistor

FPGA: Field Programmable Gate Array

FWHM: Full Width at Half Maximum

FWM: Four-wave mixing

Ge: Germanium

GPIB: General-Purpose Interface Bus

HWP: Half Wave Plate

InGaAs: Indium, Gallium and Arsenic

InP: Indium, Phosphor

LED: Light Emitter Diode

LIDAR: Light Detection and Ranging

MDF: Mode Field Diameter

MMF: Multi-Mode Fibre

NFAD: Negative Feedback Avalanche Diode

OP-Amp: Operational Amplifier

OSI: Open System Interconnection

PBS: Polarized Beam Splitter

PCB: Print Board Circuit

PDA: Personal digital assistant

PDC: Parametric Down-Conversion

PDE: Photon-Detection Efficiency

PNS: Photon Number Splitting

QBER: quantum bit error rate

QED: Quantum Electro-Dynamics

QKD: Quantum Key Distribution

RAM: Random-Access Memory

RC: resistance-capacitance

RNG: Random Number Generator

R_{qi}: Internal quench resistor

SAM: Separate-Absorption and Multiplication

SAGM: Separate-Absorption, Grading and Multiplication

SECOQC: Security Communication based on Quantum Cryptography

Si: Silicon

SMF: Single-Mode Fibre optic

SPAD: Single-Photon Avalanche Diode

SPCM: single photon counting module

TCKD: trusted couriers of key distribution

TCSPC: Time-Correlated Single Photon Counter

TEC: Thermo-Electric Cooler

TIA: Time-Interval Analyser

TTL: Transistor-Transistor Logic

V_{Br}: Breakdown voltage

List of Presentations and Publications

5th April 2016: Superior School of Computer Sciences, National Polytechnic Institute, Mexico City, Talk Title: *"Quantum Key Distribution (QKD) system"*.

6th- 8th April 2016: Innovation Match MX, 1st International forum of Mexican talent, Guadalajara Mexico, Conference title: *"Quantum Key Distribution (QKD) hand-held system"*.

11th April 2016: Culiacan's Technologic Institute, Culiacan Sinaloa, Mexico, Talk title: *"Quantum Key Distribution (QKD) hand-held system"*.

29th-31th March 2017: 6th CONACYT Scholars in Europe Symposium, European Parliament, Strasbourg, Talk title: *"Negative Feedback Avalanche Diode (NFAD) characterisation"*.

31th May – 2nd June 2017: Innovation Match MX, 2nd International forum of Mexican talent, Mexico City, Conference title: *"The LED as low cost single-photon source"*.

Publication: E. Linares-Vallejo, N. Dahnoun, J. G. Rarity, *"*The LED as low cost single-photon source*", Revista Internacional de Investigacion e Innovacion Tecnologica,* vol. 5, No. 29, Nov-Dec 2017

In preparation: Paper: *"Sine wave cancelation as active quenching technique for a InGaAs/InP APD"*

Chapter 1.

Optoelectronic devices used in QKD systems.

The design of electronic devices to detect or generate light (optoelectronics) revolutionized the telecommunication area, when light began to be used to transmit information. The development of Light Emitting Diodes (LEDs) led on to an improvement with miniaturization of laser sources after development of the laser diode [1, 2, 3]. The electronic light sources also brought the development of photodetectors such as photodiodes [3]. These two types of devices began photonics engineering.

Photonics engineering is playing an important role in quantum photonics (a branch of the optics that study the properties of the photons). However, the traditional light sources and photodetectors are useless when we want to create and detect light as individual photons. Therefore, the developing of single photon sources and detectors is driven by applications which require the generation and measurement of photons [1, 4, 5, 6]. This chapter describes the photon sources and detectors used in quantum optics applications. Appendix A studies the connection between classical optics and quantum optics.

1.1 The type of light used in QKD systems

The light used in QKD systems (see Appendix B for details of the QKD) needs certain properties that other types of light do not provide. Ideally a QKD system needs a train of single photons. However, to obtain that train of single photons is complicated and expensive [7, 8], because classical light produces Poisson random trains of photons. Lasers can generate an approximate train of photons; when strongly attenuated (by neutral density filters) a string of laser light pulses can contain mostly no photons and occasionally one photon and rarely more. Such pulses can be generated by basic electronics [9, 10, 11] driving LED's and laser diodes. The type of light that contains a true single photon stream is known as anti-bunched light [9], while lasers produce coherent light with Poisson statistics, neither bunched nor anti-bunched. Standard incoherent light sources (e.g. LED's and light bulbs) produce thermal light with bunching of photons on timescales related to the light bandwidth.

The differences between these three types of light can be represented in figure 1.1.

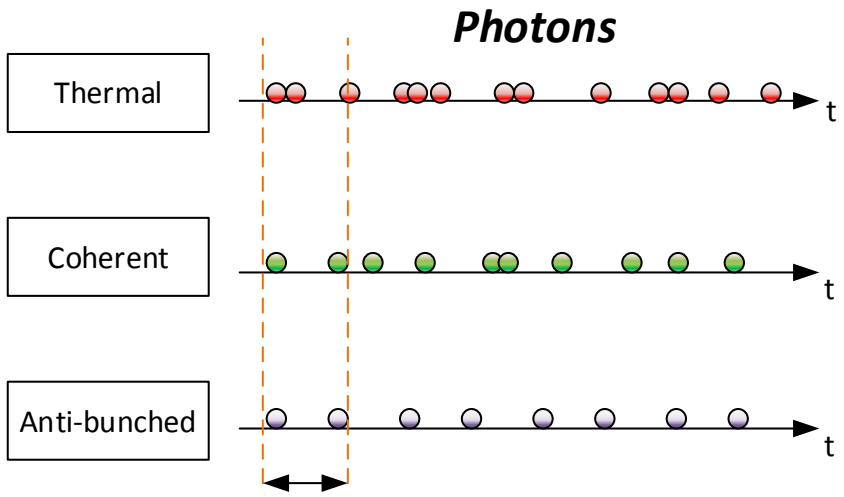

Figure 1.1: Graphic difference between three types of light: Thermal, Coherent and Anti-bunched. The time gap between the emitted photons is constant in the anti-bunched light, which shows an isolation of photons, generating a chain of single photons.

This figure is a basic representation of the differences between the three types of light. Nevertheless, the differences are deeper and they can be explained with detail through the Poisson distribution. Which relates to the types of light within the QKD system with more accuracy.

1.1.1 Poisson statistics applied to the light distribution

Poisson statistics can analyse the light sources under three regimes of statistical distribution: super-Poissonian, Poissonian and sub-Poissonian, the first two regimes are suitable for the classical optics theory that model the light source as an electromagnetic wave [1, 7]. However, anti-bunched light can only be analysed through sub-Poissonian distribution, because the light is quantified by single photons.

Therefore, the Poisson distribution equation (1.1) is applied using the number of photons (N) and the mean photon number (μ) [1, 7, 9]. However, the usage of Poisson distribution is highly recommended when the light is generated from a pulse source [9]. When the light source is continuous and fluctuating we can also look at analysis using time correlation functions [7]. The probability $p(N, \mu)$ to emit a number N photons per pulse given the mean photon number μ is given by,

$$p(N,\mu) = \frac{\mu^N e^{-\mu}}{N!} \tag{1.1}$$

When the mean photon number is 1 ($\mu = 1$), the probability of producing more than one photon per pulse is high. This distribution is associated with coherent sources [7]. Figure 1.2 illustrates a mean photon number equal to 1 with a bar graph.

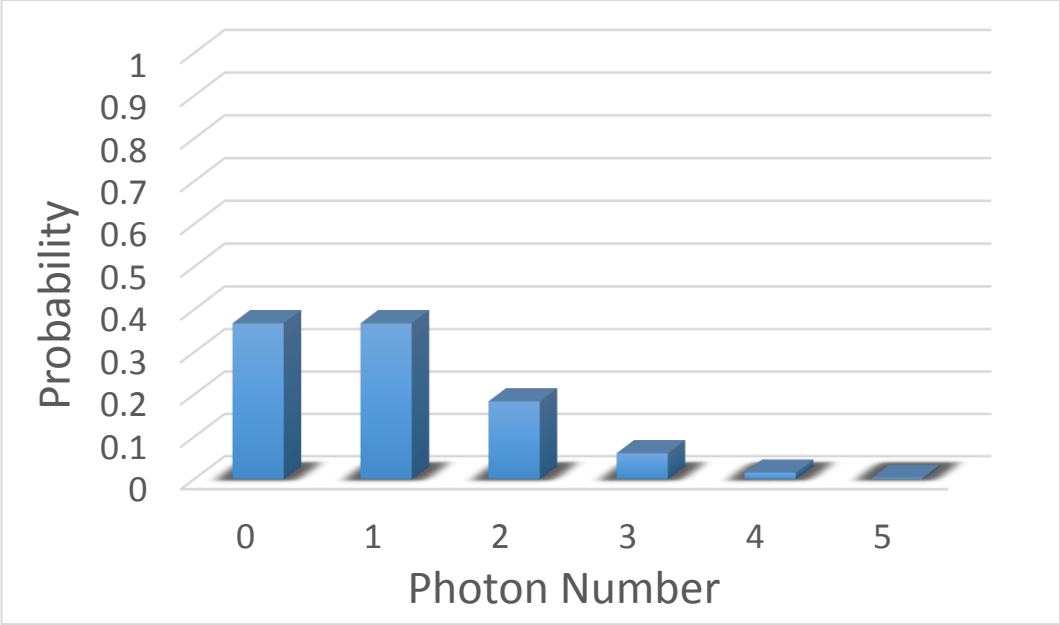

Figure 1.2: The probability of photon emissions with N photons per pulse when the mean photon number (μ) is 1.

The number of photons per pulse has a similar probability when it is 0 and 1, the probability of 2 photons is above 0.1 (or 10%). The probability becomes negligible when the number of photons is greater than 5. However the high probability of $N>1$ for $\mu = 1$ infringes the security of the QKD system opening it to a photon number splitting (PNS) attack [9]. When μ is under 1, the probability of having more than 2 photons per pulse decreases, reducing the probability of success in the case of a PNS attack, Figure 1.3 illustrates another bar graph for three different values of μ.

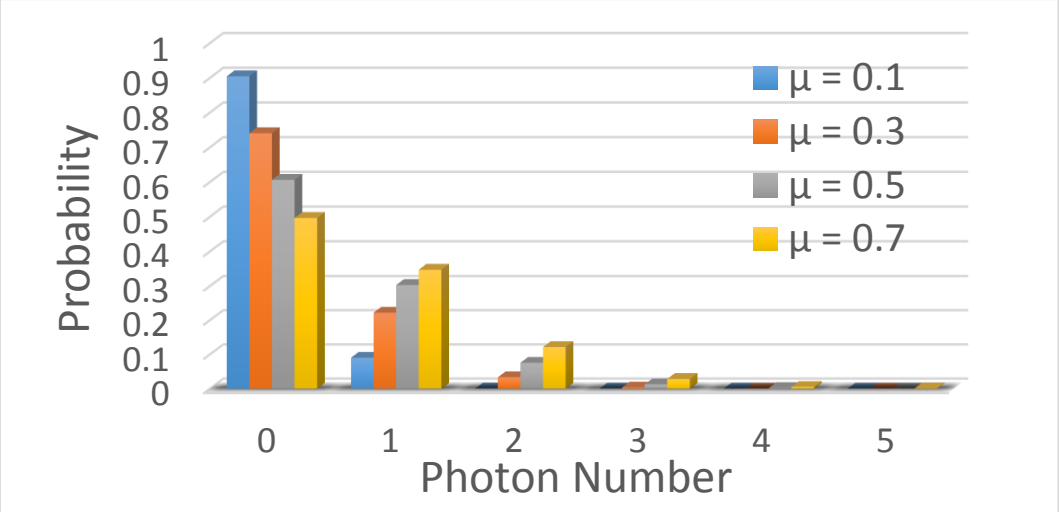

Figure 1.3: The Probability of light pulses to contain *N* photons when the mean photon number (μ) is 0.1, 0.3, 0.5 and 0.7 photons.

The probability of the light pulses to contain more than two photons falls drastically when $\mu = 0.1$, therefore the mean photon number (μ) is important when the photon number per light pulse is estimated through the probability of the equation (1.1).

Although an ideal light source ideal for a QKD system is single photon source it proves to be expensive and complex [9]. A solution is to replace the true single photon source emulating its desired characteristics (i.e. no emission $N>1$)), with other light source such as a laser or LED. In the following section we go into a little more detail of the properties of example single photon and classical light sources that affect the security of the QKD system.

1.2 Photon sources

In the following we briefly review some ideal single photon sources and then the LED and laser used as approximate-single-photon-sources

1.2.1 Single Photon Source

The ideal single photon source have a probability of 100% to emit a single photon and 0% multiple-photon and vacuum pulses, the photons emitted are indistinguishable and the gap time between photons is constant, however there are many factors that affect the photon emission, therefore the single photon sources are divided into two types [8]:

- Deterministic
- Probabilistic

The Deterministic single photon source is the type that's closest to the ideal because the photon emission is one per demand, the process of emission can be related directly to single quantum emitters or with the ensemble-based emitter technique [8], the single-emitters could be single atoms, single molecules even an electron-hole pair in a quantum dot. The radiative transition between two of its quantum states is suitable to produce a single photon, emitted into one or several spatio-temporal modes [12].

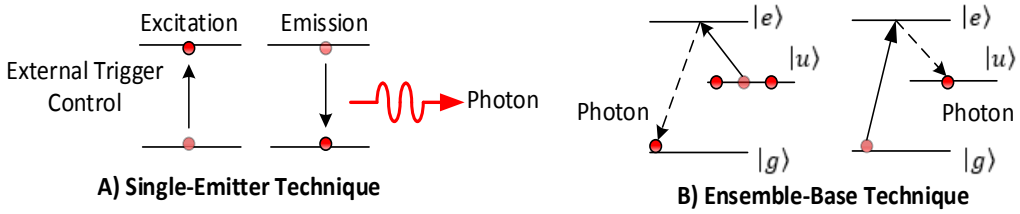

Figure 1.4: Deterministic single photon source using: A) Single-emitter technique, B) Ensemble-based technique.

The probabilistic (or heralded) single photon source exploits the generation of photon pairs where one photon is used to herald the approach of other photon [13]. It often involves a pulsed laser excitation of a nonlinear optical material to emit pairs of photons in thermal states [7, 8, 12]. To avoid producing multiple photon-pairs the average occupancy of each pair pulse is kept low but after heralding by the detection of one of the two photons the probability of the heralded photon can be high.

The probabilistic sources can use parametric down-conversion (PDC) [8] or four-wave mixing (FWM) [14] to generate the pairs. As example PDC uses a short wavelength pump laser to illuminate the material with a χ^2 optical nonlinearity, creating two photons under the constraints of momentum and energy conservation, figure 1.5 illustrates the PDC process [8].

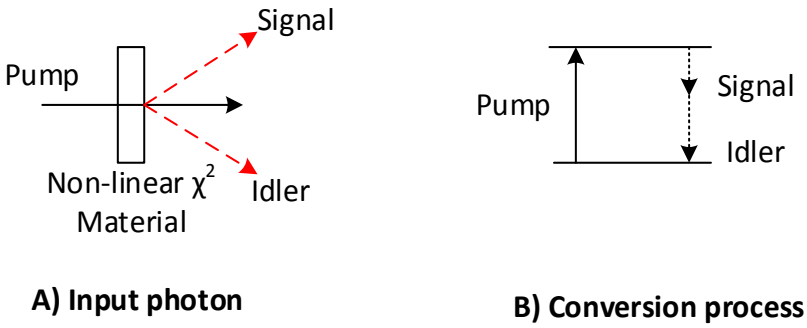

Figure 1.5: A) Input photon is convert in two photons, B) The conversion process creates multiple wavelengths from the energy and momentum conservation.

Furthermore, of the wavelength, the constraint of energy and momentum is used in the emission of photons and their direction, therefore it represents an advantage in many applications although the inherent dispersion of transparent material is only controllable with the temperature [8]. Examples of transparent crystals used:

- KD*P (Potassium di-deuterium phosphate)
- BBO (Beta Barium Borate)
- $LiNbO_3$ (Lithium Niobate)
- $LiIO_3$ (Lithium iodate)

These types of crystals can influence the χ^2 nonlinearity required for the PDC due to the fact that these materials are commonly strong in the distribution nonlinearity**,** however there is a disadvantage presented in the spatial-mode of the photon pairs, the photon pair is created in multi-mode cones surrounded by a pumping laser, therefore their collection efficiency by single-mode fibres is reduced [8].

1.2.2 The Light Emitter Diode (LED)

The LED is a semiconductor device related to semiconductor diodes, but the LED produces an electroluminescence when it is forward polarised with a voltage. Without any external stimulation the LED has an electron-hole recombination due to the temperature (thermal

excitation), but it is not enough to generate an ostensible light emission [1]. Therefore, the spontaneous photon emission requires an electric current (injection) to stimulate the interaction of electrons (*minority carriers*) and holes (*majority carriers*) at the depletion layer. The recombination between the depletion layer begins to increase when the electric current circulates through the LED, but this current has a direct relation to the forward bias voltage applied to the LED, when this voltage reaches a threshold the electroluminescence starts and this threshold voltage is called on-voltage (V_{on}), figure 1.6 illustrates an energy diagram and the curve voltage-current $(V-I)$ of the LED.

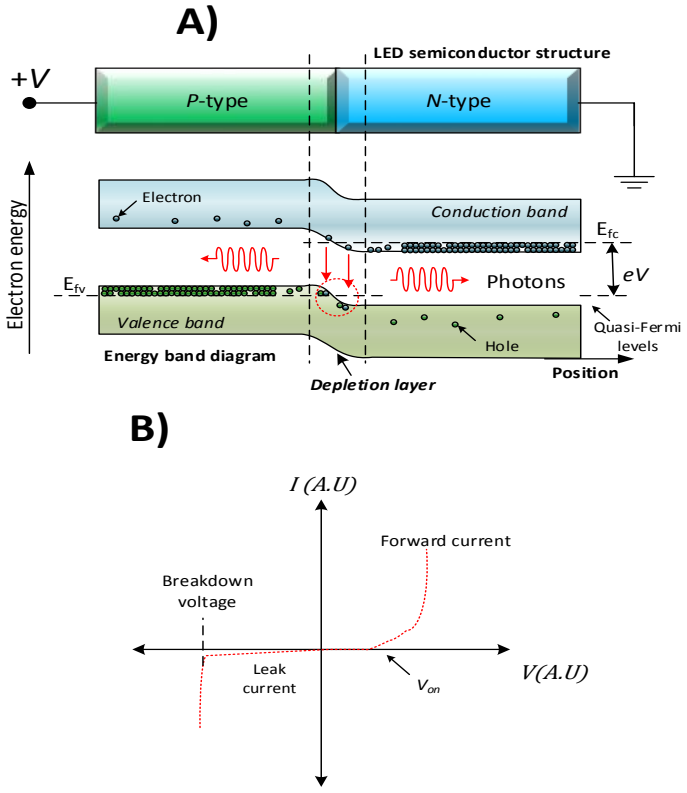

Figure 1.6: A) Energy diagram of the LED, the depletion layer marked by the vertical dashed lines is where the recombination occurs, the horizontal dash lines represent the quasi-Fermi levels when the LED is forward biased, and the red dashed circle indicates the recombination. B) $(V-I)$ Curve of the LED obtained through equation (2.5), V_{on} indicates the threshold to start the electroluminescence due to minority and majority carrier recombination.

The recombination in the depletion layer is formed by two types of recombination: radiative and non-radiative. The non-radiative recombination only involves the minority carriers transferred from the conduction band to the valence band, this transference does not release any photons and the non-radiative recombination is common in other semiconductors such as generic diodes or transistors [3].

When the transference of minority carriers is excessive, a spontaneous photon emission occurs and it continues as long as the injected carriers last. The recombination has a lifetime (τ) after the injection ends which can be determined by the equation (1.2)

$$\frac{1}{\tau} = \frac{1}{\tau_r} + \frac{1}{\tau_{nr}} \tag{1.2}$$

Where τ_r is the radiative recombination lifetime and τ_{nr} is the non-radiative recombination lifetime. An indirect consequence of the recombination is the wavelength of the spontaneous photon emitted, because the bandgap energy (E_g) separates the conduction band and the valence band. Hence, the minority carriers had to cross it to reach the valence band, and the frequency of the spontaneous photon emitted has an energy greater than E_g. Thereby, the wavelength (μm) of the photon emitted is determined by the equation (1.3).

$$\lambda_g(\mu m) = \frac{1.24}{E_g(eV)} \tag{1.3}$$

Therefore, V_{on} changes with respect to the LED colour e.g. a red LED has a V_{on} at 2V but a blue LED has a V_{on} at 3.2V [15]. The bandgap wavelength (λ_g) is characteristic for a specific semiconductor alloy [1], but the light emitted by an LED is not concentrated in λ_g but in a spectral distribution such as figure 1.7. This LED spectral width is determined by the equation (1.4) [1].

$$\Delta\lambda(\mu m) \approx 1.45\lambda_p^2 K_B T \tag{1.4}$$

Where $K_B T$ is expressed in eV and the peak wavelength is λ_p (μm).

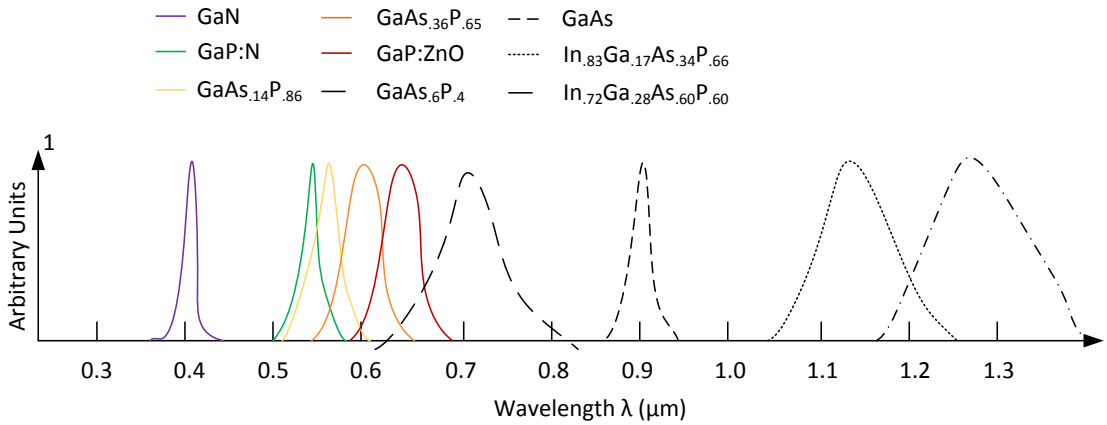

Figure 1.7: Spectral density compared with the λ for different semiconductor materials and therefore different bandgaps [1], the peak intensities are normalized to the same value and the increasing spectral linewidth is a result of its proportionality of λ_p^2.

The peak wavelength of emission is close to the bandgap wavelength λ_g (eq 1.3) which is dependent on the semiconductor alloy inside the LED. There are some semiconductor alloys which are composed by three different elements allowing them to tune the wavelength of the light emitted. The light with a short wavelength (ultra-violet and visible) is a result of materials with a wide bandgap (>2eV)

Direct-band-gap materials are chosen for LED's because this leads to high internal efficiency. This happens when the radiative lifetime is much faster than the non-radiative lifetime. Table 1.1 represented the semiconductor materials with their wavelength of emission.

Semiconductor Material	Wavelength of emission (μm)
GaAs	0.87
GaSb	1.70
InP	0.92
InAs	3.50
InSb	7.30
$Al_xGa_{1-x}As$	0.75 – 0.87
$In_{1-x}Ga_xAs_{1-y}P_y$	1.1 – 1.6

Table 1.1: Semiconductor materials used in the LEDs and their λ emission, the subscripts x and y denotes the compositional mixing ratio thus AlGaAs are ternary semiconductors and InGaAsP are quaternary semiconductors [1].

The LED as a light source has an advantage in comparison to single photon sources; it is commercially available, it has a low cost and low consumption of energy. However the radiative recombination does not stop as soon as the external stimulation ends but leads to an emission tail. In the following we show how with a proper electronic circuit, the

radiative recombination tail can be removed and with appropriate attenuation short pulses with one or two photons per light pulse can be generated.

1.2.3 Laser Diode

The laser is an optical oscillator that comprises of a resonant optical amplifier [1, 2], an analogy of the laser could be the electronic oscillators [1, 3] where an amplifier has a controlled feedback, and figure 2.18 illustrated this analogy.

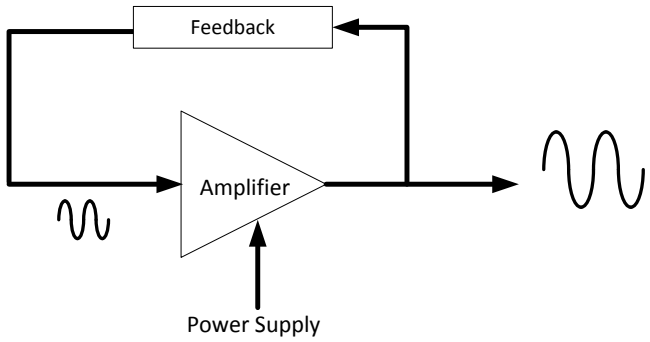

Figure 1.8: The Basic Scheme of an oscillator.

The type of energy pumped is related to the gain medium, because when the medium is solid or liquid, the external stimulation is a light with a different λ, and when the medium is gaseous or a *semiconductor,* the external stimulation is an electric current or pulse [1, 2]. After this brief explanation about the laser beam, the semiconductor material is used as a gain medium to allow the creation of the opto-electronic device known as an injection laser diode.

The laser diode has a highly doped *p-n* junction which is fabricated from a direct-gap semiconductor material [1, 2, 3], thus the cavity is defined in the p-n junction gap. The mirrors are cleaved in the semiconductor material along the p-n junction. A semiconductor crystal (also cleaved) has a behaviour of gain medium. Therefore, the device becomes an optical amplifier with a feedback and the semiconductor crystal is converted in to an optical oscillator, satisfying the laser conditions previously described.

The laser diode has a similar condition to the LED, because both are injected by an electric current through the p-n junction. Nevertheless, there is a fundamental difference in the light emitted, in the LED it is product of the spontaneous emission and the laser diode is stimulated. Figure 1.11 illustrates the structure of the laser diode and the light emission when it is forward-biased [1, 2].

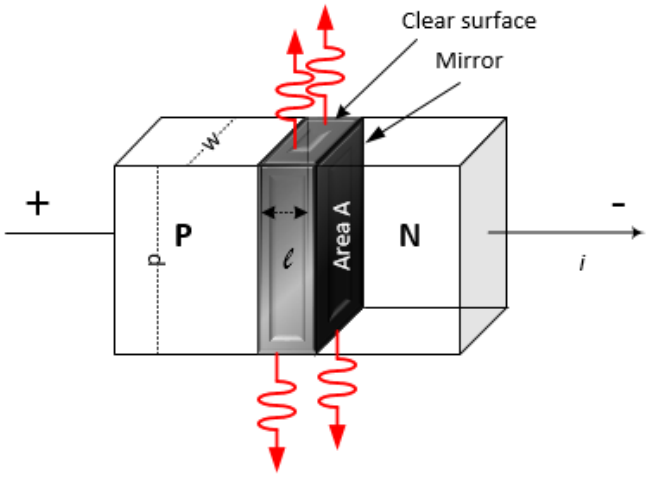

Figure 1.9: The scheme of a laser diode structure, where the injection is forward biased through the p-n junction with two parallel surfaces that act as mirrors [1].

As in the LED, the laser diode also has an electron-hole recombination lifetime but now much faster due to stimulated emission. The gain coefficient at its peak value γ_p [1] is given by

$$\gamma_p \approx \alpha\left(\frac{J}{J_T} - 1\right) \tag{1.5}$$

Where α is the thermal-equilibrium absorption coefficient. J is the injected current density and J_T is the current density required to make the semiconductor transparent. The equation (1.5) does not have a reference to radiative recombination, but J_T involves the radiative recombination as equation (1.6) represents [1].

$$J_T = \frac{e\ell}{\eta_i \tau_r}\Delta n_T \tag{1.6}$$

Δn_T is the injected-carrier concentration and ℓ is the thickness of the active region, e is the electron charge, η_i is the internal quantum efficiency and τ_r is the radiative electron-hole recombination lifetime. J and J_T are depend of the current injected to the laser diode [1]. The light and current curve for a laser is shown in figure 1.10.

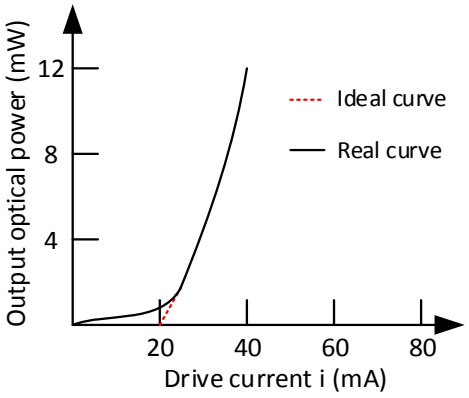

Figure 1.10: Light - Current curve, the ideal curve has an immediate increment but the real curve has a slight increment (LED like) from the origin (0mA) to the threshold, after that above threshold the light power increases is linearly with current [1].

The curve plotted (figure 1.10) also relates to the radiative recombination lifetime, current and wavelength through equation (1.7) [1].

$$P_o = \eta_d (i - i_t) \frac{1.24}{\lambda_0} \tag{1.7}$$

The radiative recombination lifetime is determined by the external differential quantum efficiency η_d, because it is a product of emission efficiency and internal quantum efficiency $(\eta_e \eta_i)$. The emission efficiency is associated with the loss of the light transmitter through the mirrors, and internal quantum efficiency $\left(\frac{\tau}{\tau_r}\right)$.

The wavelength in the laser diode also depends on the semiconductor material used such as the LED. However, the spectral distribution is completely different because the laser light is generated by stimulated emission [1]:

Which makes the laser linewidth much smaller than LED's as is illustrated in figure 1.11. The main differences between lasers and LED's are discussed in chapter 2, although the discussion about which light source is suitable for a QKD system is discussed in section 1.4.

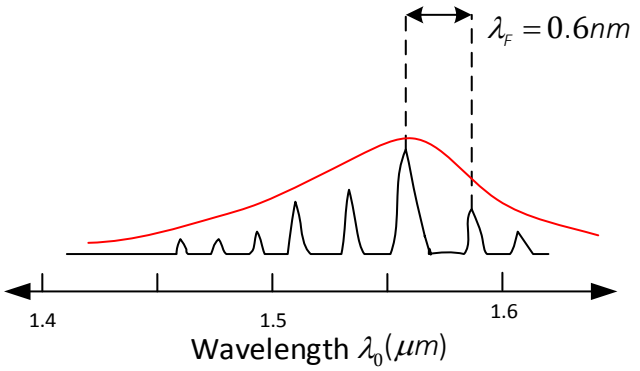

Figure 1.11: Spectral distribution of a 1550 nm, the laser distribution is considerably narrower than the LED illustrated in figure 1.7. Furthermore, each peak represents an electromagnetic mode of the laser cavity with a peak at 1550nm and mode separation 0.6nm given by the cavity length. A 1550nm laser is used to characterise and test the photodetectors in chapters 3 and 4.

In summary, the wavelength in a laser diode can be selected through the gain medium (such as the traditional lasers) which is a semiconductor material of group III to V. The spectral width is relatively large due to the transitions between the energy bands or between energy levels, within these fast transitions there is a homogeneously broadened tendency within the semiconductor materials used as a gain medium [1]. The spatial holes burning, permits simultaneous oscillations of several longitudinal modes, also the spatial hole burning is presented in short cavities, furthermore the spatial hole burning permits fields of different longitudinal modes along the resonator to reduce the overlapping. The semiconductor resonator has a length *d* which is considerably smaller than other types of lasers, and therefore the frequency spacing of adjacent resonator modes that are determined by $\upsilon = \frac{c}{2d}$ are relatively large [1].

The laser diode described in the example of figure 1.11 of which its central wavelength (λ_0) is 1550nm, uses an InGaAsP crystal as a gain medium with a length of 580µm. The refractive index (n) of this crystal is 3.5 therefore the resonator modes by $\nu_F = \frac{C_o}{2nd} \sim 74Ghz$, this frequency can be related to a free-space wavelength spacing (λ_F) through the next relation $\frac{\lambda_F}{\lambda_0} = \frac{\nu_F}{\nu}$, then $\lambda_F = \frac{\lambda_0^2}{2nd} \sim 0.6nm$ [1].

1.3 Photodetectors

A problem when using weak light pulses is their detections, the photodiodes can detect a certain amount of light and with an external electronic circuit the detection is amplified. But there is a minimum amount of light that a photodiode can detect. Below a noise threshold, the detection is hidden. By using internal amplification from an electron avalanche, the Avalanche Photodiode (APD) is able to detect low amounts of light. This structure is also the basis of the single-photon avalanche diode (APD), in appendix C section C.2.3 we discuss the APD.

1.3.1 Single-Photon Avalanche Diode

The APD has a good amplifier method due to the cascade of electron-hole pairs, but when the light has a low intensity such as, the detection is focused on single photons, then the linear gain APD is not suitable. However, there is an APD exclusively designed to operate beyond the breakdown voltage and detect single-photons; the Single-Photon Avalanche Photodiode (SPAD). The SPAD is also known as a Geiger-mode APD because its operation is similar to the principle of the operation from the Geiger-Müller tube [15]. The Geiger-mode starts when the bias voltage is fixed beyond the breakdown voltage, provoking an extremely sensitive situation such as a single photon absorption that can precipitate an avalanche and produce a large current pulse.

1.3.1.1 SPAD Structure

The SPAD has a similar structure to the APD illustrated in figure C.8, but the SPAD presents an extra property, the detection of single photons. The Si-SPAD gives high detection efficiencies (50%) for wavelengths below 1.1µm [1, 8, 16, 17]. The spectral region has a dependency on the type of semiconductor material used in the SPAD e.g. the Germanium (Ge) in the SPAD allows detections at 1.3µm but with low detection efficiencies (15%).

The InGaAs tertiary alloy grown on an InP substrate allows detections at 1.55µm and SPAD's with detection efficiencies above 10% [17] have been demonstrated and commercialised. The InGaAs/InP structure is known as Separate-Absorption, Grading and Multiplication (SAGM). Figure 1.12 illustrates the SAGM structure [16], band structure and electric profile.

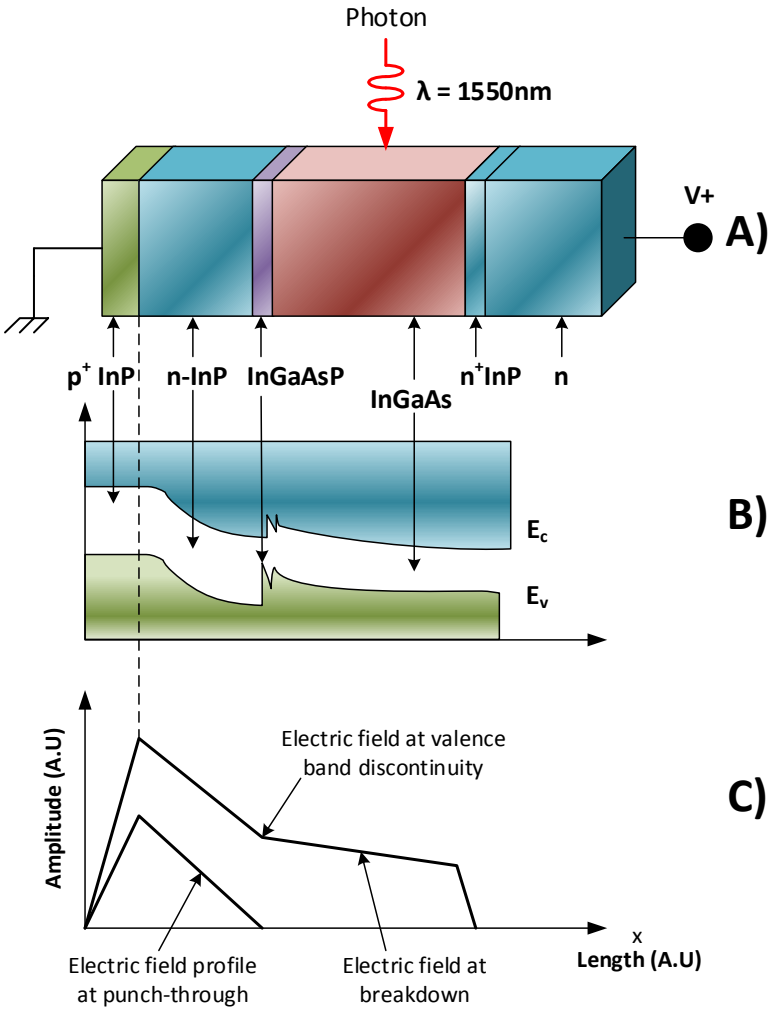

Figure 1.12: A) InGaAs/InP SPAD structure, B) The valence band presents a discontinuity at the hetero-interface, C) The SPAD electric field between the punch-through and breakdown point.

The photon is absorbed in the InGaAs layer which generates an electron-hole pair, and the electron is pulled towards the cathode. The hole drifts through the InGaAs layer towards the InGaAsP layer, which ensures an efficient transfer of holes to the InP layers [16, 18]. There are three InP layers in figure 1.12 (n^-InP, n^+InP and p^+InP), the n^+InP is a buffer where the electrons arrive by the sweeping of the electric field and p^+InP could be considered the source of electrons, but the n^-InP layer is a multiplication region which undergoes impact ionization (section C.3.2). The importance of the InP layers lie within the reduction of low multiplication noise which is achieved with carriers of higher-impact ionization coefficient, and for the InP layers there are the holes which satisfy that condition (the holes are swept to the multiplication region) [16].

The ideal SPAD produces avalanches immediately after the single photon absorption and successively without any delay, but the real SPAD has features, which make successive single photon detections impossible [19].

1.3.1.2 SPAD Features

The avalanche generates a large current pulse that must be quenched to prepare the SPAD for the next single photon arrival, but the avalanche quenching creates a time lapse in which the single photon is not detected, that lapse of time is called dead-time. After the dead-time, the SPAD enters in to a recharge-time in which the single photon can be detected, but the current created by its arrival is not sufficiently large enough, once the recharge-time is completed, the SPAD has the conditions to produce an avalanche that generates a large pulse such as the first single photon absorbed.

The dead-time and recharge time are not the only undesired features, due to the extremely sensitive SPAD status under the Geiger-mode, the minimal collision between the electron-hole pairs can produce uncontrolled avalanches. The temperature has a direct influence on the electron-hole pair provoking their movement, thereby the impact ionization is unavoidable and an avalanche begins and consequently a current pulse.

The SPAD are normally used for photon counting and avalanches which are provoked by the thermal influence, these are called *dark-counts*, the dark-count Poissonian fluctuation represents an internal noise source in the SPAD [19], although there are some SPADs that integrate a cooling system that reduces the temperature and the dark-counts considerably [17, 19, 20].

The thermal influence is not the only cause of uncontrolled avalanches. There are traps in the multiplication region that must be depopulated after an avalanche has occurred and before the bias voltage can be restored [8], but there are still carrier remnants of the previous avalanche such as electrons (or hole) in those traps, these carriers can provoke uncontrolled avalanches and these avalanches are called *after-pulses*.

The after-pulsing effect increases or reduces its probability to occur as a function of the temperature by $K_B T$. The traps in the multiplication region increase their capability when the temperature is lower, hence the probability of after-pulses increases, but when the temperature is higher the trap capability is reduced [17, 21], figure 1.13 illustrates the

SPAD with a latency time after the detection, the after-pulsing effect and dead-time effect.

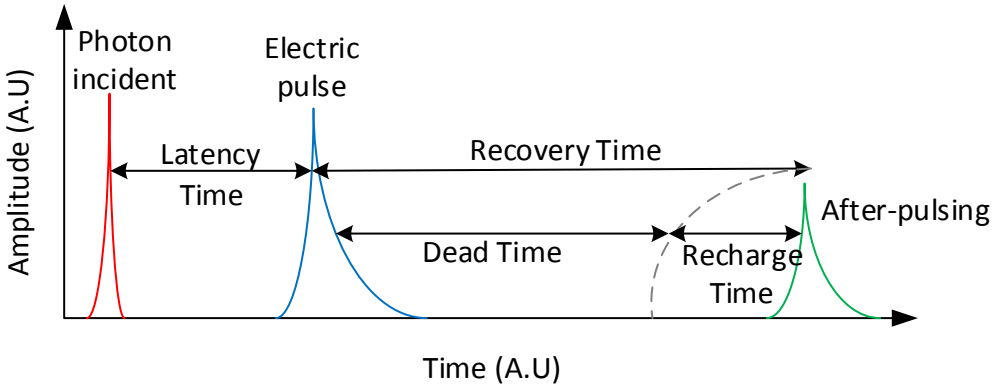

Figure 1.13: The SPAD under a photon detection (red), passes a certain time until this absorption generates an electric pulse (blue) the recovery time that includes the dead-time and a charge time where the after-pulsing (green) has a probability to appear.

An important feature of the SPAD is the *photon detection efficiency* (PDE) because it increases as a function of the bias voltage over the breakdown voltage. The PDE is related to quantum efficiency and the electron-hole pair probability to start an avalanche [17, 19], this probability is called trigger probability because sometimes the single photon that is absorbed does not start the avalanche, the trigger probability (P_{tr}) is determined by the equation (1.7)

$$P_{tr} = 1 - e^{-V_E/V_C} \tag{1.7}$$

Where V_E is the bias voltage over the breakdown (excess bias voltage), V_C is the characteristic voltage that depends on the depletion layer thickness and the impact ionization [17]. The ratio of sensitivity to the total area (ε) also has an influence on the PDE [19], and thereby the PDE is determined by the equation (1.8).

$$PDE = \eta \varepsilon P_{tr} \tag{1.8}$$

The SPAD alloy material has a direct influence on the PDE [1, 16, 17], the Si-SPAD has a PDE of around 75% and the InGaAs/InP SPAD is around 20% [1, 16]. When the avalanche is compared to other avalanches through their Full Width at Half Maximum (FWHM), there is a time variation. This variation is called *jitter* or timing jitter and it is defined, as the uncertainty in the detection time of an avalanche with a fixed arrival time of incident photons [16, 21, 22, 23, 24]. An ideal timing jitter is below 100ps and constant, real SPADs

have a timing jitter of around 400ps but it can reduce if the PDE is increased [20-24], figure 1.14 illustrates the timing jitter effect in a SPAD.

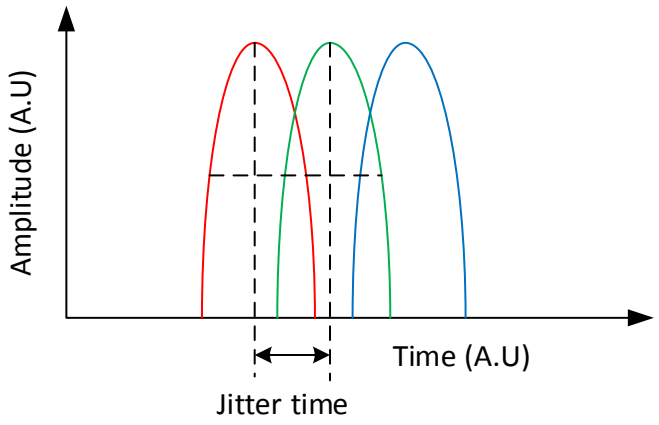

Figure 1.14: The jitter time is normally measured from the FWHM of the detections although there are certain features that can be modified such as the temperature and excess bias voltage.

The SPAD features can be modified with a proper avalanche quench method through an external circuit, but this circuit design requires some SPAD electrical properties and the best way to analyse those properties, is through representing the SPAD with passive components. The equivalent circuit is represented in the relation of the reverse bias voltage polarization, and figure 1.15 illustrates the SPAD equivalent circuit.

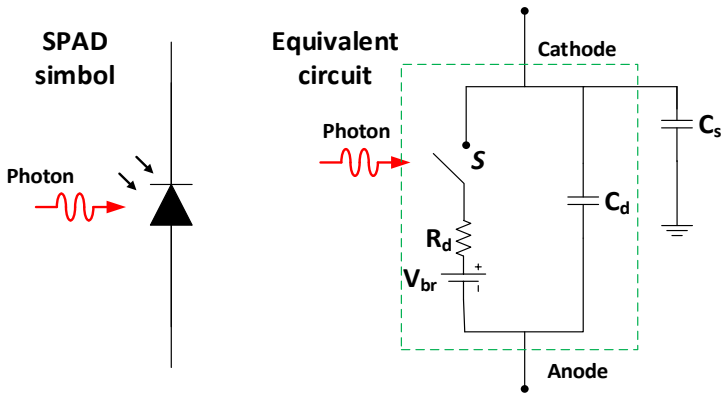

Figure 1.15: SPAD equivalent circuit, $\mathbf{R_d}$ is diffusion resistance, $\mathbf{C_d}$ is diffusion capacitance, $\mathbf{C_s}$ is stray capacitance and $\mathbf{V_{Br}}$ is breakdown voltage.

The junction capacitance (C_d) and stray capacitance (C_s, produced between cathode and a load) are responsible for the recharge time because when a single photon arrives (switch *S* closed), The bias voltage in the cathode passes by the diode resistance (R_d) but is reduced by the breakdown voltage, this reduction provokes a discharge in C_d and C_s which were previously charged by the bias voltage, both capacitances have fast changes as a

function of the current but not as a function of the voltage, when *S* is open again the recharge time of both capacitances are influenced by an external load resistor [20, 25] .

1.3.1.3 Passive Quenching circuit

The passive quenching circuit is the most simple circuit for SPAD, this circuit only has two resistors connected in series, one resistor is used as a load (R_L) to limit the current, and the other is used as an impedance coupler (R_S) for an amplifier connection. When the SPAD does not have any avalanche, the voltage and current have asymptotic steady-state values and those parameters are determined by the equation group (1.9) [25].

$$I_{steady} \cong \frac{V_E}{R_L} \tag{1.9a}$$

$$V_{steady} = V_{Br} + R_d I_{steady} \tag{1.9b}$$

The breakdown voltage (V_{Br}) is equal to V_{steady}, if I_{steady} is small it means that R_d is much smaller than R_L. The quenching time (T_q) is set by the total capacitance (C_d+C_s) and by R_d in parallel with R_L [25].

$$T_q = (C_d + C_s)\frac{R_d R_L}{R_d + R_L} \cong R_d(C_d + C_s) \tag{1.10}$$

The recovery time (T_r) has a similarity with T_q but the charge of C_d+C_s is only limited by R_L, therefore T_r is determined by:

$$T_r = R_L(C_d + C_s) \tag{1.11}$$

The value of R_L has a significant impact on the SPAD, but there is a minimum value that should be held to avoid that I_{steady} exceeds 20µA. The junction inside of the SPAD can normally hold currents up to 20µA [25], beyond that current the SPAD structure is damaged provoking short-circuit.

The passive quenching circuit has different configuration modes, figure 1.16 illustrates basic passive quenching circuits for voltage mode and current mode.

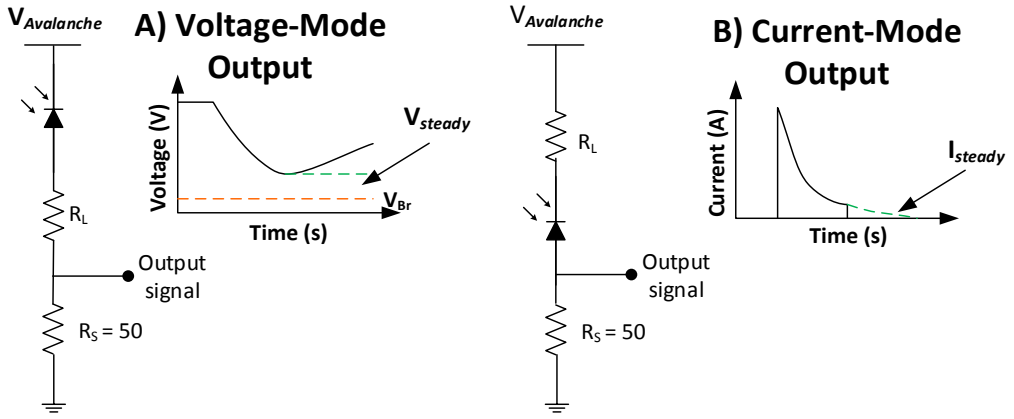

Figure 1.16: Schematic diagram of the basic passive quenching circuits for different operation mode: A) When there is a detection the voltage has a falling and after return to original value (V_{steady}), but if I_{steady} is considerable small V_{steady} is near to V_{Br}. B) When there is a detection the current through the SPAD arise almost instantly and fall exponentially until a step-down (quench current; I_q), but I_{steady} is close to I_q the quenching will delay more time.

The current mode has advantages over the voltage mode, because the capacitance does not stop abrupt current changes, but it does stop abrupt voltage changes.

1.3.1.4 Active Quenching circuit

The SPAD has a fast restore if the Geiger-mode can be activated at will, therefore the breakdown voltage is a virtual switch because a bias voltage under it changes the SPAD to APD, but a bias voltage over the breakdown voltage puts the SPAD in Geiger-mode and vice versa. There are several active quenching circuits but the most simple is a gate coupling also known as gate operation (a type of active quenching), figure 1.17 illustrates the gate operation active quenching circuits with DC and AC gate coupling.

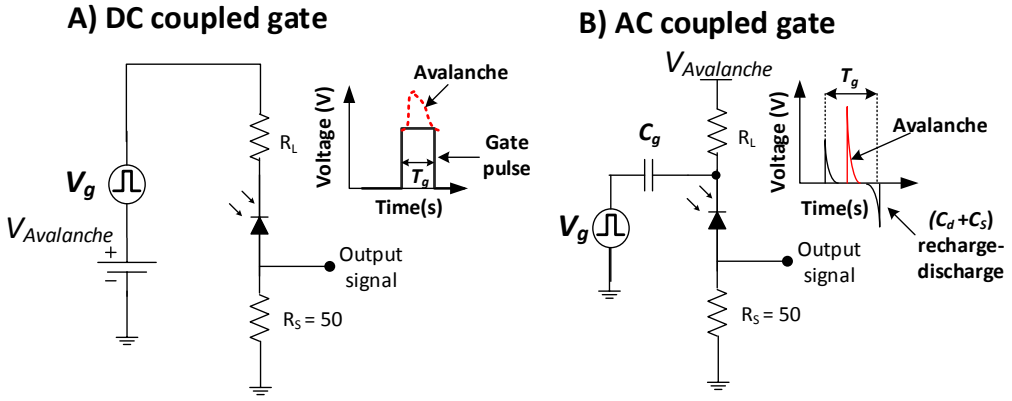

Figure 1.17: Electronic scheme of the gate operation active quenching circuit: A) DC coupled gate. B) AC coupled gate.

The DC gate coupling circuit easily achieves an avalanche control, because the bias voltage source is added to the gate pulses. However, this configuration injects the gate pulses to the avalanches, therefore the single photon arrivals are mixed with the gate pulses. The AC gate coupling isolates the bias voltage of the gate pulse source by using a coupler capacitor (C_g), but this capacitor attenuates the amplitude of the gate pulses ($V_{g'}$), hence the real gate pulse amplitude (V_g) is obtained by a capacitive divider [25].

$$V_{g'} = V_g \frac{C_g}{C_g + C_d + C_s} \tag{1.12}$$

The attenuation by C_g is dismissed because normally the frequencies used in the gate pulse source are higher, hence C_g has values over 10nF that it allows frequencies over 1MHz to pass [25]. The gate pulse width has an influence on the SPAD avalanche recovery, because the gate pulse modifies the avalanche width and this modification is determined by the equation (1.13).

$$T_{gi} \cong R_L C_g \tag{1.13}$$

Where T_{gi} is the time influenced by the gate pulse to the avalanche, there is an additional signal added to the avalanche. The transients produced by the discharge of the capacitances (C_d and C_s) are mixed with the avalanche, although there are several techniques to discriminate the transients of the avalanches [25, 26, 27]. There is other type of active quenching methods such as the free running active quenching circuit, which quench the avalanche though of a comparator and a feedback connected between the load resistor (RL) and the cathode of the SPAD [25, 26].

1.3.2 Negative Feedback Avalanche Photodiode

The SPAD has a performance limitation with respect to the photo counting rate and the absence of photo numbers, that limitation is traced back by a positive feedback inherent to the impact ionization driving avalanche process [28]. The Negative Feedback Avalanche Photodiode (NFAD) is a relatively new SPAD, that monolithically integrates a resistance as a negative feedback to the device structure [28, 29], this resistance allows a rapid self-quenching without parasitic effects such as active quench techniques, some NFAD models integrate multiple active regions which corresponds to several (until four) diodes

connected in parallel [30], figure 1.18 illustrates the NFAD structure and its equivalent circuit.

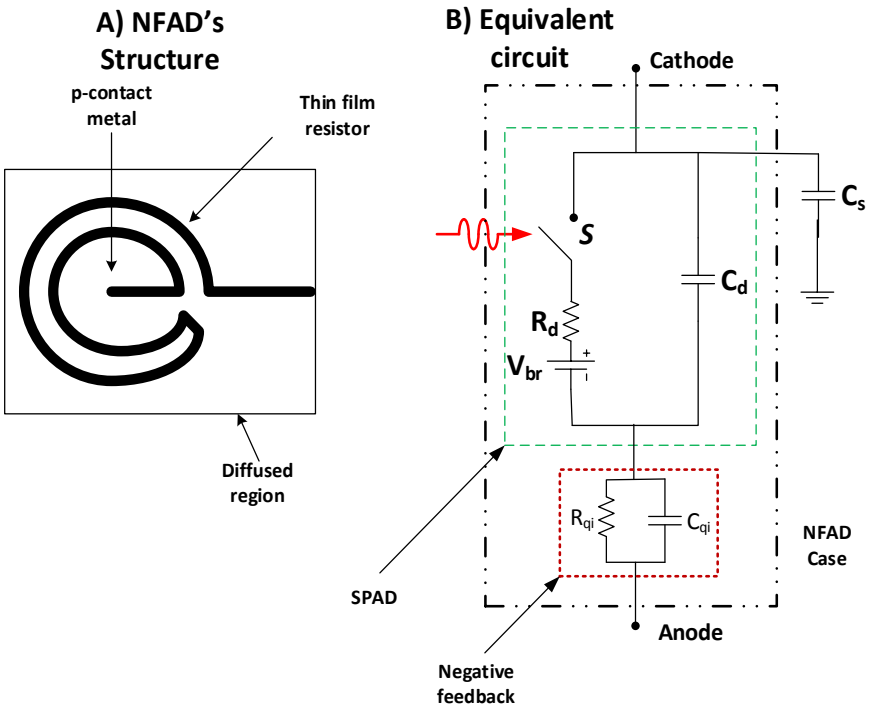

Figure 1.18: A) NFAD structure with a thin film resistor integrated, B) Equivalent circuit which has a certain similarity with figure 2.21, but in the red dashed square there is a quench resistor (R_{qi}) with a parasite capacitance (C_{qi}) [28,29].

This internal resistance (R_{qi}) reduces the recovery time after each avalanche, because R_{qi} removes any possible effects of C_S and C_{qi} is too small to be considered. Therefore the recovery time is reduced in comparison with the traditional passive quenching circuit, the equation (2.33) determines the recovery time for the NFAD (T_{Nr}).

$$T_{Nr} = R_{qi}C_d \tag{2.33}$$

This resistance has a value of around 1MΩ that exploits the passive quenching [28, 29]. The benefits of this monolithic resistance integration are not only in the recovery time reduction, it also reduces the carrier trapping as it has a direct impact on the after-pulsing effect reduction [31]. However, the resistance also reduces the avalanche amplitude hence it is essential to add extra amplifiers to observe the current pulses produced by the avalanches [28].

The negative feedback produces a current during the detection that induces a voltage fall, and the excess bias voltage close to the breakdown voltage that quenches the avalanche itself. Figure 1.19 illustrates a typical avalanche in the NFAD.

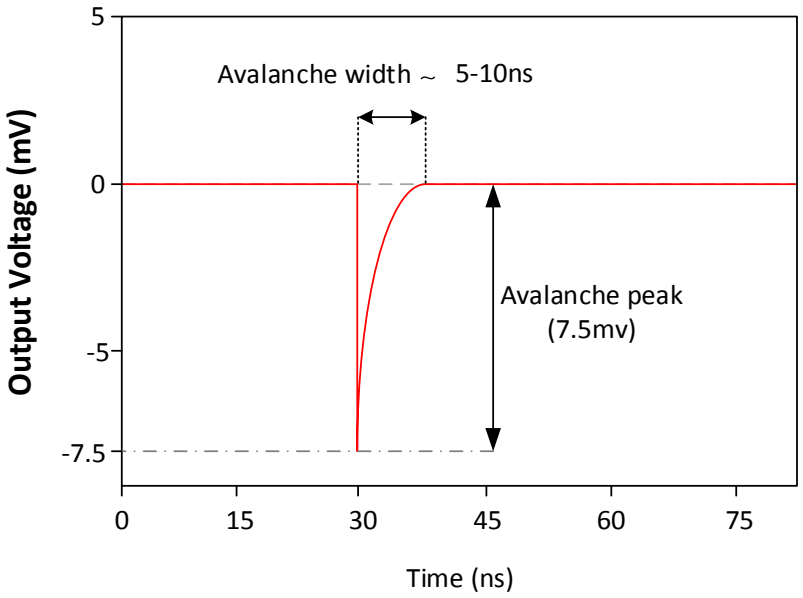

Figure 1.19: Typical avalanche in the NFAD, the duration of this avalanche does not exceed the 10ns [30].

Due to the avalanche being close to the V_{Br}, the avalanche does not have a long time of duration, therefore the avalanche is quenched by itself each time that a photo detection occurs [31]. The NFAD presents several advantages in comparison of typical InGaAs SPAD, such as self-quenching without a need of external electronic quench circuit [29 ,30], a low after pulsing probability and low jitter on free-running mode [23, 28, 32, 33].

The choice of quenching resistor is based on the latching current of the device. When there is a latching current of I_L and a quench resistor of value R_Q then the voltage at the device drops by $V= I_L R_Q$. This voltage has to be enough to bring the device below breakdown. For example in the case of the NFAD the latching current is of order 10 uA and the quench resistor chosen is 1.5 MΩ thus generating a quench of 15V easily enough to quench the avalanche when biased only a few volts above breakdown.

The free-running mode on NFAD is the most attractive of this SPAD [34], because this reduce dark-counts considerably (even at room temperature) and increase PDE to around 10%.

1.4 Optoelectronic devices used in commercial QKD systems

The previous sections (1.2 and 1.3) describe the sources and detectors used in QKD experiments [8, 9, 35, 36], but there are two companies which have advanced QKD technology to such a grade, that they are near to the commercial step [37, 38]. ID Quantique® offers two models of the QKD system:

- Cerberis QKD Blade
- Clavis^3 QKD Platform

Although ID Quantique® does not reveal technical information about light sources and photodetector usage in systems, it does reveal the capability of the pulse rate repetition of the emitter at 1.25GHz. However, the company gives information of its SPAD with low noise, in use with a Continuous Wave (CW) laser which is modulated and attenuated, which confirms the unviability of single photon sources used in QKD systems for reasons explained in section 1.1.

In the case of Toshiba's QKD system, Toshiba® is more explicit about the photodetectors used in its system, it uses its self-differencing InGaAs SPAD but at room temperature [39]. The light source is a CW laser with a modulator and attenuator system, but recently Toshiba® developed its quantum LED at 1550nm for telecommunication purposes [40]. The frequency of operation in InGaAs SPAD has been increased beyond 2 GHz, this frequency achieves a maximum count rate of 1 GHz and hence the speed of transmission in Toshiba's QKD system achieves 1 Mbps.

Both companies claim their systems can achieve long range (> 100 km). Hence, the wavelength used in these systems is 1550nm, as is used for standard long range optical telecommunications. The present work characterises SPADs that detect photons with that wavelength, in table 1.2 it compares the SPADs used in commercial QKD systems with the SPADs used in this thesis work.

	Single Photon Avalanche Diodes (SPADs)		
	ID210 (gated)	**ID230(Free-running)**	**Toshiba (gated)**
Dead-time (µs max)	100	100	10ns
Dark-counting (CPS)	*400-2000 in SMF@100MHz*	50 (at 203K)	100 (at 55 % PDE)
PDE (% max)	25	15	55
After-pulsing (%)	No data	20 (at 183K)	2.2 (at 293K)
Timing Jitter	<200ps	<100ps	<250ps

Table 1.2: SPAD used in commercial QKD systems, ID Quantique® report several dark count information for the model ID210 [41], which depends if the detector is in a gate or free-running mode and the type of fibre used. The model ID230 reports the dark counting through curves at the PDE indicated in the table in paper [42].

The dead-time of ID210 is considerably longer in comparison to Toshiba, the main reason is the gating frequency because ID210 only reaches 100MHz of trigger but Toshiba is 1GHz [43], and it helps to reduce dead-time. As explained in the table 1.2 of the product description note [41], the dark-counting in the model ID210 depends on the type of mode used, the PDE efficiency and the type of fibre optic used which could be Single-Mode Fibre (SMF) or Multi-Mode Fibre (MMF). The dark counting in gate mode (with 1ns of effective gate width) is reported between 0.4 up to 2CPS when the gate frequency is 100kHz for a SMF-A, the dark-counting increases when the fibre is swapped and the maximum dark-counting is at a range between 8 and 40 CPS with a MMF, this range increases 1000 times when the gate frequency is 100MHz and thereby the dark-counting range is 400 to 2000 CPS for a SMF-A and 8000 to 40000 CPS for a MMF.

When the ID210 is in free running mode, the dark-counting has a stable range which is from 1000 up to 13500 CPS for a SMF-A and 7500 up to 14500 CPS for a MMF. The cooling system in the ID210 is a three stage Peltier cooler with a cooling time of 7 minutes [41]. Dark-counting is related directly to PDE and for this reason Toshiba has high dark-counting, ID210 presents the half of that PDE due to the gate mode, and finally at free-running mode it is 15%, this PDE is expected for InGaAs SPAD [42]. The after-pulsing probability has a high percentage in ID230 due to the cooling, Toshiba's SPAD reduces that probability for the room temperature.

The SPADs performance shown in table 1.2 is a reference for the characterisations of SPADs in chapter three and four.

1.5 Summary

The optoelectronic devices are a link between electronics and optics, resulting in photonics. The quantum optic applications such the Quantum Key Distribution (QKD) needs suitable photon sources and detectors, because of the generation and detection of light is on the quantum scale. For this reason we have analysed the type of light sources available and the Poisson statistics of constant light sources such as lasers and LED's. There are three main photon sources, the most desired is the single photon source but its cost and its conditions to work, make it an unsuitable candidate for a QKD system [9, 10, 11]. For this reason, we analysed the possibility of using ordinary light sources such as LEDs and laser diodes, which in normal conditions have an excess of higher photon number pulses and this makes them unsuitable for quantum application. However when we attenuate them to less than 0.1 photons per pulse with neutral density filters and drive them with short pulse electronic circuits they can make approximate single photon sources.

The photodetectors used in quantum applications are ultra-sensitive to low amounts of light, there are versions of Avalanche Photo Diodes (APDs) that can detect single photons (Single-Photon Avalanche Diode or SPADs). Thanks to the Geiger mode an APD can detect single-photons through the generation of the electron cascade per photon detected. However, there are certain wavelengths that can only be detected by certain semiconductor materials, and the most popular for telecommunication purposes is the InGaAs/InP.

Although the InGaAs SPAD can detect single photons, it has several parameters of consideration such as: the dead-time of recovery, dark-counting, Photon-Detection Efficiency (PDE), after-pulsing probability and timing jitter. To reduce the undesirable parameters and increase the detection efficiency, there are two main modes that have been developed (free-running and gated) which are operated by quenching circuits such as passive and active quenching circuits. Nevertheless, the free-running mode is exploited in an efficient way through a new model of SPAD. The Negative Feedback Avalanche Photodiode (NFAD) introduced a thin film resistor in the semiconductor structure, the advantage of this SPAD lies in the reduction of recovery time and in the number of trapped carriers per avalanche, and this last property considerably reduces the after-pulsing probability.

Chapter 2.

Fast Optical Pulse Circuit for Alice

A QKD system needs to use single photons to ensure its security, but as it was discussed in section 1.2.1, a single photon source requires several conditions and materials and there is not a 100% probability of emitting single-photons at will. The LED and laser light pulses can be attenuated considerably in order to achieve a low photon emission [44], the attenuation reduces the mean photon number down to values of 0.1 to 0.3 photons, and thereby the probability of emitting more than one photon is reduced.

The laser diode has several characteristics which make it an ideal candidate for a QKD system, in fact most QKD experiments use lasers with attenuators to produce single photons [9, 11, 45]. However, these QKD experiments cover long distances which require light pulses with a high optical power. When the distance between Alice and Bob is short (less than 1m), the use of laser diodes begins to be an obstacle in the miniaturization and security of the system.

This chapter analyses a comparison between LEDs and laser diodes, their optical characteristics, why the LED is better for short distances, and ways to reduce the QKD system's size and cost [9]. It also discusses electronic circuits to achieve fast optical pulses with a low photon number generation and their feasibility in the real world.

2.1 Laser diode versus LED

The LED has certain similarities with the laser diode due to their structure, but when the laser diode operates beyond the current threshold, coherent laser light is emitted. The laser light is characterised by its narrow linewidth (emitting at a specific wavelength), its optical coherence and its emission into one (or a few) spatial modes. These features are important at the moment in order to choose the right optoelectronic device for a QKD system without compromising the security of the system.

2.1.1 The coherence length

The laser diode has an advantage over the LED because the laser light emitted has coherence, which it is kept in the light wave for a certain length, e.g. a laser diode L635P5 [46] has a central wavelength (λ_0) at 635nm and almost 0.25nm of spectral bandpass ($\Delta\lambda$). Using the coherence length equation (2.1) [1],

$$l_c = \frac{{\lambda_0}^2}{\Delta\lambda} \tag{2.1}$$

The coherence length $l_c$of the laser diode is determined at 1.61mm, and as a reference, a multimode Ne-He laser with a central wavelength at 633nm has a coherent length of 20cm [1]. The coherence length of the LED is much less than the laser diode because the spontaneous light emission and its radiation pattern, avoids any possible coherence after a certain length. Such as the previous explanation about the laser diode coherence length, for the LED, real model parameters were also used as an example for its coherent length. The LED MCL053HPD/5 has a central wavelength of 700nm and a spectral bandpass of 15nm [47], applying the coherence length equation for the LED wavelength parameters again, its coherent length is 32.7µm.

Although the coherence length of the LED is small in comparison to the laser diode, this inconvenience can be solved if the transverse coherence properties are considered by Duligall et al. [48]. Through the double slit system in front of the LED, the separation between the slits is adjusted until the interference effect stops. This method is applied in the Bristol QKD system although instead of the double slit system, it used a pinhole system [9].

2.1.2 Spatial distribution

The LED has an integrated lens to shape the radiation pattern of the light emitted. This redirection not only depends on the integrated lens, it also involves the LED structure. The light generated at the depletion layer can cross an LED's substrate before being released outside, this type of LED is called surface-emitting. There is an enhanced structure that releases the light without crossing any substrate, the light is released from the edge of the junction region and this structure has a better efficiency at that moment to emit light. In figure 2.1 it illustrated these two structures.

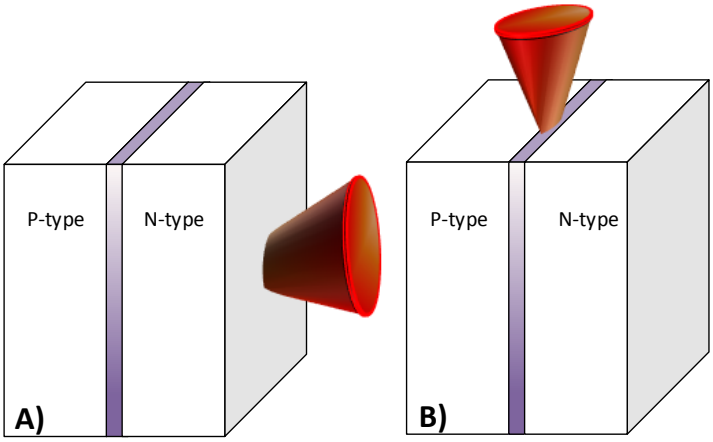

Figure 2.1: LED's structures, A) Surface-Emitting. B) Edge-Emitting

The surface-emitting structure normally has an integrated lens for a far-field radiation pattern. When there is an absence of a lens, the radiation pattern has a shape of a Lambertian radiator [1], the light intensity has a variation as a function of the cosine of the emission angle (θ). When the lens is integrated, the pattern can be extended as a function of the type of lens used, these lenses can be hemispherical or parabolic and figure 2.2 illustrated these three types of radiation patterns.

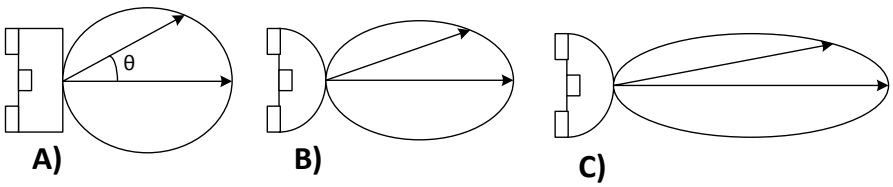

Figure 2.2: Types of radiation patterns: A) Lambertian pattern, when there is not a lens. B) Pattern with hemispherical lens. C) Pattern with parabolic lens.

The case of the edge-emitting structure is identical to the laser diodes. The radiation pattern is so narrow that the pattern can be modelled by $\cos^n(\theta)$ and θ is greater than 1. The laser diode pattern depends on its active layer dimensions l and w, the angular divergence in the plane perpendicular and parallel of l and w. In figure 2.3 it illustrated the laser diode pattern.

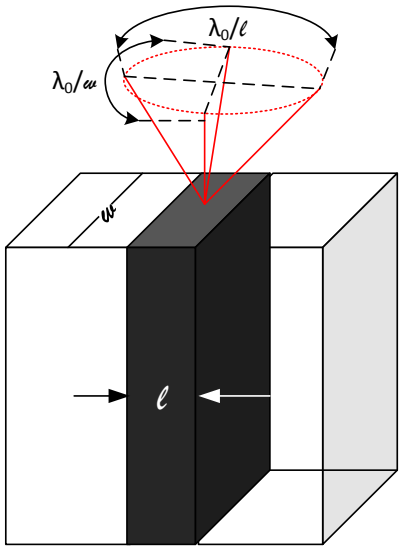

Figure 2.3: Angular distribution of the laser diode pattern, the central wavelength has an important role to define the shape of the optical beam.

For a QKD system the collimation is considered important because it avoids an increment of loss during the detection, some laser diode models have a divergence angle so small (below 0.5°) that the beam radius increases a few μm after 300 meters [1, 49, 50]. These characteristics indicated an excellent quality of laser and its light is considered collimated. However, the LED does not have the same behaviour and it is necessary to collimate its light emitter.

To solve this problem, the Bristol QKD system integrates a diffraction grating to collimate the matrix of 2x2 LEDs [9]. The experimental results with this collimation technique are acceptable, and proves that an LED can be collimated with low cost optical components.

2.1.3 Linewidth

Section 1.2 also described the spectral distribution of the LED and laser diode, but this description is focused on the type of semiconductor material used in the LED, and the factors that determine the spectral distribution in the laser diode. Such as the LED, the wavelength of the laser diode depends on certain materials added to the semiconductor substrates, e.g. a laser diode with a central wavelength of 670nm is doped with GaInP [1].

The LED has a wide spectral distribution and then its central wavelength has a variation greater than the laser diode, in figure 2.4 it illustrated this difference of spectral distribution between a laser diode and an LED.

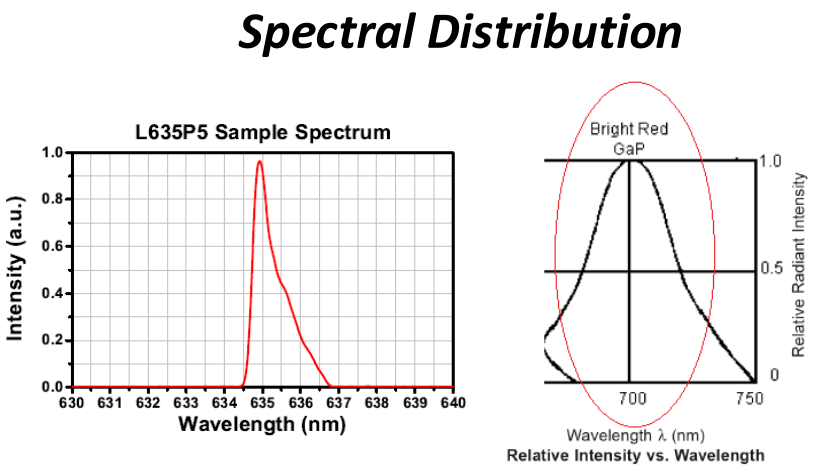

Figure 2.4: A) The spectral distribution of the laser diode L635P5 [46], B) The spectral distribution of LED MCL053HPD/5 [47].

The central wavelength between a laser diode and another has a variation from 0.1nm until a few nm. This represents a hole in the security of a QKD system, because Eve (through a monochromator) can identify the multiple light sources in Alice, unless there is only one light source and optical modulator to select a specific quantum state per pulse, but this option increases the cost, complexity and size of the system. The LED can avoid this with an optical bandpass filter, thereby all the light pulses have the same central wavelength [9].

2.1.4 The best candidate for a light source in a QKD system

The previous sections compare three optical characteristics (coherence, spatial distribution and linewidth) of the LED and laser diode. The laser diode has certain advantages over the LED and makes it an ideal candidate. However, its use is recommended for long distances [36, 38, 49] and when the cost of the system is not an design parameter.

The LED has been used in some QKD systems including the Bristol QKD system, which received good critics in the security communication based on the quantum cryptography (SECOQC) international conferences [44]. The LED used as a light source in a QKD system that covers short distances (< 1m), has excellent cover in the security of the system and any inconvenience described in the previous sections can be solved with low costs and easy methods.

The electric requirements of the laser diode such as a current control for its threshold current, is indicated as a problem by Lowndes et al [9] when the rate repetition of the light pulses are high. Although it can be solved with electronic circuits, in order to produce low photon numbers per short pulse injected, there is a high possibility that the threshold current is not reached, this scenario makes the laser diode in to a super-luminescent LED [1].

A design of an electronic circuit which can drive an LED to generate fast light pulses becomes a solution to replace a laser diode. However, it is necessary to know the response of the LED at high frequencies, such as the maximum modulation bandwidth that an LED can hold, and consider the effect of high frequency pulses of the production of minority carriers and radiative recombination.

2.2 LED modulation bandwidth limit

A limitation in the LED when it is applied with electrical signals (continuous or discrete), is the LED response time since the electric signal is applied until the light emission. This delay is due to the lifetime (τ) of the minority carriers [1], which start the radiative

recombination. The injected carrier concentration and recombination process can be modelled by a first-order linear differential equation (2.2) [1], allowing to know the carrier concentration behaviour under a continuous signal e.g. a *sinusoidal signal*.

$$\frac{d(\Delta n)}{dt} = \mathcal{R} - \frac{\Delta n}{\tau} \tag{2.2}$$

Where $\mathcal{R}$ is the electron-hole injection rate, arising from the electric current injected in the LED (a signal), and Δn is the concentration of excess electron-hole pairs. However, a zero cross signal can have a different effect on the light emission, due to the exponential decay of Δn with a constant time. This behaviour represents a limitation for signals at high frequencies, but this inconvenience can be easily solved if the signal sits on a DC bias and we work in the small signal limit.

Thereby, the light emitted can be modulated by the injected current $i = i_0 + i_1 cos(\omega t)$ and the output light power is $P = P_0 + P_1 cos(\omega t + \phi)$ [1]. This example is for a sinusoidal signal $v_1 \sin(\omega t)$ but voltages and currents are out of phase 90° and for this reason the current is represented as a cosine function [52]. The relationship between injected current and output light power can be modelled by a transfer function in the equation (2.3) [1].

$$\mathcal{H}(\omega) = \frac{P_1 \cos(\omega t + \phi)}{i_1 \cos(\omega t)} = \frac{P_1}{i_1} e^{j\phi} = \frac{\Re}{1 + j\omega t} \tag{2.3}$$

The responsivity $\Re$ is involved during the modulation due to the relationship between optical power and electric current. The transference function $\mathcal{H}(\omega)$ is characteristic of resistor-capacitor circuits and this is due to the LED properties such as resistance presented when it is applied with a current and capacitive effects. The LED bandwidth depends on the light pulses rise time and it has a direct influence on the bandwidth; if the rise time is short, the bandwidth is large.

The rise time is a result of the radiative and non-radiative time expressed in equation (1.2), i.e. the rise time is the recombination time. Therefore, the bandwidth is $B = \frac{1}{2\pi\tau}$ which includes τ as the rise time. However, for the QKD system we need to drive the LED with pulses to achieve approximate single photon generation.

Driving with discrete electronic signals are necessary to control the duration of light pulses and in this case requires an analysis of the impulse response (rather than small signal response) of the LED.

2.2.1 Analysis of the LED transient response

The LED has a certain response to fast electrical pulses when the LED is energised and de-energised. The LED response is modelled through its equivalent circuit as shown in figure 2.5.

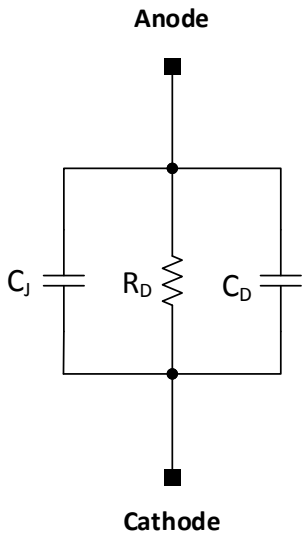

Figure 2.5: LED equivalent circuit in forward polarization, where C_J is the capacitance of the junction (despised), R_D is the resistance of diffusion and C_D is the capacitance of diffusion.

This resistive-capacitive circuit generates a certain response, which consists of the superposition of the LEDs natural response and force response. The components (R_D and C_D) are determined through the equations e.g. the resistance of diffusion (R_D) is determined by equation (2.4).

$$R_D = \frac{K_B T}{e^- i_0} \tag{2.4}$$

Where i_0 is the current at an initial time (when the pulse starts) and $\frac{K_B T}{e^-}$ has an approximate value of 25mV at room temperature (300K). The capacitance of diffusion (C_D) is determined by the equation (2.5).

$$C_D = \frac{e^- i_0 \tau_p}{2 K_B T} \tag{2.5}$$

The expression τ_p is the recombination time of carriers in the LED after a discrete function (a pulse). The electronic (current) time constant is determined by R_D and C_D in parallel.

$$\tau = R_D C_D \tag{2.6}$$

The capacitance C_D current is represented by the differential equation (2.7) because C_D does not oppose abrupt changes of current.

$$i(t) = C_D \frac{dV(t)}{dt} \tag{2.7}$$

The first response to the analyses of the equivalent circuit is the step response when it is energised at an initial time (t = 0). Figure 2.6 illustrates a Direct Current (DC) analysis of the equivalent circuit with a current distribution and a load resistance (R_L), because normally the LED is connected to a proper R_L.

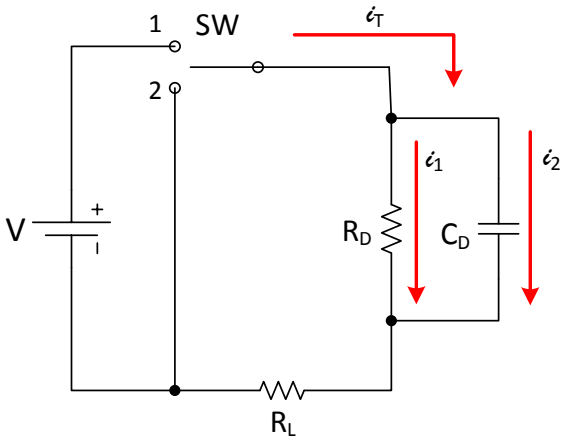

Figure 2.6: The LED Equivalent Circuit showing the current distribution.

When the switch is in position 1, the total current i_T is equal to i_2 because C_D behaves as a conductor at an initial time (assuming that C_D is discharged). Hence, i_T is determined by the equation (2.8).

$$i_T = {}^{V}/_{R_L} \tag{2.8}$$

After the initial time (soon immediately) C_D begins to charge and this charge is determined by the substitution of equation (2.7) in (2.8). Since i_1 is 0, the charging voltage is as a function of time and it is represented by the equation (2.9).

$$V(t) = \frac{V}{R_L C_D} \int dt \tag{2.9}$$

This equation represents the voltage slope charge of C_D from the initial time when the switch is closed until the circuit enters in to a steady-state. Once reaching the steady-state, C_D is considered fully charged and it is considered as an open circuit, hence there is a new equivalent circuit illustrated in figure 2.7.

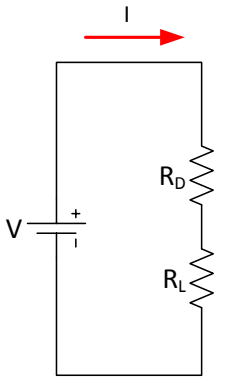

Figure 2.7: LED equivalent circuit showing when it is in a steady-state.

Kirchhoff's voltage law easily determines the total current (I) and the voltage for each resistor. The step response of the LED is expressed in the equation (2.10) and due to R_D is at parallel with C_D, the total current in the LED is represented by the equation (2.11).

$$V_{R_D} = V - V_{R_L} \tag{2.10}$$

$$I = \frac{V}{R_D + R_L} \tag{2.11}$$

The natural response is determined by the absence of any power supply, so the switch is in position 2 (figure 2.6). In this situation, C_D stored energy when the switch was in position 1 and now it is considered as a voltage source. Therefore, the Kirchhoff's current law is applied but without the main voltage source (V), hence the summation of i_1 and i_2 is 0 and the differential equation is expressed as the equation (2.12).

$$\frac{V_{C_D}(0^+)}{R_{eq}} + C_D \frac{dV_{C_D}(0^+)}{dt} = 0 \tag{2.12}$$

The expression 0^+ indicates the initial conditions and R_{eq} represents an equivalent resistance of the parallel connection between R_D and R_L. Furthermore, C_D corresponds to

a decrease in exponential when the equation (2.12) is solved. This solution includes a time constant which is different from the equation (2.6) because R_L is considered in the natural response analysis

$$V_{C_D}(t) = Ae^{S_1 t} \tag{2.13}$$

The time constant S_1 is $-\frac{1}{R_{eq}C_D}$, A represents the voltage stored by C_D and it was expressed as an initial voltage when the switch passed to position 2 (V_0). Thereby, the natural response of the LED during the discharge of C_D is expressed in the equation (2.14).

$$V_{C_D}(t) = V_0 e^{-\frac{t}{R_{eq}C_D}} \tag{2.14}$$

The total response of the LED is determined by the summation of the step response and the natural response, which is shown in the equation (2.15).

$$V_{C_D Total}(t) = V - V_{R_L} + V_0 e^{-\frac{t}{R_{eq}C_D}} \tag{2.15}$$

The graph of this equation shows the behaviour of the LED when a fast electrical pulse is applied, as shown in figure 2.8.

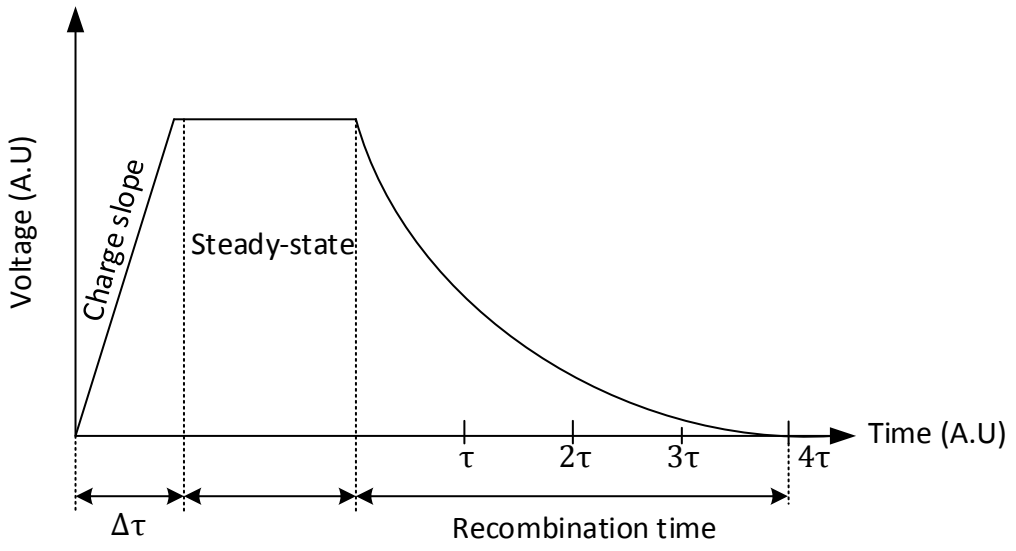

Figure 2.8: A Graph showing the LED under a fast electrical pulse. When the LED is energised, C_D begins to charge until it reaches a steady-state when the pulse ends, it begins the discharge of C_D in the depletion zone. τ represents the recombination time as shown in the equation (3.3).

The recombination time is a surplus after the fast electrical pulse excitation and represents a problem with generating a suitable short pulse and mean photon number discussed in section 1.1.1. However, it is possible to reduce the recombination time through electronic circuits and thus turn the LED into a good approximation to a single photon source [9, 11].

2.2.2 Solutions to reduce the Recombination time

The previous section explains the recombination tail in the depletion layer when the LED is forward biased. To stop the recombination quickly it is necessary to reverse biased the LED soon after the fast electrical pulse excitation. When the LED is reverse biased the potential barrier increases and the electrons in the depletion layer are swept out into the n-side. This recovery also depends of the potential applied and the mobility of the electrons. In figure 2.9 we illustrate the energy diagram of the LED when it is reverse biased.

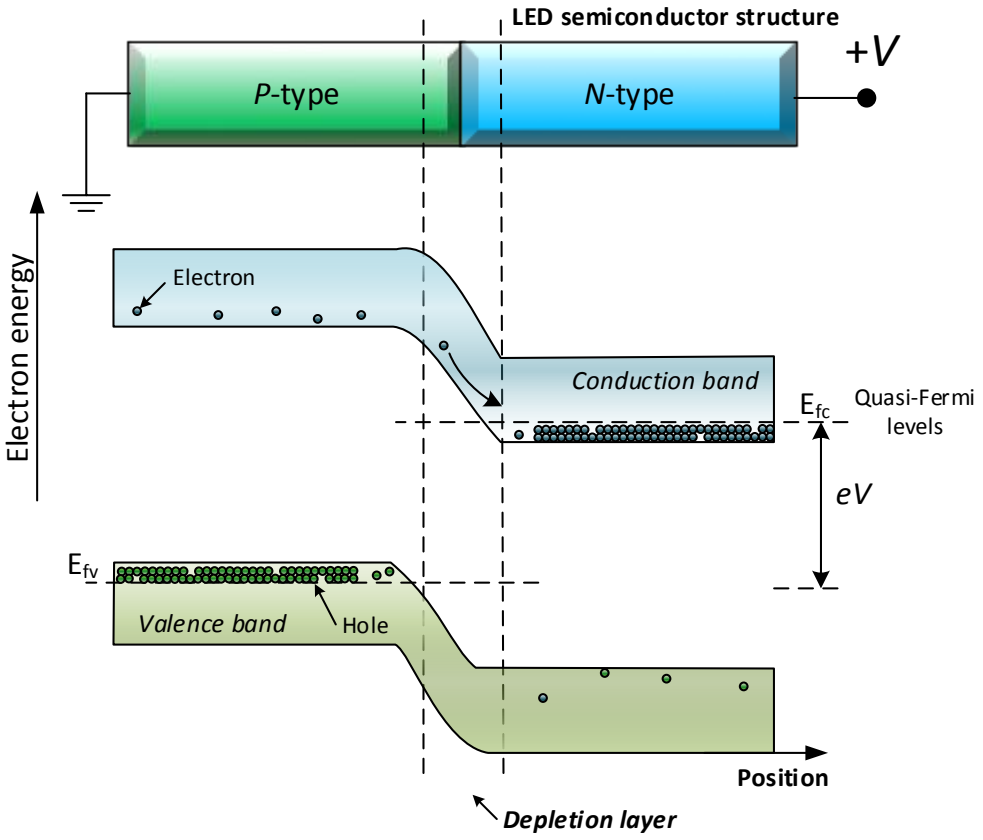

Figure 2.9: When the LED is reverse biased, the potential barrier in the bandgap and the depletion layer increase, this provokes that all the in the depletion layer return to the n-side.

The reverse bias in the LED can be achieved by:

- Monolithic integrate circuit.
- Discrete circuit.

Both circuits inject fast electrical pulses and immediately after the pulse ends, there is a reverse bias in the LED. For example, the amplitude of the pulses could be 7V, sitting on a -2V offset voltage to reverse bias the LED. Hence, 5V forward bias overpasses V_{on} and -2V are used to sweep out excess minority carriers, ensuring the spontaneous photon emission is stopped after the end of the pulse. Figure 2.10 illustrates the electrical pulse proposed to excite the LED.

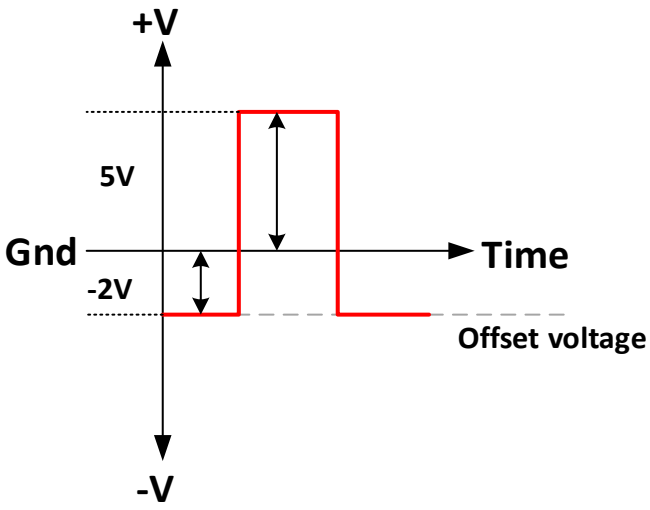

Figure 2.10: The electric pulse has 7V of amplitude, 2V are under the ground reference and the voltage over the ground (Gnd) reference corresponds to the forward bias voltage that will start the spontaneous photon emission.

The repetition rate of optical pulses is limited by the width of the electric pulses [9]. A high repetition frequency of the fast electrical pulse is required to ensure a high rate of photon emission (at ~0.1 photons per pulse). Typically it is necessary a frequency of over 100MHz to achieve 10^6 detected photons per second assuming a channel loss of 10dB which would acceptable lengths of raw key to be generated in seconds. It is also advantageous to have a short pulse of <1ns duration to allow gated detection reducing dark count and background light counts in the system.

2.3 LED Driver circuits

Ever since the production of LEDs, there have been multiple circuits to drive them. Although the LEDs have been closely related to the digital electronics, e.g. the first LED display design was the 7-segment display which showed a number processed by digital logic. Hence, the LED driver used in digital electronics is a direct connection with the logic gate as illustrated in figure 2.11.

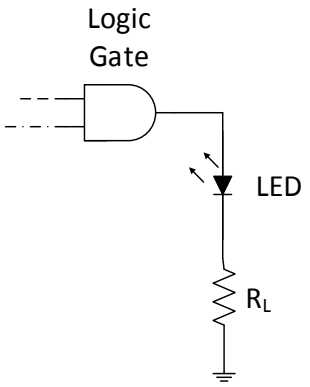

Figure 2.11: Schematic diagram of an LED connected to a logic gate (AND).

The LED power supply requirements are not considerably high, they only require a forward bias voltage normally set between 1.8V and 3.3V (depending on the LED colour), with a forward current of around 20mA. Therefore, the circuit illustrated in figure 2.11 is suitable. However, if the LED requires more current or the LED driver circuit has to supply more than one LED, it is necessary to setup a proper circuit between the logic gate and the LED. A common solution to this problem is to use a transistor in common-emitter mode and use its current amplifying properties as illustrated in figure 2.12.

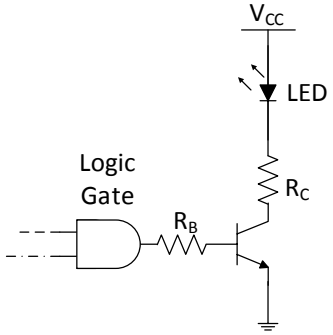

Figure 2.12: The Coupling circuit used to connect the logic gate and the LED, the circuit is a transistor NPN in common emitter configuration, where R_B is the base resistor, R_C is the collector resistor.

The LED frequency limitations are previously explained in section 2.2.1 but it is also necessary to mention some parasitic effects within the circuit driver as shown in figures 2.11 and 2.12. The logic gate has a certain frequency response, but its output power is reduced considerably when there is a load, because the connection distance introduces inductive and capacitive effects and thus, it is necessary to consider an impedance coupling circuit with the LED.

For a coupling circuit similar to the circuit in figure 2.9, it is necessary to analyse the transistor's features at the frequency used for the light communication [53, 54]. When the transistor is subjected to a higher frequency, it shows internal inductive and capacitive effects [3]. Figure 2.13 shows an illustration of the equivalent circuit of the transistor NPN at low-frequency conditions and with high-frequency conditions.

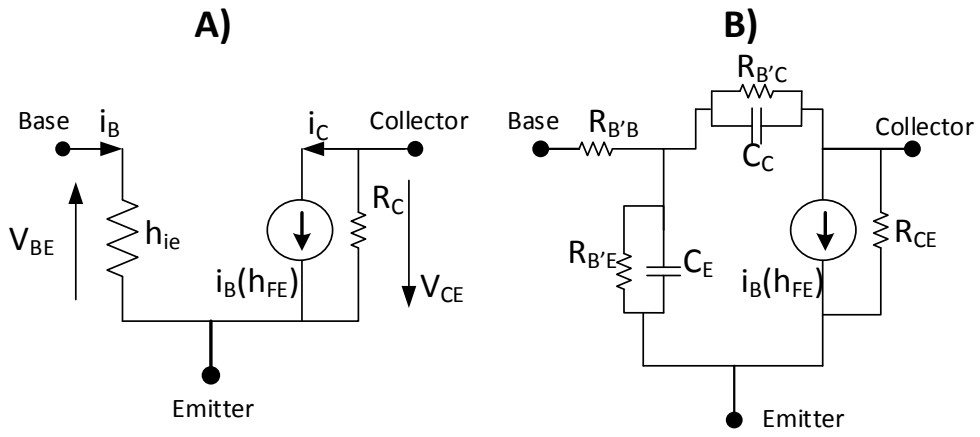

Figure 2.13: The Hybrid model π of the bipolar junction transistor (BJT) NPN in common emitter configuration at: A) Low frequency conditions. B) High frequency conditions.

Where V_{BE} is the base-emitter voltage, V_{CE} is the collector-emitter voltage, $R_{B'B}$ is the base spreading resistance, $R_{B'E}$ is an internal base node to emitter resistance, R_{CE} is a collector to emitter resistance, $R_{B'C}$ is a feedback resistance from internal base node to collector node, C_E is a diffusion capacitance of the emitter base junction and C_C is a space charge capacitance of the base collector junction and hFE is the hybrid parameter forward current gain, common emitter.

The LED also presents undesired effects due to high frequencies such as inductive parasites through the metallic connection to the p-n junction. Normally, this effect is dismissed at low frequencies, but should be considered when the LED is excited by microwave frequencies [54].

Other electronic devices can be suitable for a driver such as Field-Effect Transistors (FET) [55], ultra-high frequency operational amplifiers (Op-Amp) and high frequency BJT such as the BFG198 transistor [56, 57].

2.3.1 High-Speed LED Drivers

The THS3202 is a high-speed Op-Amp that operates a frequency of 2GHz with a unity gain [57], this Op-Amp is suitable for the offset voltage proposal because many of the properties in Op-Amps are a comparison between the non-inverter and inverter inputs. Therefore, when there is an absence of electric pulses, the LED reference can be set at a negative voltage. Furthermore, the THS3202 has the property of dual voltage supply which makes any negative voltage reference easier.

The Op-Amp driver has some advantages such as a high amplitude in the electric pulse, but reverse biasing the LED is not simple and this technique is widely analysed in topics of power electronics especially H-bridges [58]. The rate repetition of the frequency proposed to generate single-photons is >10MHz with fast electrical pulses of 1ns [9]. Therefore, the electronic devices must be suitable for holding frequencies in the range of GHz, even if the rate repetition is in order of MHz, because the electrical pulse duration is shorter than the switching time in electronic devices (normally in the order of hundreds of nanoseconds).

2.4 LED Drivers proposed for Alice

The Op-Amp THS3202 has an application circuit proposed by the manufacturer which exploits its bandwidth, this application circuit is supplied by the manufacturer in an evaluation module [59], which is already assembled and it is suitable to test the offset voltage. The discrete circuit is built using RF transistors such as the BFG198 with a configuration that is suitable for high frequencies (8GHz of bandwidth).

2.4.1 Evaluation Module of the Operational Amplifier THS3202

This module has two different circuits but using the Op-Amp, which operate at different voltage gains in the signal output, the first circuit has a voltage gain of -1 or +2 depending on which input is used and for analysis purposes in which both inputs are analysed, as shown in figure 2.14 which illustrates the first circuit in the evaluation module of Op-Amp THS3202.

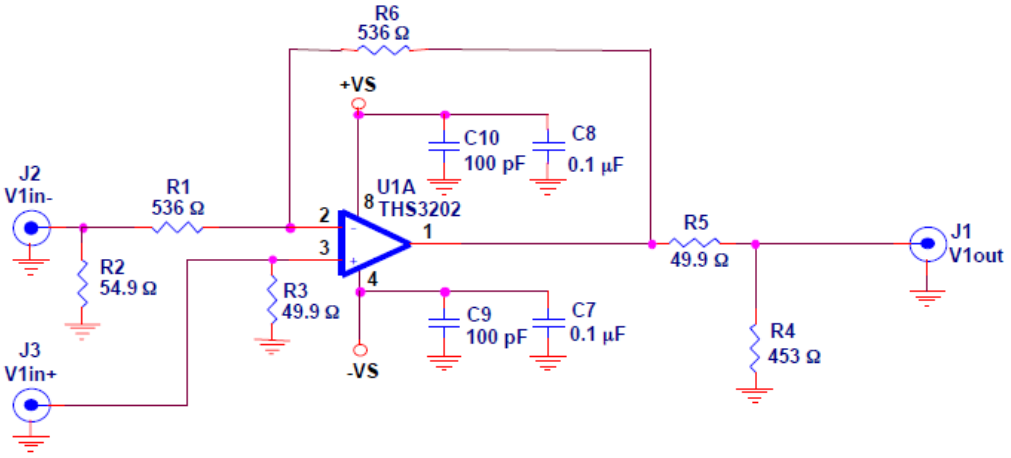

Figure 2.14: Test circuit 1 of the two Op-Amps in the evaluation module taken from [59].

The voltage ratio gain is defined in different ways depending on which input is used. If used, then the inverter input of the voltage gain is defined by the following equation (2.16) [59].

$$G_{Voltage} = -\frac{R_6}{R_1}\left(\frac{-R_4||50\Omega}{R_4||50+R_5}\right) \tag{2.16}$$

This circuit has a slight gain error due to R_4 and it is included in the equation. Although, R_6 defines the total voltage gain, the gain obtained is -0.474 (without units) due to the negative gain. The non-inverter input has another voltage gain equation with R_1, which includes a slight error such as in equation (2.16).

The product R_2 is also considered as part of the error and the equation (2.17) determines the voltage gain in the non-inverter input.

$$G_{Voltage} = \left(1+\frac{R_6}{R_1+R_2}\right)\left(\frac{R_4||50\Omega}{R_4||50+R_5}\right) \tag{2.17}$$

The gain obtained by this equation is 0.911 (without units) and it is suitable for an LED driver. The second circuit in the evaluation module has free resistor spaces that should be connected to the inverter input. This circuit is suitable for being modified without affecting the print board circuit (PCB) of the module, as shown in figure 2.15 which illustrates the second circuit of the module.

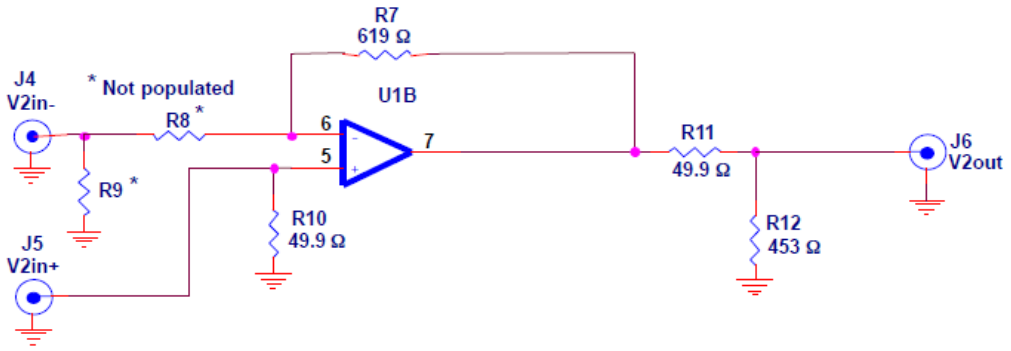

Figure 2.15: Test circuit 2 of the two Op-Amps in the evaluation module taken from [59].

The gain error in this circuit is determined by R_{11} and R_{12} i.e. the value is identical to the gain of the inverter input in the first circuit. The modifications in this circuit for a proper LED driver includes a feedback resistor, because the voltage gain should be equal or greater than 1 but without affecting the frequency stability. Therefore, the resistors placed in the spaces of R_8 and R_9 have a value similar to circuit 1 to ensure the frequency stability, nevertheless, R_7 is modified to increase the gain nearer to 2.

2.4.2 Switching Driver with Discrete Components

This circuit is based on a half-bridge used in the power electronics [58]. Therefore, the LED should have a terminal connected to the ground or rail voltage (typically 5V) (i.e. the cathode is connected to the ground or the anode to a power supply). The other terminal should be connected to a switching circuit that is activated by the fast electrical pulses, but there is also another circuit which supplies a voltage to reverse bias the LED under the absence of the fast electrical pulses (dead-time).

The switching driver is formed by a group of circuits which control the current in the LED. Because of this, it is easier to control a discharge than a stimulation and hence the LED anode which is directly connected to 5V. A block diagram of the circuit operation is shown in figure 2.16.

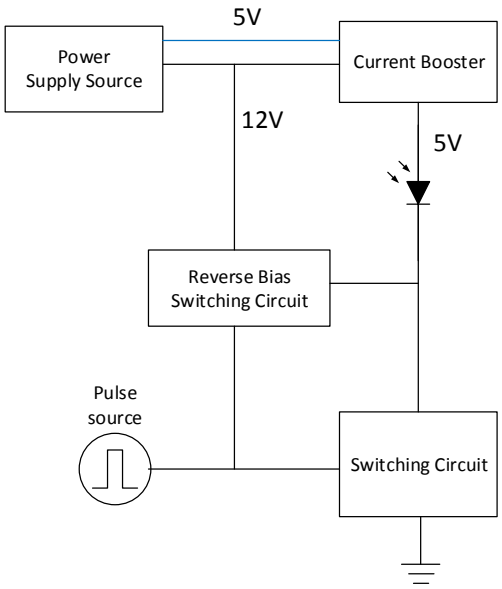

Figure 2.16: The Block diagram of the switching circuit proposed as an LED driver.

The current in the anode should be sufficient to avoid any falling voltage which would result in a low photon rate emission from the LED. To solve this problem, it is added to another circuit to ensure a high current level and to ensure stability. This circuit is known as a current booster and its schematic diagram is illustrated in figure 2.17 below.

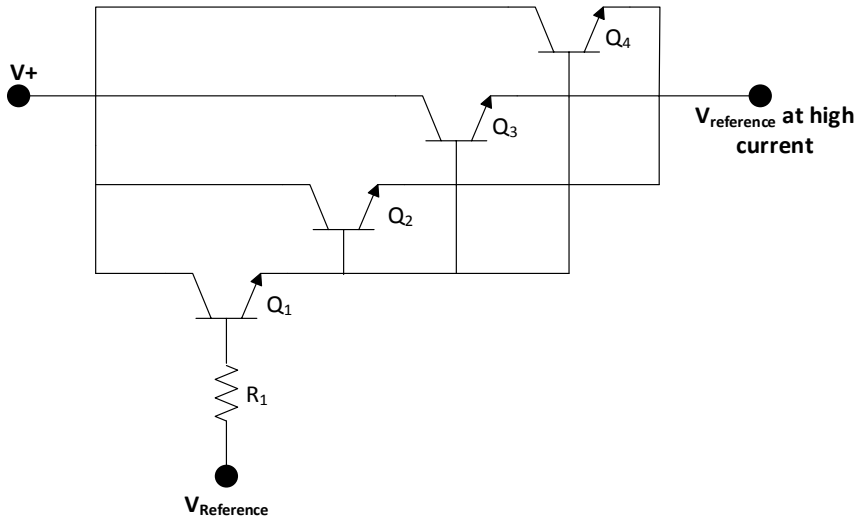

Figure 2.17: Electronic schematic diagram of a current booster circuit.

The current booster circuit is composed by 4 NPN transistors in a common base configuration, this configuration is commonly used as a voltage regulator because there is no current gain but there is a voltage gain. Hence, the current booster circuit has a reference voltage (5V) that's controlled by the transistor Q_1 and the current is increased

by three transistors (Q_2, Q_3 and Q_4), this circuit has another voltage supply (12V) of more current than the voltage. The maximum current supplied by this circuit in theory is 1A but in practice, the LED does not demand more than 100mA (for an ultra-bright LED).

The fast electrical pulses have a rate repetition of >10MHz and thereby the switching circuit and the reverse bias switching circuit should be designed such as a tuned circuit. This means that both circuits should isolate their inputs from the pulse source in DC but not in an Alternating Current (AC). Moreover, these circuits should avoid any filtration of switching frequency to the power source, as shown in figure 2.18 which illustrates the schematic diagram of the switching circuit.

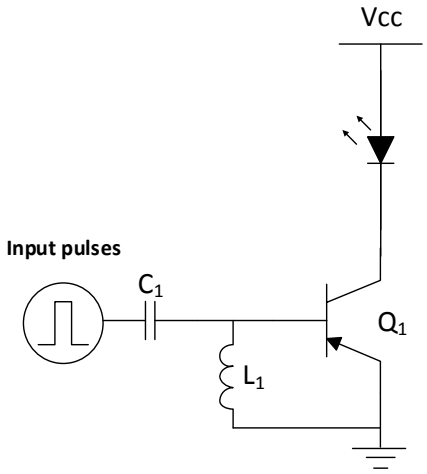

Figure 2.18: Schematic diagram of the switching circuit.

The capacitor is isolated in DC with the transistor and only the pulses cross it to the base. Therefore, the inductor ensures that the operation point obtains the maximum efficiency of the transistor (also used in amplifiers class C) [3].

Therefore, every time a fast pulse crosses the capacitor and reaches the transistor base, the transistor enters to a saturation and closes the circuit between the LED and the ground. The reverse bias switching circuit has two transistors to control a reverse bias voltage in the cathode of the LED, and the transistor Q_1 is in the cut-off region which only enters the saturation region when receiving the fast electric pulse.

These two regions control the operation of the transistor Q_2 and thus, supply a voltage to the cathode of the LED. During the absence of the fast electric pulse, the Q_2 is in the saturation region but when the fast electric pulse is present, the Q_2 enters the cut-off region by stopping the voltage being supplied and allowing the switching circuit to work

properly, as shown in figure 2.19 which illustrated the schematic diagram of the reverse bias switching circuit.

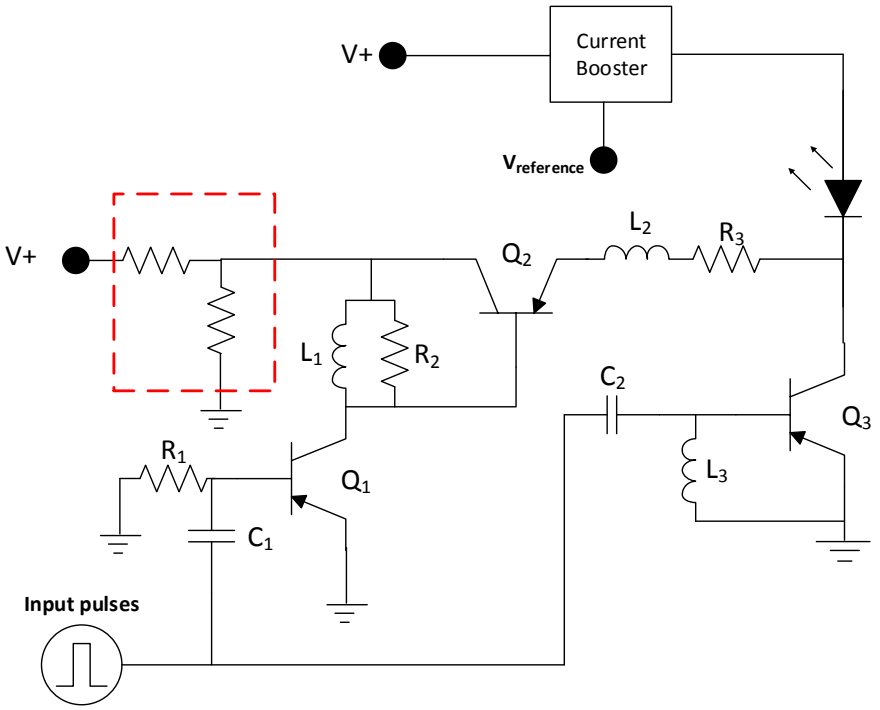

Figure 2.19: Schematic diagram of the reverse bias switching circuit, the red dashed line square box indicates a voltage divider to adjust the voltage in the collector of Q_1 and Q_2.

The base of Q_1 is coupled with a capacitor to the input signal and R_1 ensures the cut-off of Q_1 in the absence of a fast pulse. Inductor L_1 has the function to set the current in the collector of Q_1 on AC conditions and R_2 in DC conditions. The resistors enclosed in the red dashed line square are a control for the reverse bias voltage (voltage divider) in the collectors of Q_1 and Q_2.

Inductor L_2 stops the filtration of the switching frequency from the switching circuit. However, during the pulse fall, there is a lapse in time when Q_2 and the switching circuit have a saturation region coincidence. This effect is widely studied in the H-bridges which provokes the damage of one of the two transistors involved in the commutation [55, 56]. This case is not an exception and hence, it introduces the R_3 resistor to reduce the current during the coincidence lapse time.

The voltage difference between the anode and cathode of the LED should be -2V during the dead-time, although this difference could be larger, and it can increase the current on the switch circuit or the reverse bias switching circuit.

2.5 The Experimental test

The experimental test of the LED's drivers requires an optical arrangement where the LED light can be forwarded to a photo-detector. The elements of this optical arrangement are an LED model TLHR4400 of Vishay®, with a λ of 625nm and a forward voltage and current of 2V and 10mA respectively. An aspheric lens ACL2520U-DG6 of Thorlabs® which concentrates the light on the multi-mode fibre optic (MMF) model FG105LCA of Thorlabs® with a 105um core diameter and 0.22NA.

The light intensity of the fibre is monitored with a Thorlabs® power meter model PM100D (photodetector S130C), to adjust the distance between the lens and MMF. This distance is estimated by the equation (2.18).

$$\frac{1}{d_1} + \frac{1}{d_2} = \frac{1}{f} \tag{2.18}$$

The focal length (f) of the lens is specified at 20.1mm and the distances d_1 and d_2 are adjusted at a value determined by f, although the distances can be adjusted experimentally by moving the lens until obtaining the maximum optical power. Thereby, the distances obtained are 28.5mm for d_1 and 93.5mm for d_2, and when these values are applied to (2.18) it results in a value close to f. Figure 2.20 illustrates a scheme of the optical array.

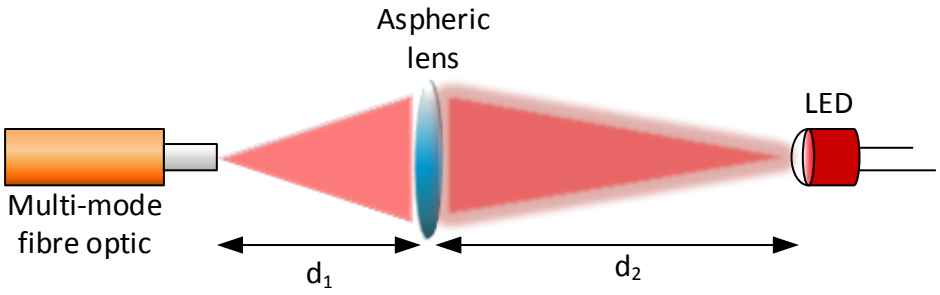

Figure 2.20: Scheme of the optical array for an optical coupling.

The generation and measurement of the optical pulses requires certain equipment. The electrical pulses are generated with a pulse generator model 81101A of Agilent Technologies®, and monitored by an oscilloscope (4GHz model DSOS-404A of Keysight Technologies®).

The optical pulses are detected with a single photon detector module of iDQuantique® model iD-100-50-MMF, with a time resolution of 60ps and a detection efficiency of 25% at 600nm. The photon detections obtained are registered through a Time-Correlated Single Photon Counting (TCSPC) module PicoHarp 300 of PicoQuant®, which the acquisition resolution on the TCSPC fixed at 512ps. Sufficient to measure the optical pulses of widths greater than 1ns.

The scheme diagram of the experimental system can be illustrated through figure 2.21.

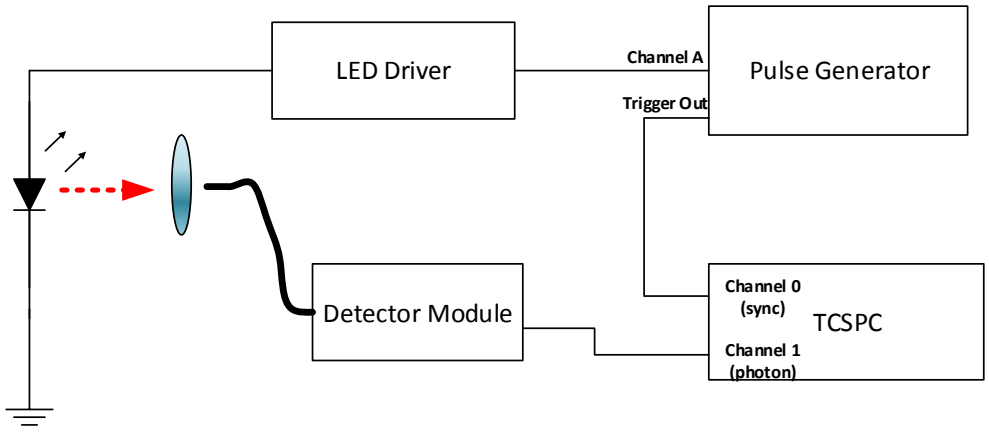

Figure 2.21: Scheme diagram of the connection between the equipment used in the experimental system.

The LED drivers proposed in section 2.4 are supplied by the dual power source model EL302RT of Aim-TTi®, with an adjusted variable from 0 to 30V and 0 to 2A. The impedance between the pulse generator, LED drivers and LEDs has an important role, and it is settled at 50Ω to avoid signal reflections of the electric pulses.

The electric pulses amplitude is fixed at a maximum value of 2.5V (maximum possible) on the pulse generator, and the electric pulse width is fixed in 3 different values: 1, 2 and 5ns. The rate repetition of these pulses are fixed at 10MHz, although this frequency could be less but it has a direct influence on the brightness and hence, the photon count rate.

2.6 Experimental results

Before testing the LED circuit drivers, it is necessary to note the natural response of the LED. Therefore, an LED test with a direct connection to the pulse generator can bring information about the LED, and its response to fast electrical pulses.

2.6.1 Control test results

The TCSPC registers the optical pulses in to histograms and the utility software displays several measurements, but the most important measurements are the photon count rate and the Full Width Half Maximum (FWHM) of the optical pulse [60]. This parameter is obtained by the tracing of the time distribution of all the curves, in which the peak value is the main reference. Table 2.1 lists the measured width of optical pulses with their corresponding electrical pulses.

Electrical pulse width	Optical pulse width	Photon count rate
1ns	*No emission*	*No emission*
2ns	6.65ns	$3.4x10^3$
5ns	8.19ns	$1.82x10^3$

Table 2.1: Optical and electric pulses widths with their corresponding photon count rate.

The optical pulse generated is around 4ns wider than the electric pulse for 1ns pulses, there are no emissions from the LED. Figure 2.22 illustrates the TCSPC histograms of the time delay between the electrical pulse trigger and photon detection plotted in Matlab.

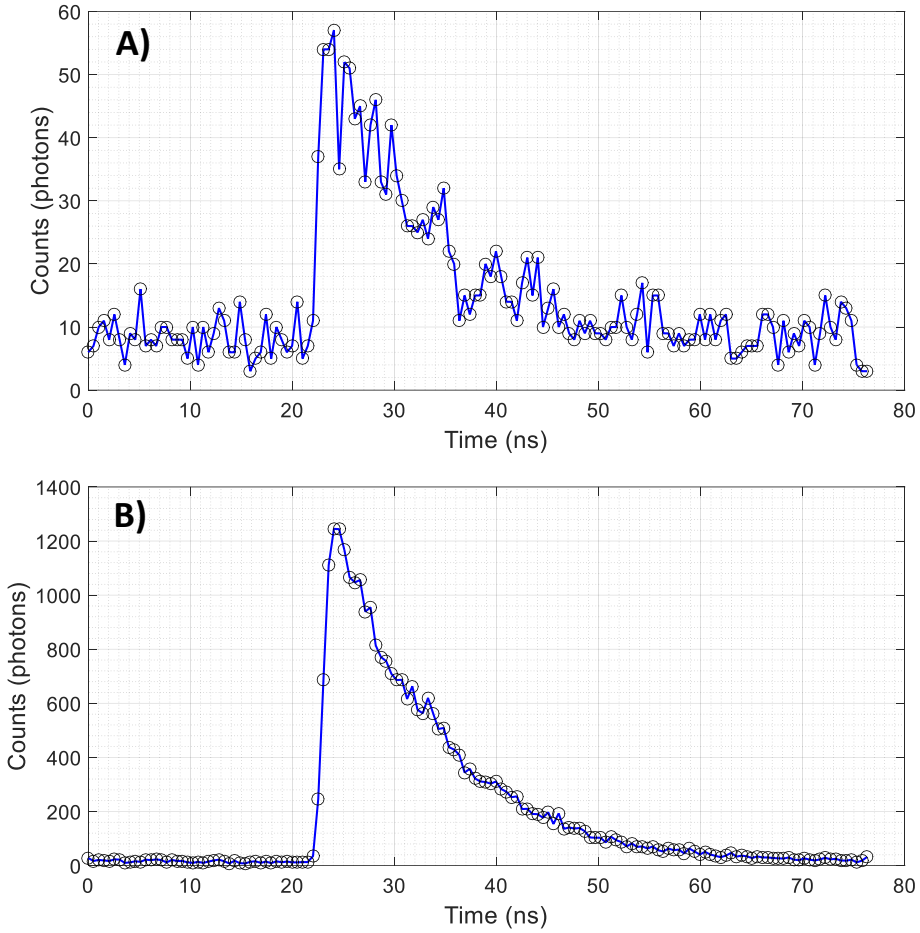

Figure 2.22: Optical pulses registered with a TCSPC: A) Optical pulse corresponding to an electric pulse width of 2ns. B) Optical pulse corresponding to an electric pulse width of 5ns.

2.6.2 The Operational Amplifier THS3202 test results

The evaluation module has the characteristics to use a dual voltage supply mode or a single voltage supply mode. But for the experimental test, the evaluation module uses a dual voltage supply mode to introduce the offset with a negative voltage. Also, it is necessary to reduce the frequency repetition to 1MHz to appreciate the exponential shape.

The optical pulses have a considerable reduction on their width when compared to the optical pulses in the control test, and an important fact is the photo emission with an electric pulse width of 1ns. However, the photon count rate in all the pulse widths used is under 10^4 CPS. Table 2.2 concentrates on the optical pulses width for the experimental test with the Op-Amp.

Electric Pulse width	Op-Amp THS3202	
	Optical pulse (FWHM)	Photon count rate
1ns	1.53ns	6.37×10^2 CPS
2ns	2.04ns	7.22×10^2 CPS
5ns	5.56ns	1.95×10^3 CPS

Table 2.2: Optical pulse widths and their corresponding photon count rate for the Op-Amp THS3202.

The width reduction is more evident when the optical pulses of the Op-Amp are compared to the control tests optical pulses. Figure 2.23 illustrates the optical pulses obtained with the Op-Amp for 1ns and 2ns.

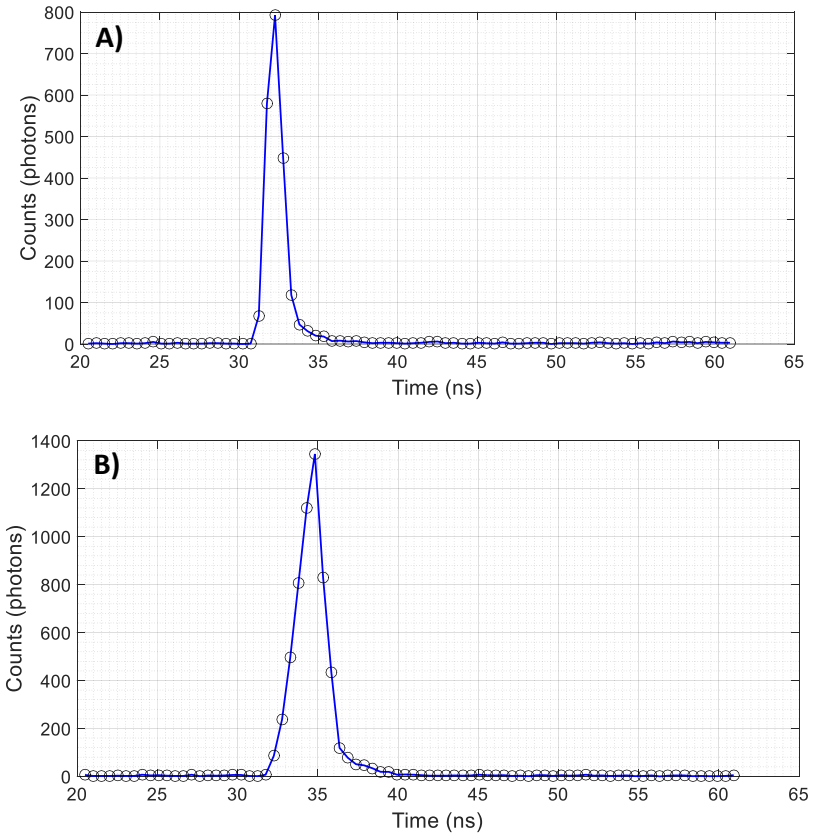

Figure 2.23: Optical pulses registered with a TCSPC by the Op-Amp: A) Optical pulse corresponding to an electric pulse width of 1ns. B) Optical pulse corresponding to an electric pulse width of 2ns.

These results confirm the success of quenching the radiative recombination with the Op-Amp through the offset voltage. Although, there is a restriction of the photon emission that could represent a problem for the QKD system [9].

2.6.3 The Switching Driver results

This LED driver is not a proper amplifier but it can control the current through the LED. Unlike the Op-Amp driver, the switching driver does not need a high amplitude to activate the circuits because they are controlled by the current. The currents on the transistor bases do not pass 5mA (theoretical estimation) to saturate them, hence the control is ensured. When the LED is connected to the switching driver, it presents a considerable brightness for pulse widths of 5ns. For 2ns and 1ns, this brightness is greater than the Op-Amp Driver but less than 5ns. The electrical signals are similar to the simulation and they are illustrated in figure 2.24.

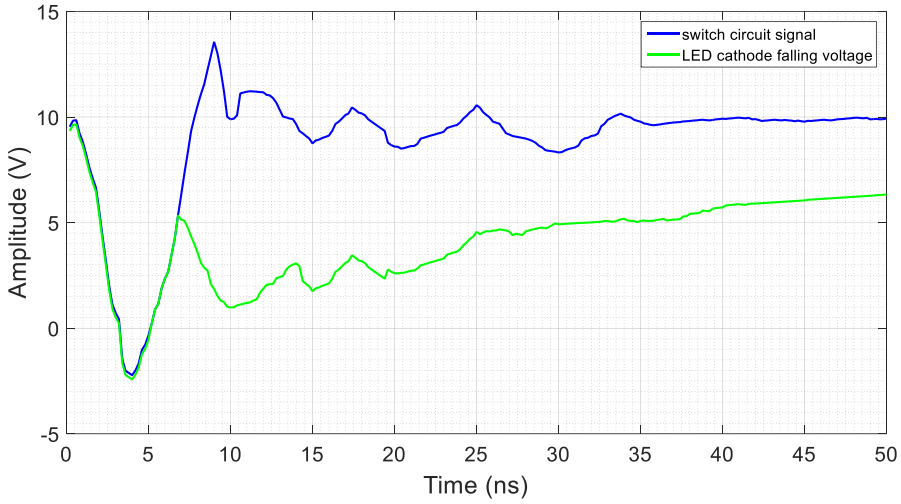

Figure 2.24: Electrical signals obtained with an oscilloscope probe from the switching driver, the green signal is the cathode falling voltage and the blue signal is the switch signal on the base transistor Q_2 of the schematic diagram as shown in figure 2.19.

There is a recharge zone that delays some decades of nano-seconds to restore the initial voltage, a particular feature in figure 2.24 is the reverse voltage on the cathode. This voltage level is due to the resistor values on the voltage divisor because they are not precision resistors. However, this level of voltage does not affect the brightness of the LED.

The optical pulses achieved with the switching driver circuit have a good performance because they reduce the width excess on the LED significantly. Furthermore, the photon count rate is nearly 10^4 CPS. Table 2.3 shows the registered optical pulses widths and their photon count rate for the times under test (1ns, 2ns and 5ns).

Electric Pulse width	Switching Driver	
	Optical pulse	**Photon count rate**
1ns	1.02ns	7.27×10^3 CPS
2ns	2.04ns	8.30×10^3 CPS
5ns	5.56ns	1.19×10^4 CPS

Table 2.3: The Optical pulses widths and their photon count rates achieved by the switching driver.

The optical pulse shape of this LED driver is considerably short such as the electric pulse, quenching the radiative recombination to the minimum after the electric pulse excitation. The comparison of these pulses with the control test pulses shows a width increment of around a few pico-seconds on the electric pulses widths of 1nS and 2ns. For 5ns, it increases to hundreds, as shown in figure 2.25 which illustrates the optical pulses obtained by the switching driver.

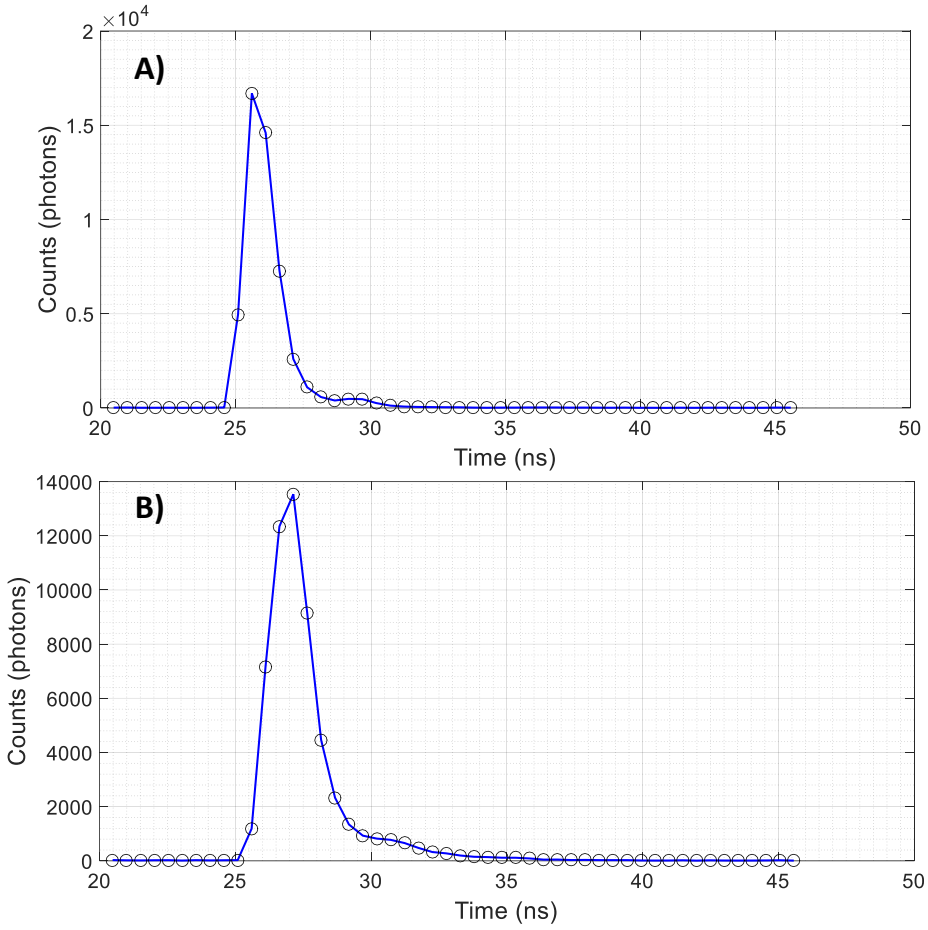

Figure 2.25: The Optical pulses registered with a TCSPC by the switching driver: A) Optical pulse corresponding to an electric pulse width of 1ns. B) Optical pulse corresponding to an electric pulse width of 2ns.

The switching driver shows more control when quenching the radiative recombination and a considerable increment on the photon count rate. This result is made possible by the combination of two circuits to quench the radiative recombination and switch the LED. The resistor between the reverse bias circuit and the switching circuit is essential to couple both circuits and prevent any damage. However, during the test, this resistor presented overheating especially when the electric pulse width is 5ns. Hence, the resistor value is increased (from 100Ω to 1kΩ) without affecting the optical pulses width and the photon count rate.

2.6.4 Comparison between test results

Both circuits can quench the radiative recombination after the electric pulse excitation, but only the switching driver reaches a high photon count rate for the electric pulse widths. The Op-Amp can be considered as a buffer circuit because there is no substantial amplification, even when the Op-Amp is supplied with a single voltage source, this increment is slight.

Hence, a solution to increase the photon count rate in the Op-Amp is to increase the electric pulse rate repetition, but it is not possible because the single photon detector module can't process the highest frequencies (20MHz is the maximum). Another suitable solution is to replace the Op-Amp for a RF amplifier such as the module block of mini-circuits® and with a Bias-Tee that introduces the offset voltage. The switching circuit presents a good performance on the optical width pulses and the photon count rate, and the overheating on the resistor between the reverse bias circuit and the switching circuit can be solved without having a considerable effect on the results.

2.7 Feasibility of the circuits in a QKD system

The circuits presented in this chapter are ready to replicate and there is not a necessity for complex circuits, both circuits have an excellent response at room temperature and achieve the optical pulses width. The Op-Amp has acceptance of several voltages in single voltage mode up to 15V, and 7V in dual voltage mode.

However, the necessity of negative voltage can result in making it complicated to supply the LED driver for a handset QKD system. Another inconvenience of the LED driver with an Op-Amp is the design copyright of the THS3202 for a possible miniaturization. Therefore, the use of an Op-Amp should be applied for training or experimental tests on prototypes, such as in this thesis work.

The switching driver works with two of the most common voltage supplies for electronic devices (12V and 5V). Although the electronic circuit could look somewhat complex, it is easy to understand with the block diagram illustrated in figure 2.16. The inclusion of a current booster can make the switch driver suitable for laser diodes, of course with certain modifications in the switching circuit and reverse bias circuit.

The switching driver can be adapted easily to a QKD system and its design with common electronic components free of patents, open the possibility to use in a handset QKD system versions [9], although it is recommended to consider the energy consumption of the LED (or laser diode), because it is reflected on the current booster in the form of heat radiation. Although during the experimental test with the switching driver the temperature never increased beyond 30°C, and there was no broken transistors due to the current demand.

2.8 Summary

This chapter analysed two LED drivers proposed to control a common LED and achieve weak light pulses, which contain few photons per pulse (according to the photon statistics in section 1.1). These light pulses are the result of fast electric pulses (in the order of nanoseconds) injected in the LED drivers.

The fast electric pulses on the LED have several effects such as, presence of minority carriers at the depletion zone after the electric pulse ends, and transients if the LED demands a considerable current. Therefore, an analysis of the LED equivalent circuit can explain the recombination times in the depletion layer through the diffusion capacitance, including transients produced by the abrupt changes of voltage (fast electrical pulses). These transients are well studied in electronics [52] and simulations.

The two electronic circuits reduce the recombination time tail on the LED. The Op-Amp can introduce a negative voltage in the cathode without problems, and the model used during this analysis supports high frequencies. The switching driver is a proposed design based on power electronics to apply a voltage to the cathode greater than the anode of the LED.

This action is equivalent to an off-set such as the Op-Amp does, but in the switching driver circuit there is a subtraction of the anode voltage minus the cathode voltage. The experimental test results reveal some recombination time quenching, but only the switching driver produces adequate brightness for a quantum communication between Alice and Bob. The current control in the switching driver opens the possibility of using commercial laser drivers such as the ONET1101L [51], this monolithic integrated circuit is designed to operate at a high-speed of data transference. Furthermore, the ONET1101L can reach currents of 100mA which can be adjusted through a programmable input equalizer.

Chapter 3.

Single photon detection using a Negative Feedback Avalanche Diode

Section 1.3.2 discussed the structure and some characteristics of the Negative Feedback Avalanche Diode (NFAD), but the NFAD has more properties that were not mentioned in chapter 1. In this chapter, we discuss in detail the properties of the NFAD described in its NFAD patent by Itzler et al. [29], furthermore we discuss the advantages of the NFAD compared to the InGaAs SPAD.

Some literature references such as [28] briefly described an NFAD based on InP alloy mixed with the InGaAs, and other references such as [61] and [23] describe some characteristics of an NFAD model already discontinued (family D and E). Therefore, in this chapter we have characterised and analysed an NFAD model PGQ-001-1550TOT from Princeton Lightwave® [30].

This NFAD model is optimized for wavelengths between 0.95µm and 1.6µm, hence the NFAD is suitable for a QKD system that operates over a long distance [21, 62]. The NFAD cooled to <225K shows low dark counts and with dead time and after-pulsing hold off of order 10us can operate up to rates ~50000/sec which is the typical maximum when the

fibre length is above 100km [36]. Here we are interested in testing the NFAD at high temperatures (230K-265K) where after-pulsing times are much shorter and operation at rates up to 10^6/sec with high dark counts makes it suitable for daylight range-finding applications [63].

3.1 Properties of the NFAD

The NFAD design in figure 1.18 illustrates the thin-film resistor located over the photodiode structure [29]. The main contribution of the thin-film resistor is to increase the operation speed (more than 10MHz), to a SPAD which operates at wavelengths above 1000nm. Although the NFAD is a relatively new type of SPAD according to the patent by Itzler et al. [29], the basis of the NFAD concept lies in publications which describe the integration of a resistor as part of the SPAD itself [64, 65].

However, early NFAD proposals suggested the use of a Metal Resistor Semiconductor or MRS, and the semiconductor materials such as silicon have null efficiency for wavelengths greater than 1000nm. Due to the short absorption coefficient of the silicon, even for semiconductor materials (group III-V or II-VI) which are suitable for wavelengths greater than 1000nm, the structure of an MRS Photodiode makes it impossible to use these materials [65].

For this reason, a thin-film resistor is integrated to a typical InGaAs SPAD to introduce a negative feedback. The thin-film resistor provides a passive self-quenching but avoids stray capacitance. Thereby, a thin-film resistor which has a high value (beyond 1MΩ) and the internal capacitance of the SPAD (~0.4pF), considerably reduce the RC time constant to under 1µs. This time is translated to a fast avalanche recovery after a single photon detection and a fast-quenching of the avalanche during the single photon detection.

A fast recovery after an avalanche makes the NFAD interesting for quantum applications such as: quantum communications, LIDAR systems, quantum computing and quantum cryptography. The self-quenching reduces the complexity of the external circuit, and avoids external capacitances which normally reduce the speed of SPAD's.

Another property of the NFAD is the low noise in free-running mode [34], furthermore new NFAD models introduce thermo-electric cooling to reduce the dark-counting in the absorption material. For QKD systems tested at 100-307km there is a need to minimise dark counts by cooling to very low temperatures and this leads to the need to use after-pulse hold-off times of 8 up to 115µs. Here we are interested in investigating higher temperature operation for LIDAR applications where dark counts are dominated by high backgrounds and after-pulsing might be reduced by shorter trap lifetimes. Advantages of the NFAD compared to a SPAD

The reduction of dead-time after the single photon detection is not the only advantage of the NFAD. When the avalanche is stopped quickly and is immediately re-armed afterwards, the amount of carriers stuck in trap energy states in the multiplication region is reduced, and the after pulsing probability is also reduced. For typical SPADs, the only way to reduce the after pulsing probability is by adding an extra delay after the dead time, this delay time allows for the carriers that were trapped to have been released and thereby the after-pulsing probability is almost neutralized.

However, that delay time increases the dead time and reduces the speed for detecting single photons, this is self-defeating for a QKD system that requires a high speed of communication. Therefore, the NFAD covers some deficits which the typical InGaAs SPAD has and the new NFAD models include an extra layer of InP which decreases the low parasite effects after the rapid self-quenching [28] considerably.

The NFAD has four properties that overcome an InGaAs SPAD but it does not mean that an NFAD is completely superior to the InGaAs SPAD. A rapid avalanche quench has the benefits previously explained, but the time reduction of the avalanche also directly affects the avalanche amplitude. This problem is discussed in [29] which analyses the NFAD pulse response in the presence of dark-counts, the pulse amplitude is around 15-20mV when the breakdown voltages exceed 0.5V, and the amplitude can increase in proportion to the excess bias voltage over the breakdown voltage.

There are advantages and disadvantages when the excess bias voltage is increased. A key advantage is the increment of the pulse amplitude and the photon detection efficiency. But the disadvantages are also notable including an increase of the total quench time, and the after-pulsing probability.

Another characteristic is the jitter timing on the NFAD, its structure (InGaAs/InP) decreases the slope of the energy step, and this represents an effective barrier which reduces the lower field strengths [33]. This is translated in a reduction of the NFAD jitter time although the InGaAs SPAD jitter time can also be reduced if the excess bias voltage is increased [20]. But as explained previously, an increase of excess bias voltage can bring undesired effects.

3.2 Setup of the experimental assembly

The NFAD does not require any complicated circuitry due to its internal quench characteristics. Photodetection leads to negative current pulses and these pulses are collected at the cathode and amplified in a 50 ohm RF-amplifier. A reverse bias voltage exceeding a *breakdown voltage* (V_{Br}) of the NFAD is applied at the cathode by a bias tee. The circuit used for this characterisation is recommended by the NFAD manufacturer Princeton Lightwave® [28, 66]. Figure 3.1a illustrates the schematic diagram of the circuit and figure 3.1b illustrates an image of the NFAD used during the characterisation.

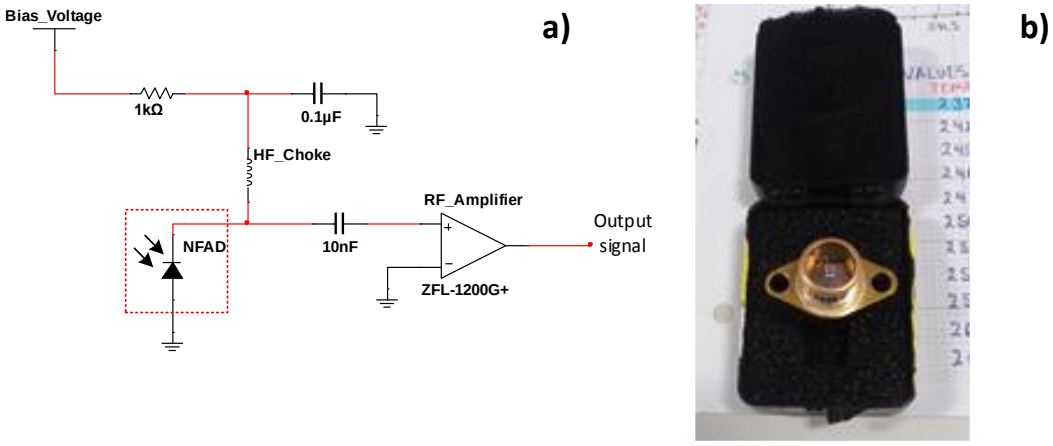

Figure 3.1: A) A Schematic diagram of the typical application circuit recommended by the manufacturer. B) An image of the NFAD used in the characterisation of this chapter.

The cooling system inside the NFAD consists of a Thermo-Electric Cooler (TEC) with a thermistor for monitoring the internal temperature, thereby the first step in the characterisation is representing the thermistor graph curve, which is illustrated in figure

3.2 using the Steinhart-Hart equation (3.1), with the constants shown: A: 1.6529×10^{-3}, B: 2.2102×10^{-4} and C: 4.1874×10^{-9} [30].

$$Temperature = \left[a + b\ln(R) + c(\ln(R))^{-3} \right]^{-1} \quad (3.1)$$

Where R is the resistance of the thermistor at a certain temperature (K) and there is additional information from the manufacturer, which recommends the user does not exceed the limits of the TEC as registered in table 3.1. The lowest temperature used for the characterisation is 237.87K and corresponds to a thermistor with a resistance of 100KΩ. The TEC is controlled by a TEC module TED-200C from Thorlabs®. This module measures the thermistor-resistance and has an integrated ammeter to monitor the current through the TEC.

TEC Current	1.5A max
TEC Voltage	1.9V max
Thermistor	2.20kΩ at 298.15K
Thermistor Constants	A= 1.6529×10^{-3}, B= 2.2102×10^{-4} C= 4.1874×10^{-4}

Table 3.1: TEC Specifications provided by Princeton Lightwave.

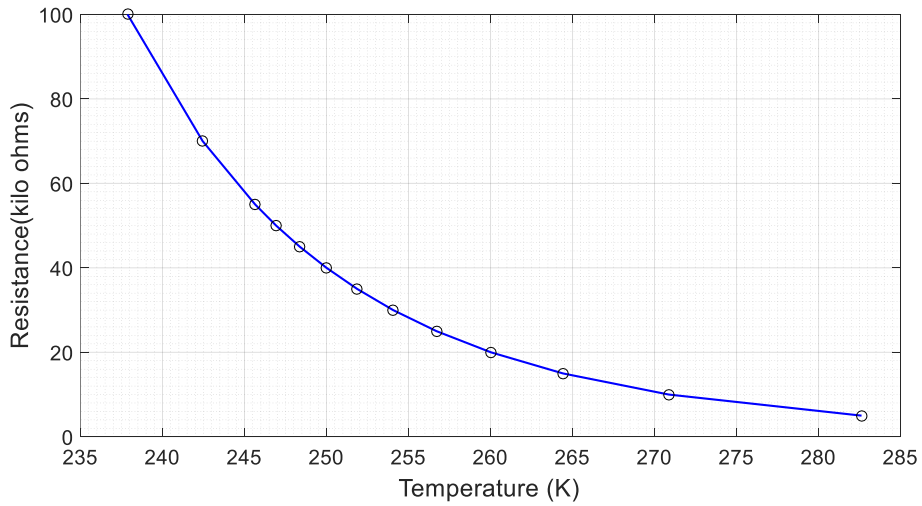

Figure 3.2: The temperature curve of the NFAD thermistor obtained from equation (3.1).

The NFAD is mounted in a proper optical assembly using a cage system from Thorlabs® to adjust the light beam, which is in three axes (x, y and z), this adjustment helps in the alignment between the NFAD detection area dimension (22µm of diameter) and the light beam. The light beam is supplied by the laser module PRO-800 from Thorlabs® for continuous wave (CW) with a λ of 1550nm, this beam is transmitted by a single-mode

fibre optic (SMF) model P1-SMF28E-FC-2 from Thorlabs®. The NFAD is highly sensitive to light and requires a light tight mounting to avoid light leakage modifying the optical measurement. Hence, the NFAD is mounted in a rigid base and coupled with the optical assembly. Once the NFAD is already in the optical assembly, the characterisation can start and the first NFAD to be properly analysed is the breakdown voltage (V_{Br}). The manufacturer recommends an operating voltage range of 70V and 80V, although the V_{Br} is intrinsically related to the internal temperature of the NFAD.

It is important to reliably determine the threshold voltage when the NFAD begins to operate in Geiger-mode, then V_{Br} is defined. The internal quench resistor (R_{qi}) is determined when the NFAD is forward biased, the voltage and current parameters for this configuration are specified by the manufacturer. Thereby, the forward voltage is fixed at 1.5V and the current is 1µA, hence R_{qi} is determined to be 1.5MΩ.

The initial temperature for this V_{Br} analysis is 237.87K and the final temperature is 282.64K, the reverse bias voltage is supplied with a power source meter model 2450 from Keithley® and the initial value of the reverse bias voltage is fixed at 80V. This voltage is exceeded with small voltage steps with the purpose of finding V_{Br} but also to avoid damaging the NFAD.

Although the test circuit illustrated in figure 3.1a includes a current limit resistor, the current supply is fixed in the power meter at 1.5µA to prevent any damage. The V_{Br} is plotted as a function of the temperature curve and is illustrated in figure 3.3.

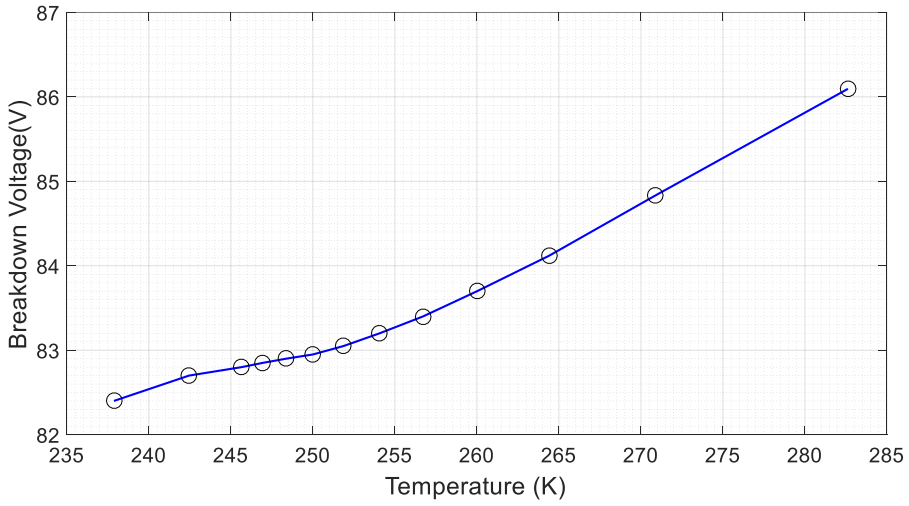

Figure 3.3: Breakdown voltage (V_{Br}) as a function of the temperature curve obtained experimentally.

The alignment of the laser has relevance in characterising the Photon-electron Detection Efficiency (PDE). However, the fibre terminal with the laser beam can't be connected directly to the NFAD or aligned, because the beam radius increases proportionally with the separation from the NFAD. This results in a beam spot bigger than the NFAD detection area. Therefore, the laser beam must be coupled with the NFAD detection area through an optical lens system.

The laser beam has a divergence angle at the fibre tip that is equal to the sine of the fibre numerical aperture (0.14) resulting in an increment of the beam radius. Therefore, the laser beam must be collimated before being aligned. The mode field diameter (MFD) of the fibre used (SMF28) is 10.5±0.5µm at 1550nm, the collimator proposed should have an anti-reflective coating effective to 1550nm to avoid losses by reflection. The collimator proposed is the F220FC-1550 from Thorlabs® with a focal length of 11.29mm. Once knowing this parameter, it is possible to obtain the divergence angle (θ_D) through the equation (3.2).

$$\theta_D = \left(\frac{D}{f_1}\right)\left(\frac{180}{\pi}\right) \tag{3.2}$$

Where D is the MFD of the fibre and f_1 is the collimator focal length and thereby $\theta_D = 0.053°$, corresponding with the minimum value specified by the manufacturer and the beam radius has a negligible increment. The laser beam diameter after the collimation, is specified at 2.1mm by the manufacturer but the NFAD detection diameter is smaller than the beam diameter.

Therefore, an aspheric lens is placed at an arbitrary distance but this aspheric lens must have a similar focal length as the collimator, thereby the aspheric lens used is C220TMD-C with an anti-reflective coating effective at 1550 and a focal length (f_2) of 11.00mm. The laser beam spot over the NFAD's detection area dimension (diameter) should be similar to the MFD of the fibre used, and its value is obtained through the equation (3.3).

$$\phi_{spot} = \frac{4\lambda f_2}{\pi D_{beam}} \tag{3.3}$$

The parameter as the focal length (f_2) and laser beam diameter (D_{beam}) are given by the manufacturer. Thereby, the laser beam spot diameter is 10.3µm that is approximated to

the fibre's MFD. Figure 3.4 illustrates a scheme of the optical arrangement to couple the fibre tip and the NFAD detection area.

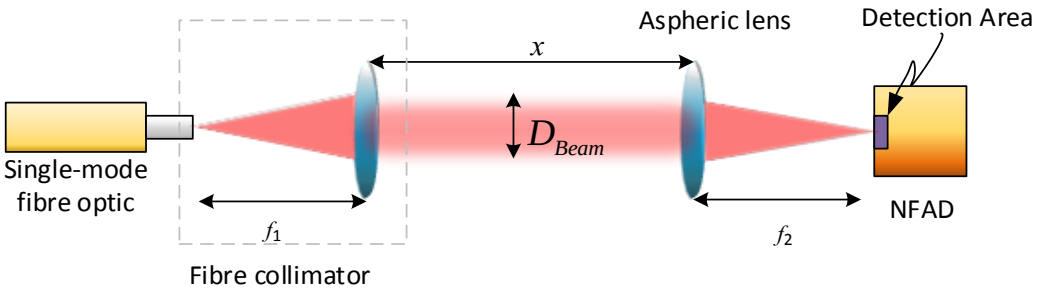

Figure 3.4: The SMF is connected to a fibre collimator with a focal length (f_1) of 11.29mm, its beam diameter (D_{beam}) after the collimation is 2.1mm. The distance (x) between the collimator and aspheric lens is 30mm, that corresponds to the lens tube length used to mount them. The aspheric lens is separated 11.00mm (f_2) from the NFAD detection area.

Another way to couple the laser beam spot with the NFAD detection area is through the magnification of the optical arrangement. The fibre collimator has a fixed focal length but the distance between the aspheric lens and the detection area is not already fixed. Therefore, a suitable adjustment of this distance can result in a complete coupling and the magnification equation (3.4) helps for this coupling.

$$\frac{D_1}{D_2} = \frac{f_1}{f_2} \tag{3.4}$$

The fibre mode diameter D_1~9μm while the detector diameter D_2=22μm. Hence an ideal relation between focal lengths is 1:2, but to ensure all the beam falls on the detectors the focal length of the fibre collimator and aspheric lens are chosen almost equal and the magnification is ~1.03, ensuring even diffraction edges of the beam are collected onto the NFAD.

The optical arrangement illustrated in figure 3.4 is mounted in an X-Y-Z translator, since the distance between the aspheric lens and NFAD's detection area, corresponds to the z-axis and it should be adjusted until achieving the magnification rate previously estimated. However, the NFAD's window has a diameter of 10.06mm [30], and therefore the X-Y alignment is performed carefully to achieve the best possible laser beam alignment.

3.2.1 Laser Beam alignment

The X-Y axis alignment between the optical arrangement and the NFAD's detection area, is performed through two different adjustments; coarse and fine adjustments. However,

in both adjustments the laser beam must be attenuated, because the NFAD is focussed on single-photon detection and a huge amount of photons would saturate or damage it.

The laser module has an integrated attenuator but at maximum attenuation, the laser beam achieves a minimum optical power of 0.5mW. However, the laser beam can be heavily attenuated through fibre optic attenuators and an attenuator module model MN924C from Anritsu®, and thereby the optical power can be reduced to pico-watt levels.

The optical power is measured by a power meter model PM100D and with an InGaAs photodiode model S155C which are both by Thorlabs®. Through the attenuator module, the optical power is adjusted to 7nW, then the NFAD is biased at an arbitrary voltage 20V below V_{Br} (to avoid the Geiger-mode).

Thereby, the X-Y adjustment begins through current measurement with the power source meter. However, this is a job of aligning two very small spots in two dimensions hence, the adjustment takes some time, and steps to ease this are described in the following.

3.2.1.1 Coarse adjustment

The beam spot diameter is increased temporarily by replacing the single mode with a multi-mode fibre optic (MMF), this MMF is the same mode that was used in the chapter three experiment (FG105LCA).

The larger spot is easier to find by monitoring the photocurrent, as it is scanned over the NFAD's detection area. Once the maximum current is achieved, the MMF is replaced by the SMF and the X-Y adjustment continues until reaching the maximum current possible (4.7nA).

Apart from contributing to the laser alignment, the coarse adjustment also determines the NFAD's photocurrent and dark-current. The NFAD is biased until finding the 'punch-through' voltage, which is easily identified by a sudden current increment when the laser is activated, this current-voltage relation is plotted in a graph that is illustrated in figure 3.5.

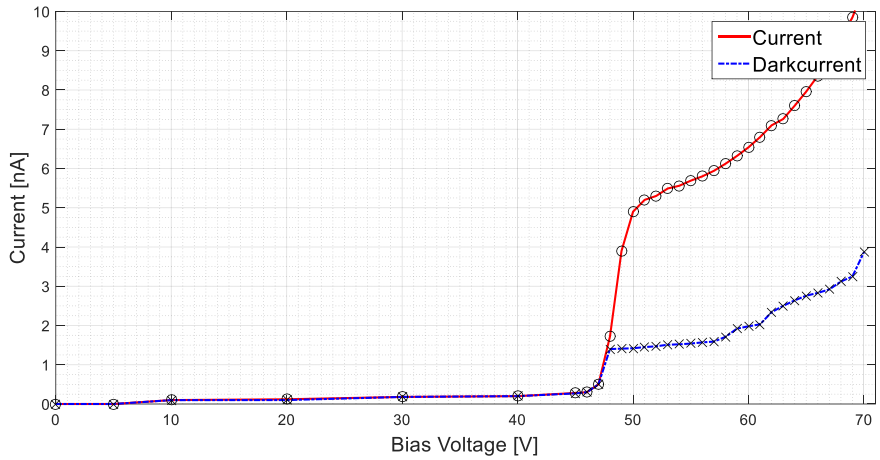

Figure 3.5: Reverse bias current as a function of voltage under laser illumination.

The punch-through voltage is located at 50V and at this voltage, the NFAD has a unity gain and hence it behaves as a simple photodiode. Once the punch-through voltage is located, the dark-current is measured when the laser is deactivated and it is determined at 1.4nA. The dark-current is subtracted from the current achieved at the punch-through voltage, thereby the photocurrent is determined at 3.6nA (5nA-1.4nA) and the quantum efficiency is determined by the group of equations (C.7) in appendix C, which results in 41%.

3.2.1.2 Fine adjustment

The power meter presents variations at a range of hundreds of pico-amps and there is a possibility of skipping the maximum current value during the coarse adjustment. Therefore, a way to verify the alignment (or re-adjust in case) is through photon detection, and the laser beam must be attenuated again.

The photocurrent value is converted to the number of electrons per second (Ne^-) when the photocurrent is divided by e^-. The amount obtained is 2.06x10^{10} (20.630Ge^-) electrons per second and this amount would saturate the NFAD under the Geiger-mode, hence the new attenuation must produce an amount of 1x10^6. This attenuation increment is determined to be around -43dB using the equation (3.5).

$$ATT = 10\log_{10}(Ne^-) \tag{3.5}$$

Once adjusting the attenuator module with the extra attenuation, the NFAD is reverse biased at 85V and cooled to the minimum temperature (237.87K).

The NFAD is in Geiger-mode, hence it can detect photons that are counted through the Time-Correlated Single Photon Counter (TCSPC) module, the same model used in the experimental test of chapter two (PicoHarp 300 of Picoquant®). The X-Y translator is adjusted again (minimally), and the alignment is considered successful when the maximum photon count rate possible is obtained. Therefore the PDE characterisation has the best precision and additionally, the optical power of the laser beam with the attenuation increment (-43dB), the optical power is around 0.35pW.

3.3 Dark-count and Noise threshold adjustment

The NFAD test circuit illustrated in figure 3.1a is relatively simple. However, there are possibilities of noise leakage that could affect the dark and light count measurement, most of the components in the circuit are enclosed in module blocks of mini circuits® and only two components are added separately, these components are a capacitor of 0.1µF and a resistor of 1kΩ.

The Bias-Tee block model ZFBT-6GW+ couples the DC bias and separates the avalanches, but the avalanches are so weak (-1.5mV approximately). Therefore, the Bias-Tee RF output is connected to an amplifier model ZFL-1200G+ and thereby the avalanches are amplified, figure 3.6 illustrates the setup diagram for the dark count and noise threshold adjustment.

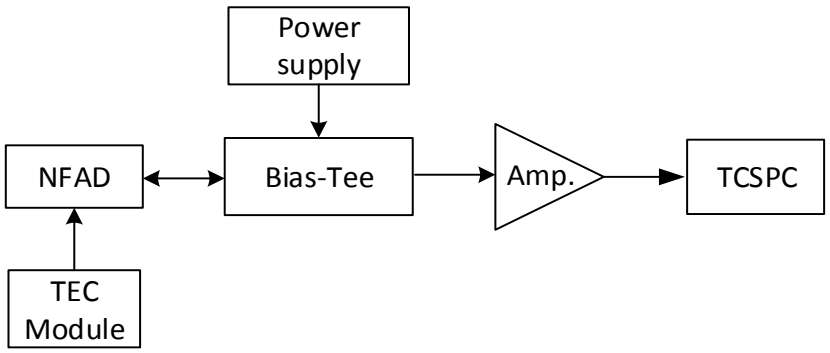

Figure 3.6: Setup diagram for dark count characterisation. The NFAD block is mounted in a Printed Circuit Board (PCB), which connects the NFAD with the TEC module and the Bias-Tee. The Bias-Tee is the main node among the NFAD, Power supply and the Amplifier (Amp). Finally, the amplifier is connected to the TCSPC.

However, there is an inconvenience with the amplifier used. The avalanches are inverted and although it would not normally represent a problem, the TCSPC module used to register the photon counting only accepts negative pulses [60]. The solution is a signal inverter which is connected between the Bias-Tee RF output and the amplifier. Thereby, the original polarity of the avalanches are held after the amplification.

3.3.1 Noise threshold adjustment

The noise is introduced by the NFAD when it is reverse biased and also the amplifier, we do not expected the bias-tee to contribute noise although noise will be picked up from external sources such as the TEC controller. To check this the TEC controller and the amplifier are activated while the NFAD is off to avoid any avalanche (even by dark-counting). The noise signal is registered by an oscilloscope of the same model used in the experimental test of chapter two.

The oscilloscope's waveform is configured at infinity persistence and hence any signal is registered permanently. This noise control test has a duration of 30 minutes to dismiss any transients provoked by external sources, and thus to avoid any confusion with the natural noise of the amplifier. Figure 3.7 illustrates the noise registered during this control test by the oscilloscope.

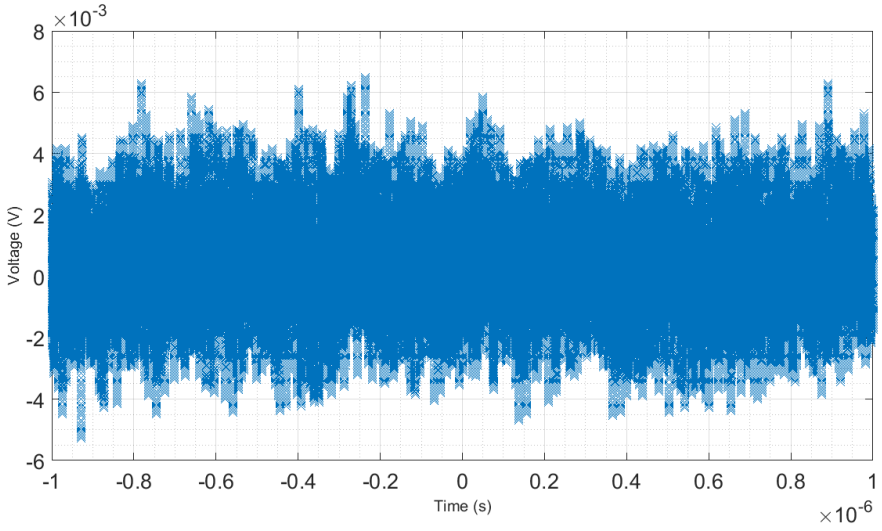

Figure 3.7: Noise measurement after 30 minutes of the amplifier and TEC controller, it is possible to observe a background noise of around +/-2 mV but no transients.

This control test reveals some noise introduced by the amplifier and the TEC controller, but with the NFAD deactivated, therefore it is necessary to know the noise introduced by the NFAD and Bias-Tee. The reverse bias voltage is fixed at 50V (punch-through voltage) and the TEC controller is fixed with an arbitrary temperature (250K), for another 30 minutes, the noise is measured but this time there is no significant change, although there are presences of sporadic transients, in figure 3.8 the noise measurement is illustrated.

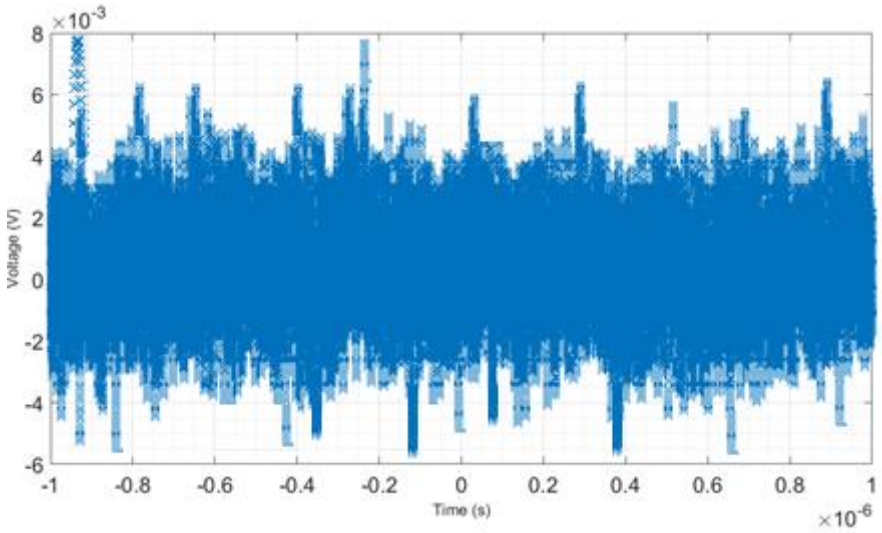

Figure 3.8: Noise measurement after 30 minutes with the NFAD reverse-biased. The noise registered does not change significantly when the NFAD is cooled or at room temperature but still, there are occasional transients.

The noise amplitude (after the amplifier step) is determined around 4mVpp although there were transients (no capture in figure 3.8) with 30mV peak. Hence the TCSPC discriminator level is fixed over 30mV, but it is important to accurately determine the border between the noise and avalanches.

3.3.2 Dark-count threshold adjustment

The dark-counting is the best option to determine the threshold border between the noise and avalanches, because the light-counting increases the number of avalanches (and amplitude), provoking a false perception of the noise-avalanche threshold border. The dark-count measurement test requires a certain temperature and a reverse bias voltage over V_{Br} to enter Geiger-mode operation. The temperature is fixed at 250K with an excess bias voltage at 0.3V over V_{Br}, these values put the NFAD in Geiger-mode operation and through the oscilloscope, and then the presence of dark-counting is confirmed.

The oscilloscope is swapped by the TCSPC to easily locate the dark-counting threshold level, then the TCSPC threshold level is adjusted in steps of 5mV up to 150mV. The same operation is repeated for the noise and then noise and dark-counting can be graphed as a function of the threshold voltage. Figure 3.9 illustrates a comparative graph between the noise and dark-count (counting) as a function of mV.

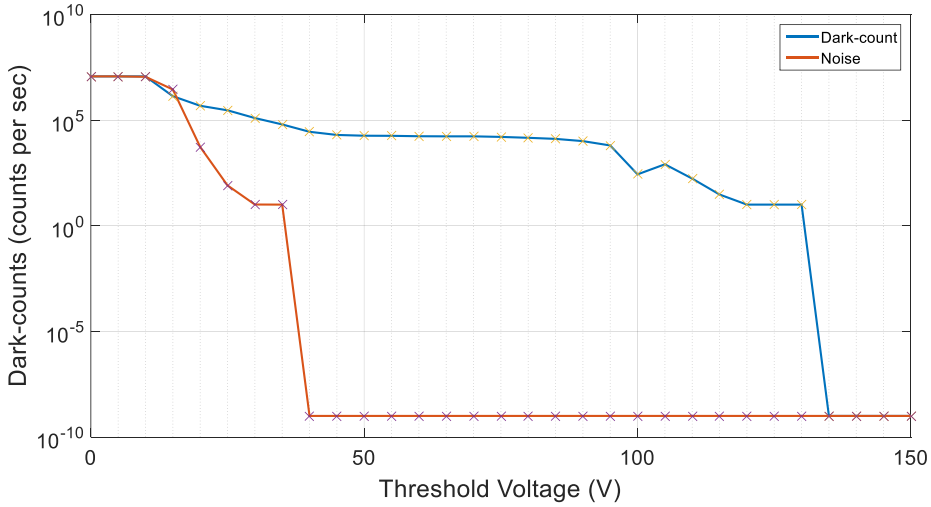

Figure 3.9: Comparative chart between noise and dark-count at 250K. At 50mV, it is possible to observe a stable dark-counting.

There is a threshold voltage in which the noise is completely discriminated and the dark-counting prevails, at 45mV the noise is not registered anymore and the dark-counting begins a steady-stable counting until reaching 80mV. Therefore, the TCSPC threshold voltage is fixed at 50mV, to avoid all possible noise influence on the counting.

3.4 Recharge time measurement

The NFAD as a SPAD has a recovery time after the avalanche as a result of a single photon detection, this recovery time is the product of a dead time (of which there is no detection) and a recharge time. The temperature and reverse bias voltage is set with the same parameters as section 3.3.2 and the oscilloscope's configuration remains on infinity persistence.

After 20mins a waveform is obtained which shows the dead time and the recharge time clearly. To obtain the best quality of this measurement, the oscilloscope screenshot is sampled by a Matlab® program and figure 3.10 illustrates the waveform at infinity persistence in Matlab® graph format.

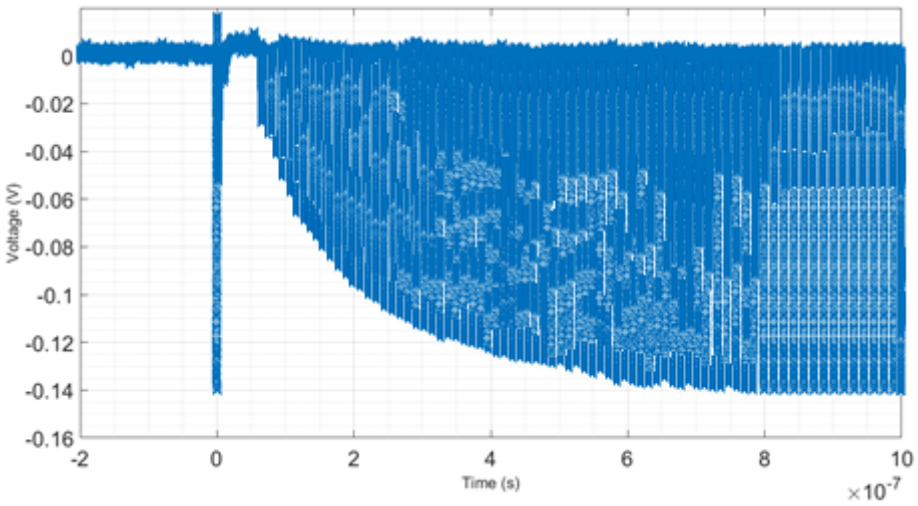

Figure 3.10: Infinity persistence of the NFAD at 250K, the charge time starts from 200ns ($2x10^{-7}$ s) and finishes at around 600ns ($6x10^{-7}$s). This graph is obtained from a sampling of a screenshot oscilloscope using Matlab.

The dead time is short (≈50ns) in comparison to the recharge time which ends at around 600ns. This recharge time shape is due to the terminal capacitance recharging for the next avalanche, the value of the capacitance is specified by the manufacturer at 0.4pF but it is possible to obtain this parameter through an approximation method (least square).

The values used for these approximations are: the time from the trigger detection (0.0s) to the NFAD completely charged at 600ns (τ), the initial amplitude of the charge is 140mV (amplified) but the capacitance is determined by $\frac{\tau}{R}$ the resistance value obtained experimentally in section 3.2 and therefore the relation previously mentioned, results close to 0.4pF which is near to the terminal capacitance of 0.4pF specified by the manufacturer [30].

3.5 Dark-count Characterisation

The dark-count measurements require absolute darkness to avoid the filtration of parasite light. In order to determine the degree of darkness where the NFAD is close, it is cooled to the minimum temperature obtained in the graph of figure 3.2 (237.9K) and 0.5V over V_{Br} with the intention of undergoing a minimisation of background counts [20, 21].

This measurement (control test) is performed in day light time and the dark-counts are registered with the TCSPC, so the result obtained in this control test is $2.5x10^4$ counts per second (CPS). The next measurement is developed at night time with the windows covered and any possible light sources switched off. Furthermore, the optical assembly is covered with two black fabrics to ensure absolute darkness inside of the optical assembly, and the result of this test is $1.8x10^4$ CPS.

A results comparison reveals a small amount of light leakage which occurs when the optical assembly is uncovered. This leakage was fixed with a black fabric, after another measurement in day time and with the laboratory illumination, the result is near to the measurement in conditions of complete darkness. The success of the light leakage reduction is due to the NFAD spectral response, because the light in the infrared region can be absorbed by the black fabric.

3.5.1 Dark-count as a function of reverse-bias voltage

The dark-count has a relation to the temperature and the reverse bias voltage is the best way to analyse this relation. The NFAD is fixed at a certain temperature and the reverse bias voltage is increased in steps of 0.2V, thus, the resolution of dark-count versus temperature would have a resolution suitable for an analysis. Figure 3.11 illustrates a graph of dark-counts as a function of the reverse bias voltage on a logarithmic scale.

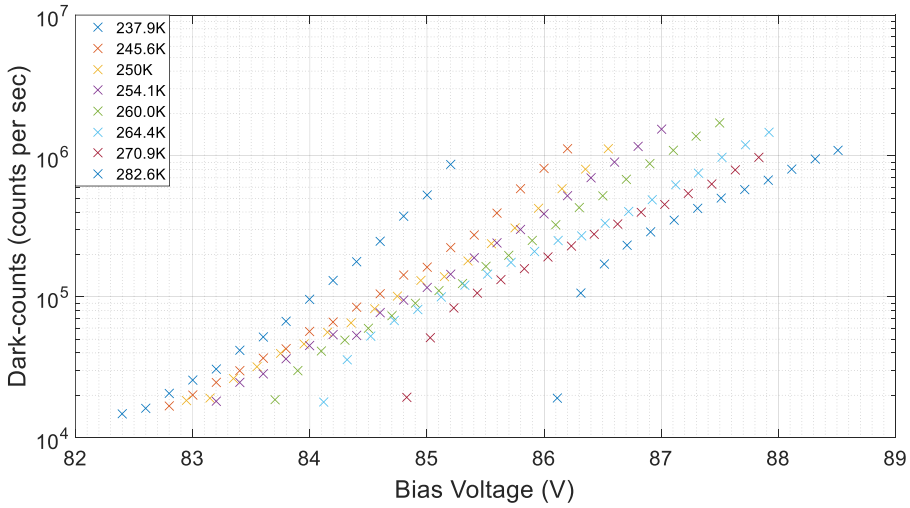

Figure 3.11: Dark-count as a function of reverse bias voltage on a logarithmic scale.

The initial count is 1.8×10^4 CPS for normalization purposes and a proper comparison with details between curves. Temperatures with over 250K have a different shape to those with under 254.1K. Over 250K, we see a turn-on at a higher initial dark-count, then a linear increase (on log scale = exponential increase) with voltage. Under 250K the increase is slightly super-linear directly from the 1.8×10^4 baseline (increases faster than exponential). The super-linear behaviour may be due to after-pulsing at low temperatures (section 3.7). The temperature range of 250K and 254.1K has a low turn on count and a roughly linear increment, and is thus deemed a good operating regime.

3.5.2 Dark-count as a function of excess bias voltage

The graph of figure 3.11 shows dark-counts as a function of the reverse bias voltage, but it is possible to detail the dark-counts as a function of the excess voltage over V_{Br}. Thereby, the NFAD is fixed again at a temperature of 237.9K and this time, the graph is only evaluated as a function of the excess voltage over V_{Br}, as shown in figure 3.12 which illustrates a graph of dark-counts as a function of excess voltage over V_{Br}.

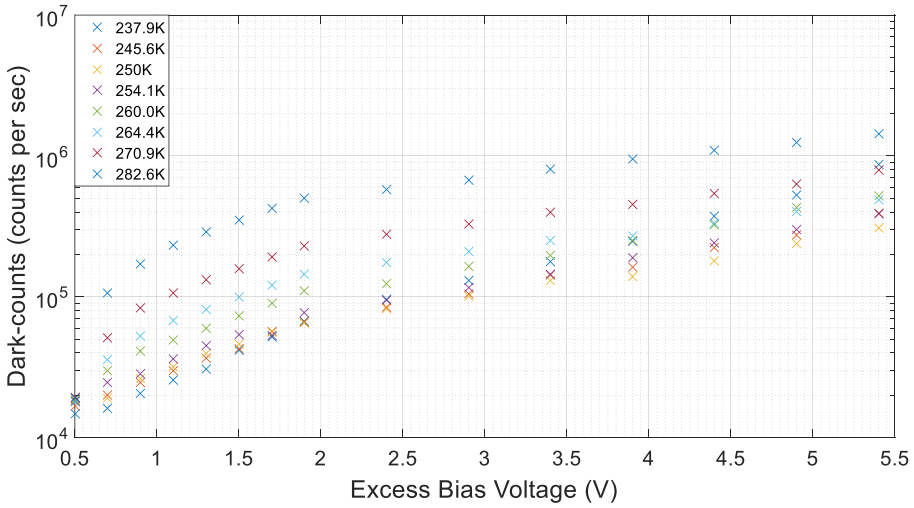

Figure 3.12: Dark-count as a function of the excess bias voltage over V_{Br} on a logarithmic scale.

This graph shows the increment of the dark-counting with more detail, the difference between exponential and logarithmical increments disappear. However, the linearity in the temperature range previously indicated is kept (with a slight variation), confirming an optimal temperature for dark-counting control.

3.5.3 Dark-count as a function of temperature

The temperature has a direct effect on the dark-counting that can be shown in a graph of dark-counts as a function of the temperature illustrated in figure 3.13. The excess bias voltage over V_{Br} is fixed at a certain value and the temperature is incremented.

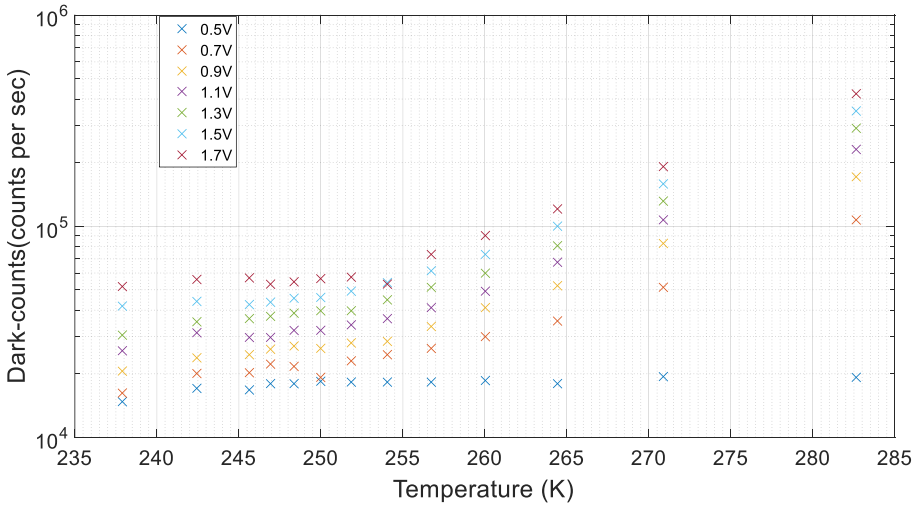

Figure 3.13: Dark-counts as a function of the temperature on a logarithmic scale.

The dark-counting with the minimum excess bias voltage (0.5V) does not present a considerable variation, but it is after 0.7V when the increment of the dark-counting has a notorious increment after 255K. Before 255K the dark-counting remains relatively stable (with slight variations). The NFAD has an acceptable temperature response when compared to other SPAD's [20, 21].

Some QKD simulations consider the dark counting range obtained in this dark-count characterisation as acceptable for decoy-states [67]. Furthermore, there are reports of dark counting rates near to 1 CPS [68], but this count rate is achieved with cryogenic methods that would restrict the NFAD to scientific research purposes. When the temperature in the SPADs go down to cryogenic levels, there are other detrimental features such as reduced PDE and increased after-pulse [34].

3.6 Photon Detection Efficiency (PDE) Characterisation

The PDE measurement represents the probability of registering a count when a photon arrives to the detection area of the NFAD. In [69] two methods are proposed to perform A SPAD's PDE measurement:

- Calibrated light source
- Single photon correlation

The single photon correlation method is used with a parametric down conversion source and two single photon detectors, and there are some experiments that used this method for several purposes [70, 71]. Also this method can be used to measure the PDE of a SPAD, but it is not recommended for detectors with a diameter smaller than 100µm; the NFAD has a diameter of 22µm, then the single photon correlation method is discarded.

Therefore, for the PDE characterisation of the NFAD (the calibrated light source method) is used. To perform this method it is necessary to choose the type of light source, which could be a CW laser or pulsed laser. During the laser beam alignment in section 3.2.1 a CW laser was used, although theoretically it does not matter what type of light source is used (both should give similar results), as long as the light source is heavily attenuated to reduce the mean photon number. The NFAD recovery and after-pulsing can lead to

distortion when a CW laser is used and this could generate a PDE measurement with errors.

Therefore, it is recommended to use a pulsed laser with a rate repetition (f) below the dead time (τ_D) i.e. ${}^{1}/_{\tau_D} > f$ [69]. The dead time (including recovery time) of the NFAD is estimated at around 600ns according to the measurement in figure 3.9. Therefore, the rate repetition of the pulsed laser is 500 kHz which satisfies the condition previously mentioned (${}^{1}/_{\tau_D} = 1.67\ MHz$).

Another reason to use a pulsed laser in the PDE characterisation is the ease of detecting any saturation on the NFAD and more important any after pulsing which could contribute to an error in the measurements. After setting the rate repetition of the pulsed laser, it is heavily attenuated to reduce the mean photon number to less than one photon per time arrival [69].

The attenuator module used during the alignment process is adjusted until an optical power of 1.28nW is obtained. After this pre-attenuation, fibre attenuators are added to include 43dB which results in 64.2fW, the reason for this attenuation is to achieve around 500kphotons per second and this amount is determined by the equation (3.6).

$$n = \frac{P_{optical}}{E_{ph}} \tag{3.6}$$

This equation is proposed in several references such as [1], but in [69] it is recommended to determine the incident photons per second ($\boldsymbol{n}$) over a SPAD detection area. Once the number of incident photons per second is determined, the mean photon flux can be obtained through the equation (3.7)

$$\mu = \frac{n}{f} \tag{3.7}$$

The optical power of the pulsed laser ($P_{optical}$) in the equation (3.6) is obtained with the same optical power meter that was used in section 3.2.1, although any measurement with this device is only accurate with a CW laser. The photon energy (E_{ph}) is determined through the equation (A.26) in appendix A for *1.55μm*, and thereby the mean photon number (μ) in the equation (3.7) is around one photon per pulse.

Once the optical power of the pulsed lased is adjusted, it is connected to the NFAD through an optical arrangement which is previously illustrated in figure 3.4. Thereby, the experimental assembly for PDE characterisation is complete, and figure 3.14 illustrates the setup diagram.

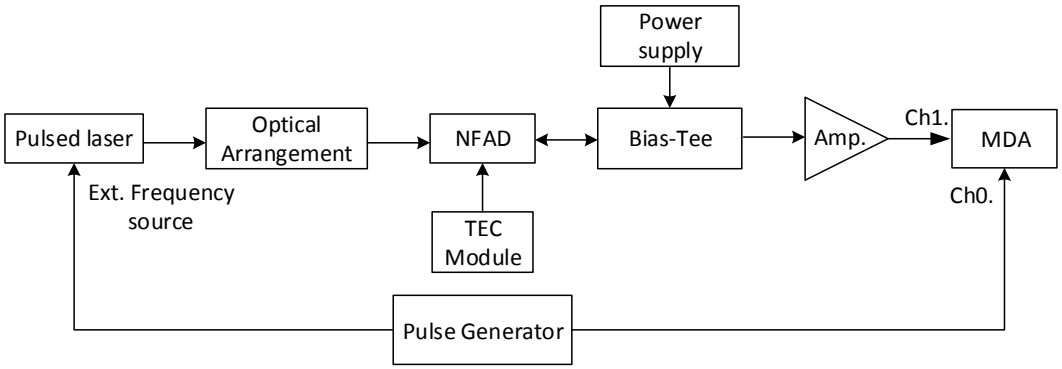

Figure 3.14: The Setup diagram to measure the PDE of the NFAD. This diagram looks similar to figure 3.6 but there are some differences such as: The pulsed laser as a light source (PDL800 from PicoQuant®) and its rate repetition is controlled by a pulse generator, also the pulse generator is connected to a Modulation Domain Analyser (MDA) module which replaced the TCSPC. Furthermore it includes a block that represents all the optical arrangement described in section 3.2.

There is change in the final block which registers the photon arrivals; the TCSPC is replaced by a Modulation Domain Analyser (MDA) Module model HP 53310A of Hewlett-Packard test and measurement products® (now Keysight Technologies®). This change is due to important considerations in the moment when measuring the PDE and these considerations are discussed in the next section.

3.6.1 TCSPC vs. MDA module

The TCSPC of Picoharp® is designed for fluorescence spectroscopy purposes, therefore the histogram generated by the TCSPC uses a laser timing pulse as start and detected photon as stop. However when we want to measure count rates the histogram scheme being a single stop scheme loses all counts after the first stop and a fraction of the total photon emission would be counted [60, 72]. Therefore, the count rate measurement is done independently of the histogram which allows extra photon counting to be registered.

This extra counting represents a problem in the moment of characterising the PDE of the NFAD, because the count rate includes the after pulses and increases the PDE. To

determine the PDE through the light count rate obtained with the TCSPC, it is necessary to use the equation (3.8).

$$PDE = \frac{Light\ Counts - Dark\ Counts}{n} \tag{3.8}$$

This equation includes a correction to remove the contribution of dark counts, and the result of this subtraction is divided between the incident photons per second on the detection area. Thereby, there is a direct relationship between the numbers of photons detected and the numbers of photons that should arrive. Figure 3.15 illustrates the PDE determined by the equation (3.8).

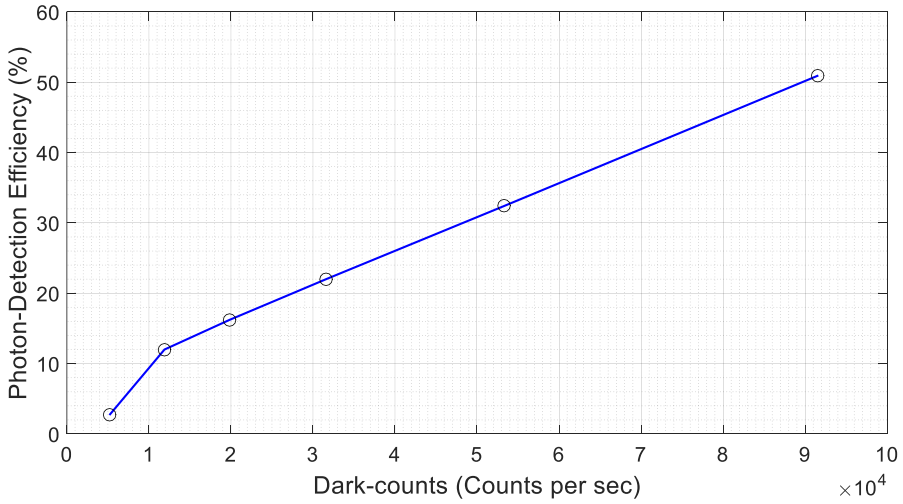

Figure 3.15: The PDE as a function of dark-counting at 250K. This graph is obtained with the equation (3.8) and the percentage reached 50%.

There is a notorious inconsistency between the graph of figure 3.15 and the several experiments which report InGaAs SPAD (and NFAD) PDE, efficiency does not get beyond 15-30% [8, 20, 21, 23, 61]. This is a result of the after pulse contribution which is not accounted for in equation (3.8).

Nevertheless, there is an easy way to measure the NFAD's PDE without any correction to the equation (3.8), and that is using gated count rate measurements and in fact the Modulation Domain Analyser (MDA) module actually has a function to directly measure the ratio between start and stops in a time gated fashion. This uses the MDA in the time-domain mode where it essentially performs a TCSPC function and can give a direct reading of the percentage of starts that are stopped to estimate PDE.

Figure 3.16 illustrates the probability of photon arrival measurements in the NFAD with 1 MHz of rate repetition pulse laser (for demonstration purposes), and optical power conditions previously mentioned. We see that it is possible to isolate the photon detections from the laser pulse through a time window in the MDA and measure the probability of a light count isolated from the later after-pulses. Separate measurements with laser on and off allows a light and dark count probability to be measured and the PDE estimated through the equation (3.9).

$$PDE = \frac{(Prob(Light\ pulses) - Prob(Dark\ counting))}{\mu} \quad (3.9)$$

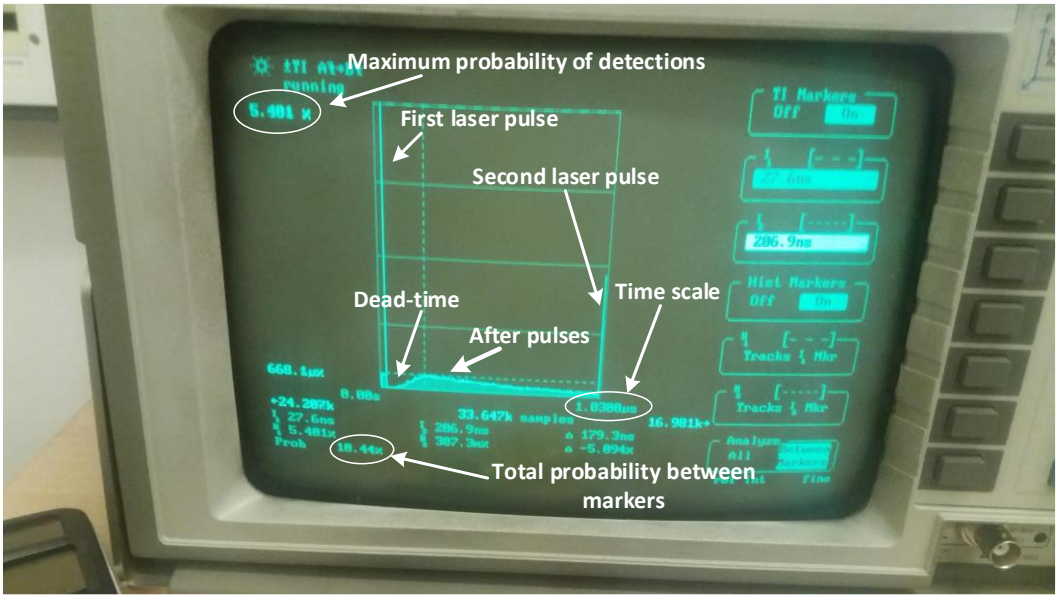

Figure 3.16: A Photograph of the MDA module screen, there is a measurement of photon detections with the NFAD which shows the two detected light pulses. Following both pulses there is the dead time and after-pulses. The MDA measures the probability of stop events to occur within a specific range of time defined between markers. Using 30,000 stop events for each PDE estimate reduces analysis errors to acceptable levels.

Where μ is the mean number of photons per pulse set to be <<1. The NFAD's PDE is reduced to a subtraction between the probability of light pulses detected at a range of time and the probability of dark counts at the same range of time as the light pulses. This subtraction has a purpose of removing any dark count influence from the light pulses. When pulse repetition rate is low the after-pulsing has decayed away before the next

pulse and dark counts could be estimated in an equal width gated window several nanoseconds before the light pulses).

3.6.2 PDE as a function of reverse-bias voltage

The reverse bias voltage value controls the NFAD mode of operation through unity gain, avalanche gain and Geiger mode operation. The voltage in excess of breakdown also affects the PDE directly. To plot this influence, the NFAD is fixed at certain temperatures as seen in section 3.5.1. Thereby, the reverse bias voltage is increased in steps of 0.2V. Figure 3.17 illustrates the PDE measured as described in section 3.6.1 plotted as a function of the reverse voltage.

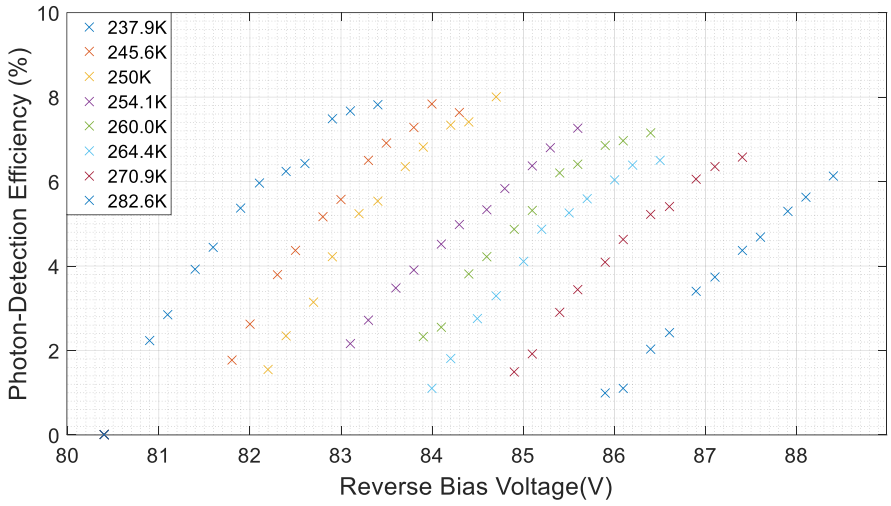

Figure 3.17: The PDE as a function of the reverse bias voltage for different temperatures.

At low temperatures the PDE increases rapidly with overvoltage, for instance at 237.9K, the PDE rises to saturation value around 8% within 2.5V. For a range temperature between 260.0K and 282.6K, the PDE has an increment more linear and the saturation for temperatures (254.1K and 282.6K) is not clearly defined.

The PDE has a maximum peak value at 250K and after that temperature there is a slight decrement to 6% for 282.6K, these peak values are achieved when the NFAD has a high reverse bias voltage. It is difficult to observe the PDE close to breakdown possibly due to our choice of voltage steps to avoid noise in the discriminator but clearly at higher temperatures a slower growth of PDE with overvoltage reduces the first point 'turn-on' PDE.

3.6.3 PDE as a function of excess bias voltage

A plot of the PDE as a function of a quantified excess bias voltage over V_{Br} can show this tendency with more detail. Thereby, the PDE is plotted as a function of the excess bias voltage over V_{Br} and the PDE tendencies for each temperature are visible with more clarity. The excess bias voltage over V_{Br}, starts at 0.5V and it is increased in 0.2V until reaching 3.0V, and the set of temperatures used in this plot are the same as the previous section. Figure 3.18 illustrates a graph of the PDE as a function of an excess bias voltage over V_{Br}.

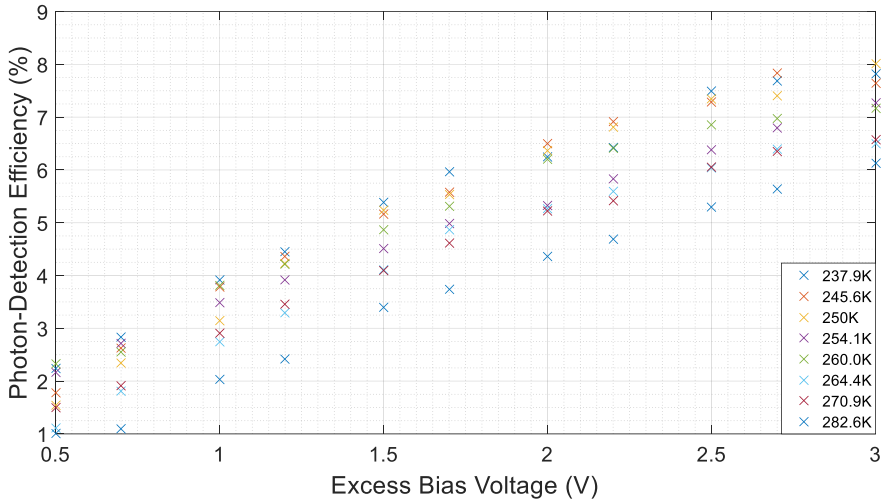

Figure 3.18: The PDE as a function of excess bias voltage upon V_{Br} at different temperatures.

0.5V over V_{Br} is the start point for the PDE and the linear increment is clearer. The steady-state where the PDE reaches a maximum value for 237.9K starts at 2.5V over V_{Br}, and for the temperature range of 245.6K to 264.4K (which starts at 2.7V). After 264.4K it is not possible to appreciate any steady-state tendency, which results in a linear increment until reaching the maximum voltage (3.0V over V_{Br}).

The PDE is sensitive for the changes of the excess bias voltage with an increment that is almost linear (below 264.4K), and although the excess voltage plays an important role in the PDE increment. It is the temperature that defines the maximum PDE (at 250K) near to 8%, after this percentage there is a decrement until falling to near 6% for a temperature of 282.6K. The graphs of figures 3.17 and 3.18 show a relationship between the temperature and the PDE.

3.6.4 PDE as a function of temperature

There is a relationship between the PDE and temperature which was observable in the previous measurements, but a plot of the PDE as a function of temperature can disclose more details about this relationship. The PDE as a function of temperature is performed with an excess bias voltage fixed at a certain value and the temperature is increased (from 237.9K). Figure 3.19 illustrates a graph of the PDE as a function of temperature.

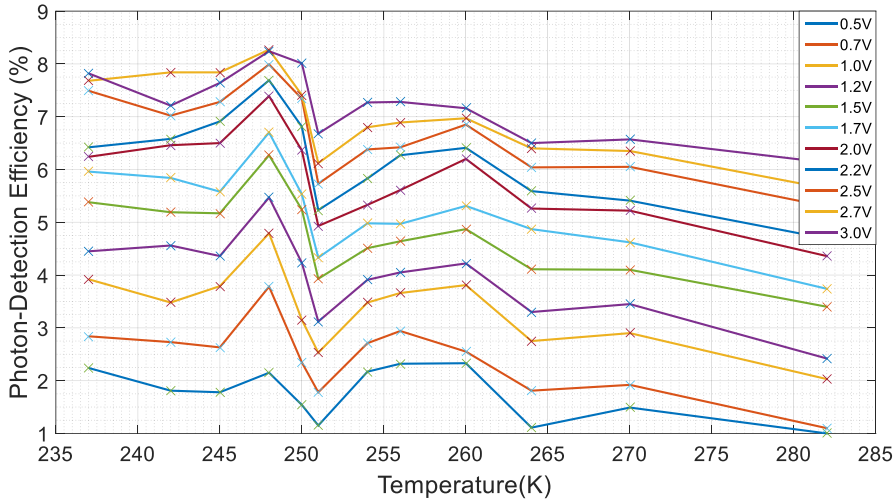

Figure 3.19: PDE as a function of temperature for different excess bias voltages over V_{Br}.

This graph is more conclusive on the relationship between the PDE and the temperature than the previous graphs illustrated in figures 3.17 and 3.18. The overall trend is a drop in efficiency as temperature rises for all over-voltages. The fluctuations are likely to arise from uncertainty in our estimation of breakdown voltage.

The PDE is thus only weakly influenced by temperature but it is the excess voltage over V_{Br} that defines the PDE percentage level. Therefore, a high excess bias voltage can reach a high PDE but there could be some collateral effects like an increment of dark counting which we discuss in the next section.

3.6.5 PDE as a function of Dark Counts

In section 3.5.1 and 3.5.2 it discussed the increment of dark counts when the reverse bias voltage is increased, although during the PDE measurement any dark-counting contribution is supressed through the equation (3.9), it is important to analyse the

relationship between the PDE and dark counts. This analysis is performed with a superposition of the gated PDE percentage as a function of reverse bias voltage, and the dark counts (estimated by direct counting in the TCSPC) as a function of reverse bias voltage. Thereby, it is possible to plot the PDE as a function of dark counts in figure 3.20.

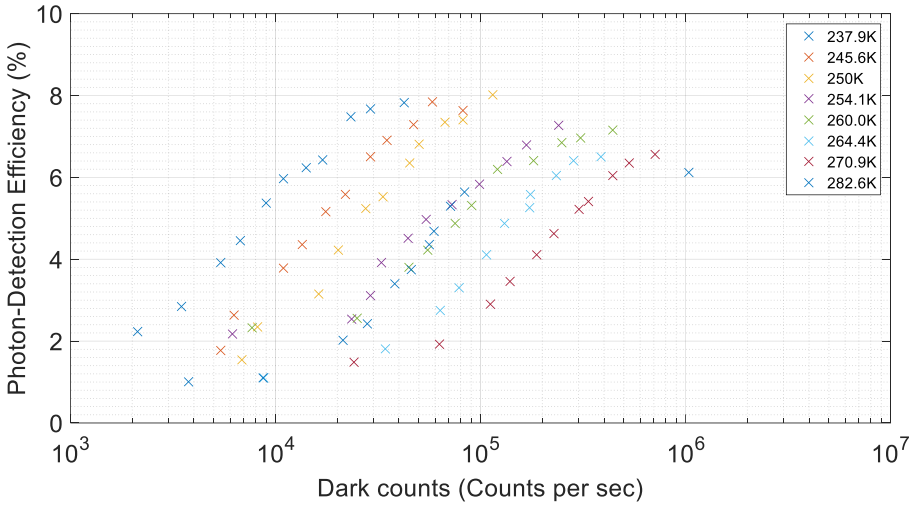

Figure 3.20: The PDE as a function of dark counts for different temperatures on the logarithmic scale.

The first observable detail is the presence of low dark count outliers for higher temperatures for instance at a temperature of 282.6K 1% of efficiency corresponds to <10,000 dark counts/sec. These dark count values may indicate dark counts fall below discriminator threshold before light. Otherwise we clearly see a linear increment until reaching a certain dark count value, after this value the PDE begins to saturate.

As expected, at low temperatures the relation between PDE-dark counting does not overpass 10^5 counts per second, after 250K the relation increases until reaching 10^6 counts per second. Above 10^6 counts per second we expect to see reductions in efficiency measured due to dead time saturation effects. However the linear increment part of the PDE implies an exponential increase of dark counts with voltage beyond breakdown.

3.7 After-pulsing Probability Characterisation

The after-pulsing characterisation can be a hard parameter to measure, due to the nature of self after-pulsing [22] but not impossible. Such as the previous parameters measured, the after-pulsing requires certain setup conditions as a rate repetition at 6 kHz to obtain a clear after-pulsing lifetime, measured through the TCSPC but in autocorrelation mode. Figure 3.21 illustrated the setup diagram for after-pulsing temporal distribution measurements.

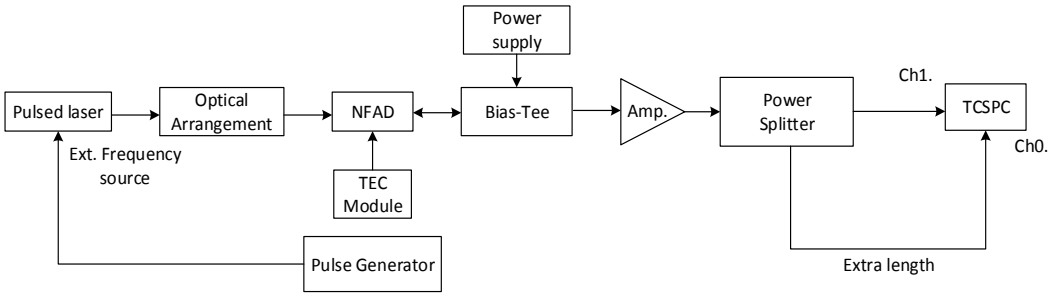

Figure 3.21: Setup diagram to measure after-pulsing lifetime distributions. This setup is similar to figure 3.14, but the difference lies on a power splitter which divides the signal from the amplifier (Amp.) in to two identical signals. However, there is a considerable length between the connections of channel 0 and 1 (channel 0 is longer), this extra length is to avoid the signal stopping itself from allowing it to see all the after pulses arriving shortly after.

With 6 kHz of rate repetition in the pulsed laser, the time gap between pulses is 167µs and thereby any possible influence of the next light pulse is supressed. After obtaining the after-pulsing lifetimes, they are post-processed with a software program in LabVIEW of National Instruments®, which applies a temporal window to the after-pulsing lifetime and thus, any dark-counting contribution is discarded.

Although the TCSPC shows the after-pulsing lifetime distribution in terms of counts as a function of time, it is possible to convert into probability as a function of time using again the MDA module, once the MDA obtains the after-pulsing lifetime distribution (after 50,000 samples) the highest probability is registered because it corresponds to the high photon coincidence, and through a simple math conversion the after-pulsing life distribution is converted in terms of probability as a function of time.

The main reason why the temporal distributions are not obtained through the MDA is because the MDA, despite being useful, is also a very old instrument that does not have a digital link interface such as a USB port.

3.7.1 After-pulsing temporal distribution and energy trap activation

During the post-processing, the after-pulsing lifetimes are represented as a function of time, there are a total of 20,000 bin samples for each after-pulsing lifetime as each bin represent 512ps. The after-pulsing decay curves are plotted in figure 3.21 from which decay times can be calculated.

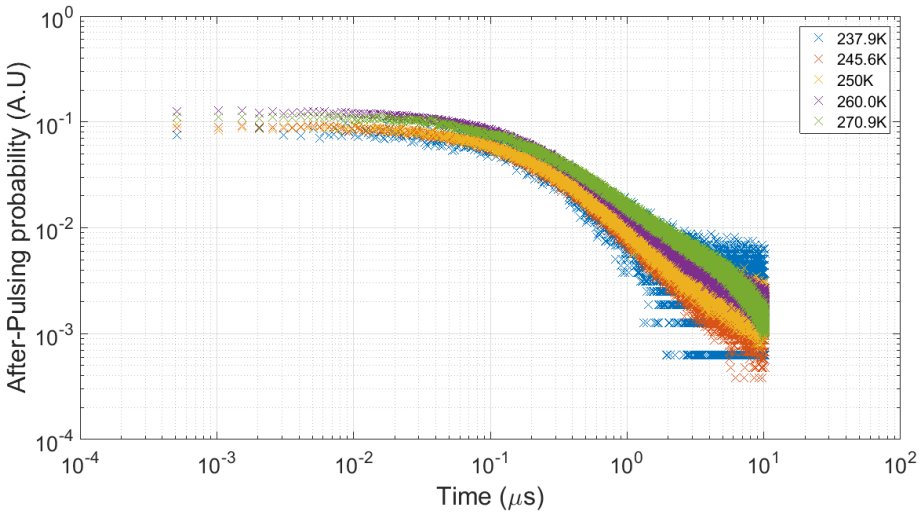

Figure 3.22: After-pulsing temporal distributions for 5 temperatures on logarithmic scales. When the temperature is cold (237.9K), the after-pulsing temporal distribution has a short lifetime tendency, which is increased when the temperature is also increased.

It is possible to observe in the after-pulsing lifetime at 237.9K, there is only dark-counts after 1µs. This dark-counting tendency is reduced when the temperature is warmed e.g. at 270.9K in 10µs, there is not traces of dark-counts. Furthermore to show the after-pulsing lifetime it is also possible to estimate the traps energy activation, and again a program in LabVIEW® is used but the lifetime of the traps are obtained first.

The best option to obtain the lifetime of the traps is to use an approximation method, and the fit approximation method is a combination of least square and Levenberg-Marquardt. The exponential fitting sub-instrument of LabVIEW® requires a time scale which is obtained from the multiplication of the number of samples and the resolution. Thereby, the mathematical model used for the fitting is represented in the equation (3.10).

$$y[i] = ae^{bx[i]} + c \tag{3.10}$$

The sub-instrument of LabVIEW® releases the amplitude (a) and the damping (b) of the exponential function, and the c is 0 because the after-pulsing temporal distributions do not have a specific value. The variable i represent the number of bin used to replicate the time scale $x[i]$ and the function resultant $y[i]$, figure 3.23 illustrates the after-pulsing temporal distribution at 250K and its exponential fit.

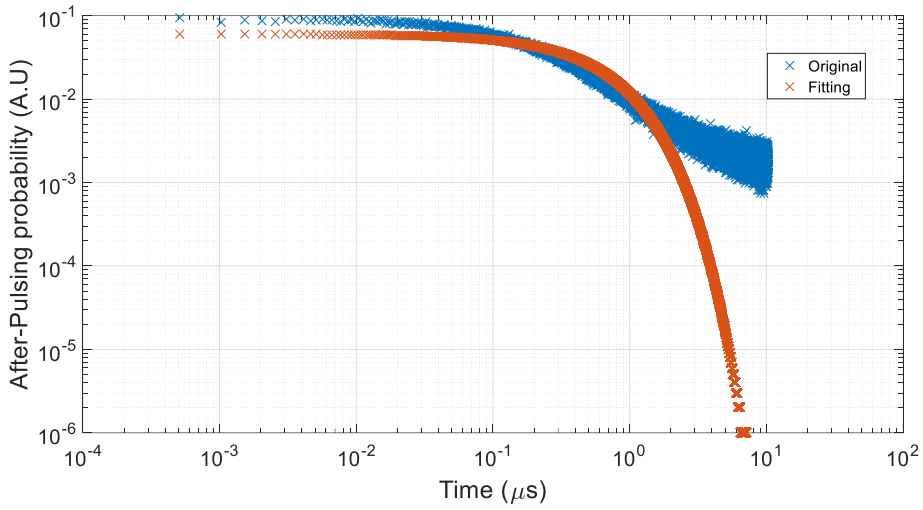

Figure 3.23: After-pulsing temporal distribution at 250K and its exponential fitting.

The trapping lifetime (τ_i) is part of the after-pulsing probability and therefore, the probability can be modelled through a mathematical model expressed in the equation (3.11) [22].

$$P_{AP} = \sum_{t=0}^{N} \frac{A}{\tau_i(E_a,T)} e^{\frac{t}{\tau_i(E_a,T)}} \tag{3.11}$$

This mathematical model is widely accepted to describe the temporal distribution of the after-pulsing and accounts for the existence of a limited number of trap families in the semiconductor [22]. In the equation (3.11) it described the probability of a trap being filled during an avalanche event (A) and the lifetime of a trap τ_i (which is as a function of energy activation E_a and temperature T) Therefore, $-\frac{t}{\tau_i(E_a,T)}$ is the damping factor obtained during the exponential fitting of the after-pulsing temporal distributions, table 3.2 registered the damping factors obtained with the fitting and their corresponding lifetime traps.

Temperature (K)	Damping factor (μs^{-1})	Trapping lifetime (ns)
237K	-1.1384	878ns
245K	-1.3672	731ns
250K	-1.6365	611ns
260K	-1.9353	517ns
270K	-2.0960	477ns

Table 3.2: The Damping factors obtained with an exponential fitting and their corresponding trapping lifetimes for the temperatures.

After obtaining the trapping lifetimes of the after-pulsing temporal distributions, it is easy to obtain the activation energy of the traps through the Arrhenius equation (3.12) [73].

$$\tau_i = \frac{1}{\sigma v N} e^{\frac{E_a}{k_B T}} \tag{3.12}$$

Where σ is the trap cross section, v is the average thermal velocity of carriers to be trapped and N is the effective density of states of the relevant band. Both v and N are directly proportionated by the temperature (T), and therefore $\sigma v N$ has an overall dependence on T^2 and, $\frac{1}{\sigma v N}$ can be replaced by $\frac{1}{T^2}$ and perform another fit with the lifetimes obtained previously. The fitting recommended [22, 73] to obtain the energy activation of the traps is a linear fit, thus the equation (3.12) is converted to a linear function using the power law.

$$\ln(T^2 \tau_i) = \frac{E_a}{k_B T} + C \tag{3.13}$$

The equation (3.13) is linear and its slope corresponds to the energy activation, then it is easy apply a linear fit using a sub-instrument of LabVIEW. The plotting of equation (3.13) is performed with $\ln(T^2 \tau_i)$ as a function of $\frac{1}{K_B T}$, and thereby figure 3.24 shows the plotting of equation (3.13) and its linear fitting with LabVIEW sub-instrument fitting.

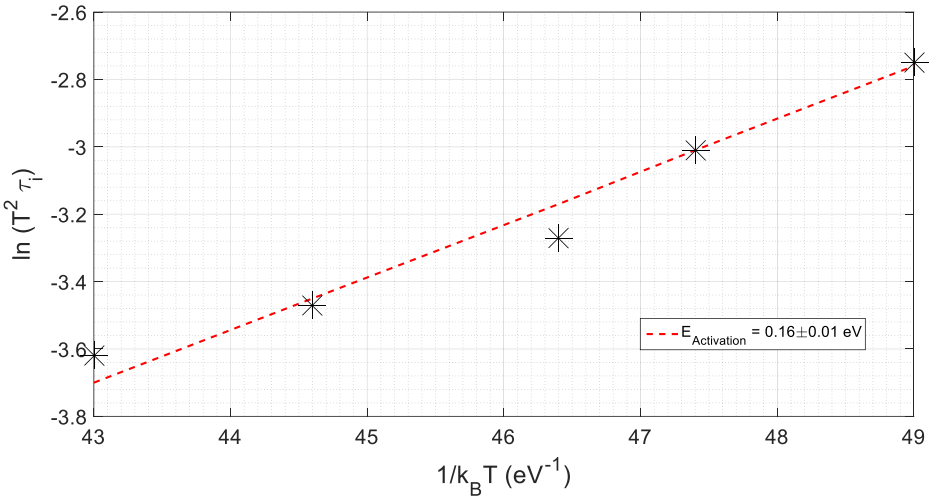

Figure 3.24: The Arrhenius plot obtained from the lifetime traps as a function of k_BT. The linear fit estimated the activation energy at 0.16±0.01eV.

The activation energy obtained (0.16eV) indicates the position of the traps in the bandgap, values in the range between 0.05eV and 0.22eV indicate a shallow region (near to the conduction band). Some experiments obtained similar results [22] but [74] reported 0.18eV, these values are attributed to a divacancy in the InP gain region.

When the temperatures are high (above 200K), the shallow traps are not seen as they empty quickly (<100ns) by thermal excitation. Hence only the smaller number of deeper traps with the activation energy around 0.16 eV are seen. Shallower traps dominate when the temperatures are low (below 200K) such as it is reported in [22]. Here we are interested in higher temperatures and our TEC cannot reach temperatures below 237K.

To analyse the after-pulses and effects of several conditions such as: reverse bias, temperature and delay factors, it is preferable to measure the total after-pulsing probability which is discussed in the next section.

3.7.2 Total after-pulsing probability

The total after-pulsing probability is measured through the MDA module but this time configured as an auto-correlator, to register all the pulses (after pulses and dark counting) after the photodetection, in figure 3.25 it illustrates a connection scheme of the domain analyser module in auto-correlator mode.

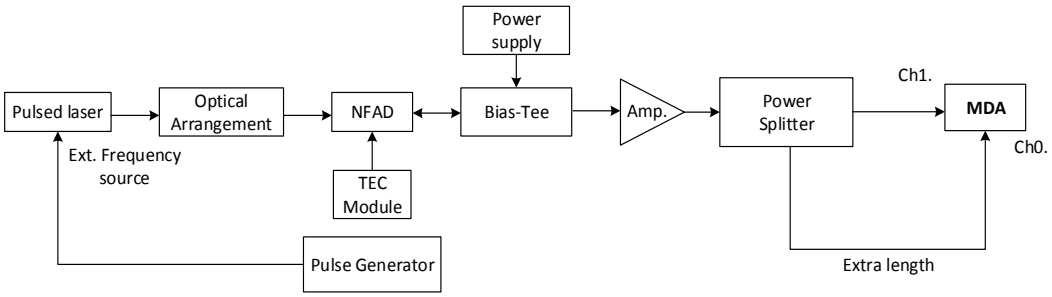

Figure 3.25: Scheme of the modulation domain analyser module connection in auto-correlator mode. The output of the amplifier is connected to a power splitter, the cable connected to channel 0 (start channel) is longer than the cable to channel 1 (stop channel). This avoids the photodetection start from stopping itself thus allowing us to measure the after-pulses arriving a short delay after.

Again, the lack of a modern USB connection prevents us performing measurements for the post-analysis process. (A general Purpose Interface Bus (GPIB) exists but requires a specialist interface and program to capture the measurements [75]). For this reason, the total after-pulsing measurement is performed directly from the MDA module screen, as shown in figure 3.26 which illustrates a measurement of the MDA Module.

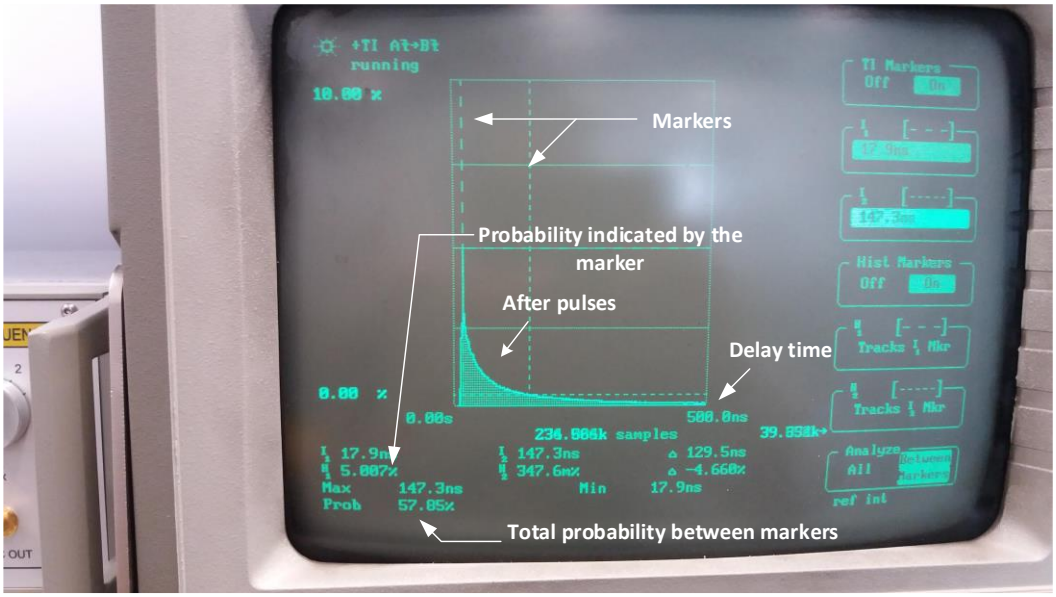

Figure 3.26: The Measurement on the Modulation Domain Analyser (MDA) Module Screen at a full scale delay time of 500ns. The probability function displays the probability of an after-pulse between the markers.

The after pulses are registered after the photodetection dead time and displayed in a delay time histogram (the start pulse delay time means we avoid stopping with a copy of the photodetection pulse).

The smooth histogram is reached after an adequate number of samples (>100,000 samples) are taken to obtain smooth measurements such as the measurement illustrated in figure 3.26. The sampling time is fixed at 3ms and the time for the measurement is 10 minutes, but a short delay time can skip the after pulse and a long delay time can reduce the accuracy, to distinguish the border between after pulses and dark counting. This condition is clearly observable in figure 3.27, which illustrates the after pulses measured at a delay time of 10µs.

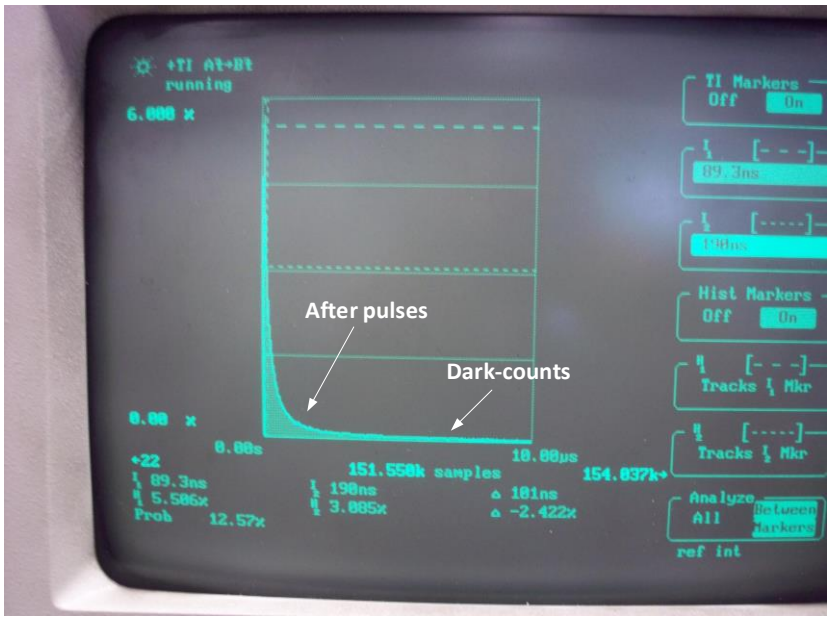

Figure 3.27: Measurement on the MDA module screen of the total after-pulsing probability at a delay time of 10µs.

This delay time shows the steady-state region that represents dark-counting with more detail, and the comparison between figure 3.26 and 3.27 situates the border between the after-pulses and dark-counts around 2µs. Therefore, from this time up to 10µs there are only dark-counts, but it is necessary to trace several delay times for a total after-pulsing probability measurement.

3.7.2.1 Total after-pulsing probability as a function of delay time

The delay times that are proposed to measure the total after-pulsing are 100ns, 500ns, 1µs, 2µs and 5µs. During these delay times, the temperatures are fixed at different values and the excess bias voltage is fixed at 0.5V, to measure the total after-pulsing probability. The temperature affects the after-pulsing probability significantly [20, 21, 61], hence it is expected to observe high probabilities when the NFAD has cold temperatures.

In figure 3.28 it illustrates a graph of the total after-pulsing probability as a function of delay time after dead-time and the temperature effects.

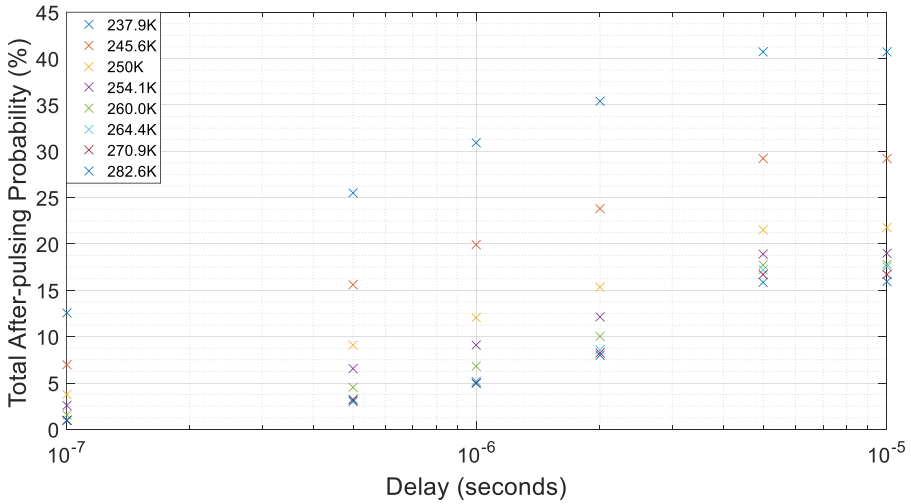

Figure 3.28: Total after-pulsing probability as a function of a delay time for 0.5V of excess bias voltage over V_{Br}.

The total after-pulsing probability has a continuous increment until reaching 2µs of delay time, after that time the total probability shows a certain stability. This stability also represents the dark-counting and therefore, a suitable delay time to perform the measurements is around 2µs±500ns. However, the total probability contains a certain amount of dark counting, to determine the total dark-counting probability (P_{Dark}) the equation (3.14) is used.

$$P_{Dark} = (D_{CR})(\Delta T) \tag{3.14}$$

Where D_{CR} is the dark-counting rate, ΔT is the delay time. Thereby, the total dark counting probability is plotted as the total after pulsing probability, in figure 3.29 it illustrated a graph of the total dark counting as a function of the delay time.

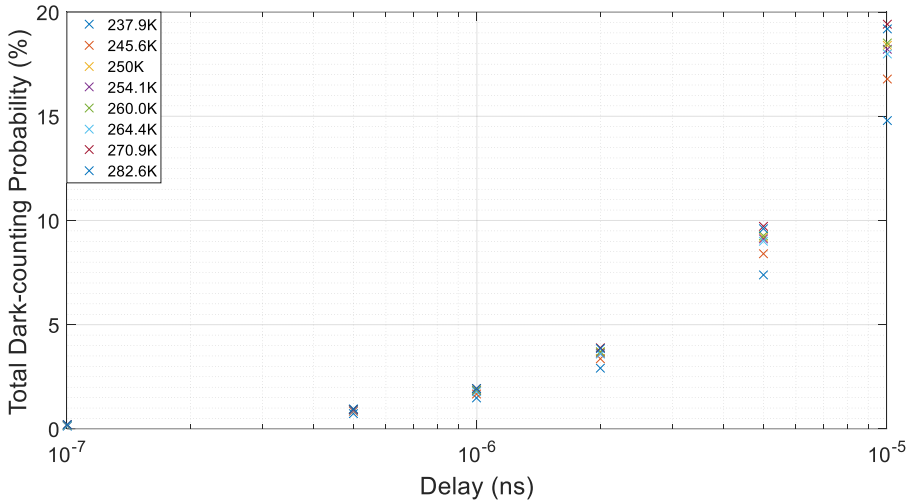

Figure 3.29: Total dark counting probability as a function of a delay time for 0.5V of excess bias voltage over V_{Br}.

The total dark counting probability is smaller than the total after pulsing probability in figure 3.26, but large enough to be significant, and must be subtracted.

3.7.2.2 Total after-pulsing probability as a function of excess bias

The excess bias voltage also has a relation to the total after-pulsing probability, because an increment of PDE also means an increment of electrons trapped, as discussed in section 1.3.1 [20, 22, 23, 24]. Hence, figure 3.30 illustrates the total after-pulsing probability as a function of the excess bias voltage at different temperatures.

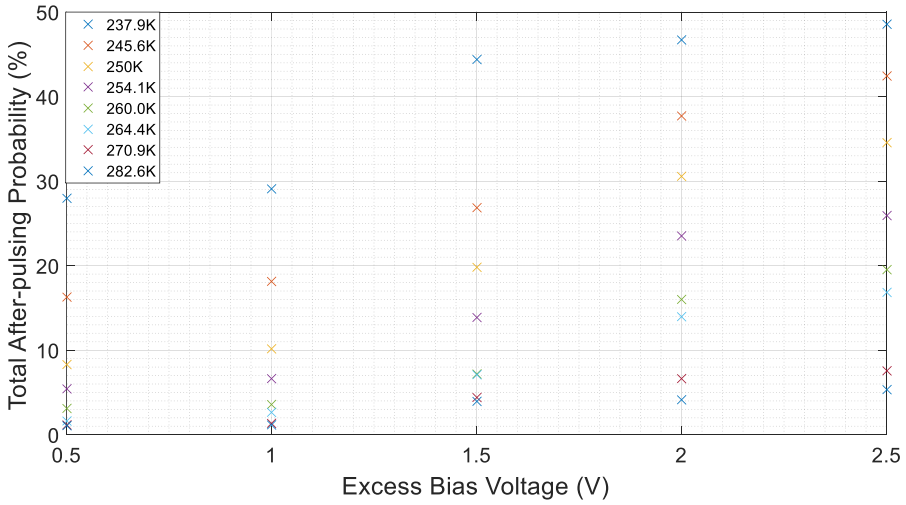

Figure 3.30: Total after-pulsing probability as a function of excess bias voltage over V_{Br} at 2µs of delay time.

It was expected that there would be similar behaviour such as dark-counting and PDE measurements as a function of excess bias voltage, as discussed in sections 3.5.2 and 3.6.2. Thereby, it confirms a direct relationship in the total after pulsing probability by the excess bias voltage [24, 75]. After 1V of excess bias voltage the total probability arose until reaching a higher percentage (75% for 237.9K), but in the temperature range between 250K and 254.0K the total probability stayed at 50%, confirming again that the temperature range is suitable for QKD applications [11, 21, 77].

3.7.2.3 Total after-pulsing probability as a function of temperature

The previous total after-pulsing probability analysis shows a certain relationship between the probability percentage and the temperature, this relationship effect is fully documented in other SPAD characterisations and analysis [20, 21, 25]. Furthermore, the total probability as a function of the temperature has relevance, since the previous characterizations showed a certain linear dark-count increment and a PDE over 7%, figure 3.31 illustrates a graph of the total After-pulsing probability as a function of temperature.

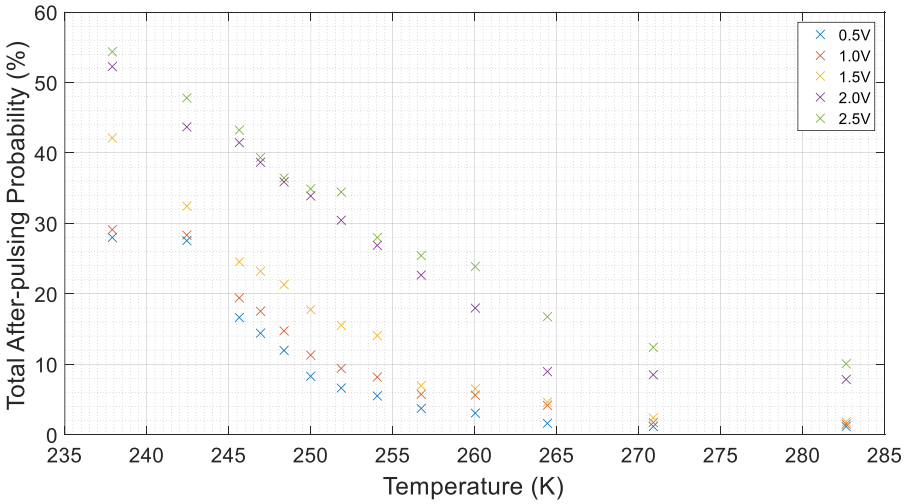

Figure 3.31: Total after-pulsing probability as a function of temperature at 2µs of delay time.

This graph shows more detail with the temperature's influence on the total after-pulsing probability. The total probability reaches a minimum value when the NFAD is cooled at 264K, after that temperature the total probability presents a stability between 264K and 282K (room temperature), also it confirmed a direct increment effect by the excess bias voltage.

The decrement of the total probability from 237K to 264K is almost linear except for the curve that corresponds to 2.5V with an excess bias voltage, this little increase could be provoked by noise factors that are amplified by the excess bias voltage. The total after-pulsing probability measurements are similar to other NFAD measurement reports [23, 34]. During the total after-pulsing probability characterisation, a suitable temperature range (between 250K and 254.06K) was found and an excess bias voltage (0.5 and 1.0V) for a moderate after-pulsing probability percentage is around 10% but applications of quantum communications are suitable [21].

3.8 Timing Jitter Characterisation

Just like the After-pulsing probability characterisation, the timing jitter characterisation also requires light pulses but the rate repetition is fixed at 20MHz, so the timing jitter is measured through several photon coincidences with a TCSPC. After these histograms are compared to each other through their Full Width Half Maximum (FWHM), these histograms are illustrated in figure 3.32, in which the counts are plotted as a function of excess bias voltage over V_{Br} at 250K.

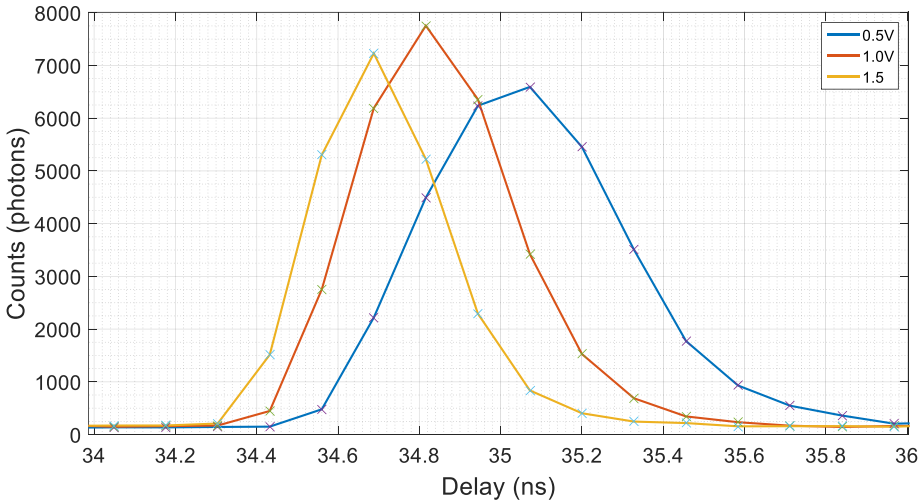

Figure 3.32: Histogram of photon detections of 250K at different excess bias voltages.

The photon detections are registered through the histograms, but only their FWHM can be used for the timing jitter measurement. The manufacturer specifies a typical timing jitter at 300ps and a maximum of 400ps [30], the timing jitter measured from the FWHM histograms has a value of 384ps, except for the FWHM at 0.5V which is 640ps. Figure 3.33 illustrates the timing jitter measured from the histogram of figure 3.32.

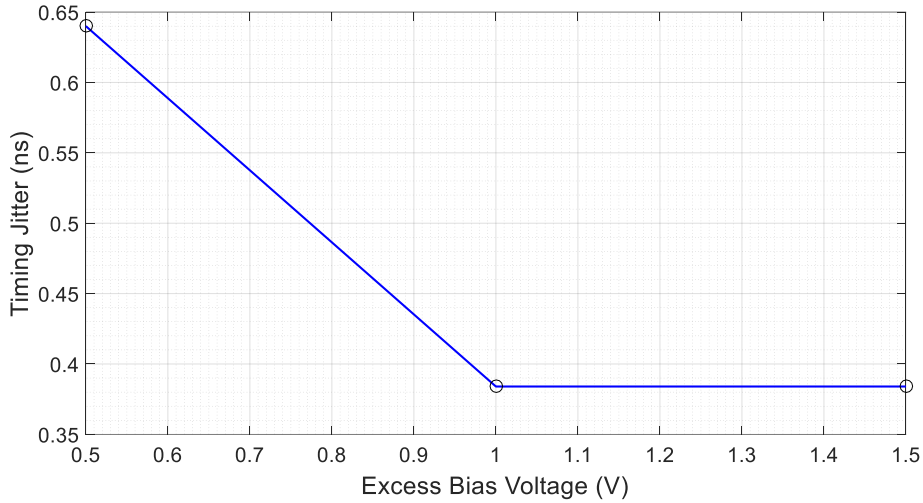

Figure 3.33: Timing jitter measurements as a function of excess bias voltage over VBr at 250K of temperature.

At 0.5V of excess bias voltage, the timing jitter has a maximum value of 640ps that even overtakes the maximum specified by the manufacturer, but when the excess bias voltage increases, the timing jitter goes down to a value of 384ps (near to 400ps). The timing jitter can also be plotted as a function of temperature, but the histograms are compared at different temperatures. The excess bias voltage is at a fixed value of 0.5V over the V_{Br} corresponding to the temperature discussed in figure 3.3. Thereby, the photon detection histograms are plotted in figure 3.34 at different temperatures using the TCSPC.

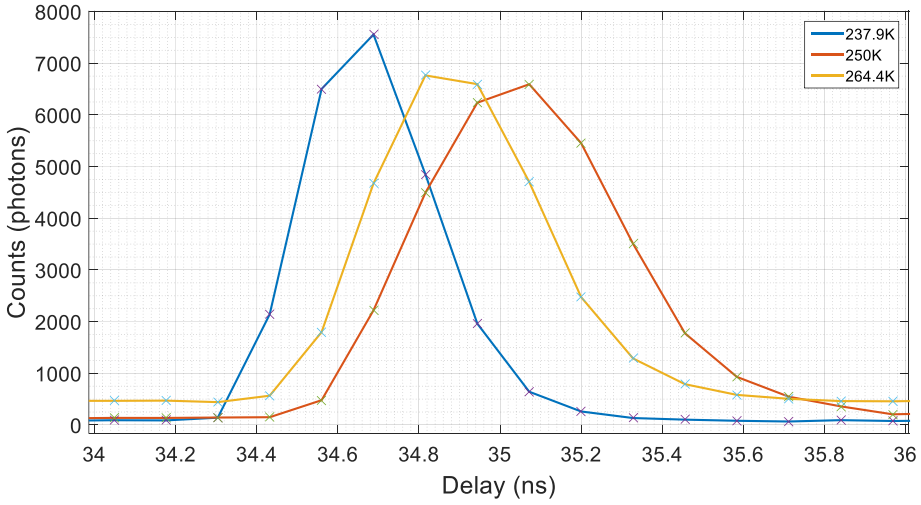

Figure 3.34: Histogram of photon detections at 0.5V of excess bias voltage at 3 different temperatures.

The FWHM of each histogram is measured and registered. Then, the timing jitter is plotted as a function of the temperature in figure 3.35.

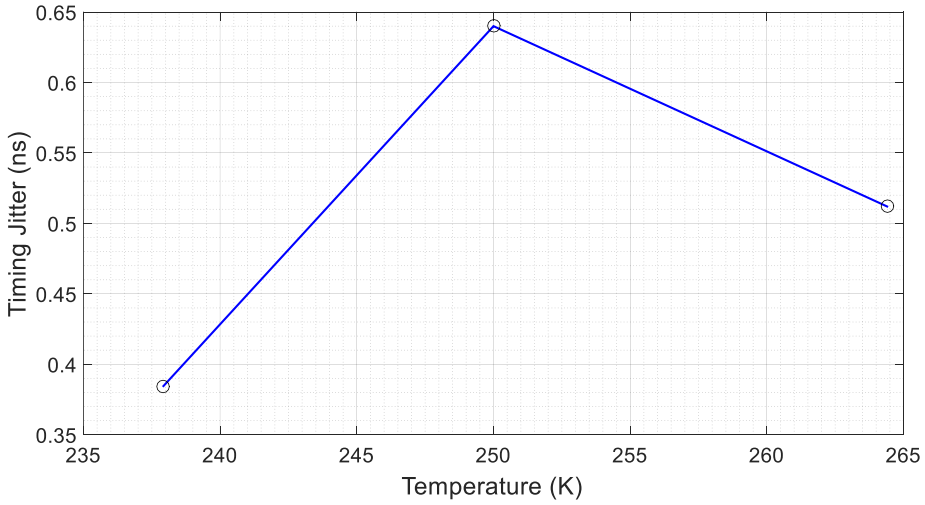

Figure 3.35: Timing jitter measurements as a function of temperature at 0.5V over V_{Br}.

The timing jitter at 237.9K is close to the typical timing specified by the manufacturer [30]. After, there is an increment higher than the maximum specified and after this the timing falls again.

Therefore, the timing jitter shows a certain stability when the excess bias voltage overcomes 1V until reaching 1.5V (figure 3.33), but the timing jitter as a function of temperature has a completely different behaviour, it is possible for the differences between the reverse bias used at these temperatures to overcome V_{Br}. However, the timing jitter is normally characterised as a function of excess bias voltage at only one temperature [20, 23, 34].

3.9 Summary

This chapter analysed the characterisation of an enhanced SPAD passive quenching method which is represented by the NFAD which is SPAD exploits the passive quenching properties without a complex electronic circuit and associated stray capacitance [28, 29]. However, the model used during the characterisation does not have to integrate a proper fibre optic [30], hence it was necessary to assemble a proper experimental arrangement that enclosed the optical coupling and electrical connection into a compact set up. The mount of the NFAD on the experimental arrangement then required an alignment to the optical fibre delivery before the characterisation. The unity gain efficiency of the NFAD

was estimated to be 41% using a laser attenuated to 7nW. This is lower than the value quoted for typical InGaAs APD's but reflects losses in the optical coupling from fibre to detector.

The NFAD when wired up as an electronic device can also pick up noise that could affect the characterisation measurement. We find that most noise was discriminated against (section 3.3.1) by adjusting the threshold level in the TCSPC. Thereby, the influence of the noise is reduced for the characterisation of the next sections to 3.3. In addition, the noise is also discriminated in section 3.6 where the MDA (modulation domain analyser), also has an adjustable threshold.

The dark counts increase dramatically (exponentially) with voltage beyond breakdown. At low over-voltages the dark count does not increase much over the temperature range of 230-270K (section 3.5.1 and 3.5.2) but at the highest over-voltages of 2.5V an order of magnitude increase in dark count is seen in this temperature range. In the PDE characterisation we see a linear increment of efficiency until reaching a maximum value of around 8% efficiency at temperatures lower than 250K while at higher temperatures the highest efficiency was not reached by 2.5V. This efficiency is consistent with the values reported by other researches which specify 10% of efficiency [61, 76]. The use of pulsed illumination and direct measurement of probabilities in the MDA module avoids the overestimation of efficiency by gating out after-pulsing.

The after pulsing characterisation was divided in to two parts: an analysis of the trap levels which are responsible for after-pulses and the total after-pulsing probability. The measurement of activation energy of the traps required to measure the temporal distribution of the after-pulses, because their lifetimes represent the lifetime of the traps. Thereby, the after-pulsing temporal distributions are fitted to an exponential function with the purpose of obtaining the trap lifetimes (registered in table 3.2). Lifetimes are all below 1us falling to 500ns at 270K suggesting that after-pulsing problems are much less at high temperatures (but of course dark counts rates are high). The lifetime of the after-pulsing as a function of temperature allows the construction of an Arrhenius plot through which the trap activation energy of ~0.16 eV is determined.

The results obtained from the trap levels analysis and total after pulsing probability are consistent with the results of other works [22, 61, 76], which proved a clearly influence of temperature in the nature of the after-pulses, but also there are other factors which could

affect the after-pulsing probability. In section 3.7.2.3, the excess bias showed a high influence in the total probability, reaching a percentage >50% at 237.9K. However at higher temperatures. The jitter time characterisation showed a time close to the manufacturer specifications, although at 0.5V the timing jitter exceed the maximum specified.

Chapter 4.

Sine Wave Gating and Subtractive Cancellation

This chapter analyses the advantages of the sine wave gating as an active quenching technique for a SPAD [78-81], the previous chapter analysed a SPAD (NFAD) which exploits an integrated passive quenching technique. However, the result of the NFAD characterisation shows a dead time near to 600ns and significant after-pulsing distortion. For applications such as QKD that dead-time represents an upper limit on the rate of key transmission between Alice and Bob [36].

Although there are active quenching techniques that aim to reduce the SPADs dead time through different methods such as gating pulses [26, 31], these types of methods introduce parasitic signals with the same shape and sometimes amplitude as the photon-detection [27].

Therefore, a variation is proposed in this work to the sine wave gating technique, this variation supresses the sine wave without using any narrow bandpass filters such as other researches that use a sine wave gating [78-81], instead using interference to cancel the sine wave transmitted by the device with another out of phase sine wave.

4.1 Classical Gate Pulsing vs. Sine Wave Gating

The traditional active quenching is represented by a square wave signal or pulse gating, such as it was discussed in section 1.3.1.4. However, the drastic changes of level voltage which is inherent to these type of signals, represent a problem due to the internal and parasite SPAD capacitances (figure 1.15). To avoid the SPAD capacitances effects, there are some methods such as band pass filters or the use of a sine wave signal. The next sub-sections discuss the characteristics of both type of gating signals in depth.

4.1.1 Pulse Gating

The pulse gating method as an active quenching technique consists of pulses (square wave) of high amplitude and a repetition rate (normally at a range of MHz), these pulses are injected through a capacitive coupling to the cathode of the SPAD. However, the SPAD has an internal capacitance that is charged and discharged with each pulse. Figure 4.1 illustrates the pulse gating effect on a SPAD equivalent circuit and an unbiased InGaAs APD model G8931-4 from Hamamatsu®.

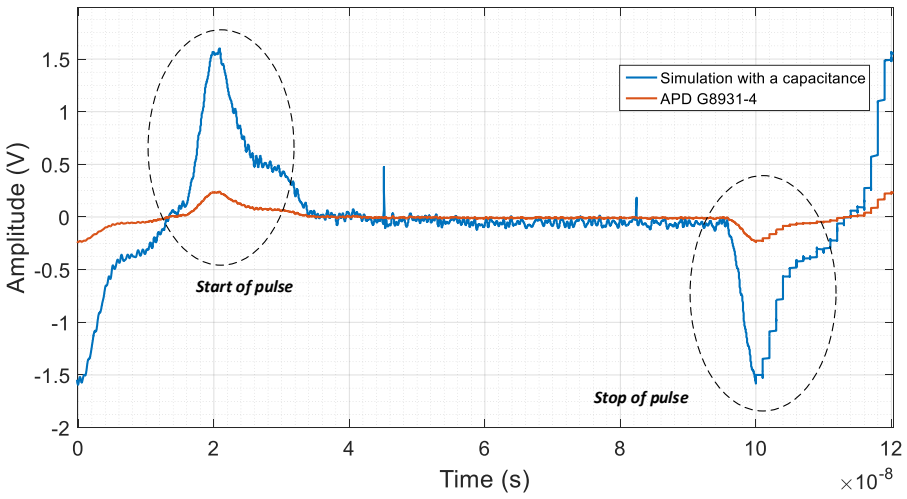

Figure 4.1: Pulse gating driven by 10MHz, and 2.5V of amplitude for a simulation of a SPAD by a capacitance driven by a gate pulse, and by an APD (G8931-4) in dark conditions and without any reverse bias voltage driven.

When a photon detection occurs in the SPAD with the pulse gating, the detection is combined with the charge-discharge pulses of the SPAD internal capacitance, this combination makes the photon measurement difficult. To illustrate this combination of pulses the G8931-4 is replaced by an InGaAs APD designed specifically for single-photon applications; the PGA-308 of Princeton Lightwave®. This SPAD is fixed to 0.5V beyond its breakdown voltage without any illumination, therefore the detection corresponds to a dark count (figure 4.2).

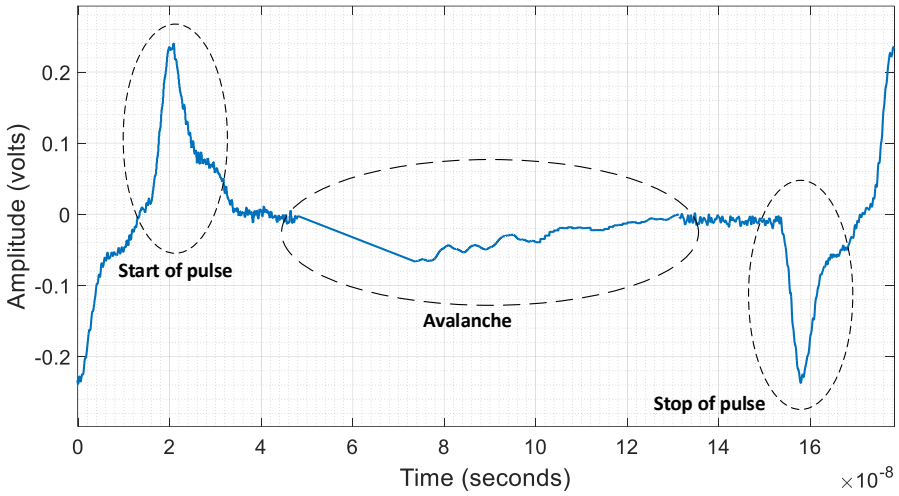

Figure 4.2: Avalanche (dark count) with pulse gating at 10MHz of rate repetition and 25% of duty cycle per pulse.

The pulse gating has a direct improvement on the after-pulsing reduction, because the photons are only detected when the detection occurs within the pulse gate duration [82], if the detection occurs between pulses, there is no possibility to register a detection and therefore there is a considerable reduction of the after-pulse contribution to the photon count rate. Also the short gate pulses mean a reduction of the number of carriers trapped during the avalanche.

The photon detection efficiency (PDE) is directly related to the pulse gate amplitude and its bias with respect of V_{Br}, e.g. if the pulse gate has an amplitude of 5V but it is biased 4V below V_{Br}, only 1V exceeds V_{Br} and therefore the PDE would be low. Commercially available detectors simple set a discrimination level above the pulse edge level which reduces also the detection of smaller avalanche signals. It has been shown that capacitive pulses can be attenuated through a self-difference technique [27, 82], and once the avalanche is isolated, it can be amplified and shaped for the analysis with a TCSPC. Such

devices are not commercially available and require carefully tuned external delay lines to match pulse repetition rate.

4.1.2 Sine Wave Gating

The sine wave has an advantage over the pulses when it is injected to the SPAD, the SPAD internal capacitance allows the sine wave to pass without modifying its properties severely, just changing its phase and amplitude. Figure 4.3 illustrates the sine wave signal through a SPAD.

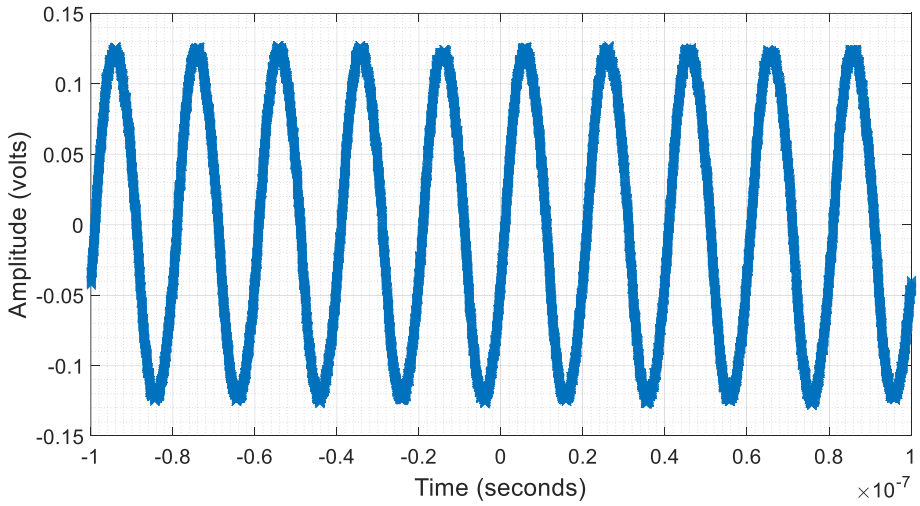

Figure 4.3: Sine wave signal through the SPAD in unity gain mode (input sine wave of ~5Vpp is attenuated by the SPAD).

The photon detection will sit on the sine wave and hence it is necessary to suppress the sine wave through low-pass filters such as is proposed in [78-81], the low-pass filters do not affect the avalanche considerably (the avalanche rate repetition is lower than the sine wave signal frequency) and almost suppresses the sine wave signal, but there is a considerable increment in the complexity of the SPAD electronic system, such as it is illustrated in [79, 83, 84].

Therefore, in this chapter the sine wave signal cancellation is proposed without affecting photon detection signals, through the wave interference. Thereby, the sine wave signal cancellation is achieved by adding another sine wave signal with the same frequency, the same amplitude but with a phase shifted by π to cancel the sine wave signals, and only the avalanche remains without increasing the SPAD electronic system.

4.2 Sine wave signal suppressing through wave interference

Such as mentioned previously, the sine wave signal used as gating in the active quenching scheme can be cancelled through wave interference. The gating signal is a sine wave with a defined amplitude and frequency, but the signal used to cancel is a cosine wave with the same amplitude and frequency than the signal used as a gating signal, the equation (4.1) represent these signals.

$$A\sin(\omega t+\phi)=a\sin(\omega t)+b\cos(\omega t) \tag{4.1}$$

There is a linear combination (due to the wave equation linearity) and therefore the principle of superposition can be applied, thereby both signals can be suppressed. The gating signal $y_{gating}=A_0\sin(\omega t)$ and cancellation signal $y_{cancellation}=A_0\sin(\omega t+\phi)$, to use a trigonometric identity it is recommended to *change the sine function for a cosine function* and represent both signals in a unique equation.

$$y_{total}=y_{gating}\pm y_{cancellation} \tag{4.2}$$

Thereby, the trigonometric identity $\cos a+\cos b=2\cos\left(\frac{a+b}{2}\right)\cos\left(\frac{a-b}{2}\right)$ is applied to equation (4.2) and also the superposition principle is applied:

$$y_{total}=2A_0\cos(\frac{\phi}{2})\cos(\omega t+\phi)=A(\phi)\cos(\omega t+\grave{\phi}) \tag{4.3}$$

The equation (4.3) has two important components: $A_0(\phi)=2A_0\cos(\frac{\phi}{2})$ contains the amplitude of the signal which results from the wave interference, and $\acute{\phi}=\frac{\phi}{2}$ is the phase shift of the signal which results from the wave interference. In resume, the result of the wave interference between two sine waves with the same frequency and amplitude is a new sine wave, but with a gap product (of a mean-gap) and an amplitude which is dependent on a shift phase. Then there is two cases: destructive interference and constructive interference, and for the sine wave gating proposed only the *destructive interference* is desired. Additionally it is important to mention, that both signals have been synchronized and have the same amplitudes, on the contrary any trigonometric identity is not useful and it is necessary to use phasor calculation.

4.3 Experimental Assembly

The SPAD used to test the sine wave gating is the PGA-308 with certain advantages over the PNA-208 (NFAD). It is fibre pigtailed which allows direct connection to the laser fibre thus avoiding any delicate alignment tasks. A lower temperature than the NFAD can be reached (221K minimum) and lower dark-counts. However, the SPAD is more sensitive to transients in the voltage and current, as it has no internal limiting resistor. Therefore the experimental array is covered in aluminium foil to avoid possible noise transients. The test circuit used for the sine wave gating method is slightly different than that used for the NFAD. The main difference lies in the SPAD terminal where the photon detection pulses are collected, which for this experiment is the anode. Also an impedance is added when it is near to the cathode and coupling the sine wave signal with the SPAD, in figure 4.4 it illustrates the electronic scheme of the test circuit.

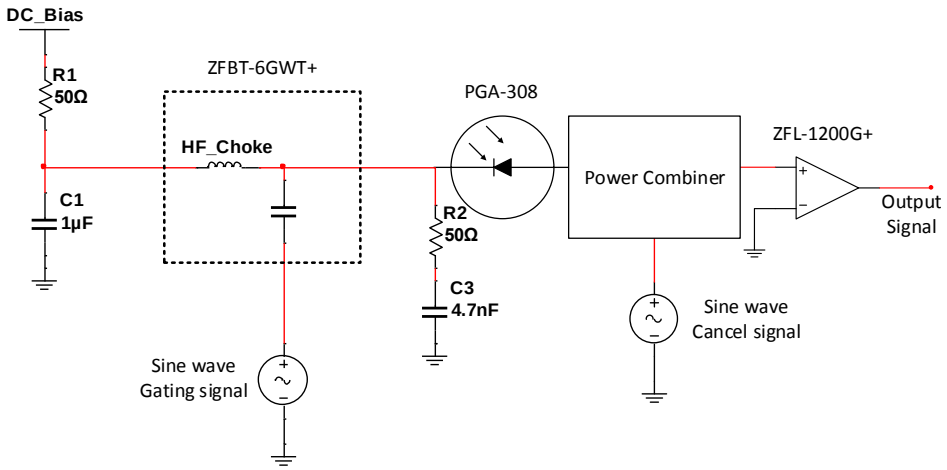

Figure 4.4: Test circuit electronic Schematic, the bias-tee is used to couple the DC voltage and sine wave signal, the power combiner is used to couple the gating sine wave with the cancelling sine wave, and a power amplifier is used to amplify the photon detection pulses.

Most equipment used in this experiment is the same that was used with the NFAD characterization except for the sine wave source. This source is a waveform generator model 3162 of LeCroy® with two isolated channel outputs with a separated control of amplitude, frequency and phase.

4.3.1 Photocurrent and thermistor curve of the SPAD

The fibre-pigtail connection makes the photocurrent measurement simple, this measurement has the same procedure as that for the NFAD photocurrent. The SPAD is reverse biased at room temperature from 0V to 40V, in this voltage range the current through the SPAD is around 980pA (a possible leakage-current or a source meter stochastic behaviour), when the reverse voltage overcomes 40V it starts a current increment that stops at 42V, that is the photocurrent. In the voltage range of 40V to 42V, the punch through voltage is passed and the current rises to reach a steady value of around 5.4nA when the laser illuminates the SPAD, but at 47V there is avalanche gain. As in the NFAD characterisation, the photocurrent is obtained through the subtraction of the SPAD currents, when the laser illuminates and the dark current when the laser is off (1.3nA) at the region 42V and 46V. Thereby, the photocurrent is 4.1nA and corresponds to 5nW of the laser optical power, but this amount of power indicates a unity gain quantum efficiency of 0.86 (86%) saturates the SPAD. Therefore, the laser is attenuated at -43dB to obtain 10^6 electrons per second, figure 4.5 illustrates the SPAD current curve.

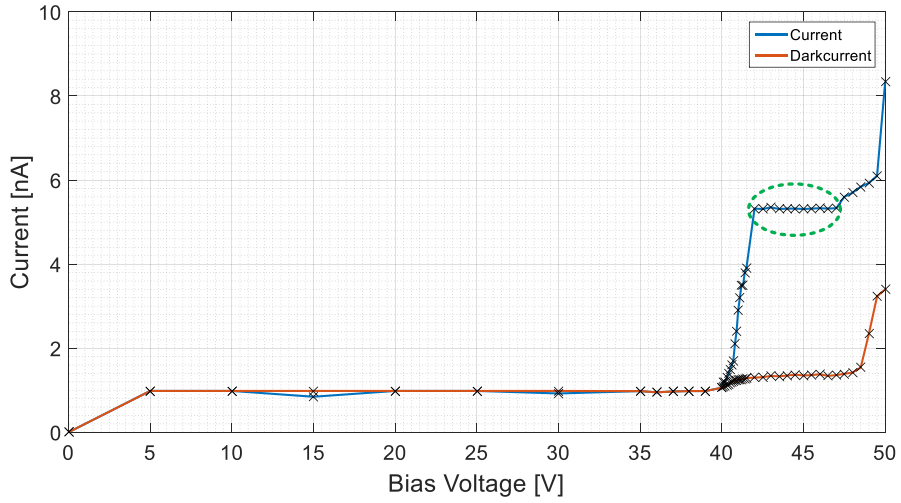

Figure 4.5: Current and dark-current through the SPAD as a function of a reverse bias voltage, the plateau zone (in the dash green circle) corresponds to the unity gain.

The Steinhart-Hart thermistor constants in the SPAD are different to NFAD, therefore the constants used to obtain the NFAD thermistor curve are not useful, the new constants are $A=0.8642\text{x}10^{-3}$, $B=3.3085\text{x}10^{-4}$ and $C=0.0660\text{x}10^{-7}$.

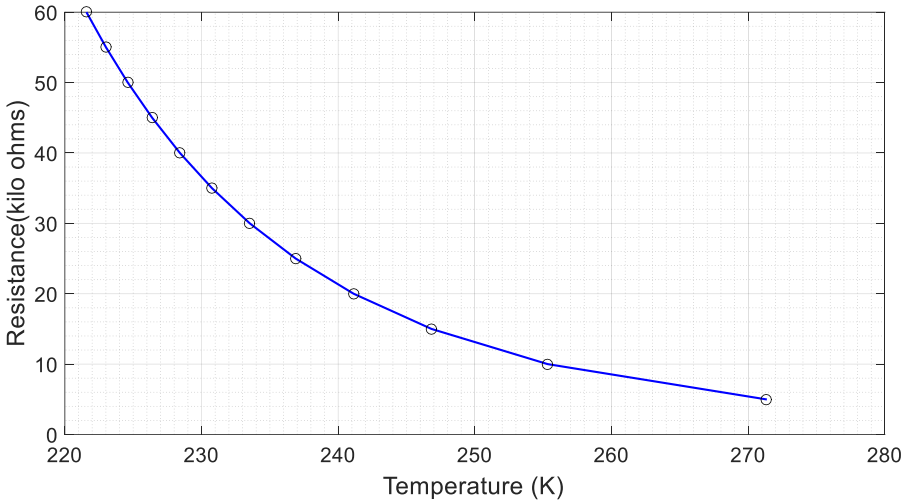

Figure 4.6: PGA-308 (SPAD) thermistor resistance (kΩ) versus temperature (K).

The thermistor curve of figure 4.6 has a certain similarity to the NFAD thermistor curve, but the range of resistance is higher in the NFAD.

4.3.2 Breakdown voltage characterisation

The SPAD has different Geiger parameters to the NFAD, therefore the characterisation used in the previous chapter is not useful for this experiment. The main Geiger mode parameter to obtain is the breakdown voltage (V_{Br}) with the purpose of knowing the Geiger mode-Avalanche threshold. Figure 4.7 illustrates V_{Br} as a function of temperature.

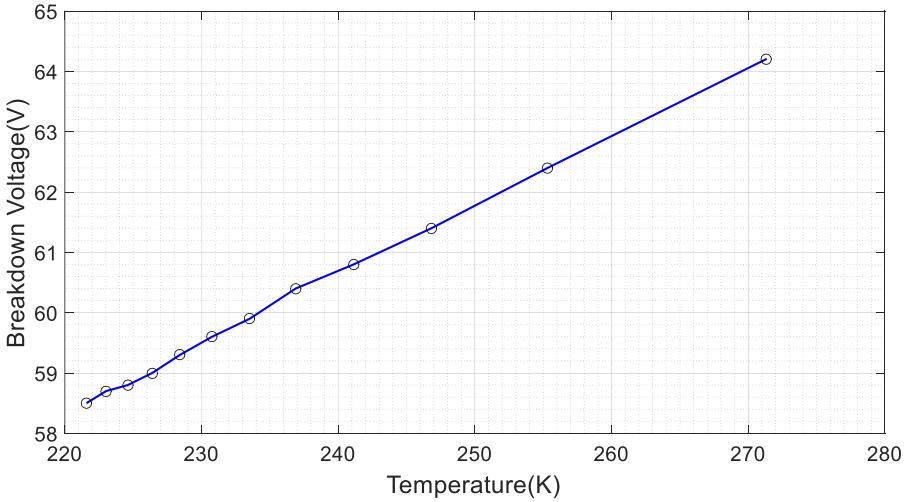

Figure 4.7: Graph of V_{Br} as a function of temperature.

4.3.3 Dark-count and noise threshold adjustment

The noise in the SPAD test circuit is reduced thanks to the aluminium foil and its proper shield, the noise signal is illustrated in figure 4.8.

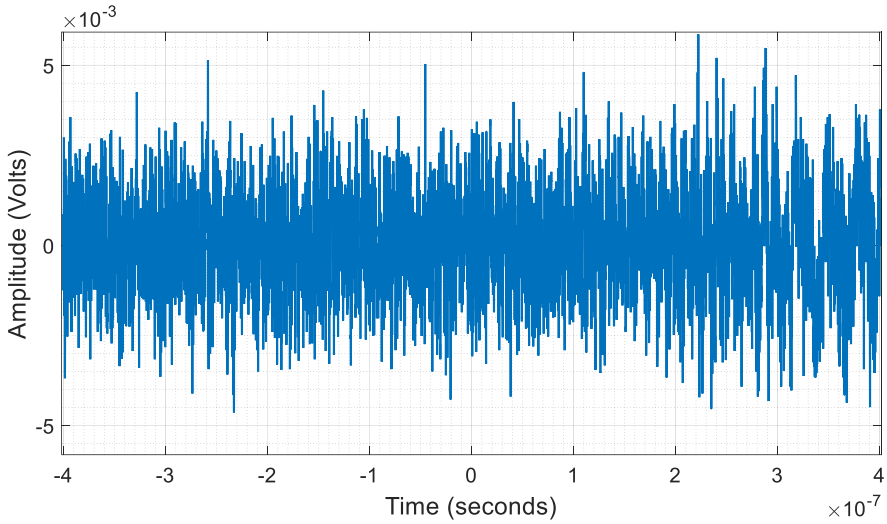

Figure 4.8: Noise signal in the SPAD with infinity persistence.

The noise amplitude is small but there are some transients that can increase the amplitude. Therefore, when the V_{Br} value is determined at different temperatures, the next step in this experiment is to know the threshold between dark-count and noise, through a measurement with the TCSPC it can determine the noise threshold with a better accuracy (such as section 3.3.1).

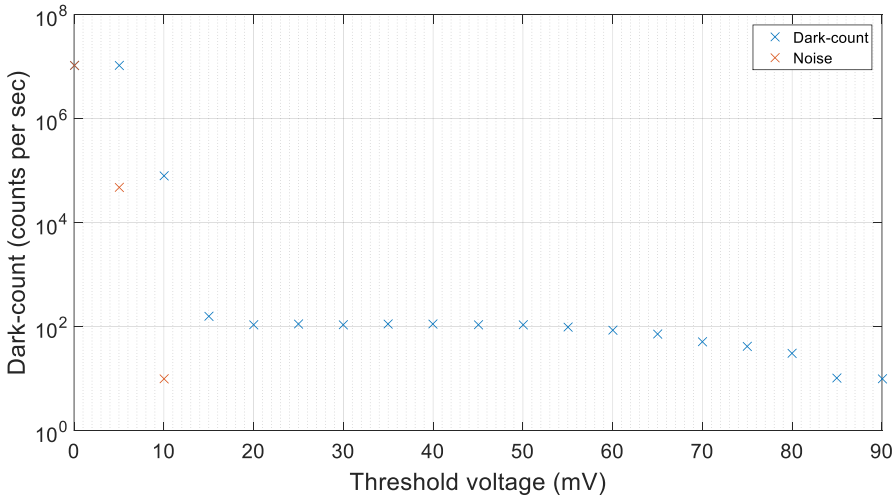

Figure 4.9: Dark-count and noise measurement comparison with the TCSPC to obtain a threshold voltage between them.

The graph in figure 4.9 shows a noise fall at 10mV of threshold but the dark-counting has a plateau, this plateau starts from 15mV to 90mV therefore 20mV is a suitable value as a threshold voltage between the noise and the photon detection.

4.3.4 Sine wave cancelation with the oscilloscope math utility

The first attempt to test the sine wave cancelation is with the oscilloscope math utility, the sine wave gating has an amplitude of 1.0Vpp and a frequency of 50MHz, and the reverse bias voltage is below the breakdown voltage 0.2V to avoid any avalanche.

The output of the SPAD is amplified because the avalanche is small, but the sine wave is also amplified and its amplitude can damage the oscilloscope channel, hence a power combiner is connected between the amplifier and the oscilloscope, the cancelation sine wave is connected in another channel and it is adjusted in amplitude, frequency and phase shift to be 180° shifted from the attenuated sine wave gate.

The oscilloscope math utility creates a virtual channel that is a product of the subtraction between the gating and cancelation sine wave signal, in figure 4.10 it illustrates both sine wave signals and the subtraction signal.

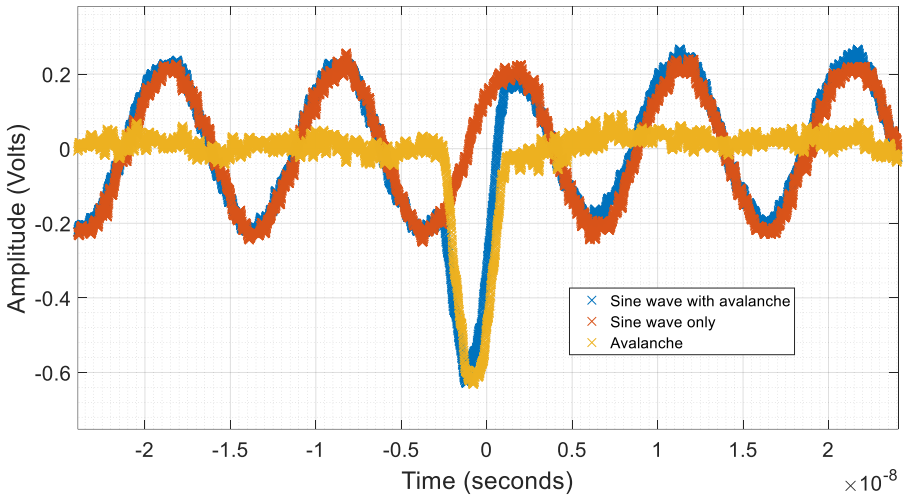

Figure 4.10: Signals of the sine wave with avalanche, sine wave only and avalanche extracted by oscilloscope math utility.

It is possible to observe a small protuberance in the gating signal that corresponds to the avalanche in the SPAD, and the avalanche is isolated through the oscilloscope math utility.

4.3.5 Sine wave cancelation with a power combiner

The oscilloscope math utility proved the sine wave cancelation hypothesis, but this math utility does not consider factors like the imperfect impedance coupling or an involuntary phase shift. The power combiner can replace the math utility but this utility uses a proper subtraction operation. The power combiner adds two signals into one output. The sine wave gating amplitude is connected to one input of the power combiner and the cancelation sine wave is connected to the other input.

Once both are connected to the power combiner, the phase shift and amplitude of the cancelation sine wave is changed experimentally until the sine wave gating signal is almost completely cancelled. During this experimental process the SPAD has a reverse bias voltage at 20V to avoid the negative part of the sine wave that could damage the SPAD.

When the sine wave gating is attenuated to the minimum amplitude possible (below 5mVpp), the reverse bias voltage is fixed at 0.2V below V_{Br} with a TEC temperature of 233K, Figure 4.11 illustrates the avalanche in the SPAD without sine wave gating and with sine wave gating.

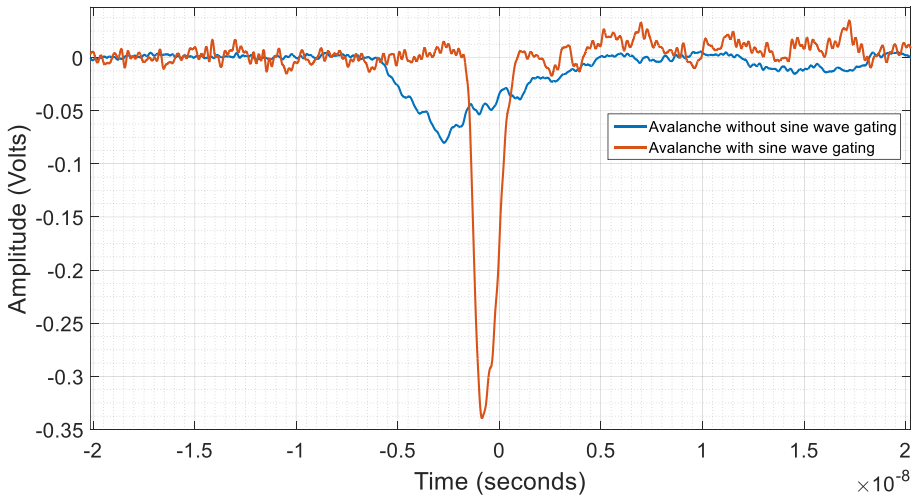

Figure 4.11: SPAD's avalanches without the sine wave gating signal and with the sine wave gating signal.

The avalanche with sine wave gating has a width reduction of 8ns compared to the avalanche without sine wave gating, but the main improvement of the sine wave gating is reducing the dead-time.

4.3.6 Dead time comparison

The NFAD has around 600ns of recovery time and the SPAD without sine wave gating is around 1µs, in figure 4.12 it illustrates the infinity persistence of the SPAD without sine wave gating.

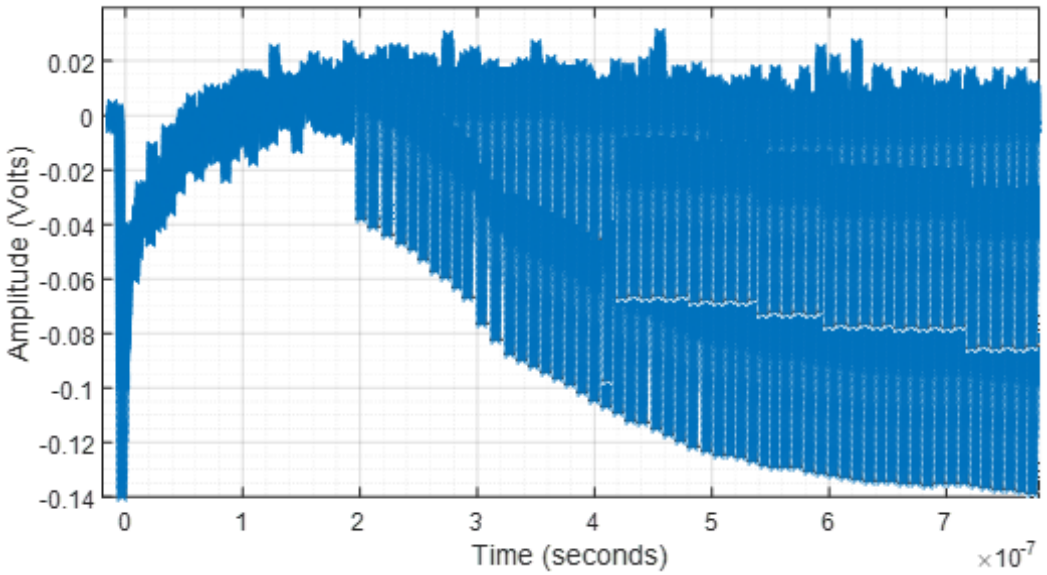

Figure 4.12: SPAD infinity persistence without sine wave gating sampled with Matlab from an oscilloscope screenshot.

The SPAD without sine wave gating has a larger dead time because the test circuit works as a passive quenching circuit. For the sine wave gating test, the amplitude of the sine wave is increased to the maximum (5Vpp). The wave generator can hold that amplitude until reaching 100MHz, over that frequency the amplitude falls to 1.5Vpp.

When the sine wave gating is applied to the SPAD, the positive half cycle of the sine wave activates the SPAD Geiger mode, after that cycle ends and the negative half cycle starts, any avalanche under the Geiger mode stops abruptly. Figure 4.13 illustrates the SPAD breakdown and recovery time with the sine wave gating using the oscilloscope infinity persistence mode.

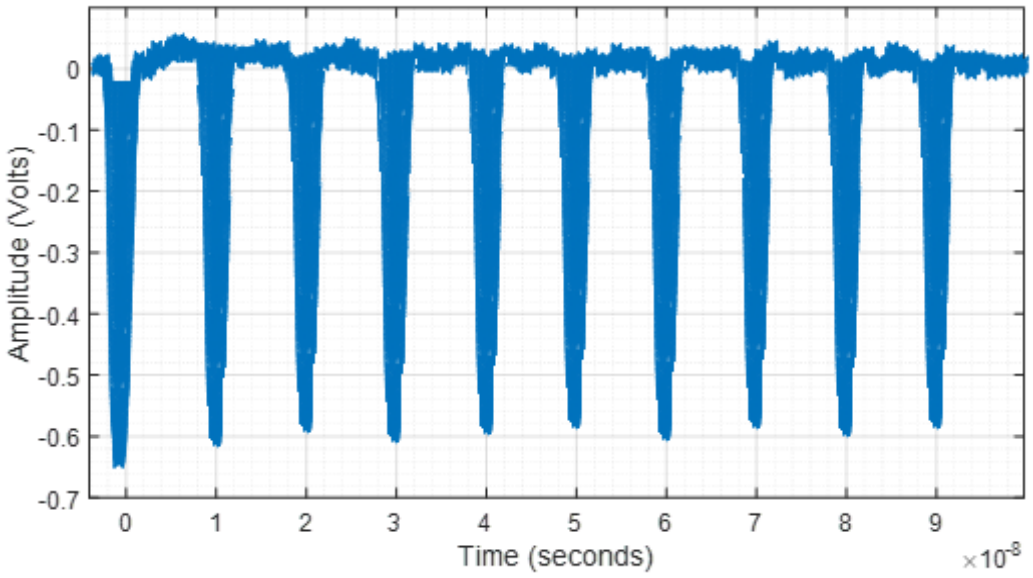

Figure 4.13: Infinity persistence mode image with sine wave gating of the SPAD with the cancelation circuit working (sampled with Matlab from an oscilloscope screenshot).

The SPAD dead time with sine wave gating is limited only by the negative component of the sine wave and we can detect another pulse after only one sine wave cycle of 10ns. Once the dead time with the sine wave gating is measured, the next step of the experiment is to analyse the effects of the sine wave gating on the SPADs properties such as dark-counting, photon-electron detection efficiency (PDE), after-pulsing probability and timing jitter.

4.3.7 Sine wave gating with a frequency at 1.6GHz

After showing a successful operation at 100MHz we aim to extend this to >1GHz because modern QKD systems operate in this frequency range [85, 86]. The waveform generator used previously cannot reach frequencies above 160MHz. Hence, the waveform generator is replaced by frequency synthesizers ADF4355 of Analog Devices®. These synthesizers are mounted in evaluation modules that make it easier to use. The maximum frequency reachable for the synthesizer is 6.8GHz but at frequencies below 1.5GHz, the sine wave signal is distorted hence 1.6GHz is a suitable frequency for a sine wave gating signal. The phase shift resolution of the synthesizer is 38 bits, but it can only manage four possible amplitudes controlled by pre-set attenuators (-4dBm, -1dBm, 2dBm and 5dBm), this restriction in the amplitude adjustment represents a problem for the cancelation of the gating signal.

Therefore the amplitude of the cancellation signal is adjusted by a phase shift between two sine wave signals, thereby the cancelation signal can increase or decrease its amplitude. The sine wave gating signal is generated by just one synthesizer with 2dBm of amplitude (400mVpp), after the gating signal is sent to an amplifier model ZFL-2000+ of mini-circuits® with +20dB of gain.

The sine wave signal has an amplitude of 3.5Vpp and exceeds V_{Br} by 1.75V at each positive half cycle of the gating signal, thereby the gating signal is injected to the SPAD with the frequency and amplitude desired. However, at 1.6GHz it is not possible to suppress the gating signal such as figure 4.13, analysing frequency spectrum of the sine wave gating signal without any cancellation and with cancelation in figure 4.14.

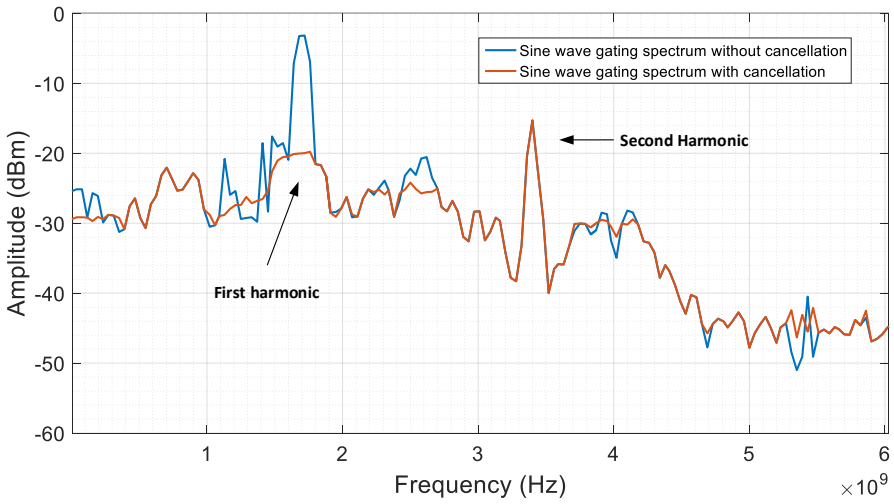

Figure 4.14: Frequency spectrum of the SPAD when there is a sine wave gating signal at 1.6GHz, without and with cancellation. But there a harmonic at 3.2GHz which is two time the frequency of the gate signal.

There is something that generates that second harmonic and the possible responsible is the SPAD's natural response when the SPAD is under high frequencies. To confirm this hypothesis, it is necessary to observe the frequency spectrum of the gate signal at several frequencies below of 1.6GHz.

If the hypothesis is correct, the second harmonic component should be decrease until disappear. The first harmonic component corresponds to the sine wave gating and the second harmonic should be a distortion signal due to the SPAD or other non-linear circuit component.

To confirm the hypothesis previously postulated the sine wave gating frequency is reduced and through the frequency spectrum it is measured the second harmonic with and without cancellation. Figure 4.15 illustrates the frequency spectrum of the sine wave gating signal without cancellation and with cancellation at 850MHz.

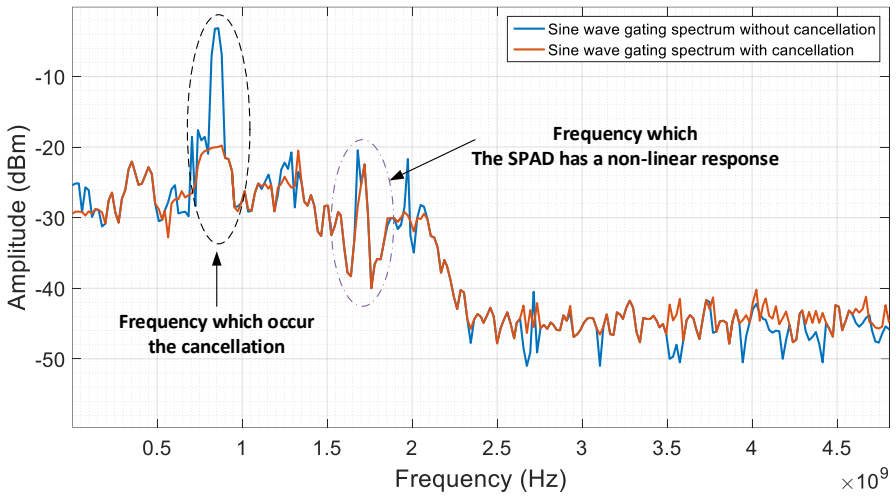

Figure 4.15: The frequency spectrum of the sine wave gating signal with and without cancellation, confirms the hypothesis about a SPAD natural response (non-linear). The first harmonic of the sine wave gating signal is attenuated considerably and the second harmonic at ~1.7GHz still present but attenuated in comparison with figure 4.14.

At 850 MHz (approximately) there is the first harmonic which is possible to cancel, but the second harmonic at 1.7GHz is present yet but with less amplitude. Normally, this feature would not represent a problem if the avalanche is considerably bigger than the remnants of the sine wave signal cancellation, but the avalanche is smaller than the sine wave gating signal. Therefore, the SPAD works as a high band pass filter when the frequency of the sine wave gating signal is higher than 1GHz, furthermore it is possible that the SPAD response time is not fast enough to produce avalanches at high frequencies.

Before thinking of any possible solution about these two issues, first it is necessary to find the hypothetical SPAD's frequency inflection point where the SPAD's non-linear responses appear. If there is not a non-linear response from the SPAD, it is recommendable to use a GHz sine wave generator which uses monolithic frequency sources. In case that it is not possible to avoid the use of frequency multipliers, it would be necessary to use another sine wave signal in which its only purpose is to cancel the second harmonic, this idea was proposed in Restelli's work [82] to cancel the harmonics of a 1.25GHz gate pulse, and to solve the small avalanche issue it is possible to use a power amplifier in the sine wave

gating signal. A high amplitude of a sine wave gating can overpass the SPAD's V_{Br} by several volts in a short time lapse (picoseconds), during the positive half cycle of the sine wave gating signal. Because the duration time of this positive half cycle is extremely short, there is no possibility of damaging the SPAD.

4.4 SPAD Characterisation with Sine Wave Gating

The sine wave gating appears to work well at 100MHz, so there is a restricted study (but detailed) to this frequency range for now. The characterisation of the SPAD properties are made in both conditions of gating i.e. with and without sine wave gating and the measurement of the SPAD without the sine wave gating is fixed at 0.2V and 0.5V over V_{Br}. These voltages configure the SPAD in a Geiger mode but under passive quenching conditions, thus it is possible to make a comparison between the active quenching with sine wave gating and passive quenching. For the sine wave gating we use 5Vpp amplitude sine wave and a DC bias at *0.2V, 0.5V, 0.7V, 1.0V, 1.2V and 1.5V below* V_{Br} such as mentioned in section 4.3.6.

The measurement of PDE for the SPAD with sine wave gating has the possibility of change, if the pulsed laser is synchronised or not. Therefore, the PDE characterisation is performed in both conditions (synchronised and not synchronised), although the total after-pulsing probability measurement could be performed with and without any synchronisation, there is a possibility of obtaining wrong measurements when it is not synchronised, because the positive half cycle of the sine wave gating introduces the SPAD in the Geiger mode. But this measurement is performed with the same conditions as the NFAD characterisation in section 3.7.2, i.e. the rate repetition of the laser pulse is 6 kHz.

The timing jitter measurement uses 20MHz of repetition rate to produce a suitable counting rate, but such as the PDE and the total after-pulsing measurement, the timing jitter measurement is also performed with and without synchronisation with the laser pulse. There is expectations that the synchronisation can affect the timing jitter, because when the SPAD receives the whole laser pulse during the positive half cycle of the sine wave, it could change the histogram which is used to measure the timing jitter.

4.4.1 Dark-count Characterisation

The dark-counting characterisation starts with the lowest temperature possible (221K), the dark-counting is measured with each increment of temperature until reaching 271K. Figure 4.16 illustrates a graph of the dark-count measurement with and without the sine wave gating.

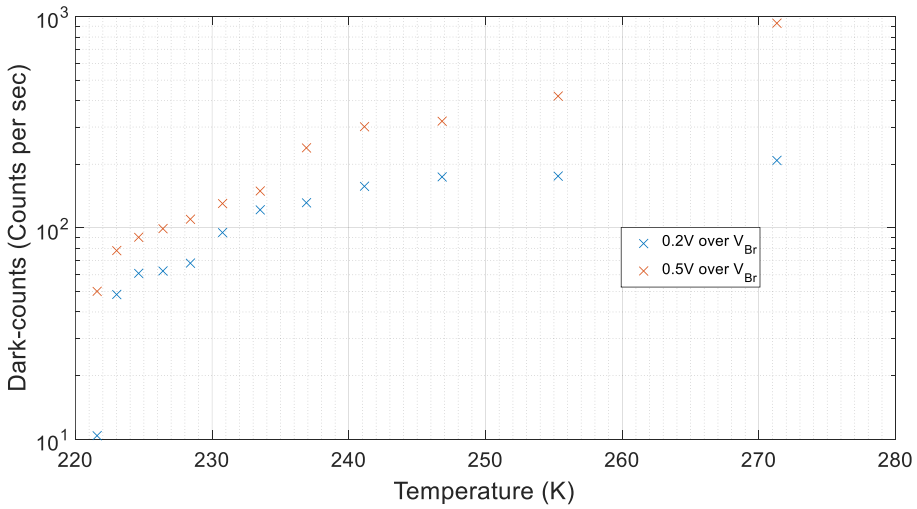

Figure 4.16: A Graph of dark-counting measurement as a function of temperature without the sine wave gating signal.

There is not a considerable difference between the measurements of 0.2V and 0.5V over V_{Br}, these results are even expected and they are not so different to the dark-counts measurements of section 3.5.3 with the NFAD. The dark-count measurements with a sine wave gating signal could be higher than these two measurement (figure 4.16), but not considerably high as the NFAD's dark-count measurements. Then, the reverse bias voltage is fixed at several voltages under V_{Br} level and the dark-count is registered in figure 4.17.

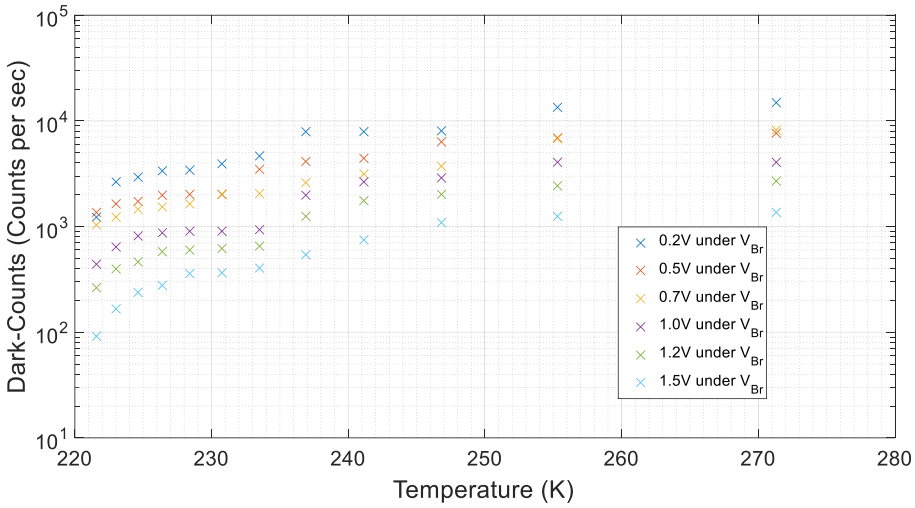

Figure 4.17: A Graph of dark-counting measurement as a function of temperature with the sine wave gating signal.

This figure shows a similar behaviour to figure 4.16 when there is no presence of any sine wave gating, but the dark-counts are 2-5 times higher. As the maximum overvoltage ranges from 1V to 2.3V we might expect much higher dark counts but this confirms that sine wave gating can control the amount of dark-counting. From 248K to 271K, there is certain steady-state behaviour if the measurements of figure 4.17 are compared to the NFAD measurements of figure 3.13.

The low dark count is possibly due to the short positive-half cycle of the sine wave starting from below breakdown leading to the device being on for less than half a cycle and quenched below breakdown for more than half a cycle. The effects of the sine wave cycles in the SPAD can be more notable during the PDE characterisation, when the SPAD receives light pulses.

4.4.2 PDE characterisation

The SPAD does not require alignment to adjust the photon incidence on the detection area (due to the fibre pig tail). Thereby, the SPAD's PDE measurement is only affected by the temperature, light attenuation, excess of bias voltage over V_{Br} and the synchrony between the laser pulses and the positive half cycle amplitude of the sine wave gating signal. This PDE characterisation is made as *the NFAD's PDE characterisation* i.e. through the MDA that measures the probability of photon incidence for different temperatures (section 3.6.1).

The setup diagram for the PDE measurement with and without any synchronisation is illustrated in figure 4.18. The differences between the NFAD's setup diagram (figure 3.14) and the SPAD's setup diagram are the inclusion of the signal wave generator, the power combiner, and the position of the bias-tee.

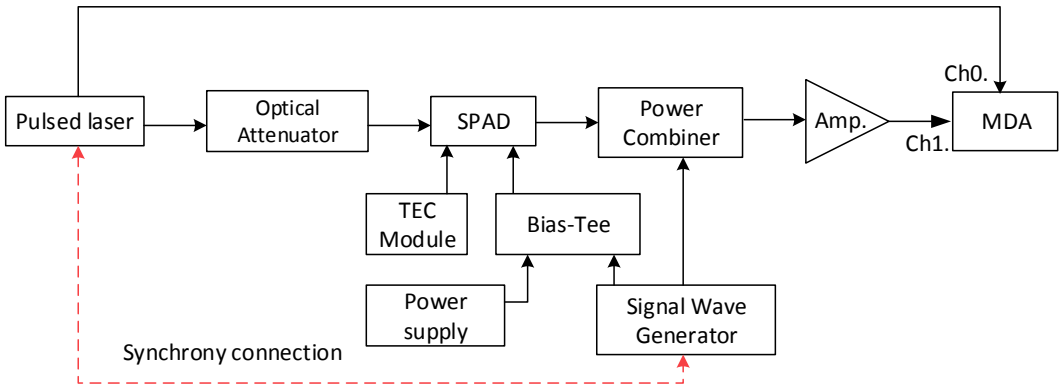

Figure 4.18: PDE measurement setup diagram for the SPAD with the sine wave gating signal with or without synchronisation between the pulsed laser and the signal wave generator, the red segmented line indicates the synchronisation connection between: the pulsed laser and the signal wave generator (when it is required).

The first measurement is the dark-counts at the same time lapse in which the photon detection probability appears, to subtract with the photon detection probability and thereby only the PDE remains (applying equation (3.9)). However, the photon detection probability (which is approximated to the PDE) can change considerably if the laser pulse is synchronised with the sine wave gating signal, then two PDE measurements are performed: without any synchronisation and with synchronisation.

Before measuring the PDE with a sine wave gating signal (synchronised and not synchronised), a PDE measurement is performed without any sine wave gating signal as a reference measurement. Thereby, the PDE without any sine wave gating is measured with the same procedure of the NFAD's PDE measurement shown in section 3.6.1. Then, figure 4.19 illustrates the PDE without any gating signal for 0.2V and 0.5V over V_{Br}.

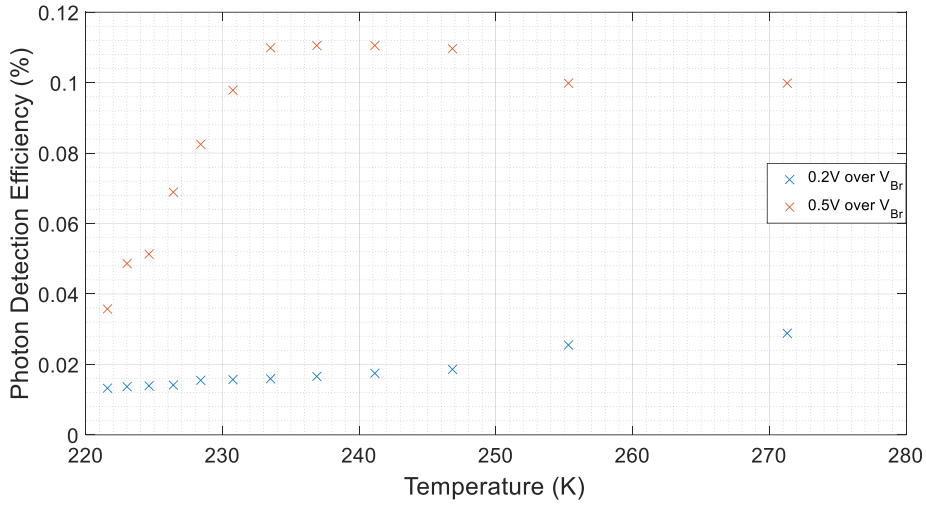

Figure 4.19: PDE control measurement for the NFAD without any gating signal, the excess bias that were voltages used are: 0.2V and 0.5V.

The PDE efficiency without any gating is considerably low, because at 0.5V over VBr there is a maximum efficiency of 0.11% and for 0.2V over VBr, the efficiency of 0.2V over VBr is lower than 0.5V with maximum efficiencies of 0.025%. Therefore, any presence of sine wave gating with a positive half cycle, should be greater than these PDE measurements (as long as the amplitude is greater than 1.0V peak). Furthermore, between the PDE measurements with sine wave gating, there is a possibility that the synchrony of the gating signal and laser pulses increase the PDE percentage by two times.

4.4.2.1 PDE measurement without synchronisation

The measurement is performed without any synchronisation between the signal wave generator and the laser pulse module. Before injecting any sine wave gating signal, the SPAD is reversed bias up to 0.2V under V_{Br}, after this bias voltage setup the sine wave gating signal is injected. The purpose of this procedure is to avoid any forward bias voltage which could compromise the SPAD integrity. Then, the bias voltage levels mentioned in the introduction of section 4.4 are fixed one by one, and the probability measured in the MDA is subtracted with a previous measurement of dark-counting probability. Figure 4.20 illustrates the PDE as a function of temperature.

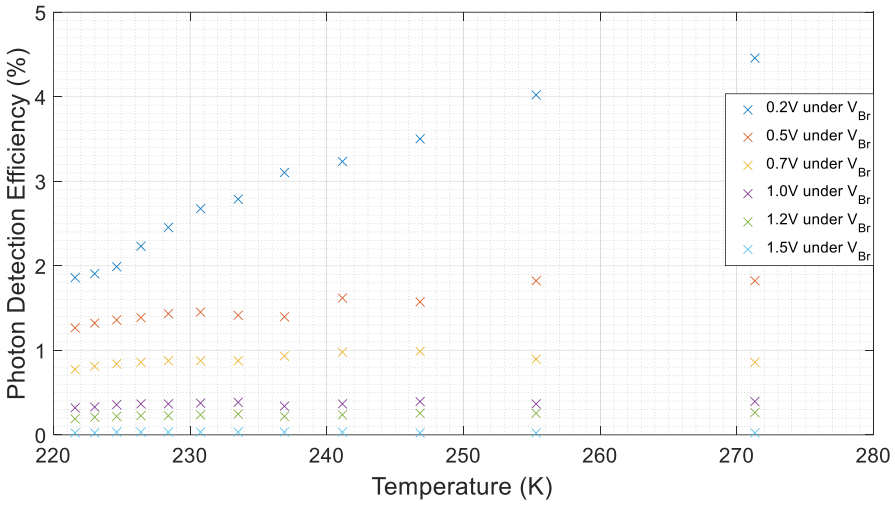

Figure 4.20: PDE measurement with a sine wave gating signal but without any synchronisation with the pulse laser module, as a function of temperature for different bias voltages under V_{Br}.

There is a clear increment in the PDE because the positive half cycle peak reaches an equivalent excess bias voltage, e.g. when there is a presence of a sine wave gating signal which amplitude is 5Vpp, there is 2.5V of positive half cycle which overpasses the 0.2V fixed until reaching V_{Br} and after overpassing V_{Br} to reach excess bias voltage of 2.3V and this voltage is an equivalent of a fixed excess bias voltage (as the excess bias voltages used in figure 4.19).

With the PDE measurements for each bias voltage fixed under V_{Br}, it is possible to represent the PDE as a function of bias voltage under VBr which is illustrated in figure 4.21.

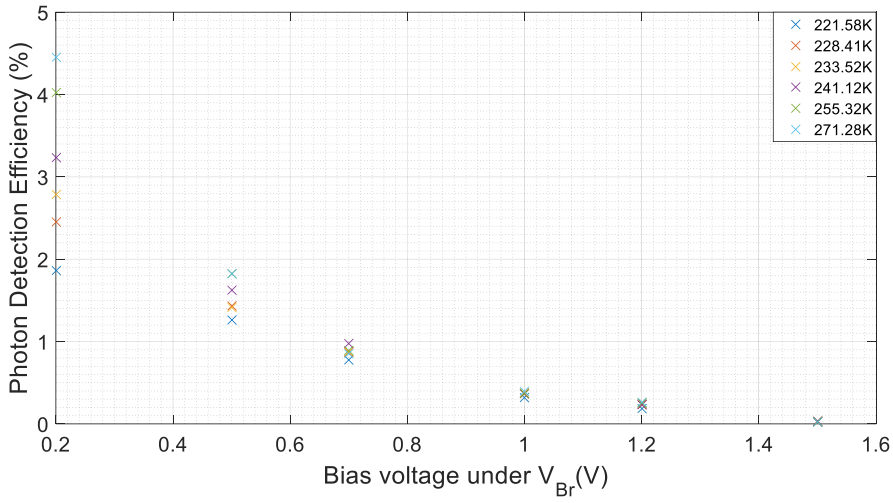

Figure 4.21: PDE measurement with a sine wave gating signal without any synchronisation with the pulse laser module, as a function of bias voltage under V_{Br} at different temperatures.

The graphs of figures 4.20 and 4.21 give an idea of which temperatures and bias voltages are the maximum PDE percentages. The PDE measurement as a function of temperature has a clear difference with the NFAD's PDE measurement, because while the NFAD's PDE percentage is highest for low temperatures, the SPAD's PDE percentages are highest when at high temperatures.

This effect might be due to relatively lower dark counts at higher temperatures arising from gated operation.

4.4.2.2 PDE measurement with synchronisation

When there is a coincidence between the laser pulses and the positive half cycle of the sine wave gating signal, the SPAD can detect the laser pulses with more efficiency than in the absence of the coincidence laser pulse and positive half cycle (such as the previous section). Such as the PDE's measurement without any synchronisation, the PDE measurement uses the same bias voltages under VBr as a function of temperature (figure 4.22).

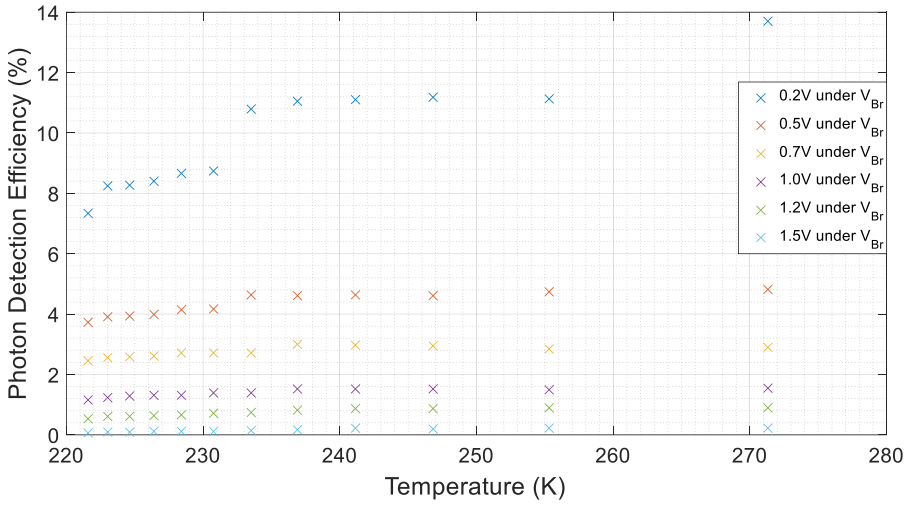

Figure 4.22: The PDE measurement with a sine wave gating signal with synchronisation between the pulse laser module and the wave generator, as a function of temperature for different bias voltages under V_{Br}.

Such as figure 4.21, the PDE measurement with synchronisation between the pulsed laser module and the signal wave generator can be represented as a function of the bias voltage under V_{Br} in figure 4.23.

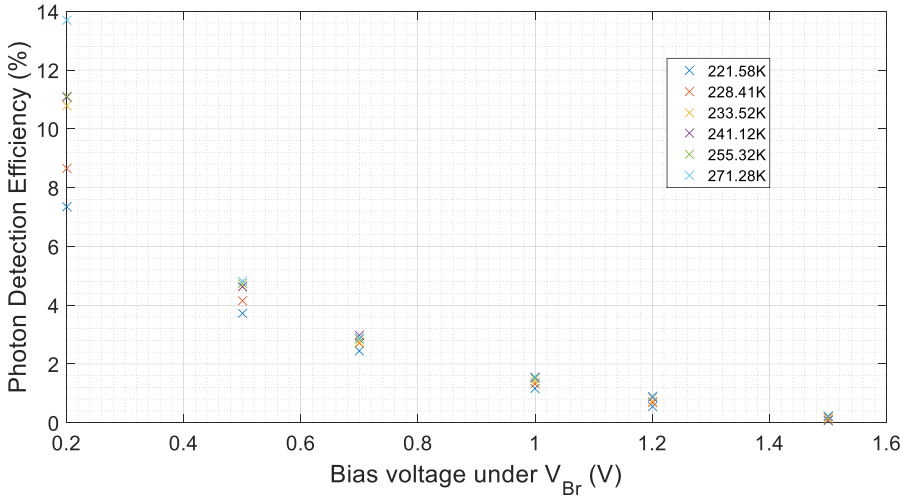

Figure 4.23: The PDE measurement with a sine wave gating signal with synchronisation between the pulse laser module and the signal wave generator, as a function of bias voltage under V_{Br} at different temperatures.

We see that the PDE when synchronised can be almost three times the unsynchronised PDE confirming the suggestion that the diode is effectively on for less than 1/3 of a cycle. In both cases of synchronisation (with and without), there is a maximum PDE at high temperatures confirming the effects of the positive half cycle peak (previously

mentioned). In the PDE graphs as a function of bias voltage under V_{Br}, there is a clear exponential decay which the maximum PDE is at 0.2V under V_{Br}. Given the low dark count measured (fig. 4.17) this opens the possibility of using the SPAD for QKD applications at temperatures up to 270K.

4.4.3 Total after-pulsing probability characterisation

The after-pulsing probability without sine wave gating has a continuous pattern such as in section 3.7.2, but when the sine wave gating is applied, the after pulsing probability has a discreet pattern, this effect is due to the negative half cycle stopping any possibility of an avalanche. The positive half cycle has an amplitude of 2.5Vp but the DC bias voltage is -0.2V below V_{Br}, therefore, only 2.3V exceeds VBr (2.5V-0.2V).

With a pulsed laser synchronised with the positive half cycle, a considerable increment of the PDE is shown, therefore it is not rare if the after pulsing probability could have a considerable percentage. Figure 4.24 illustrates an image of the modulation domain analyser screen with the total after-pulsing probability measurement.

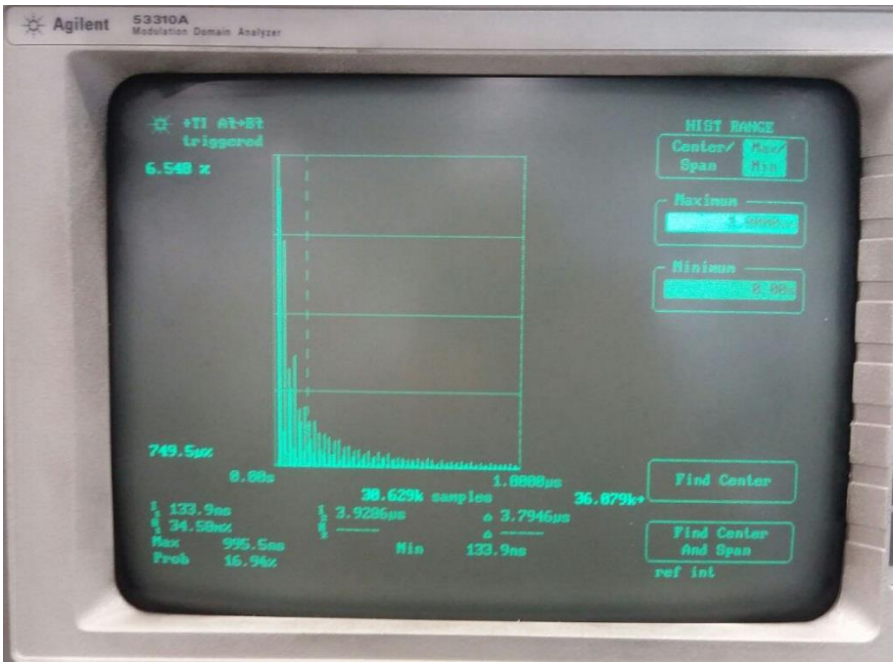

Figure 4.24: The After-pulsing probability measurement with sine wave gating at 233K.

These time gaps where there is no presence of after-pulses are considered dead times provoked by the negative half cycle, although these dead times in the after pulsing

probability measurement could suggest a reduction of the total probability, the fact is that the total probability is not affected because the positive half cycle exceeds V_{Br} for 2.3V.

Thereby, there is a generation of strong avalanches and therefore the total after-pulsing probability has a high percentage, and this percentage is duplicated when there is a synchrony of laser pulses and positive half cycles.

Figure 4.25 illustrates a graph of the total after-pulsing probability without a sine wave gating signal, and the sine wave gating signal in both synchrony conditions (with and without synchrony) as a function of temperature.

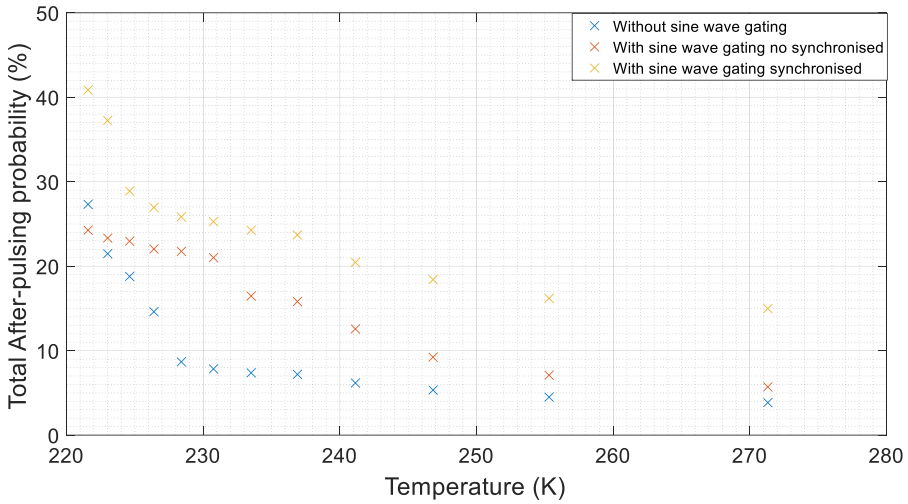

Figure 4.25: The total after-pulsing probability with and without sine wave gating as a function of temperature for 2μs of delay time.

The total after-pulsing probability with sine wave gating has a different curve shape than without sine wave gating due the long dead time of the ungated thus passively quenched signal. 221K the total after-pulse probability without sine wave gating is higher than with sine wave gating possibly because after-pulse lifetime is long but this drops as after-pulse lifetime shortens and they disappear into dead time. Above 230K the ungated device shows low (<10%) after-pulsing. In the case of sine wave gating the device is turned on again within 10 nanoseconds allowing short lifetime after-pulses to appear. However again the fall in total after-pulsing with temperature brings the synchronised result down to ~15% around 270K.

4.4.4 Timing jitter characterisation

The SPAD jitter characterisation is similar to the NFAD characterization (section 3.8) because the bias voltage can be adjusted at a certain level under V_{Br}. Thereby, when there is a positive half cycle of the sine wave gating, its peak represents an equivalent of excess bias voltage. Such as in section 4.4.2, it is necessary to have a timing jitter measurement of control i.e. without sine wave gating signal with the purpose of having a timing jitter reference, for this control measurement only two excess bias voltages are used which form the histograms in figure 4.26.

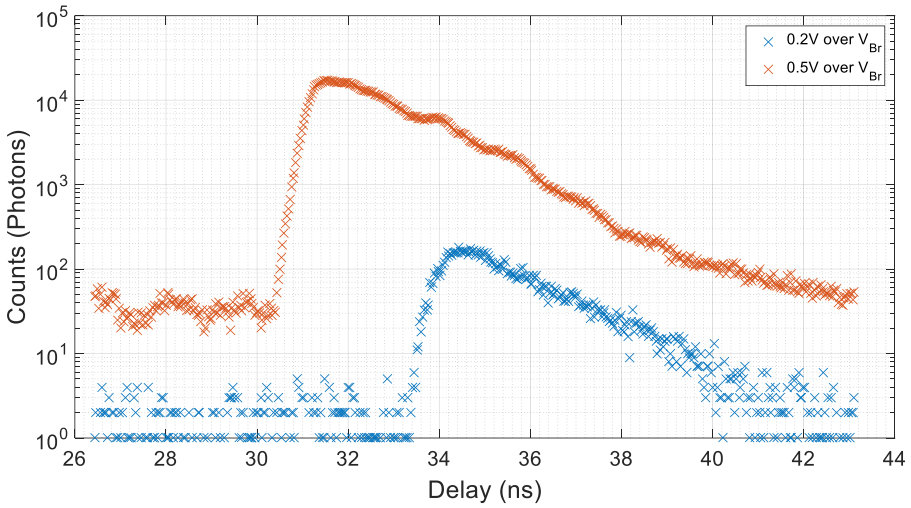

Figure 4.26: Histogram of the laser pulses without any sine wave gating signal for 0.2V and 0.5V over V_{Br} (at 228.41K) on a logarithmic scale to appreciate the excess bias voltage of 0.2V.

These histograms are obtained with 228.41K of temperature and due to the avalanche levels for 0.2V over V_{Br}, the histograms are plotted on a logarithmic scale. It is possible to appreciate a slight delay for the histogram of 0.2V but the FHWM is minor at 0.5V over V_{Br}. The FHWM comparison between both histograms is illustrated in figure 4.27.

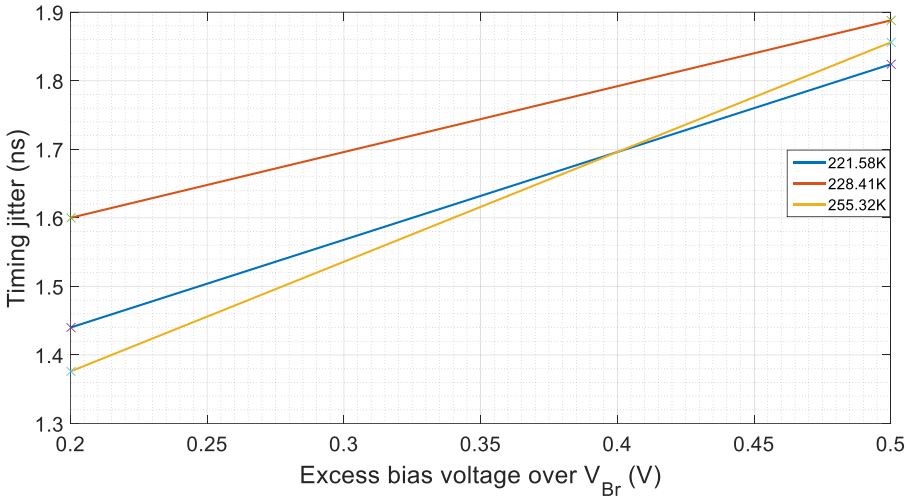

Figure 4.27: Timing jitter measurements as a function of excess bias voltage over V_{Br}, at 221.85K, 228.41K and 255.32K.

There is an increment proportional to the excess bias voltage but there is not a considerable influence on the temperature. Such as the PDE characterisation, the timing jitter characterisation is also divided between histograms measured with synchronisation and without synchronisation.

4.4.4.1 Timing jitter measurement without synchronisation

The histograms of the laser pulses are obtained without any synchronisation, and therefore it is expected that the laser pulses could have certain delay times between them. Furthermore the peak of the positive half cycle would induce a reduction of the jitter time in comparison to the measurements obtained without any sine wave (figure 4.27).

Figure 4.28 illustrates the laser pulses histograms with the sine wave gating signal not synchronised with the pulsed laser module.

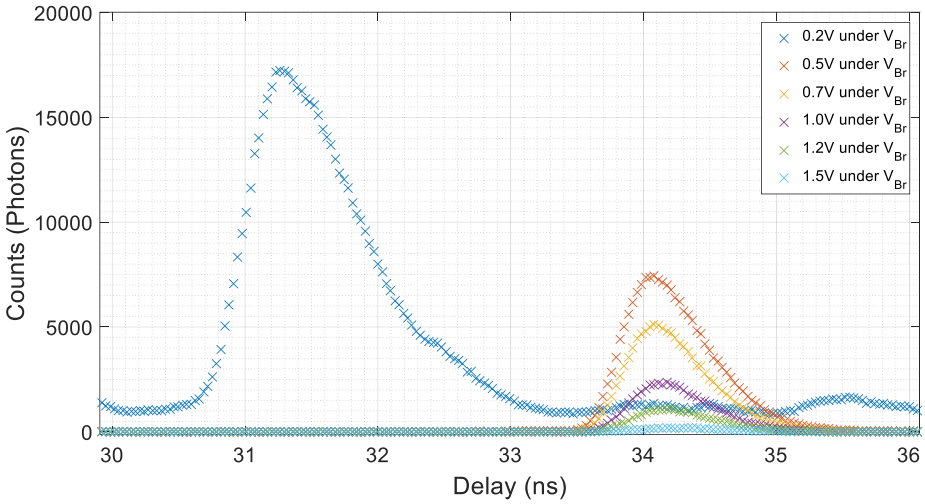

Figure 4.28: Histogram of the laser pulses with a sine wave gating signal not synchronised for several bias voltages under V_{Br}, the temperature used in these measurements is 228.41K.

There is a clear delay between the greater laser pulse and the other (such as it was expected), and there is a clear reduction of the timing jitter compared to the control measurement (figure 4.26).

Again the FHWM of each laser pulse is used to obtain the timing jitter and thereby we display the jitter in an independent plot as a function of DC bias below breakdown (figure 4.29).

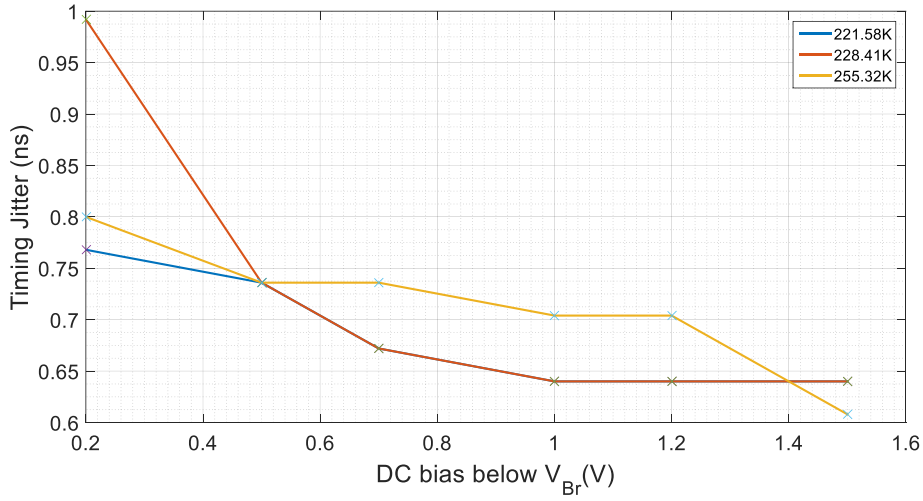

Figure 4.29: Timing jitter measurements as a function of bias voltage below V_{Br}, at 221.85K, 228.41K and 255.32K.

There is a clear reduction of the timing jitter in comparison to the control jitter measurement, the maximum timing jitter is determined in 992ps for 228.41K at 0.2V under V_{Br}, although for other temperatures (221.58K and 255.32K) the maximum timing

jitter is between the range of 800ps and 750ps, this plot proves the null relation between temperature and timing jitter.

The reduction in timing jitter as the DC bias is reduced to 1.5V is a result of the diode being turned on for a shorter time, only at the peak of the sine wave. This same behaviour is expected for the timing jitter measurement with a synchronisation between the pulsed laser module and the signal wave generator.

4.4.4.2 Timing jitter measurement with synchronisation

Basically the same procedure of section 4.4.4.1 is repeated but with the exception of the synchronisation between the sine wave generator and the signal wave generator. The synchronisation brings some features such as the reduction of time delay between laser pulses, because when the laser pulse hits the photodetector the positive sine wave gating is in its maximum peak, this effect is observable in figure 4.30.

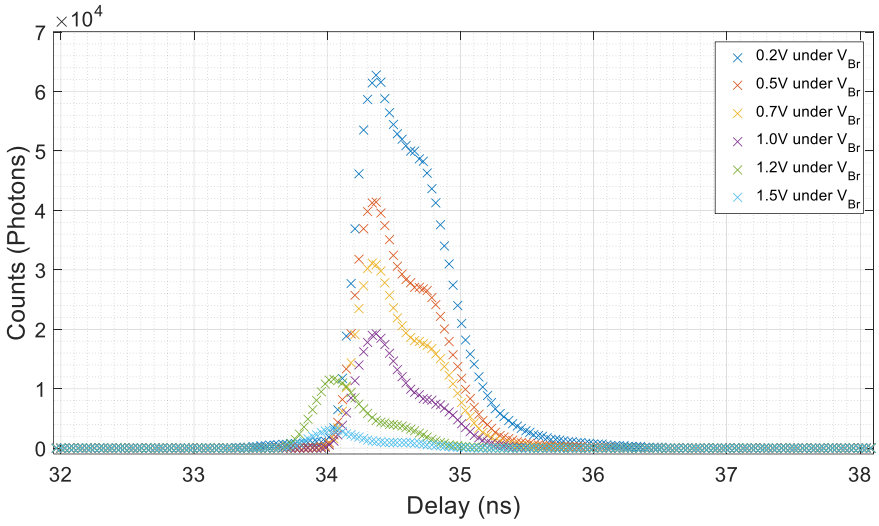

Figure 4.30: Histogram of the laser pulses with a sine wave gating signal synchronised for several bias voltages under V_{Br}, the temperature used in these measurements is 228.41K.

Different to figure 4.28, there is not a considerable delay between the laser pulses histograms. Furthermore, the high PDE is responsible for the photon counts (15000

compared to 65000) for the same bias voltage under V_{Br}, also the comparison of timing jitter between temperatures is repeated in figure 4.31.

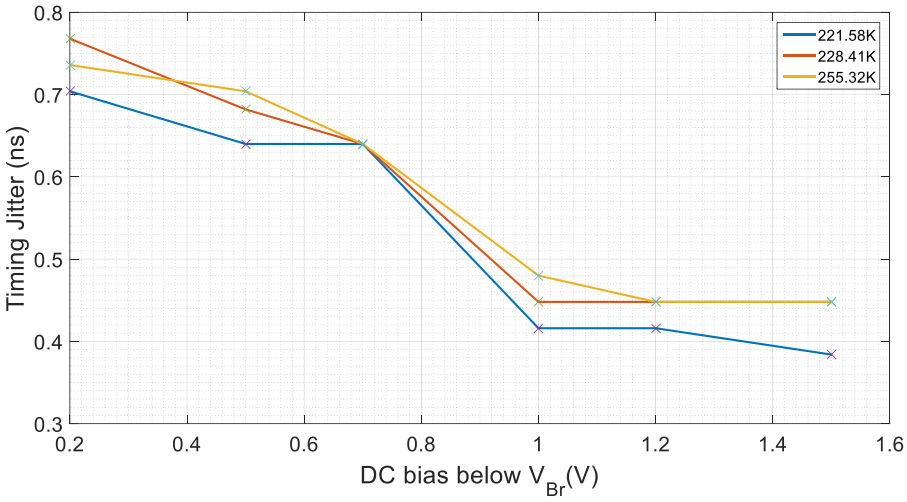

Figure 4.31: The timing jitter measurements as a function of temperature using the sine wave gating synchronised for three different temperatures.

Again we see a timing jitter improving as the DC bias is pulled below the breakdown leading to a shorter time above breakdown in the positive half cycle. There is almost no variation of timing jitter between measurements at different temperatures, this could be related to the coincidence of laser pulses and positive half cycles, and thereby the timing jitter does not have a considerable deviation such as occurs in the timing jitter plot without synchrony (figure 4.29).

4.5 Summary

This chapter analysed the sine wave gating as an active quenching technique and a variation of sine wave suppression, in two variants: synchronised between pulsed laser module and signal wave generator, or not synchronised. The sine wave signal cancellation technique shows certain advantages over the traditional pulse gating method, because it does not produce any parasite signal and there is no additional effect from the band pass filters [27, 82].

The sine wave signal cancellation as a technique for an active quenching, shows a considerable width reduction in the avalanche and dead time, but unfortunately it was not possible to use frequencies over 1 GHz. Because the experiments at 1.6GHz showed a non-linear response associated with the SPAD response for GHz frequencies, the cause of this high frequency response inside of the SPAD is the internal capacitance, which is specified at 0.25pF by the manufacturer but at 1MHz.

Due to this inconvenience, the non-linear response in any active quenching with a sine wave gating signal beyond 1GHz is discarded and the characterisation of dark-counts, photon detection efficiency, total after-pulsing probability and timing jitter are measured with frequencies below 1GHz. These measurements with the sine wave gating signal (except dark counts) were divide in to two sections: with a synchronisation between the light source (pulsed laser) and the gating signal source (signal wave generator). Thereby, a more detailed analysis is obtained of the sine wave gating and the subtractive cancellation.

During the PDE measurement, the synchronisation improved the percentage greatly to levels approaching 14% but such percentages also increased the total after-pulsing probability which could represent a problem for QKD applications.

The SPAD timing jitter also benefited from the sine wave gating signal, because the positive half cycle reduced the timing jitter and this effect was confirmed during a comparison between a control measurement (without any gating) and with the gating in whichever of its modalities (with or without synchrony), also the null relationship between temperature and sine wave gating was confirmed.

Chapter 5.

Conclusions

In Chapter one I analysed the importance of generating single photons and detecting them with the most optimal efficiency, because the QKD system requires a high rate of photons to generate the keys while avoiding multiple photon pulses where eavesdropping could be carried out. When there are more than one photon per light pulse, the information security of the QKD system is vulnerable to the photon number splitting attacks. The photon statistics help to determine the usable number of photons per light pulse through the mean photon number which for classical sources should be <0.3to minimise the number of photons per light pulse which contain 2 or more photons.

Of course the best candidate to be a light source for a QKD system should be a true single photon source (produce no pulses with more than 1 photon), but the infrastructure required to build a true single photon source is complex, robust and expensive. Therefore, semiconductor light sources adjusted to low brightness are the best candidates to be used in QKD systems, because they can be low cost and driven by simple electronics and attenuated to reduce the number of photons per pulse. Two common semiconductor light sources are the light emitting diode (LED) and the laser diode.

The generation of low photon number pulse streams in a QKD system then requires a proper optoelectronic light detector, which can detect single photons. At present the best candidate as photon detectors are the Single Photon Avalanche Diodes (SPADs).

The SPADs are avalanche photodiodes (APDs) but with a particular characteristic so that the SPADs can enter into a Geiger mode when the applied bias exceeds the breakdown voltage. The design of the SPAD and associated quenching/gating electronics allows the breakdown voltage level to be surpassed without compromising the SPAD's structure mainly by limiting breakdown currents. Different bandgap semiconductors used in the SPAD can define which wavelength are detected.

The QKD systems for long distances use InGaAs SPAD's because they work with near-infrared wavelength (such as 1.5µm. InGaAs) is typically grown on InP substrates and the best detectors use InGaAs absorption region with avalanche gain in an InP region, a so called separate avalanche gain medium or SAGM structure. When biased beyond breakdown these SPADs can create large avalanches after absorbing one single photon. However single photon detection is also accompanied by undesired effects, such as dark counts, dead-times, after pulses and timing jitter of avalanches.

A solution for the undesired avalanche effects in the SPAD is a proper avalanche quenching, soon after the avalanche begins to fall. Thereby, two types of quenching methods are proposed: active and passive. The active quenching is very fast although it requires an external signal which is coupled to the quenching circuit, but the external signal injects undesired transients that could mix with the avalanche and it is necessary to have techniques of discrimination.

The passive quenching method does not require complicated circuits, just a resistance connected in a series with the SPAD and the avalanche is self-quenched, and although this method could be considered basic in comparison with active quenching, there is a SPAD which exploits the passive quenching; the NFAD. The NFAD includes a resistance which is monolithically integrated to the device structure, such resistance allows a fast quenching without parasitic capacitance effects and has a fast recovery.

The optoelectronic devices previously mentioned are used in commercial QKD systems, such as the Cerberis QKD Blade and Clavis^3 from IDQuantique® and Toshiba's QKD system. These systems use continuous wave (CW) lasers as a light source which is modulated and attenuated to generate a train of approximate single photons. In the case of the photon detectors, the SPADs used in the commercial QKD system, are effective for a wavelength of 1.55µm, with a low dark-counting and a considerable photon detection efficiency (up

to 50%), but this efficiency is the product of active quenching systems highlighting their importance for this work.

5.1 LED Drivers

In Chapter two, it designed and tested fast pulse drivers for Alice's LED's, because fast gate pulses on the LED alone are not enough to reduce the recombination time. Therefore, it is injected with a reverse bias voltage after the fast gate pulse to reduce the radiative recombination time. Two circuits were designed and tested to quench the radiative recombination:

- A Op-Amp in a monolithic integrated circuit
- A switch driver with discrete components

The Op-Amp presents good performance at high frequencies, but the light intensity in the LED is limited by the voltage applied through the Op-Amp's output, which exceeded the LED's V_{on} (~1.80V) a little. The switching driver can manage high frequencies producing a light intensity greater than the Op-Amp, due to the extra current supply by the current booster. Therefore, this LED driver is suitable for Alice and it has an equivalent integrated circuit. The ONET1101L is a monolithic integrated circuit, it is designed to operate at a high-speed of data transference which works similar to the switching driver, but the ONET1101L has a programmable input equalizer to control the current through the LED.

5.2 NFAD Characterisation

In Chapter three it analysed the NFAD linear parameters such as the TEC temperature range, the coolest temperature achieved was 237.9K and the warmest was 282.6K (a little below room temperature). This temperature range is plotted in figure 3.2 and each temperature used for this plot has a specific breakdown voltage (V_{Br}). The minimum value of V_{Br} at 237.9K (minimum temperature) is 82.4V and the maximum V_{Br} at 282.6K is 86.2V,

the manufacturer specifies the breakdown voltage in the range of 70V to 80V [55], but it was found that the range is higher than the manufacturer specifications (figure 3.3).

During the laser beam alignment, it plotted the current as a function of the DC bias voltage. The current-voltage relation plotted in figure 3.5 showed the punch-through voltage of the NFAD (50V). Furthermore of the punch-through voltage, the current-voltage graph shows the photocurrent of the NFAD (3.6nA), which is important data to know the quantum efficiency of the NFAD through the group of equations (2.9). Thus, the quantum efficiency could be determined at 41%.

The characterisation of the Geiger-mode parameters require it to know the noise introduced by the amplifier and the NFAD itself. This noise amplitude was estimated around 40mVpp, by knowing this amplitude the TCSPC discriminator level was fixed at 20mV so as to only register the avalanches. The dark count measurements showed an exponential increment for temperatures between 250K and 260K, and linear for other temperatures outside of the range 250K – 260K when the DC bias voltage is increased (figure 3.10), confirming the influence of the excess bias voltage over VBr in the dark-count increment.

However, it was found that the maximum dark-counting under the bias voltages possible influence is 10^6 CPS. The temperature also has a relation to the dark counting increment, before 255K the dark-counting increment is relatively stable and after that temperature the increment is more notorious (figure 3.13). The excess bias voltage in joint with the temperature drastically increases the dark-counts, e.g. at 0.7V over V_{Br} the increment slope is less critical than 1.7V.

The Photo-electron Detection Efficiency (PDE) measurement was performed with a Modulation-Domain Analyser (MDA) module, because this device shows certain advantages in comparison to the Time-Correlated Single Photon Counter (TCSPC). Pulsed light sources to avoid many corrections to the light count particularly from after-pulsing. Light saturation is avoided by ensuring a low probability of detecting a photon in each pulse. With the MDA it was only necessary to arrange a start pulse from the laser to be stopped by the detection and then the total probability of the photon detections was directly measurable by measuring the probability of a stop between closely spaced (~few ns wide gate) markers. After subtracting the probability of dark counts with the same gate width a reliable estimate of the efficiency was obtained undistorted by after-pulses.

The PDE increases rapidly a function of the excess bias voltage beyond breakdown. The PDE increase stopped when the excess bias voltage reached a certain level (~3.0V), after this voltage there is no more increment and there is a clear tendency towards a plateau efficiency.

When the PDE is analysed as a function of temperature, the effect is not clearly defined although there appears to be a slow drop efficiency with temperature which may be related higher dark count rates. Finally, in a comparison of the NFAD's PDE measurements with other experiments reported [21, 73], there are strong similarities because the maximum percentage obtained in section 3.6 is around 8% while the maximum PDE reported for InGaAs SPADs of this type is around 10%.

The after pulsing probability measurement took several steps to perform it, the most important step was the use of the TCSPC because when it is in auto-correlation mode, it is possible to capture the after-pulsing temporal distributions which are fundamental in order to obtain the trapping lifetimes. These times reveal the influence of the traps on the after-pulsing probability, which is shown in an Arrhenius plot in figure 3.24. The lifetimes obtained match with other works [21] which report similar results for InGaAs SPADs and confirms a direct influence of the temperature. This work highlights the dominance of a deep trap in this device type but operation at high temperatures >250K leads to much shorter after-pulsing lifetimes that other work.

These lifetimes were in the range 400-700ns depending on temperature and led to lower total after-pulsing probabilities. At higher temperatures >250K. Total after-pulsing seen is below 10% for 1V overvoltage (in the first 2us after photodetection). However at high voltages the total probability reaches close to 50%.

The jitter timing on the NFAD is measured through the FWHM of laser pulse detections registered in a histogram. At 0.5V of excess bias voltage, the timing jitter has a maximum value of 640ps which even overtakes the maximum specified by the manufacturer, but when the excess bias voltage increases, the timing jitter goes down to a value of 384ps (near to 400ps).

5.3 Sine Wave Gating Advantages

Chapter four analysed the gated operation of the InGaAs APD in Geiger mode (SPAD). The operation with pulsed gating is investigated to illustrate the presence of parasitic spikes arising from the internal capacitance. These spikes have a similar shape to breakdown pulses and can hide the weak avalanche signal. This combination of signals represents a problem when the photon counting is measured by a TCSPC, because the level of discrimination in the TCSPC channel is high, it could provoke dismissal of avalanches with low amplitudes.

Using the sine wave signal at 100MHz instead of the gate pulse (square wave) signal as a gating has certain advantages, because the sine wave signal does not produce parasite signals such as a pulse signal does. The avalanche is mixed with the sine waves and normally it uses filters to discriminate the sine wave [83-86], therefore a technique of interference cancelation to isolate the avalanche pulses is proposed.

The sine wave gating proved it does not produce undesired effects in the SPAD's capacitance, the cancelation of the sine wave signal used as the gating is almost complete, leaving remnants of the cancel operation with an amplitude below 5mV when the frequency is 50MHz and 10mV when the frequency is 100MHz.

When the sine wave frequency reaches the GHz range, the SPAD shows a non-linear response. This was demonstrated during the test with a sine wave gating at 1.6GHz, the avalanches were present but they are not strong enough compared to the avalanches achieved with sine waves at a low frequency (MHz range). The frequency spectrum of the sine wave gating signal at 1.6GHz reveals two main components, which only one at 1.6GHz can be attenuated through the cancellation and the other at 3.2GHz prevails intact, this component can be attenuated by adding an extra sine wave signal but at 3.2GHz such as applied in Restelli's work [80].

The sine wave gating has a direct impact on the SPAD's dead time, because it is reduced from 1µs to 10ns and this reduction of time is due to the half negative cycle of the sine wave. The half positive cycle of the sine wave has a direct effect on the dark-count, PDE and after-pulsing probability.

The dark-counting presents a low increment ($6x10^2$ CPS) when the sine wave gating is applied, which in comparison with the NFAD is an important decrement. But the PDE with sine wave gating presented an increment (7%), when the temperature is raised beyond 246K. In comparison without sine wave gating, the PDE had poor performance at 0.2V and 0.5V over VBr, even below the NFAD, the PDE percentage did not reach 1% as a function of temperature.

With a sine wave gating signal, the PDE had a considerable increment in comparison of the reference measurement without any sine wave gating signal. There is a clearly influence in the temperature that contrary to the NFAD's PDE measurement, in the SPAD with a sine wave gating signal (synchronised or not) at lowest temperature the PDE is low too, but with the temperature increment also the PDE is increased. The reason of this effect could be related with the low dark-counting at higher temperatures arising from gated operation.

When the sine wave gating is synchronised with the laser pulses, the PDE had an increment of almost three times in comparison with the PDE measurements without synchronization. This PDE increment could be related with the time-on of the diode per cycle, i.e. when the diode is unsynchronised only there is an effective time-on window below of 1/3 per half cycle, and when the synchronisation occurs this 1/3 of time-on is exploited to the fullest.

The total after-pulsing probability measurement with sine wave gating had a moderate linear fall, but the maximum percentage is achieved during the test without sine wave gating (~26%) and when there is synchrony between the sine wave gating signal and the laser pulsed, the probability increase considerably (~42%) which it is assumed to the optimization of the time-on (increase the number of traps).

The timing jitter without sine wave gating does not present a considerable change as a function of temperature, the FWHM obtained is held around ~1.6ns which is greater than the NFAD's timing jitter. The timing jitter when the sine wave gating is applied (no synchronised), it has a reduction below of 1ns for a range of temperatures from 221K to 256K. When the sine wave gating signal is synchronised again the timing jitter is below of 1ns, and the comparison between timing jitter measurements with and without synchronisation lies in certain stability with respect of the temperature.

The stability was clearly visible in figures 4.29 and 4.31, the first plot had a considerable timing jitter variation for the three temperatures used, and the second plot had a slight timing jitter variation but with a clearly tendency. The timing jitter reported in chapter four with sine wave gating signal synchronised or not is close to the NFAD timing jitter reported in chapter three. Therefore, the sine wave also contributes to a reduction of the timing jitter.

5.4 Future Work

The SPAD showed a certain reduction of dark-counting with and without the gating compared to the NFAD, the sine wave cancelation reduces the dead time of the SPAD and that makes it a suitable candidate for Bob, therefore an increase of frequency at the sine wave gating can reduce the dead time to picoseconds. However, the sine wave gating at 1.6GHz showed the creation of a harmonic by the SPAD with double its frequency. Therefore, a developed sine wave gating system that includes extra cancelation signals can be added to Bob's SPAD circuitry.

This sine wave gating system can be based in the HS9000 series multi-channel synthesizers from Holzworth®, which can include the phase shifting precision of the ADF-4355, the flexibility of the amplitude adjustment and an interface communication to control it by Bob's computer.

5.4.1 Suggestion of experiment

The NFAD shows a good dead time reduction with a passive quenching circuit recommended by the manufacturer, although there is a circuit version that combines the passive quench with the active reset in the NFAD [60, 91, 92], therefore the NFAD could reduce its dead time more with the sine wave gating technique.

The NFAD cannot easily accept gate pulsing because the avalanches come from the same terminal as the bias voltage, figure 6.1 illustrates the circuit proposed for the sine wave gating in the NFAD.

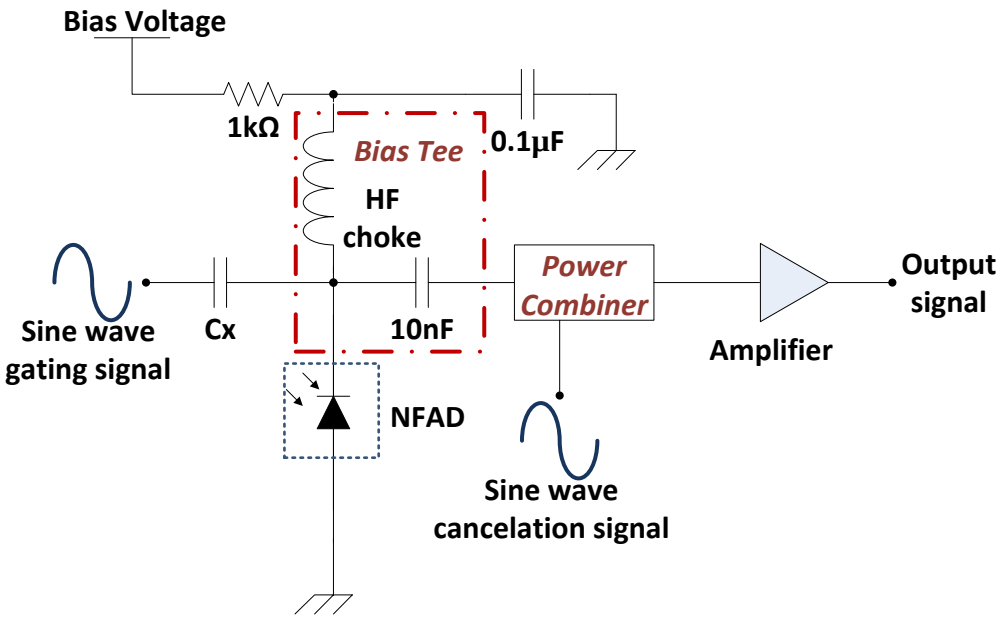

Figure 5.1: NFAD circuit with Sine wave gating and cancelation, Cx is the coupling capacitor for the sine wave signal.

Just like the SPAD, the NFAD is also fixed below V_{Br} and applies a sine wave signal though a capacitor Cx, the half positive cycle activates the Geiger mode but the avalanche is mixed with the injected signal. The power combiner is used to inject the gating and cancel signals, both signals are cancelled such as the experiment in chapter five.

It is expected that an after-pulsing and dark counting reduction would happen, the PDE is related to the SMF alignment with the detection area in the NFAD, but there are some new models [55] with an integrated fibre pigtailed such as the SPAD used in chapter four.

Appendix A.

From Classical optics to Quantum optics

Physics describes how our world works (including our universe) by explaining the colour of the sky in the day and the astronomic movements of the night. Here, we study the smallest things in quantum physics. The topic has been polemical since ancient times, starting with Democritus and his view of matter with small units that he called ***atoms.*** Thousands of years passed before scientists took the concept of atoms seriously, which is now regarded as a milestone in modern physics, where the esoteric and science meet. It is at and below the atomic scale, where the seemingly impossible becomes possible; the particle (any particle) has a behaviour that depends on the observer.

For instance if the particle under observation is analysed as such, it will have the behaviour of a particle. However, when it is passed through an interferometer, the 'particle' simultaneously shows wavelike interference effects [1, 87], this is the birth of Quantum Physics. This appendix briefly describes the relationship between classical optics and quantum optics.

A.1 From Ray Optics to Electromagnetic Optics

Optics study the light phenomena and its effects, were relatively new when Sir Isaac Newton studied the light with perhaps his more known experiment; “Newton’s prism”, this experiment put the first theory of light as a ray with the next postulate.

A.1.1 Ray theory postulate

Newton described light travelling in the form of rays, which are emitted by sources and can be observed when the ray reaches an optical detector (or an object in Newton’s experiment), in addition some materials have properties of the refractive index and this can help to explain the ray theory. When an optical medium is characterized by a quantity $n \geq 1$ (refractive index), n is inversely proportional to the light speed in free space (C_0) between the light speed of the medium (C) [1, 88].

$$n = \frac{C_0}{C} \tag{A.1}$$

Therefore, the time taken by light to travel a distance $\boldsymbol{d}$ is $\boldsymbol{d}/C = n\boldsymbol{d}/C_0$ and it is proportional to the product $n\boldsymbol{d}$, which is known as the optical path length. Through an inhomogeneous medium, the refractive index $n(\mathrm{r})$ is a function of the position r = (x, y, z), the optical path length along a given path between the two points A and B is therefore:

$$Optical\ pathlength = \int_A^B n(\hat{r})ds \tag{A.2}$$

Where ds is the differential element of length along the path and the time taken by light to travel from A to B is proportional to the optical path length. Fermat’s Principle is more specific; optical rays traveling between the two points A and B follow a path so that the time of travel (or the optical path length) between two points is a minimum [1].

$$\delta \int_A^B n(\hat{r})ds = 0 \tag{A.3}$$

Fermat’s principle thus states***: Light rays travel along the path of the least time.***

Ray optics however have a limit of small dimensions and the wave theory of light can be explained beyond that limit [1, 87]. Optical wavelengths range through three regions:

Infrared, visible and ultraviolet, these three regions are comprised in an interval from 3000 μm to 10nm and frequencies above 1 THz, the wave theory of light includes ray theory; ray optics is the limit of wave optics when the wavelength is infinitesimal short. The ray theory can describe most optical phenomena, because the wavelength of visible light is much shorter than the dimensions of the usual objects that are encountered in daily life [1].

A.1.2 Wave theory postulate

An optical wave is described mathematically by a real function of position, $\hat{r}(x, y, z)$ and time *t*, denoted *u*($\hat{r}$, *t*) commonly known as the wave-amplitude-function it could satisfy a partial differential equation called the wave equation (A.4) [1, 87].

$$\nabla^2 u - \frac{1}{C^2}\frac{\partial^2 u}{\partial t^2} = 0 \tag{A.4}$$

The principle of superposition applies because the wave equation (A.4) is linear, so u_1($\hat{r}$, *t*) and u_2($\hat{r}$, *t*) represent possible optical waves and *u*($\hat{r}$, *t*) is the summation of them, furthermore the summation represents an optical wave that is also related to optical intensity *I*($\hat{r}$, *t*), this optical intensity is defined as the optical power per unit area (units of watts/cm^2) and it is proportional to the average of the square wave amplitude [1].

$$I(\hat{r}, t) = 2\langle \mathrm{u}^2(\hat{r}, t)\rangle \tag{A.5}$$

The bra-ket notation ⟨ ⟩ denotes an average over a time interval of the optical cycle, however if this cycle is shorter than the duration of a pulse of light, the duration of this optical cycle would be short (10^{-15}s) with a wavelength of 600nm [1], the optical intensity is related to the optical power P(t) through the equation (1.6), the intensity flowing into area ***A*** that is vertical to the direction of propagation of light that can be represented with an integral to the intensity [1].

$$P(t) = \int_A I(\hat{r}, t) dA \tag{A.6}$$

The optical energy (units of joules) collected during the time interval is the integral time of the optical power over the integration interval [1], because wave optics offer something that ray optics cannot offer; the phenomena of interference and diffraction,

explained when the phase has involved but wave optics like ray optics are unable to quantitatively account for some simple optical experiment observations such as the division of light at a beam-splitter, because a fraction of light reflected and transmitted turns out to depend on the polarization of the incident light, which means that the light must be treated in the context of a vector rather than a scalar, therefore electromagnetic optics encompass wave optics and again reduces ray optics in the limit of short wavelengths.

A.1.3 The Electromagnetic theory applied in light

Electromagnetic theory explains that an electromagnetic field is composed by two vector fields; electric and Magnetic, represented by functions related in position and time:

- *Electric field E(r̂, t)*
- *Magnetic field H(r̂ ,t)*

James Clark Maxwell proposed six functions of position and time to describe light in free space, these six functions are interrelated to a set of coupled partial differential equations in the free space, the electric and magnetic field vectors could be expressed in the next equations (Maxwell's equations) [1, 87]:

$$\nabla \times H = \epsilon_0 \frac{\partial E}{\partial t} \tag{A.7a}$$

$$\nabla \times E = -\mu_0 \frac{\partial H}{\partial t} \tag{A.7b}$$

$$\nabla \cdot E = 0 \tag{A.7c}$$

$$\nabla \cdot H = 0 \tag{A.7d}$$

Where the constants (in free space) are:

ϵ_0; the electric permittivity is approximated at $(^1/_{36\pi})$ x 10^{-9} $^F/_m$.

μ_0; the magnetic permeability is approximated at 4π x 10^{-7} $^H/_m$.

The operators $\nabla \cdot$ and $\nabla \times$ represent the divergence and curl.

Maxwell's equation functions (E and H) satisfy the wave equation (A.4) with a relationship between light speed in free space and the constants ϵ_0 and μ_0 using [1, 87]:

$$C_0 = \frac{1}{\sqrt{\epsilon_0 \mu_0}} \tag{A.8}$$

The wave equation (A.4) is related to the free space speed of light, that represents any of the three components (x, y, z) for the electric function (*E*) and magnetic function (*H*). The relationship between wave optics and electromagnetic optics with the constants and the scalar wave function could be applied to a lossless resonator [1], as an example. Inside a lossless resonator of volume **v,** the electromagnetic field takes the form of a sum of discrete orthogonal modes of different frequencies, different spatial distributions and different polarizations, the electric field vector is determined by the equation (A.9) [1]:

$$\varepsilon(\hat{\mathrm{r}}, t) = \mathcal{R}e\,\{E(\hat{\mathrm{r}}, t)\} \tag{A.9}$$

And $E(\hat{\mathrm{r}}, t)$ is developed in the next equation [1]:

$$E(\hat{\mathrm{r}}, t) = \sum_q A_q \mathrm{U}_q(\hat{\mathrm{r}}) e^{j2\pi\nu_q t}\, \hat{e}_q \tag{A.10}$$

Where A_q is the amplitude, v_q is the frequency, $\hat{e}_q$ is the polarization along the direction of the unit vector and U_q is the complex function for a spatial distribution characterised, the equation (A.10) is represented by q_{th} mode within a complex envelope that is normalized with the next equation [1].

$$\int_V \left|U_q(\hat{r})\right|^2 dr = 1 \tag{A.11}$$

With a cubic resonator of ***d*** dimension, the possibility of choice is that the spatial expansion functions could be set in standing waves like the next equation [1].

$$U_q(\hat{\mathrm{r}}) = \sqrt{\left(\frac{2}{d}\right)^3}\, sin\frac{q_x \pi x}{d}\, sin\frac{q_y \pi y}{d}\, sin\frac{q_z \pi z}{d} \tag{A.12}$$

Where the q in x, y and z plane are integers denoted by the index q = (q_x, q_y, q_z), finally the energy contained in the mode is expressed in the next equation [1]:

$$E_q = \frac{1}{2}\varepsilon \int_V E(\hat{r},t)\cdot E*\left(\hat{r},t\right)d\hat{r} \tag{A.13}$$

But that equation could be simplified [1]:

$$E_{\hat{q}} = \frac{1}{2}\varepsilon \left|A_{\hat{q}}\right|^2 \tag{A.14}$$

The energy in classical electromagnetic theory (E_q) can be assumed as an arbitrary non-negative value and no matter how small it could be, the total energy is the sum of the energies in all modes; Electromagnetic optics provide the most complete treatment of light within classical optics, that encompasses wave optics and the last encompasses ray optics, however classical electromagnetic theory fails to account for certain optical phenomena and this failure which became evident around the turn of this century, ultimately led to the formulation of a quantum electromagnetic theory known as ***Quantum Electro-Dynamics*** (QED) [1] and modern day quantum optics.

A.2 Mean Photon Flux and Photon Number

Quantum theory considers the light as a flux of single photons, in which each photon has a behaviour, a clear difference between the electromagnetic theory applied to the light and quantum optics can be demonstrated with the light intensity in relation to the power and energy, e.g. a monochromatic light of frequency $\boldsymbol{\nu}$ and an intensity I(r) (watts/cm^2) carry a mean photon-flux density [1].

$$\phi(r) = \frac{I(r)}{h\nu} \tag{A.15}$$

Where $h\nu$ is the energy of each photon, the equation (A.15) converts a measurement in the electromagnetic theory of light (also called classical optics) with units of energy/s/cm^2 into a quantum measurement with units of photons/s-cm^2, for the case of quasi-monochromatic light there is a central frequency $\overline{\nu}$ for all photons emitted with the same energy $h\overline{\nu}$ approximately, therefore the mean photon-flux density is just an

approximation [1]. In table A.1 we show some well-known light sources with their respective approximate mean photon-flux densities [1].

Source	Mean Photon-Flux Density (photons/s/cm^2)
Starlight	10^6
Moonlight	10^8
Twilight	10^{10}
Indoor light	10^{12}
Sunlight	10^{14}
Laser light†	10^{22}

Table A.1: The mean photon-flux density for several light sources, † (10mW He-Ne laser beam at λ_0=633nm focused to 0μm - diameter spot) [1].

The photon flux is obtained by the integral of the mean photon-flux density over a specified area [1].

$$\phi = \int_A \phi(r) dA \tag{A.16}$$

The equation above is related to the classical optic power represented by equation (A.17).

$$P = \int_A I(r) dA \tag{A.17}$$

Because of optical intensity I(r), the equation (A.17) is used to determine the mean photon flux density $\phi(r)$ in equation (A.15), the mean photon-flux density is also represented in equation (A.18).

$$\phi = \frac{P}{h\bar{\nu}} \tag{A.18}$$

It is possible to determine the mean photon number $\bar{n}$ when the mean photon-flux ϕ is applied during a time lapse *t*, the equation (A.19) shows this association between these two terms [1].

$$\bar{n} = \phi T \tag{A.19}$$

The mean photon number can be related to the classical optics, each photon has a proper energy as mentioned in section 1.1.1, this energy multiplied by the number of photons

emitted in a lapse of time represents an optical energy (joules), this energy is represented as E = PT and substituting ϕ of the equation (A.18) in the equation (A.19) the optical energy is related to equation (A.20).

$$\bar{n} = \frac{E}{h\bar{\nu}} \tag{A.20}$$

In table A.2 it condenses the photon-flux density, photon-flux and photon number with their correspondent in classical optics.

Classical Optics		Quantum Optics	
Optical Intensity	I(r)	Photon-flux density	$\phi(r) = \frac{I(r)}{h\nu}$
Optical Power	P	Photon flux	$\phi = \frac{P}{h\bar{\nu}}$
Optical Energy	E	Photon number	$\bar{n} = \frac{E}{h\bar{\nu}}$

Table A.2: The relations between classical and quantum optics for intensity, power and energy [1].

The polychromatic light has a broad bandwidth and each component of this bandwidth has a proper photon flux spectral density, the classical optical theory concepts such as intensity, power and energy and their quantum counterpart is applied like a spectral photon-flux density of the polychromatic light, this spectral photon flux is also related to a spectral photon number shown in table (2.3).

Classical		Quantum	
I_ν	$\left(\frac{W}{cm^2-Hz}\right)$	$\phi(r) = \frac{I(r)}{h\nu}$	$\left(\frac{photons}{s-cm^2-Hz}\right)$
P_ν	$\left(\frac{W}{Hz}\right)$	$\phi = \frac{P}{h\bar{\nu}}$	$\left(\frac{photons}{s-Hz}\right)$
E_ν	$\left(\frac{J}{Hz}\right)$	$\bar{n} = \frac{E}{h\bar{\nu}}$	$\left(\frac{photons}{Hz}\right)$

Table A.3: The relation between spectral photon-flux density and spectral photon flux, comparing classical and quantum optics [1].

A.3 Quantising the Radiation Field

Section 1.1.1 briefly analysed the photon energy of an electromagnetic mode inside of a cubic resonator with a volume (L^3), inside the resonator this electromagnetic mode creates and annihilates a photon and this action is represented with the operators $a^+_{\hat{k},\hat{\varepsilon}}$

and $a_{\hat{k},\hat{\varepsilon}}$ where $\hat{k}$ is a wave vector and $\hat{\varepsilon}$ is perpendicular to $\widehat{k}$, thus the electric field with position $\hat{r}$ is the new operator of the electromagnetic mode and it is represented as the sum of Hermitian-conjugate terms [7]:

$$\hat{E}(\hat{r}) = \hat{E}^{(-)}(\hat{r}) + \hat{E}^{(+)}(\hat{r}) \tag{A.21}$$

The electric field has a position and for the Heisenberg uncertainty it is possible to include a time dependence, thus field operators in equation (A.22) are expressed with a time dependence [7, 88]:

$$\hat{E}^{(-)}(\hat{r},t) = i\sum_{\hat{r},\hat{\varepsilon}}\sqrt{\frac{\hbar\omega_k}{2\varepsilon_0 L^3}}\,\hat{\varepsilon}a^{+}_{\hat{k},\hat{\varepsilon}}e^{i(\hat{k}\cdot\hat{r}-\omega_k t)} \tag{A.22}$$

$$\hat{E}^{(+)}(\hat{r},t) = i\sum_{\hat{r},\hat{\varepsilon}}\sqrt{\frac{\hbar\omega_k}{2\varepsilon_0 L^3}}\,\hat{\varepsilon}a_{\hat{k},\hat{\varepsilon}}e^{i(\hat{k}\cdot\hat{r}-\omega_k t)} \tag{A.23}$$

In these equations it is possible to observe the creation ($a^{+}_{\hat{k},\hat{\varepsilon}}$) and the annihilation ($a_{\hat{k},\hat{\varepsilon}}$) operators included, that indicates a clear connection between the electric field and quantum mechanics [89].

A.4 Quantum Optics

The idea of light as particles carrying quanta of energy has a long history. This idea had a solid proof with Arthur Compton's research team when they were bouncing off the "***quanta"*** of the electrons from light. Both particles (photon and electron but unknown at that time) had a behaviour like billiard balls, which confirms Planck's theory. So, in 1926, the concept of light quanta introduced the concept of "***photons***" and the light behaving both as a wave and a particle. This milestone marked the end of classical electromagnetic theory and the beginning of quantum theory, or quantum optics [1, 90] .

A.4.1 Photon Energy

The photon could be defined as a particle with zero mass that carries electromagnetic energy and an intrinsic angular momentum (or spin) that governs the photon polarisation;

the photon travels at a specific speed which is considered a universal constant (speed of light) that reaches its maximum value in a vacuum (C_0).

The photon energy is related to its frequency ν or $\omega = 2\pi\upsilon$ through:

$$E_{ph} = h\upsilon = \hbar\omega \tag{A.24}$$

Where h = 6.63 x 10^{-34} Js (Planck's constant) and $\hbar = \frac{h}{2\pi}$. The photon energy can also be expressed in electron-volt units (eV), the eV definition represents the kinetic energy of an electron accelerated through a potential difference of 1V.

The photon energy is related to the frequency ν (Hz), the frequency to the wavelength λ (nm) and a reciprocal wavelength $\frac{1}{\lambda_0}$ (cm^{-1}) which is sometimes considered a photon energy unit; this statement is illustrated in figure A.1.

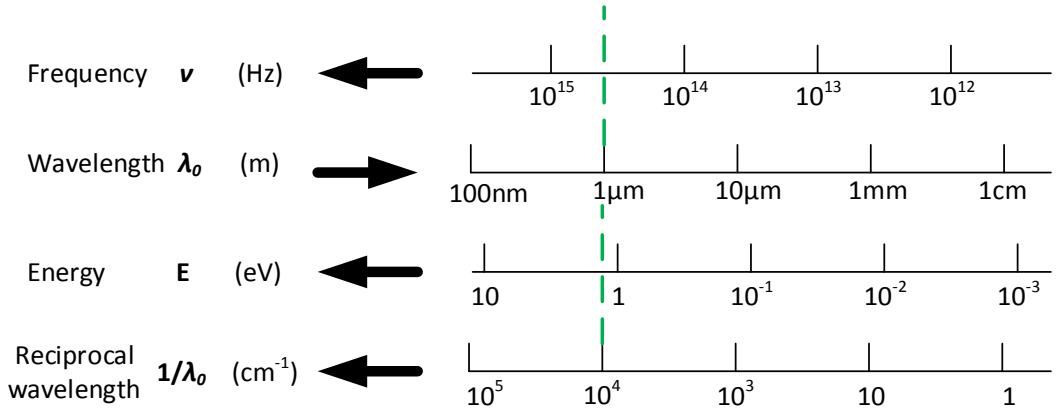

Figure A.1: Relationship between photon frequency ν (Hz), wavelength λ_0, energy E(eV), and reciprocal wavelength $1/\lambda_0$ (cm-1) [1].

Taking an example from figure A.1, a photon of 1000nm wavelength (λ_0) frequency can be determined using equation (A.25) resulting in 300 THz in a vacuum with a reciprocal wavelength of 10,000 cm^{-1}[1].

$$\nu = \frac{C_0}{\lambda_0} \tag{A.25}$$

The relationship between the frequency and energy (i.e. electron volts, eV) of the photon has a constant of proportionality **1.24eV/μm**, giving a quick way to calculate the energy (in eV) from wavelength (in μm) and photon [1]:

$$E_0(eV) = \frac{1.24}{\lambda_0(\mu m)} \tag{A.26}$$

The energy in Joules is then obtained from:

$$E_0(J) = E_0(eV) \times (1.6 \times 10^{-19}) \tag{A.27}$$

A.4.2 Photon Polarisation

In classical optics, light travels in electromagnetic waves and these waves contain: an electric and magnetic field that share the same region of the space, (but it is the electric field that is considered for the polarisation of light). At each point in space and time, the electric fields of the waves are added in vectors that the electric field continuously rotates through space and time; thereby it is defined as circularly polarized light.

However, if there are electric fields aligned in the same direction, the light is considered linearly polarized. Many light sources produce light that is composed of electromagnetic waves oriented in different directions; this type of light is known as unpolarised light. There are some materials that discriminate electric fields oriented in one direction, but allow electric fields oriented in other directions to pass through, hence these materials act as a polarizer.

Therefore, regardless of the type of light polarisation (circular, linear or unpolarised) that enters the polarizer, only linearly polarized light is able to exit the material. This process is illustrated schematically in figure A.2.

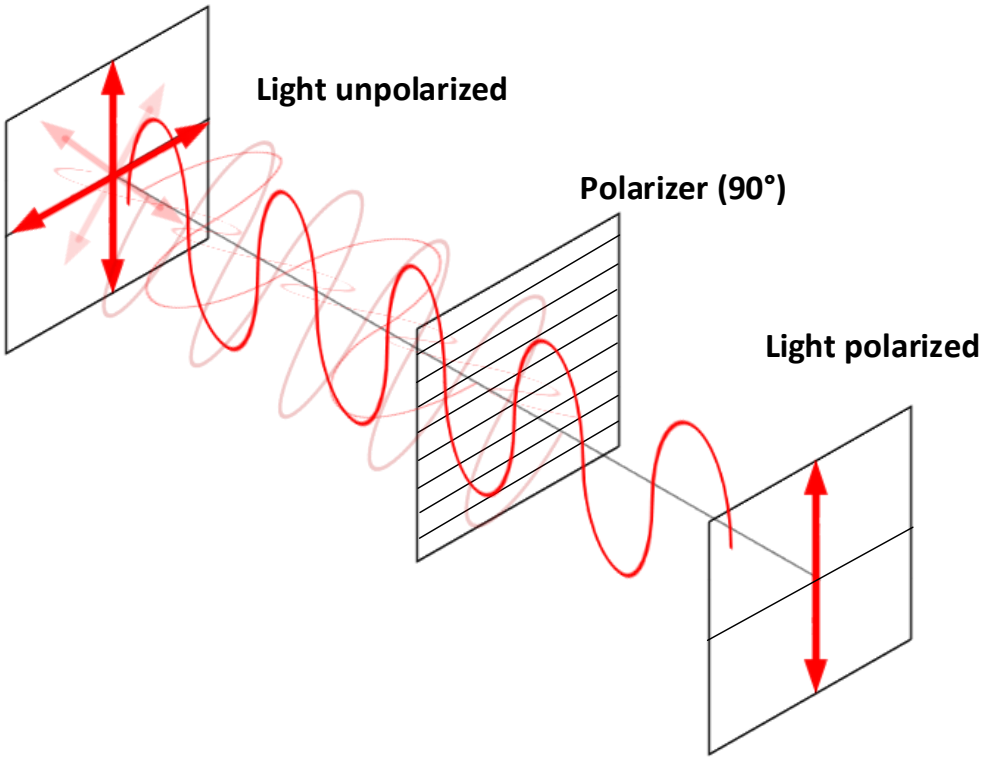

Figure A.2: The unpolarised light passes through the polarizer, then an electric field orthogonal to the polarizer is able to pass, so the light is polarized.

In quantum optics, the photons that are linearly polarized can be described by a superposition of two plane waves propagating in the *z*-direction, they always hold the same transversal distribution and polarisation (*mode*). A mode that is linearly polarized in the *x*-direction, and the other linearly polarized in the *y*-direction could be expressed with the equation (A.27) [1]:

$$E(\hat{r},t) = (A_x\hat{x} + A_y\hat{y})e^{-jkz}e^{j2\pi\nu t} \tag{A.27}$$

This electric field can also be represented by a coordinate vector system $\hat{x}$, $\hat{y}$. In this system x' and y' makes a 45° angle with the initial coordinates (x and y equal to 0). Thereby, the electric field is in terms of two modes carrying the polarized photons along the x' and y' direction; then equation (A.27) can be changed to represent the two modes as a function of x' and y'.

$$E(\hat{r},t) = (A_{x'}\hat{x}' + A_{y'}\hat{y}')e^{-jkz}e^{j2\pi\nu t} \tag{A.28}$$

The intensities (amplitudes) $A_{x'}$ and $A_{y'}$ also have a relationship with the intensities A_x and A_y through: $A_{x'} = \frac{1}{\sqrt{2}}(A_x - A_y)$ and $A_{y'} = \frac{1}{\sqrt{2}}(A_x + A_y)$. For the case in which a photon occupies the x-polarized mode, it means that the y-polarized mode is empty but there is a possibility to find the photon along the x' and y' direction. There is a probabilistic approach to finding a photon with x, y, x' and y' polarisation modes proportional to their intensities; $|A_x|^2$, $|A_y|^2$, $|A_{x'}|^2$ and $|A_{y'}|^2$. Figure 1.3 illustrates an x-polarized photon with the probabilities of x' and y' polarisation.

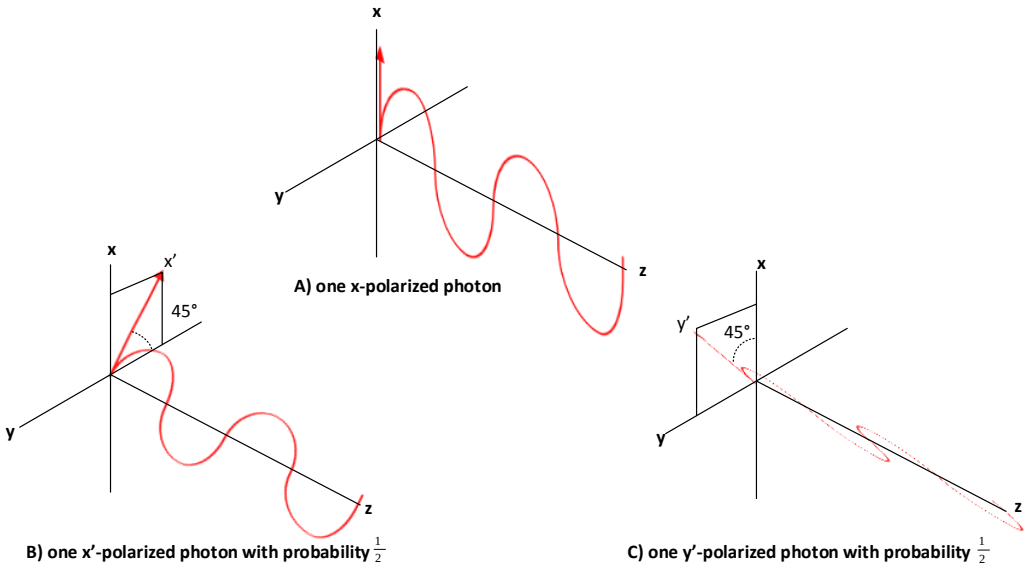

Figure A.2: A photon in the x-linear polarisation mode (A) is the same as a photon superposition of the x'-linear polarisation mode (B) and the y'-linear polarisation mode (C), with a probability of ½ of each one.

Therefore, the photon at x-polarisation has a probability to be found at x of $|A_x|^2 = 1$ and y is $|A_y|^2 = 0$, but for x' and y' the probability is $^1/_2$ ($|A_{x'}|^2 = |A_{y'}|^2$). This is a basic definition of a quantum state of the photon, but it can be clearer through the Poincare sphere. The electric field can also be analysed as photon streams and the polarisation of the electric field is determined by the photon intrinsic angular momentum (spin).

$$\mathcal{S} = \pm\hbar \tag{A.29}$$

The photon spin is directly related to Planck's constant and the photon has one of two possible spins: the clockwise sense and the counter clockwise sense with respect to the photon travel direction. The circular polarisation is composed of photons with one spin

possibility (clockwise or counter clockwise sense), but the linear polarisation consists of equal possibility of the photon travelling in the plane wave for both senses.

The photon polarisation state can be represented as a point on the Poincare sphere, which figure A.4a illustrates.

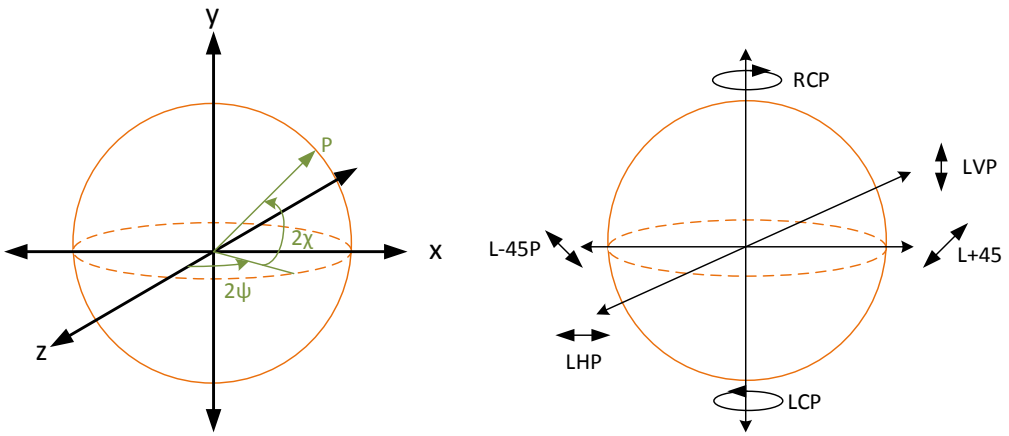

A) Poincare Sphere **B) Photon polarisation on the Poincare Sphere**

Figure A.3: A) The Poincare Sphere. B) Photon polarisation in The Poincare Sphere.

Each region of the sphere can be specified by two different angles; ψ and χ. These angles define the photon polarisation through the sphere latitude (χ) and longitude (ψ), because some sphere regions represent: the circular polarisation (poles) and linear polarisation (equator). Then, point P in figure A.4a represents an elliptical polarisation with 2ψ and2χ.

The photon polarisation would become more circular when P is close to a pole or more linear when P is close to the equator. Thereby, the North Pole indicates a spin in a clockwise sense (Right Circular Polarisation, RCP) and the South Pole indicates a spin in a counter clockwise sense (Left Circular Polarisation, LCP) [90]. On the equator, the linear polarisation changes as a function of ψ ($\chi = 0°$). When the longitude angle is 0°, the photon polarisation is horizontal but at 180° the polarisation is vertical. Between this range the polarisation could be diagonal (90°) or anti-diagonal (-90°). In figure A.4b all these types of photon polarisations are illustrated. The photon circular polarisation state considers its spin rotation as right or left ($|R\rangle$ or $|L\rangle$). Thereby, the photon circular polarisation state is defined by the equation (A.30).

$$|\Psi\rangle = \cos\frac{\chi}{2}|R\rangle + e^{i\psi}\sin\frac{\chi}{2}|L\rangle \tag{A.30}$$

If $\chi = 0$ the circular polarisation state is $|R\rangle$ but if $\chi = 180°$ the state is $|L\rangle$. These states are products of the superposition of the linear polarisation states; horizontal and vertical ($|H\rangle$ and $|V\rangle$):

$$|R\rangle = \frac{1}{\sqrt{2}}\left(|H\rangle + i|V\rangle\right) \tag{A.31a}$$

$$|L\rangle = \frac{1}{\sqrt{2}}\left(|H\rangle - i|V\rangle\right) \tag{A.31b}$$

The linear photon polarisation state is similar to equation (A.30):

$$|\Psi\rangle = \cos\frac{\psi}{2}|H\rangle + e^{i\chi}\sin\frac{\psi}{2}|V\rangle \tag{A.32}$$

The diagonal and anti-diagonal polarisation states ($|D\rangle$ and $|A\rangle$) are also products of superposition states of $|H\rangle$ and $|V\rangle$:

$$|D\rangle = \frac{1}{\sqrt{2}}\left(|H\rangle + |V\rangle\right) \tag{A.33a}$$

$$|A\rangle = \frac{1}{\sqrt{2}}\left(|H\rangle - |V\rangle\right) \tag{A.33b}$$

Any pair of these states $|H\rangle$ and $|V\rangle$ could be used to define a basis to determine the other states and hence it is possible to choose a computational basis for quantum computing or quantum cryptography.

Appendix B.

Quantum Optics Applications

Applications of optics could be instruments of astronomy, biology or glasses for people with sight problems. These devices are taken as classical examples of optics, although there are more instruments and applications that are not as well known. In particular, quantum optics is a relatively new branch of optics with applications that are still at a research stage. However, various applications exploiting photon counting are well developed.

B.1 Fluorescence Spectroscopy

Photon counting can be used to measure the fluorescence lifetime of organic molecules, and solid-state emitters (e.g. quantum dots). Pulsed excitation of these two-level systems occurs very quickly ($< 10^{-15}$ seconds) while the emission occurs after a random delay representative of the fluorescence lifetime [4].

The photon emission is a random event and each excited fluorophore has the same possibility of emitting light radiation at a specific time. The best way to illustrate this process is with a Time-Correlated Single Photon counter (TCSPC) like the PicoHarp 300 of

PicoQuant®, a fast laser pulse that illuminates a sample and when it becomes excited, it releases a fluorescence photon. Figure B.1a illustrates this process.

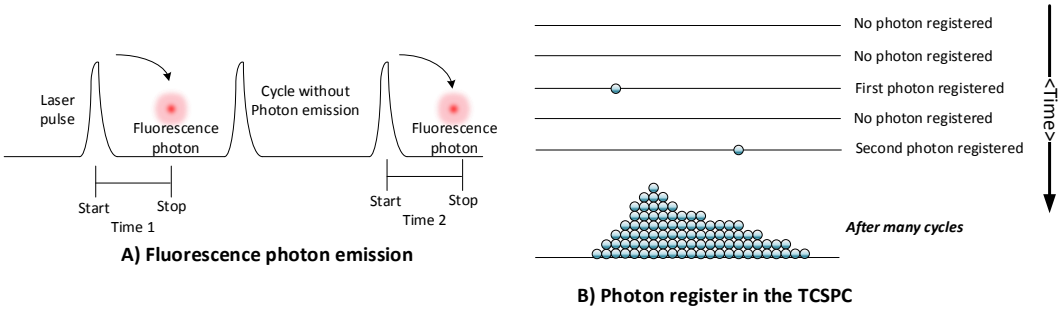

Figure B.1: A) the laser pulses excite the sample that releases a fluorescence photon and once there is a photon detection discards any other possibility of detection, B) the photon that has been released is registered on a histogram and although there are some cycles which do not produce any photons, after many cycles the fluorescence lifetime is formed [71].

Some pulses do not produce a single photon or could register noise of fake detections such as dark-counting or after-pulsing. Therefore, it is necessary to use a histogram to register each photon released. After many pulses, the fluorescence lifetime can be seen in the time interval histogram as an exponential decay, as shown in figure 1.5b.

B.2 Light Detection and Ranging (LIDAR)

An interesting quantum optics application is the metrology that uses single photons to determine phase shifts, transmission and a distance with high precision among other things. Light detection and ranging (LIDAR) uses a pulsed laser to illuminate a target and a photon counting detector measures the reflected pulses [1].

The reflected pulses have a return time that can be measured with a TCSPC. For a better understanding of how a LIDAR system works, a block scheme of the system is illustrated in figure 1.6.

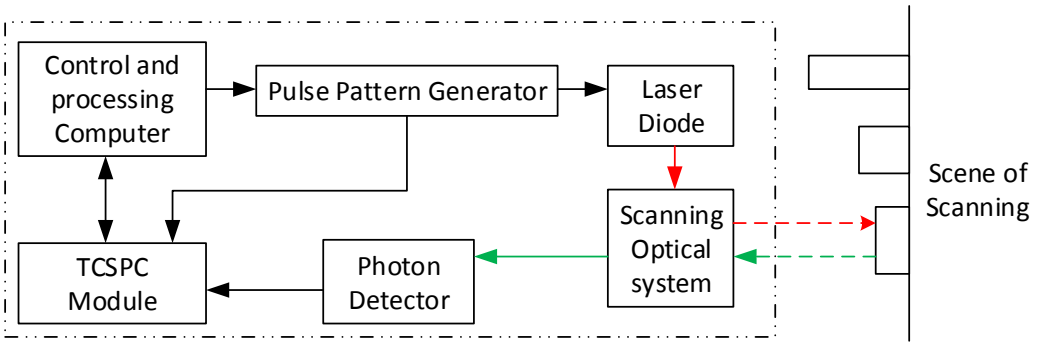

Figure B.2: Block scheme of a LIDAR system with a scanning rangefinder system [91]. The TCSPC and Control processor communicate to each other, but the control processor activates the pulse generator which controls the laser diode, the scanning system directs the light pulses to the scene and collects them after directing them to a photon detector, the photon detector sends electrical pulses to the TCSPC which compares the times between the pulse generated and pulse received.

The pulsed laser is forwarded with an optical scanning to a target at an arbitrary or unknown distance of the LIDAR system; the laser pulses have a pattern that can be continuous with a certain frequency, a single pulse or a bit stream [91].

The reflected pulses are captured by the same scanning optical system and forwarded to a photon detector (by a fibre optic). Once they are measured by the photon detector, a TCSPC measures the time delay between the pulses emitted and pulses reflected. Figure 1.7 illustrates a comparison between a pulse emitted, reflected pulse and their time correlation.

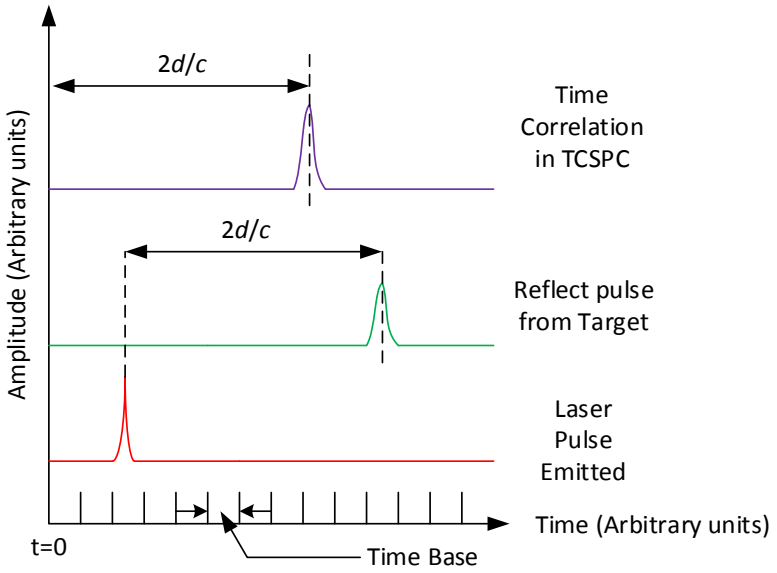

Figure B.3: Time Comparison of laser pulse emitted, reflected pulse and cross-correlation are measured in the TCSPS. The time shift $2d/c$ corresponds to the correlation time measured between pulse emitted and pulse reflected.

The correlation time has a relation $2d/c$ where d is the distance and c is light speed constant in a medium (c_0 is in the free space), a time base is used to quantify the time measurement and a computing process to determine d.

B.3 Quantum Computing

The quantum computing process information encoded in quantum states is explained in section 1.1.2 and the qubits are analogues of the traditional bits used in digital electronics. Digital electronics use logical gates like AND, OR, XOR and their variation with the NOT gate to process classical bits representing binary values (0 and 1) which are represented by logic levels. The qubit also represents binary values (0 and 1) from quantum states of the photon [7], but like the photon it also exists as a superposition of states 0 and 1.

In quantum computing, the controlled-NOT (CNOT) gate is shown as a universal gate for quantum computers as an analogy of the NAND in the conventional computing [5, 7].

B.4 Quantum Cryptography

Quantum cryptography was developed in 1984 with the idea of an optical cryptography with photon states. Although at the beginning it was considered by some as almost science fiction, Charles Bennett and Gilles Brassard demonstrated the concept of Quantum Key Distribution (QKD) in 1992 [6]. Since then many demonstrations have been made but after more than 30 years, still some conservative cryptographers view QKD with scepticism [92].

To understand QKD, it is necessary to explain the traditional communication scheme:

- Transmitter (Alice)
- Receiver (Bob)
- Communication channel (Quantum and classical)

These two parts (Alice and Bob) share the key without compromising its secrecy through four photon polarisation states ($|H\rangle$, $|V\rangle$ $|D\rangle$ and$|A\rangle$). Alice sends single photons with a random polarization state to Bob through the quantum channel, and each polarization state is recorded in a list for Alice. The photon polarization states are assigned a 2-bit binary value in which one bit represents the polarisation state basis and the other corresponds to a raw key bit.

Bob measures the polarisation state and keeps a register of each basis measured. Alice and Bob compare their respective basis registers through the classical channel, which is authenticated to avoid possible attacks by an eavesdropper (Eve). There is a 50% probability that Bob measures the right basis, so Alice and Bob can share qubits without the risk of anyone eavesdropping [93].

Unlike the classical channel, any attempt to measure the quantum channel would modify the system increasing the number of errors. Alice and Bob would detect this considerable number of errors, which is indicative of an attack. This brief description of communication between Alice and Bob is part of a protocol communication used in the QKD system known as BB84 [9, 93-97].

B.4.1 Protocol BB84

The Bennett-Brassard 1984 (BB84) protocol uses the principle of quantum mechanics to establish a random secret key, which is only known by Alice and Bob. The photon quantum state of polarisation is used to encode the qubits in the QKD system and there are four possible polarisation angles illustrated in figure 1.8 [9, 94].

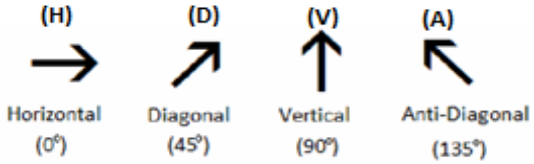

Figure B.4: The four angles (basis states) in the BB84 protocol with polarised photons.

The BB84 protocol process begins with Alice sending a stream of single photons without a specific polarisation and each single photon polarisation is fixed with one of four angles and the stream is guided to a quantum channel with the direction towards Bob. Once the stream reaches Bob, he would measure each single photon with an optical arrangement to identify its polarisation and define it as a basis state. After that, Bob assigns a binary value to each basis state to become a single photon with a basis state in a qubit.

Alice keeps a register of the basis states sent and Bob also keeps a register of the basis states measured. Once the quantum communication ends, Bob shares his register with Alice through the classical channel. This register never reveals the actual photon polarisation states, only the basis. Alice confirms which basis is correct and both parts discard the wrong measurements. Figure 1.9 illustrates the process of basis confirmation and key exchange.

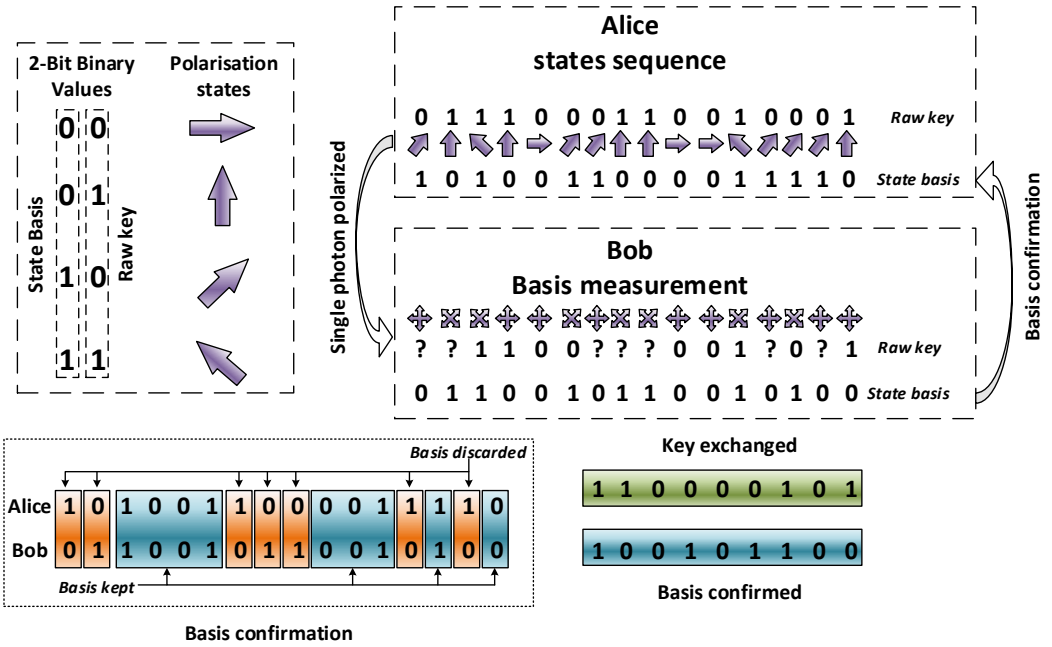

Figure B.5: The photon polarisation states are encoded in a 2-bit binary value. The most significant bit (MSB) identifies the polarisation state basis, Alice sends single photons at a random polarisation basis to Bob, although the polarisation states also contain the raw key but only the basis is confirmed through the classical channel. Alice and Bob discard the wrong basis and keep the correct basis. At the end the key is exchanged through the basis confirmation.

Alice and Bob never reveal any qubits during the basis confirmation through the classical channel. Furthermore the classical channel is authenticated to reduce any possible leak of information of the basis confirmation.

The high security of the BB84 protocol is possible due to the implementation of quantum physics in the QKD system. Hence the probability of wrong measurements by Bob is contemplated and in a certain way desired. Figure 1.10 illustrates Bob's basic optical arrangement to implement the BB84 protocol.

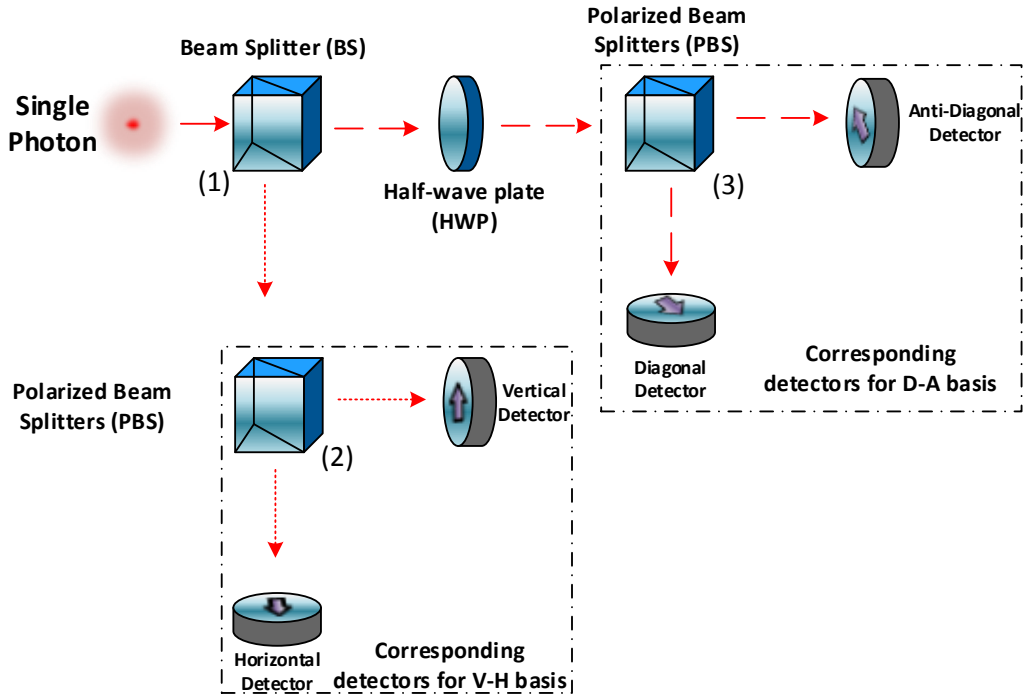

Figure B.6: Optical arrangement in Bob for the BB84 protocol implementation.

This optical arrangement (figure 1.10) contains a Beam Splitter (BS) but the photon is an indivisible particle creating a random basis required by the BB84 protocol. Therefore, the photon in point (1) would take one of two possible ways. In the case that the photon has passed through the BS, the photon polarisation would rotate 45° and thus modify the photon polarisation state by the half-wave plate (HWP). The reason for this rotation is because there is not a PBS that would manage 45° and 135° of polarisation (only 0° and 90°). In the opposite case, the photon is reflected in the direction of Vertical-Horizontal (V-H) basis detectors.

When the photon is reflected towards the V-H basis detectors, it would reach the PBS (2) first. Then, the photon can be reflected or pass through the PBS depending on its polarisation to incise on one of the two detectors. The same situation happens after the photon modifies its polarisation by the HWP and reaches Anti-diagonal-Diagonal (A-D) basis detectors. Then, the polarisation state has an important role at that moment to incise whichever of the two PBS, and this situation can be represented mathematically.

Before reaching the BS, the single photon has a specific state $|\Psi\rangle$ which has 50% of probability to reach V-H or A-D basis detectors. After the photon is reflected or passed through there is a probability of detection which is defined by the group of equations (1.12).

$$P_{\oplus,T} = \left|\left\langle \Psi \middle| \rightarrow \right\rangle\right|^2 \tag{1.12a}$$

$$P_{\oplus,R} = \left|\left\langle \Psi \middle| \uparrow \right\rangle\right|^2 \tag{1.12b}$$

$$P_{\otimes,T} = \left|\left\langle \Psi \middle| \nearrow \right\rangle\right|^2 = \left|\tfrac{1}{\sqrt{2}}\left[\left\langle \Psi \middle| \uparrow \right\rangle + \left\langle \Psi \middle| \rightarrow \right\rangle\right]\right|^2 \tag{1.12c}$$

$$P_{\otimes,R} = \left|\left\langle \Psi \middle| \nwarrow \right\rangle\right|^2 = \left|\tfrac{1}{\sqrt{2}}\left[\left\langle \Psi \middle| \uparrow \right\rangle - \left\langle \Psi \middle| \rightarrow \right\rangle\right]\right|^2 \tag{1.12d}$$

Where $\oplus$ and $\otimes$ correspond to V-H basis and A-D basis respectively, T indicates the transmission of the photon in the PBS and R indicates the reflection of the photon. Therefore, there is 16 possible combinations for the probability of the photon polarisation states and they can be registered in table 1.1.

$\lvert\Psi\rangle$	$P_{\oplus,T}$	$P_{\oplus,R}$	$P_{\otimes,T}$	$P_{\otimes,R}$
$\lvert\uparrow\rangle$	0	1	$\frac{1}{2}$	$\frac{1}{2}$
$\lvert\rightarrow\rangle$	1	0	$\frac{1}{2}$	$\frac{1}{2}$
$\lvert\nearrow\rangle$	$\frac{1}{2}$	$\frac{1}{2}$	1	0
$\lvert\nwarrow\rangle$	$\frac{1}{2}$	$\frac{1}{2}$	0	1

Table B.1: Results condensed from the group equation (1.12).

The incident photon on the BS has two and only two possible ways due to the indivisible nature of the photon, hence if the photon has a vertical polarisation state and it is reflected by the BS, this photon has all the probability (1) to be reflected and directed to the vertical detector.

If the photon with a vertical polarisation state passes through the BS, the HWP rotates the polarisation state 45° and the new polarisation state is anti-diagonal. This new polarisation on the PBS has ½ of being reflected or passed through to one of the two detectors. In this case, this polarisation measurement represents a sifting because the original polarisation state was vertical.

However, the random basis is not the only type of error, the noise, fake detections on Bob and his optical imperfections can provoke that a bit '0' becomes a bit '1' in the raw key, this type of error is measured through a Quantum Bit Error Rate (QBER) and it can be determined by the equation (1.13).

$$QBER = \frac{N_{WB}}{N_{TB}} \tag{1.13}$$

Where N_{WB} is the number of bits in error received by Bob and N_{TB} is the number of the bits received in total. The QKD system uses an algorithm to reduce the QBER and the most common is the cascade algorithm [10], but the Low Density Parity Check (LDPC) algorithm has shown a better efficiency and an increment of the security on the system [98].

The simplest attack from Eve is the measurement of the polarisation states and after directing them to Bob (intercept-resend attack), Bob receives all of the qubits before Alice reveals which basis she transmitted, and then Eve has a possibility to choose the wrong basis. The percentage to choose the wrong basis is 50%, this measurement will yield an incorrect result due to this incontrovertible fact of quantum physics. Alice and Bob upon public discussion selected a subset of their shared string and compared the values of the subset and discarded them, thereby, the presence of Eve will be revealed by discrepancies of 25% of the values in their substrings and spotting her presence [9, 93, 94].

B.4.2 Quantum Cryptography Compared with Classical Cryptography

The cryptography is defined as a technique to cypher messages and they become unreadable for unauthorized receptors. The most primitive cryptographic technique is the *scytale* from the V Century B.C, it consists of a cylinder with a strip (normally leather) which is written as a message. The cylinder was removed by just leaving the strip with a message which is not readable. To decode the message, the strip was put on a rod with the same diameter, although this method was easily broken [99].

The QKD is a cryptographic method because its message codification is only readable by the receptor (Bob), this system could be compared with other cryptographic methods and using levels of complexity reflects the first three layers of the Open System Interconnection (OSI) network [93].

1st level: The secret key agreement between two users sharing an initial small secret symmetric key and having access to a quantum channel QKD, falls in the category of physical layer security cryptographic primitives [93].

2nd level: Two-user secure payload transmission built on top of a key agreement scheme and secure link layer cryptographic primitives [93].

3rd level: Secure key distribution over a global network composed of multiple users in network layer cryptographic primitive [93].

It is impossible to gain information about non-orthogonal basis states without perturbing them, this property is used to establish a random key between two users (Alice and Bob) perfectly hidden to any eavesdropper (Eve) on the line. Therefore, QKD security is a secret key agreement in the framework of information-theory cryptography, thus, the quantum channel and classical channel combination is an advance for the quantum information science.

The QKD uses a symmetric secret key agreement technique because of the primary resources required, like the quantum channel and an authenticated classical channel. The authentication of the classic channel is obtained in different ways e.g. Alice and Bob share a short secret key in advance and operated in this regime of authentication. In this manner, QKD is a symmetric unconditionally secure secret key expansion scheme, in the

same way a cryptographic method with similar characteristics of QKD is the trusted couriers of key distribution (TCKD) [93, 99].

B.4.3 First Bristol Quantum Cryptography System.

The first QKD system developed at the University of Bristol is a low-cost QKD proposed by Duligall et al. [10]. Afterwards, this system had an update, reduction in size and cost by Lowndes et al [9], although there is a considerable difference between the first QKD system and the Bristol QKD system. The principle of the quantum cryptography is maintained, as shown in figure 1.13 which illustrates a block scheme of the Bristol QKD system.

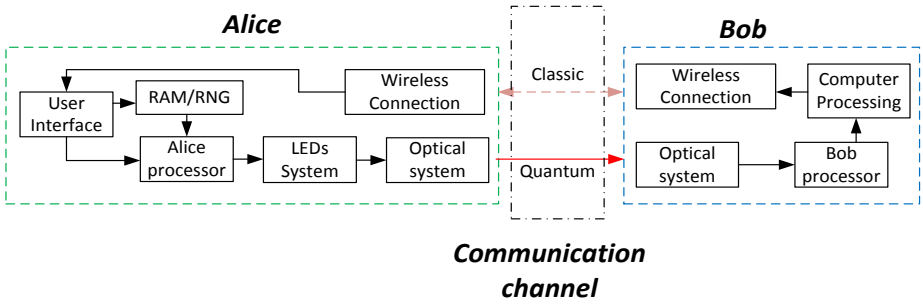

Figure B.7: Block scheme of Bristol QKD system [9]. The user interface can be a personal digital assistant (PDA), the red solid line represents the quantum channel and the dashed pale red line is the classic channel for the basis confirmation, the components of each block are described in section 1.5.1 and 1.5.2.

B.4.3.1 Alice Device

Many computing languages have a random number of generation algorithm with the purpose of delivering a random number requested by the user. Alice needs some methods such as generating a random order in the qubits. The Random Number Generator (RNG) sends some random bits that are requested by a user interface, they are stored in a Random-Access Memory (RAM) with the purpose of using it like a buffer for processing performance. At this point, the bits are not considered qubits but these bits will be converted in to qubits by Alice's processor [9].

The core of this processor is a Field Programmable Gate Array (FPGA) that controls the LEDs system and collects the bits to encode in qubits. When it receives the instruction to start the qubits transmission, the FPGA collects a random number from the RAM and

selects the polarisation states to encode the classic bits, this process is the start of qubit generation [9].

The LED driver receives a pulse that represents the classic bit and so the LED is activated, each LED has an independent driver which is formed by a delay line and a logic gate *AND,* the purpose of the circuit is that it generates fast electric pulses that activate the LEDs and so create almost single photons. The input bit signal has a free path to the logic gate input A and the same input arrives at the delay line but it is delayed and forwarded to the logic gate input B.

The variation in time of the same input in the gate releases a new bit signal with a time-on width defined by the delay line. Figure 1.14 illustrates a schematic diagram and the logic-signal time analysis.

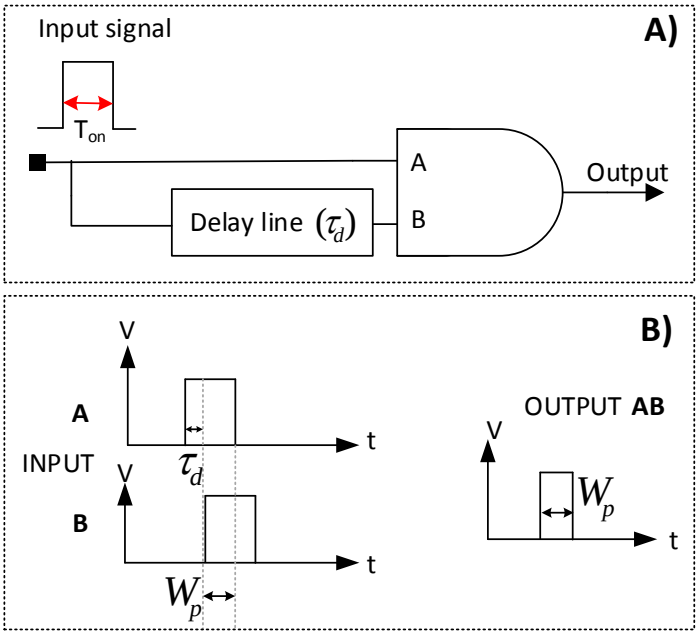

Figure B.8: Circuit interface to generate fast electric pulses and drive the LED: A) Schematic diagram, B) Logic-signal time analysis. The input signal has a width (T_{on}) and it is shared to a delay line, the input pulse delay by τ_d and the logic gate recombine these two versions of the input pulse, so the output pulse results shorter than the input pulse and the length of this output pulse is defined by T_{on}- τ_d (W_p).

This electric pulse excites a LED (Light Emitter Diode) to generate a low number of photons through weak optical pulses, although this LED stimulation is not considered a proper single photon source because the spontaneous emission produces multiple photons, and there is also no amount of considerable optical pulses with some photons greater than 1 [9, 11]. The optical pulse is forwarded to a polarizer and because of the light source, there

is a LED array of 2x2. The result is four 'single' photons sources each encoding one of the required polarisations in basis state (vertical or diagonal) and bit value (H/D = 0, V/A =1).

To ensure security, the 4 optical pulses converge in a 2D diffraction grating to collimate the optical pulses and after that, forward it to the pin holes with the purpose of reducing leakage into extra modes to avoid recognizing which LED emitted a light pulse and by inducing transverse coherence [9], This optical system is illustrated in figure 1.15.

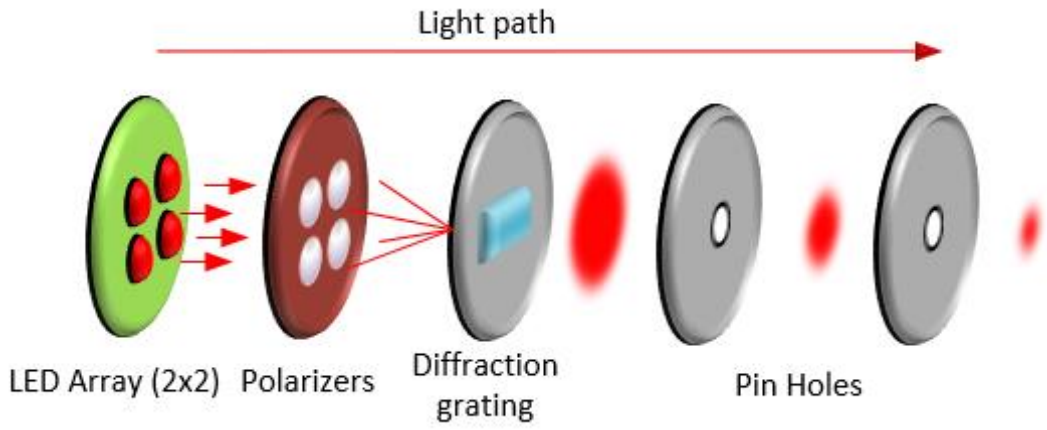

Figure B.9: Alice optical system

After all the process, since the trigger is executed by the user interface until the transversal coherence light, the qubits carried by this light beam are ready to reach the Bob optical system and the classic channel certificates where qubits have been measured in right basis using a dedicated wireless link with Bob.

B.4.3.2 Bob Device

The optical pulses coming from Alice must pass through an imaging system before it decodes the qubit. The Bob optical system collects and focus the light to collimate it in a beam and forwarding it onto a non-polarizing Beam Splitter (BS), to split the light 50:50. Half the light then travels to Polarized Beam Splitters (PBS) [9].

One PBS separates H and V light while the other is preceded by half wave plate (HWP), that rotates the light polarisation into the diagonal basis allowing an H-V basis [9]. The polarized optical pulse is thus separated at the PBS into the four polarisation channels, and passed to four detectors, one for each encoded state as described previously in section 1.4.1. Figure 1.16 illustrates the optical system of Bob based on the basic BB84 optical implementation.

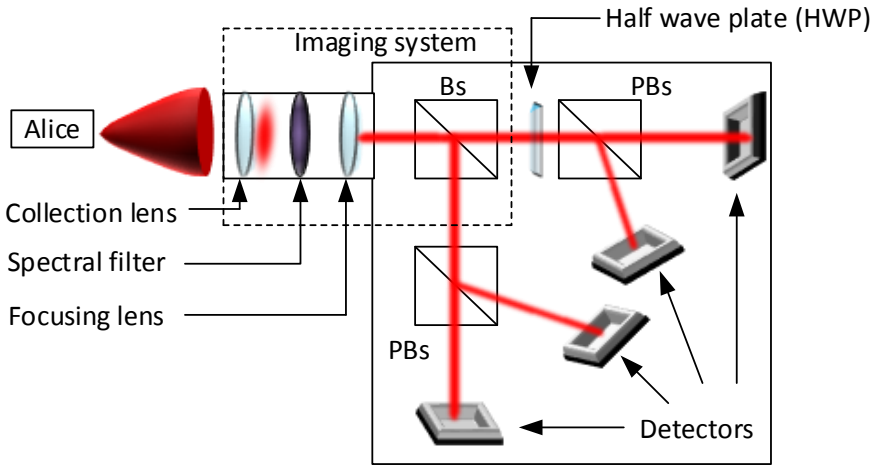

Figure B.10: Bob's Optical system with the imaging system, formed by an imaging system that contains a collection lens to reduce a possible misalignment, a spectral bandpass filter of 3nm wide at 632.8nm and a focussing lens to concentrate the beam on the BS. The single photons that incise on the BS take random directions to the PBS or the HWP that rotates 45° the photon polarization. The PBS reflects or allow the photons to pass depending on their polarisation and the detectors convert the incident photons in to electrical current pulses.

The four optical detectors are Avalanche photodiodes (Perkins Elmer C30902S) that convert each photon detection pulse into standardise electrical current pulses, in a comparator circuit. Finally, these electrical current pulses are converted into Transistor-Transistor Logic (TTL) signal. Without this, the photon detection cannot be processed by the Bob processor.

The photon detection converted in the TTL signal is not enough to decode the qubit and exchange the key. It is necessary to measure the timing of the photon arrivals to distinguish the weak optical pulses from the background. To do this, a time to digital converter developed at the University of Bristol [9, 100] allocates a time tag and detector number to every detected pulse.

The Bob processor also has an FPGA-like core and it needs to synchronize the Bob processor clock with the Alice processor clock. Hence, the time to digital converter uses a time tag system that compares the Bob processor internal clock pulses with the photon detection. At some moment, the photon detection has a coincidence with the clock pulse so the FPGA identifies and registers the clock number when the coincidence occurs. A photo detector registers the detection, and it is labelled with a tap number which is processed by a computer [9].

After Bob's computer processes the detections completely, it sends the detection time of the arrival data to Alice, and she shifts the time of her optical pulses which contain the photon polarisation states. Once all the optical pulses sent by Alice are detected, the synchronization between Alice and Bob is considered complete.

B.4.3.3 Key Exchange

Such as mentioned in section 1.3.1 during the key exchange, there are errors that can change the binary values of the raw key. The first Bristol QKD system considers three possible scenarios that could cause errors in the key exchange [9].

- Alignment and optical
- Electronic
- Background counting

The alignment of Alice with Bob is ensured by a cradle (previously adjusted) with magnets to lock Alice and avoid possible movements that could provoke a misalignment. Then, one of the four LEDs in the 2x2 array (figure 1.15) is used to quantify the counting in the detector, which corresponds to the polarisation state of the LED activated. However, sometimes the opposite detector in the polarisation state basis receives the LED pulse. Then it is possible to establish a ratio of counts on the right detector versus the ratio of the counts on the opposite detector. This relationship is known as extinction ratio.

The electronic scenario considers the detector nature as the origin of errors in the key exchange, the synchronization between Alice and Bob is fundamental to estimate the rate of errors. It uses a large amount of pulses sent by Alice. Bob shifts its clock pulses to synchronize with Alice. The duration of this process can last a few seconds but the longer the synchronization time lasts, the more successful the synchronization will be. In chapter two, the synchronization process between Alice and Bob (section 2.2.1).

At last, the background scenario considers the influence of other light sources upon the system. This scenario is characterised by the normal system operation in: day time, nightlight time, under room illumination environment and a specific light source (such as a desk lamp). The reason to consider this scenario is due to the quantum channel. Alice does not transfer the polarisation state by a fibre optic but through a free space (short

distance). During the analysis of all these scenarios, the error rate is below 11% which confirms the successful operation of the Bristol QKD system [9].

B.4.3.4 Results, SECOQC Exhibition and Improvement Recommendations

The Security Communication based on the Quantum Cryptography (SECOQC) international conference in 2008 was the first time when the Bristol QKD system was tested [9, 43]. The results demonstrated a daylight time background of 40-45kCounts per sec in the conference and a rate of bit exchange of 10kbits per sec [9, 43]. The efficiency of the LEDs to generate single photons is evaluated by their light extinction and in the SECOQC conference with an average extinction of 6.87% [43, 96].

Appendix C.

Photo-electric effect and Photodiodes

The photo-electric detector is based on the photo-electric effect discovered by Hertz in 1887 but explained theoretically in 1905 by Einstein [101], this effect consists of the transition of electrons from a lower level to higher levels, provoked by the absorption of a photon in a material (metallic), this transition results in mobile charge carriers. These carriers move and produce a measurable electric current or a conductivity, depending on if the carriers move externally or internally. When the carriers move externally this involves a photo-electric emission provoking the escape of electrons of the material, when the carriers move internally the effect involves a photo-conductivity, provoking that the excited carriers remain within the material and increase its conductivity [1, 3, 87, 89].

The photo-thermal detectors convert the photon energy into heat, although this change of temperature requires a certain time to be notable, therefore the photo-thermal detectors are generally inefficient and slow in comparison with the photo-electric detector [1], recent advances in the manufacturing and miniaturization has improved the performance of these detectors and now they have considerable applications for in the mid-infrared region [102].

C.1 Photo-Electron Emission

When a photon with large energy impact a metallic material in vacuum, an electron escapes over the potential barrier of the material and is liberated into the vacuum as a free electron, this process is called photo-electron emission although the electron release can occur within the material partially filling the conduction band [1, 87].

The energy conservation requires that the electrons been emitted from below the Fermi level where there is a large amount of them and with a maximum kinetic energy. The maximum kinetic energy is determined by equation (C.1) and also it is known as Einstein's photo-emission. The equation represents the energy conservation with the photo-electric work function labelled with *w*, this function is the energy difference between the vacuum level and the Fermi level of the metal.

$$E_{max} = h\nu - w \tag{C.1}$$

The equation (B.1) is only valid when the electron initially lies at the Fermi level, because it can receive the maximum kinetic energy specified. When the electron is not in the Fermi level, it is necessary to inject additional energy to transport it and thereby the kinetic energy is reduced to release the electron. The lowest *w* for a metal is about 2eV and the photo-detectors based on the external photo-effect, they are made of pure metal (useful in the visible and ultra-violet regions of the light spectrum) [1].

The photo-emission is different when the material is a semiconductor because the electron is released from valence band, the free electron travels in the vacuum through the band gap but once it reach the conduction band, the electron has to drift deep in the conduction band, this effect is known as electron affinity (χ). Equation (C.2) determine the maximum kinetic energy when the material is a semiconductor.

$$E_{max} = h\nu - (E_g + \chi) \tag{C.2}$$

The energy $E_g + \chi$ is equal to *w* of the equation (B.1) and its value is around 1.4eV for certain materials (alkaline), for this reason the semiconductor photo-detectors operate in the near infrared, although with some doping they can also operate in the visible and ultra-violet regions of the spectrum. In figure C.1 it illustrates the electron exchange when a photon is absorbed for materials such as metal and semiconductor.

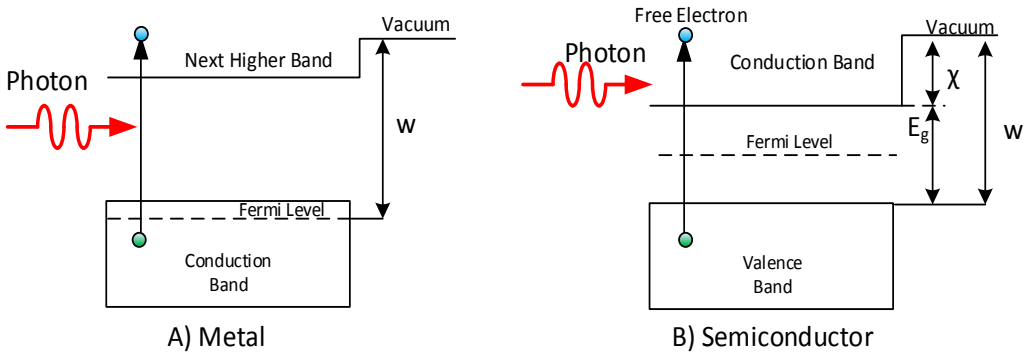

Figure C.1: Photo-emission on material: A) Metal, B) Semiconductor. The bandgap energy and electron affinity in the semiconductor material are denoted E_g and χ respectively.

When the electron-affinity is negative (Negative Electron-Affinity of NEA) in the semiconductor, it is not necessary to have a considerable energy from the photon to start the photo-emission. The conduction band edge position above the vacuum level in most of the material, thus E_g becomes a trigger for the photo-emission.

In the practice, this position of the conduction band is perform when a thin layer of n-type material is deposited on a p-material, the union of these materials can bend the band on the surface material provoking the bottom of the conduction band to be below the vacuum level [1].

The NEA detectors are sensitive to the near-infrared λ with a quantum efficiency improved and reducing undesired effects like the dark current; a small electric current that flows in opto devices even in absence of photons [1, 103], most of the photodetectors based on the photo-electric emission have the basis design of the vacuum photodiodes or phototubes and the most known is the photo-multiplier tube (PMT).

The components of the vacuum photodiode are the photo-cathode and anode, the photo-cathode can be opaque to operate in the reflection mode, or transparent and operate in the transmission mode, in the first case the photon incise provoking an electron detachment that it will be collected by the anode creating an electric current proportional to the photon detected, however this current is to small and normally the vacuum photodiodes detect photon flux Φ (photons per second) and the electric current becomes in a photocurrent.

When the detection demand an amplification as the previous example about photon detection it is necessary amplify the photocurrent, the first device known for this type of detection is the PMT that its photo-cathode is transparent and operating in transmission mode, when the photon incise in the photo-cathode it becomes in a photo-electron.

This new photo-electron impact in a plate called dynode provoking the multiplication of this photo-electron, the PMT has multiple dynodes that creates a cascade of electrons and the result is an amplification of the photocurrent by a factor around of 10^8, in the figure C.2 is illustrated the vacuum photo-diode and the PMT [1, 103].

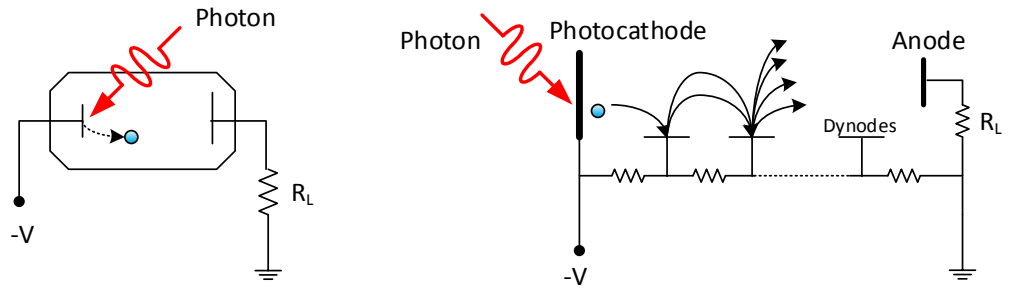

A) Photo-diode on reflection mode

B) Electron multiplication in a PMT

Figure C.2: A) The vacuum photodiode working in reflection mode, B) The PMT working in transmission mode and the electron multiplication.

C.2 Photon detectors

A photon detector is considered a opto-electronic device as that collect the photon energy and convert it in some measurable form like voltage, current, impedance and temperature, of course those measurable forms depends of electronic circuits and the type of photo detector classified in:

- Photo-electric detector
- Photo-thermal detector

The photo-electric detector is based in the photo-electric effect discovered by Hertz in 1887 but explained theoretically in 1905 by Einstein [101], this effect consists in the transition of electrons from a lower level to higher levels provoked by the absorption of a photon in a material (metallic), this transition results in mobile charge carriers.

C.3 Photodiode and Avalanche Photo Diode (APD)

The photodiode is a semiconductor device with a *p-n* junction that generates an electron-hole pair (photo-carrier) each time that a photon is absorbed, provoking an electric current when the photodiode has a reverse-bias voltage, because a forward bias voltage changes the photodiodes behaviour such as an ordinary semiconductor diode [1, 3]. The current-voltage (*i-V*) relationship is determined by equation (C.3).

$$i = i_s \left[e^{\left(\frac{e^- V}{K_B T}\right)} - 1 \right] - i_p \qquad \text{(C.3)}$$

Where i_s is the reverse current, e^- is the electron charge constant, V is the bias voltage, i_p is the photocurrent, K_B is Boltzmann constant and T is the temperature. An electron-hole pair generated under an electric field is split (electron and hole), and its parts are transported to a direction (drift). The holes are transported where there is 0V of potential (or ground) and the electrons are transported to the positive potential. Ideally electron-hole pairs are only generated in the depletion layer, but in practice the electron-hole pairs appear in several areas apart from the depletion layer, and the electron-hole pair behaviour depends on the area where the photon absorption occurs:

- The electron-hole pair generated in the depletion layer is quickly split. The electron and hole move to opposite directions when a strong electric field is present [1].
- The electron-hole pair generated outside (but near) to the depletion layer has a chance to be split and enter the depletion layer by random diffusion [1].
- The electron-hole pair generated far away from the depletion layer can't be split and transported [1].

Figure C.3 illustrates the possible areas of photon absorption and electron-holes trajectories.

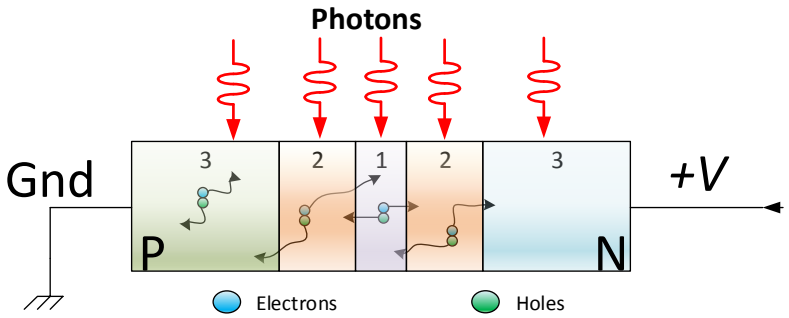

Figure C.3: The electron-hole pair is split in its electrons and holes when the photodiode is under a strong electric field, the electron and hole drift depends on the area where the photo carrier is generated and split: **1)** Depletion layer, **2)** Photon absorption far from the outside of the depletion layer, **3)** Photon-absorption far away from the depletion layer, the photodiode in this figure has ideal conditions under reverse bias [1].

The photodiode has three modes of operation:

- Open circuit, the photodiode behaves as a small photo-voltaic cell.
- Short circuit, the current in through the photodiode is the photocurrent.
- Reverse Biased, the photodiode exploits its photoconductive properties.

The open circuit mode generates electron-hole pairs in the depletion region, but the free electrons in the n-side of the depletion layer recombine with other holes from the p-side and vice versa, this action creates an electric field that produces a photo-voltage across the photodiode proportionally to the photon flux [1]. The short circuit mode generates an electric current proportional to the photon flux.

The reverse biased mode can operate with or without a load resistance, but it results in different breakdown voltage points, furthermore when there is a strong bias voltage, the electric field increases the drift velocity and reduces the transit time. Another consequence of the strong bias voltage is an increment of the depletion layer width also known as the punch-through effect, increasing the photosensitive area making the collection of light easier.

The p-n junction is not the only type of photodiode, there is a variation that contains an intrinsic layer (slightly doped) between the p and n layers, this type of photodiode is known as a ***p-i-n photodiode*** and it has certain advantages over the p-n photodiode such as bias conditions, in figure C.4 it illustrates the structure, energy-band diagram, charge distribution and the electric field distribution when the p-i-n photodiode has a reverse bias voltage [1].

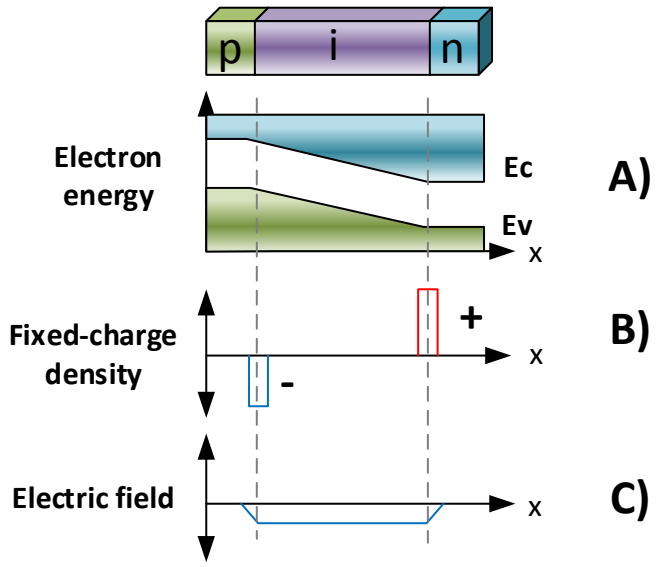

Figure C.4: The p-i-n photodiode structure, A) energy diagram, B) charge distribution, C) electric field distribution.

C.3.1 Photodiode Properties

The photodiode has several properties but this section only analyse the most important: response time, quantum efficiency, responsivity and gain.

C.3.1.1 Response Time

The response time of the photodiode is a property related to the time of diffusion for the electron-hole pairs generated, but also with their split and transportation. The response time is defined by the electron-hole pair lifetime and the diffusion time effect, this diffusion time can decrease with a certain photodiode configuration such as the p-i-n photodiode.

The resistance-capacitance (RC) time response affects the photodiode response time, although the photodiodes are generally faster than other photoconductors, because the photodiode is under a strong electric field in the depletion layer, and this electric field imparts a large velocity to the electron-hole pairs.

C.3.1.2 Quantum Efficiency

The quantum efficiency in a photodetector is defined as the probability of a single photon absorbed to generate an electron-hole pair and it contributes to the detector current, when many photons incise on the detection area, the quantum efficiency becomes a flux of electron-hole pairs that contribute to the detector current divided by the flux of incident photons [1]. Nevertheless not all the photons can produce electron-hole pairs.

The photons that are not absorbed are reflected at the surface of the photodiode or they are absorbed but without producing electron-hole pairs, the failed absorption is due to the material because it does not have sufficient depth, furthermore the electron-hole pairs generated near to the surface of the detector are quickly recombined, but this recombination does not contribute to the photodiode current [1].

The quantum efficiency (η) for a photodetector is determined by the following equation (C.4).

$$\eta = (1 - \mathcal{R})\zeta[1 - e^{-\alpha d}] \tag{C.4}$$

Where $\mathcal{R}$ is the optical power reflectance at the detector surface, ζ is the proportion of the electron-hole pair that contribute to the photodiode current, α is the absorption coefficient of the semiconductor material (cm^{-1}) and d is the photodiode depth [1]. The components of the equation (C.4) are three factors:

- $(1 - \mathcal{R})$ represents the effect of reflection at the surface of the photodetector although the reflection can be reduced with an anti-reflection coat.
- ζ is the fraction of electron-hole pairs that avoid the recombination at the material surface and contribute to the photocurrent.
- $[1 - e^{-\alpha d}]$ represents the fraction of the photon flux absorbed in the semiconductor material.

The quantum efficiency is also affected by the wavelength (λ) of the incident light, due to the absorption coefficient α having a dependence on λ. The characteristics of the semiconductor material determines the spectral window proportionally to the quantum efficiency. The bandgap wavelength (λ_g) is considered as a long-wavelength limit because the absorption cannot occur if the incident light wavelength (λ_0) is bigger than λ_g, due to

the photon energy being smaller than the bandgap energy (E_g), and the semiconductor material is passed as transparent material.

$$\lambda_g = \frac{hc_0}{E_g} \tag{C.5}$$

The equation (C.5) determines λ_g only when $\lambda_0 < \lambda_g$, but the quantum efficiency also decreases when λ_0 has smaller values, because the photon absorption is near to the photodiode surface reducing the recombination lifetime, and the electron-hole pairs recombine before being collected. For example, if α is 10^4 cm^{-1} almost all the incident photons on the photodetector would be absorbed at a distance of $1/\alpha$ that is equal to 1µm, therefore the incident light with $\lambda_0 < 400$nm its possible it would not be detected. Figure C.5 illustrates the process of light absorption.

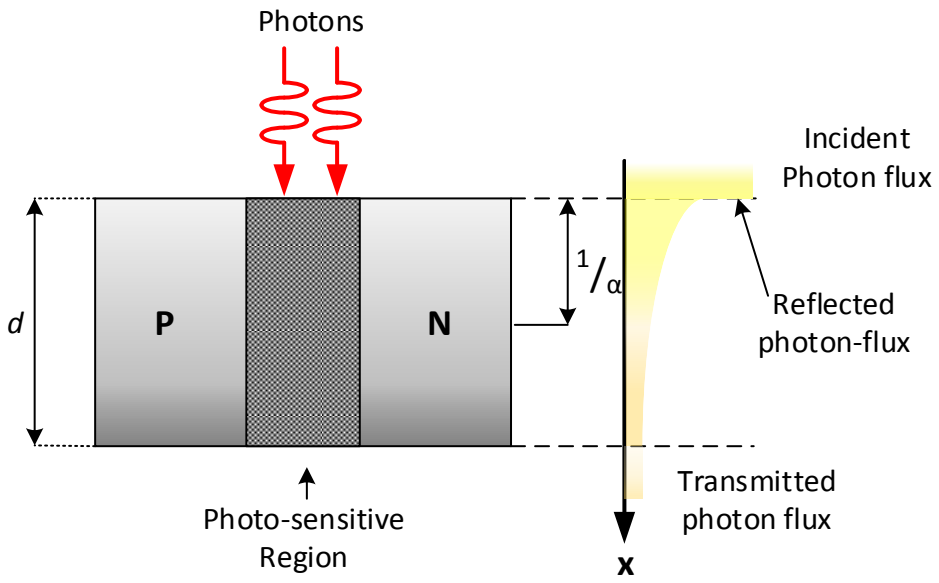

Figure C.5: Effect of the surface reflection and absorption consequences.

The quantum efficiency can be increased with a resonant cavity that traps the light, thanks to a photosensitive material on multiple layers. Therefore the photons have more probabilities of being absorbed. The quantum efficiency determines the number of electron-hole pairs generated by photon absorption, but it does not directly determine the relation between the electric current of the circuit where the photodiode is connected with the optical power of the incident light.

C.3.1.3 Responsivity

The responsivity ($\Re$) in the photodiode relates to the electron flux produced by the photon flux in the circuit and quantum efficiency (η), to analyse the responsivity the photodiode circuit is configured in a short-circuit mode, thereby the photocurrent (i_p) through the photodetector has a maximum peak when the optical power of the light is P.

$$i_p = \frac{\eta e^- P}{h\nu} \equiv \Re P \tag{C.6}$$

Therefore equation (C.6) is a proportionality between the photocurrent and the optical power. Nevertheless, the photodetector responsivity can be expressed directly with the photocurrent, quantum efficiency and λ_0 through the group of equations (C.7), the responsivity is measured in $^{A}/_{W}$ units.

$$\Re = \frac{i_P}{P} \tag{C.7a}$$

$$\Re = \frac{\eta e^-}{h\nu} = \eta \frac{\lambda_0}{1.24} \tag{C.7b}$$

There is a proportionality between responsivity, quantum efficiency and λ_0, figure C.6 illustrates a graph for an ideal photodiode of which the responsivity is as a function of λ_0 for different values of quantum efficiency.

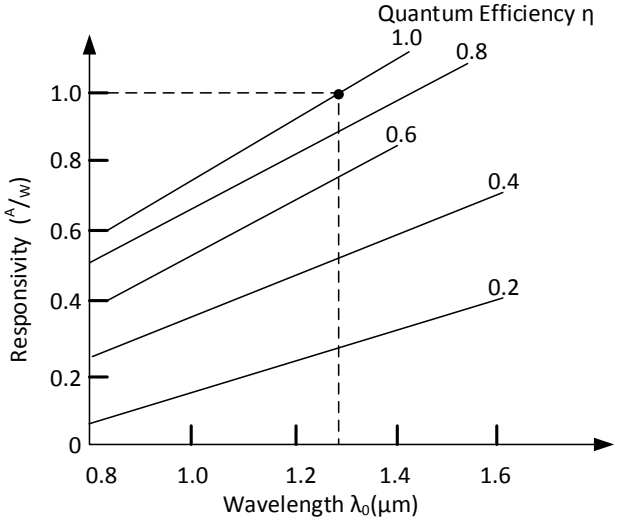

Figure C.6: Responsivity graph as a function of the λ_0 at different values of quantum efficiency, the quantum efficiency is used as a reference parameter: η=1, $\Re$ =1 $^{A}/_{W}$ at λ_0 = 1.24μm [1].

The graph shows a proportionality between $\Re$ and λ_0 because $\Re$ is defined on the basis of the optical power. However, the responsivity can be degraded if the photodiode is saturated by an excess optical power of the light incident, because there are limits in the linear dynamic range of the photodiode, this range responds to the optical power linearly due to the relation with the photon flux (Φ).

$$\Phi = \frac{P\lambda_0}{hc_0} \tag{C.8}$$

The group of equations (C.7) that are used under the assumption of each electron-hole pair, produce a charge equal to the electron (e^-) in the photodiode circuit. However many photodiodes produce an electric charge q^- instead of e^-, therefore there is a gain. The photodiode gain is defined as the average number of the electrons generated in the circuit per electron-hole pairs generated, the equation (C.9) determines the gain (G) in relation of q^- and e^-.

$$G \equiv \frac{q^-}{e^-} \tag{C.9}$$

The equations (C.6) and (C.7b) consider the gain as a unity but if it is different to 1, the gain must be considered, therefore the photocurrent and responsivity as a function of gain can be expressed as the following:

$$i_p = \frac{\eta G e^- P}{h\nu} \tag{C.10}$$

$$\Re = \eta G \frac{\lambda_0}{1.24} \tag{C.11}$$

The responsivity expressed in (C.11) exhibits an internal gain that is a product of the difference between the recombination lifetime and the transit time [1]. The electron and hole are transported to opposite sides of the photodiode, but the electron travels faster than the hole and this provokes a long recombination lifetime, therefore the electron completes the distance before the hole does [1].

C.3.2 Avalanche Photodiode Detector

The weak light has problems to generate a larger photocurrent in p-n or p-i-n junction photodiodes, therefore the avalanche photodiode (APD) becomes useful for those light conditions, and this type of photodiode converts a photon detected in a cascade or avalanche of electron-hole pairs. The APD is configured as reverse bias mode but with a high voltage that increases the electric field in the junction, thereby the electron-hole pairs acquire enough energy to produce new excited electron-hole pairs, this process is known as impact ionization.

The principle of operation of the APD is illustrated in figure C.7.

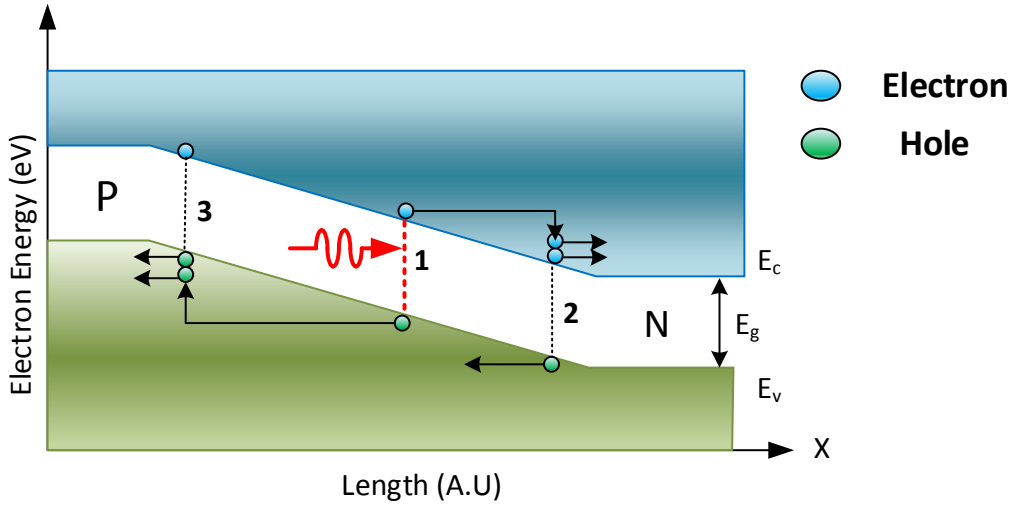

Figure C.7: Schematic representation of the APD multiplication process [1].

A photon is absorbed at point 1 (figure C.7) generating an electron-hole pair (an electron in the conduction band and a hole in the valence band), the electron is accelerated by the effect of the strong electric field, acquiring more energy with respect to the bottom of the conduction band. However, this increase of energy is not permanent and the electron acceleration is continuously interrupted by random collisions with the lattice.

The collisions provoke a partial loss of the electron energy and fixed at an average velocity, the energy obtained gives the electron an opportunity to generate a second electron-hole pair by ionized impact in point 2, now these two electrons are accelerated under the effect of the field and each electron can be a source for a further impact ionization. The holes generated at points 1 and 2, such as the electrons are also accelerated, but the movement

is to the left, each hole has a probability to create an impact ionization generating more electron-hole pairs (point 3).

The ability of electrons and holes to impact ionize is characterized by the ionization coefficients α_e for electrons and α_h for holes [1], the units of the ionization coefficients are cm^{-1} that represent probabilities per unit of length, and the inverse of the coefficients represent the average distances where the ionizations occur.

The ionization coefficients are related to the depletion layer, electric field and temperature. The temperature has a negative effect in the ionization coefficients due to increments of collisions, the collisions reduce the opportunity of an electron-hole pair to gain enough energy to ionize. The ionization coefficients (α_e and α_h) are considered as independent constants of the position and electron-hole pair histogram, thus the ionization ratio is a product between the ionization coefficients, equation (C.12) determines the ionization ratio.

$$\mathcal{K} = \frac{\alpha_e}{\alpha_h} \tag{C.12}$$

The APD structure is similar to the p-i-n photodiode, but the APD geometry is modified to enhance the photo absorption, especially in the multiplication region, this region should be thin to minimize possible avalanches provoked by the strong electric field. The absorption and multiplication regions are separated at the moment to design the APD, this type of structure is known as Separate-Absorption and Multiplication (SAM) APD.

The SAM APD has a $\mathcal{K} \approx 0$, therefore the photons are absorbed in a large intrinsic region and the photo-electrons generated drift across the APD under a moderated electric field, after the photo-electrons enter to a thin multiplication layer with a strong electric field where the avalanche occurs, figure C.8 illustrates a scheme of the SAM APD structure.

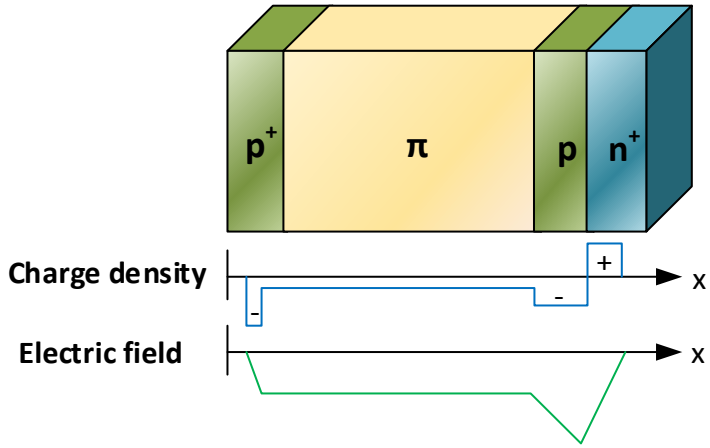

Figure C.8: SAM APD structure p^+-π-p-n^+.

The absorption region is labelled as π (slightly doped on the p-type layer) then the photo-electrons drift through the π region into the p-n junction, when the photo-electron arrives it experiences a strong pulling force from the electric field and causes the avalanche.

C.3.2.1 APD Gain

The multiplication can be provoked by both kinds of carriers (electrons and holes) but in this case only the electrons are considered, the multiplication by a single carrier (electron) fixed its address position at α_h=0, $\mathcal{K}$=0 [1], the electrons carry an electric current density (J_e) at certain locations labelled with x, and certain distances (dx), therefore the current increment can be modelled by a differential equation.

$$dJ_e(x) = \alpha_e J_e(x) dx \tag{C.13}$$

This solution of equation (C.13) is an exponential function of $J_e(x) = J_e(0)e^{\alpha_e x}$. The gain is equal to the relation $J_e(x)$ and $J_e(0)$ [1], but x represents a location in the width of the layer, therefore it is replaced with w.

$$G = e^{\alpha_e w} \tag{C.14}$$

The double-carrier multiplication involves J_e and the hole-current density (J_h), but only the electrons are injected to the multiplication region, even hole-ionizations also produce electrons, but Je is governed by:

$$\frac{dJ_e}{dx} = \alpha_e J_e(x) + \alpha_h J_h(x) \tag{C.15}$$

It is assumed that no holes are injected at $x = w,\ J_h(w) = 0$ [1]. Then J_e as a function of w is:

$$J_e(x) + J_h(x) = J_e(w) \tag{C.16}$$

When J_h is eliminated, the equation (C.17) changes:

$$\frac{dJ_e}{dx} = (\alpha_e - \alpha_h)J_e(x) + \alpha_h J_e(w) \tag{C.17}$$

The solution of the equation (C.17) for gain $G = J_e(w)/J_e(0)$, when $\alpha_e \neq \alpha_h$ results in $G = \alpha_e - \alpha_h/\alpha_e e^{w(\alpha_h - \alpha_e)} - \alpha_h$[1]. But the gain can be simplified with $\mathcal{K}$ and thereby the APD gain is:

$$G = \frac{1-\mathcal{K}}{e^{(k-1)\alpha_e w} - \mathcal{K}} \tag{C.18}$$

The total number of charge carriers crossing any plane is the same regardless of the position, when $\mathcal{K}$=0 the single carrier multiplication is represented in (2.17), when $\mathcal{K}$=∞ the *gain is unitary* because only the electrons are injected [1].

When $\mathcal{K}$=1 the APD gain of (C.18) is indeterminate and the gain is obtained directly from (C.17) resulting [1]:

$$G = \frac{1}{(1-\alpha_e w)} \tag{C.17}$$

Figure C.9 illustrates the exponential growth by a single carrier (electron) and for a double carrier (electron and hole).

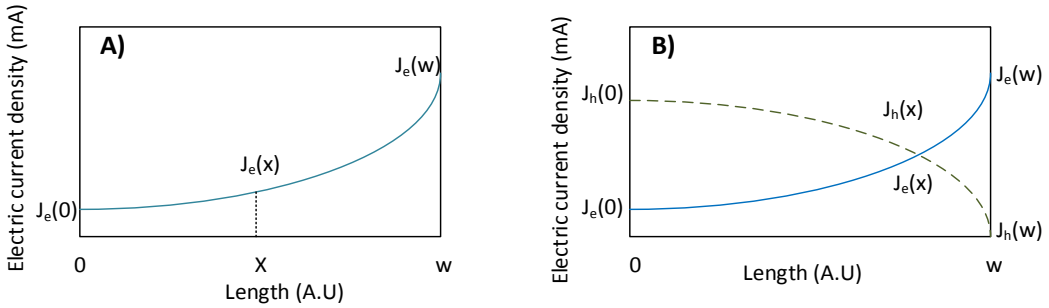

Figure C.9: A) Exponential growth of Je in a single-carrier, B) Exponential growth of the electron and hole currents as a result of the avalanche multiplication.

The semiconductor material in the APD has an important influence on the ionization ratio and thereby to the gain, Si-APD has ionization rates of around 0.1 to 0.2, but there is a Si-APD variation with a low ionization ratio as 0.006, these low ionization rates are suitable for the spectral region between 700 and 900nm.

Applications such as telecommunications use the spectral region between 1300 and 1600, therefore Si-APDs are not suitable. The semiconductor material used for that region is an alloy of Indium, Gallium and Arsenic (InGaAs), the InGaAs APD has higher ionization rates that significantly increase the responsivity and moderate the noise.

The InGaAs APD gain has a dependence on the reverse bias voltage, this dependence is appreciable when the bias voltage exceeds the punch-through voltage. The gain region begins and it is increased until it reaches the breakdown voltage, figure C.10 illustrates the current-voltage characteristic for an InGaAs SAM APD.

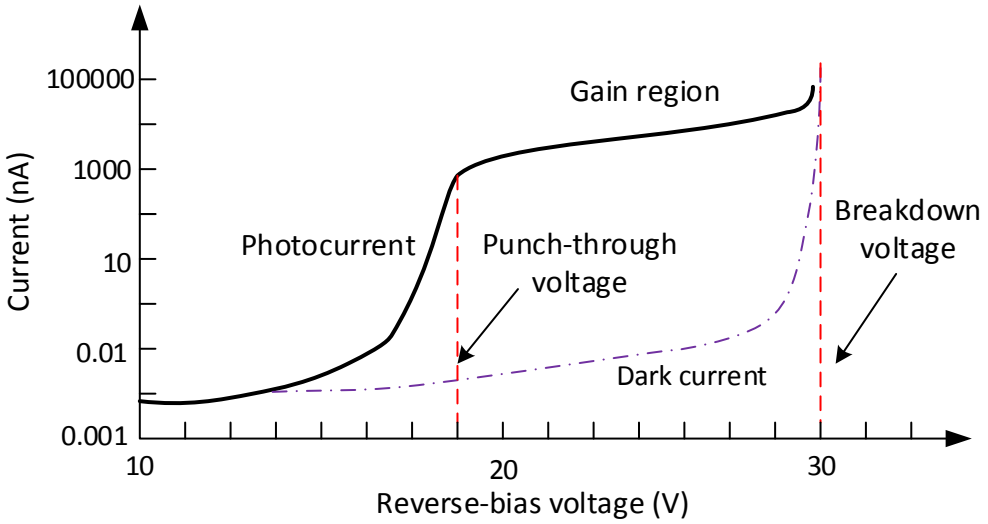

Figure C.10: Current-Voltage graph for an InGaAs SAM APD, when the reverse bias voltage is below the punch-through voltage, there is a rise of current under the light presence and this current is the photocurrent, without light presence there is a moderate current rise until it reaches the breakdown voltage and this current is the dark current. The gain region has a moderate rise slope until it reaches the breakdown voltage.

The reverse bias voltage increases the gain but also the dark current, the typical values for dark currents are around 100pA. When the bias voltage exceeds the breakdown voltage, the InGaAs APD can be damaged unless it is designed to operate voltages over the breakdown voltage, and this optoelectronic device is called Single-Avalanche Photo Diode.

C.3.2.2 APD Response Time

The APD also has a response time ruled by RC effects, but it is not the only feature that delays the response time, there is a delay from the avalanche build-up time. The avalanche build-up time is related to the multiplication process. When the photon enters the absorption region and a *photo-electron* is generated, the electron continues a trajectory with a certain velocity (v_e) until it reaches the multiplication region, at this point the electron transit time has a relation to the width of absorption (w_d) region and v_e.

The electron inside of the multiplication region still travels with a velocity v_e, the impact ionization starts to create electron-hole pairs. The hole moves to an opposite direction with a saturation velocity (v_h), such as a billiard game, the holes also cause impact ionizations that result in more electron-hole pairs, the extra pairs can also cause more impact ionizations holding a feedback loop [1].

Figure C.11 illustrates a scheme of the multiplication process, 8 steps that relate to the avalanche build-up time.

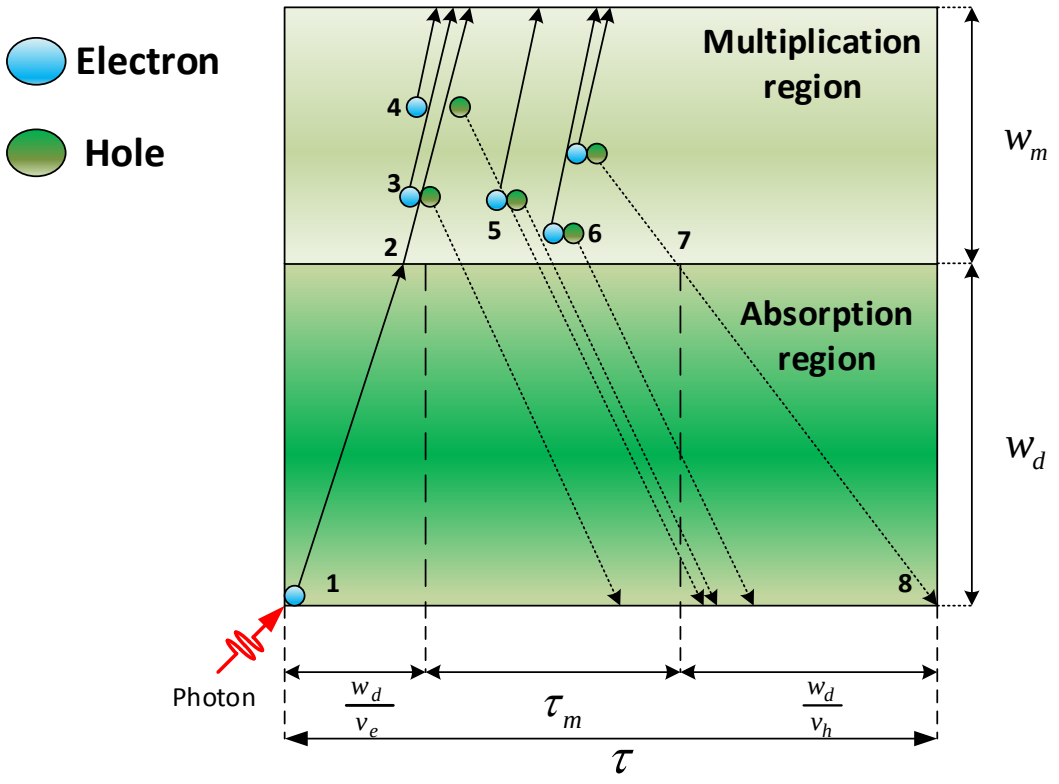

Figure C.11: The process of the avalanche build-up time in the APD.

1. When a photon incise at the absorption region, a photo-electron is generated with a trajectory at direction of the multiplication region.
2. The photo-electron enters to the multiplication region with a velocity.
3. The impact ionization start creating an electron-hole pair.
4. The multiplication of electron-hole pairs continue.
5. The holes travels at direction of the absorption region, but during its trajectory creates more electron-hole pairs.
6. The impact ionization is produced by holes.
7. The impact ionization ends and the last hole leaves the multiplication region.
8. The hole drift in the absorption region until it leaves the absorption region.

The multiplication of carriers ends when the last hole leaves the multiplication region and crosses over to the absorption region [1], the response time in an APD is determined by the equation (C.18).

$$\tau = \frac{w_d}{v_e} + \frac{w_d}{v_h} + \tau_m \tag{C.18}$$

Where w_d is the width of absorption, v_e is the electron velocity, v_h is the hole velocity and τ_m represents the multiplication time, this process is random and τ_m is determined by:

$$\tau_m = \frac{w_m}{v_e} + \frac{w_m}{v_h} \tag{C.19}$$

When $\mathcal{K} = 0$, the multiplication time (τ_m) has the maximum value, but τ_m has an average value when $0 < \mathcal{K} < 1$, furthermore this range adds the gain and ionization ratio as a factor to the equation (C.19).

$$\tau_m \approx \frac{G\mathcal{K}w_m}{v_e} + \frac{w_m}{v_h} \tag{C.20}$$

Bibliography

[1] B. E. A. S. a. M. C. Teich, *Fundamental of Photonics*. John Wiley and Sons, 1991.

[2] O. Svelto and D. C. Hanna, "Principles of lasers," 1998.

[3] R. L. Boylestad, L. Nashelsky, and F. Monssen, *Electronic devices and circuit theory*. Prentice Hall Englewood Cliffs, NJ, 2002.

[4] J. R. Lakowicz, *Principles of fluorescence spectroscopy*, 3rd ed. New York: Springer, 2006, pp. xxvi, 954 p. +.

[5] J. L. O'Brien, "Optical quantum computing," *Science,* vol. 318, no. 5856, pp. 1567-1570, 2007.

[6] C. H. Bennett, F. Bessette, G. Brassard, L. Salvail, and J. Smolin, "Experimental quantum cryptography," *Journal of cryptology,* vol. 5, no. 1, pp. 3-28, 1992.

[7] B. Lounis and M. Orrit, "Single-photon sources," *Reports on Progress in Physics,* vol. 68, no. 5, p. 1129, 2005.

[8] M. Eisaman, J. Fan, A. Migdall, and S. Polyakov, "Invited review article: Single-photon sources and detectors," *Review of scientific instruments,* vol. 82, no. 7, p. 071101, 2011.

[9] D. Lowndes, "Low cost, short range free space quantum cryptography for consumer applications: pocket size for pocket change," University of Bristol, 2014.

[10] J. Duligall, M. Godfrey, K. Harrison, W. Munro, and J. Rarity, "Low cost and compact quantum key distribution," *New Journal of Physics,* vol. 8, no. 10, p. 249, 2006.

[11] D. Gottesman, H.-K. Lo, N. Lutkenhaus, and J. Preskill, "Security of quantum key distribution with imperfect devices," in *Information Theory, 2004. ISIT 2004. Proceedings. International Symposium on*, 2004, p. 136: IEEE.

[12] M. O. a. A. G. Sinclair, "Single-Photon sources," *Contemporary Physics,* vol. 46, no. 3, pp. 173-206, 2005.

[13] S. Fasel *et al.*, "High-quality asynchronous heralded single-photon source at telecom wavelength," *New Journal of Physics,* vol. 6, no. 1, p. 163, 2004.

[14] G. Knoll, "Radiation Detection and Measurement3rd edition John Wiley and Sons," *New York,* 2000.

[15] P. A. Hiskett *et al.*, "Performance and design of InGaAs/InP photodiodes for single-photon counting at 1.55 μm," *Applied Optics,* vol. 39, no. 36, pp. 6818-6829, 2000.

[16] M. Ghioni, S. Cova, F. Zappa, and C. Samori, "Compact active quenching circuit for fast photon counting with avalanche photodiodes," *Review of scientific instruments,* vol. 67, no. 10, pp. 3440-3448, 1996.

[17] S. Pellegrini *et al.*, "Design and performance of an InGaAs-InP single-photon avalanche diode detector," *IEEE journal of quantum electronics,* vol. 42, no. 4, pp. 397-403, 2006.

[18] D. Renker, "Geiger-mode avalanche photodiodes, history, properties and problems," *Nuclear Instruments and Methods in Physics Research Section A: Accelerators, Spectrometers, Detectors and Associated Equipment,* vol. 567, no. 1, pp. 48-56, 2006.

[19] J. Rarity, T. Wall, K. Ridley, and P. Tapster, "Single photon counting for 1300-1600 nm using Peltier cooled and passively quenched InGaAs avalanche photodiodes," in *Lasers and Electro-Optics Europe, 2000. Conference Digest. 2000 Conference on*, 2000, p. 1 pp.: IEEE.

[20] D. Stucki, G. Ribordy, A. Stefanov, H. Zbinden, J. G. Rarity, and T. Wall, "Photon counting for quantum key distribution with Peltier cooled InGaAs/InP APDs," *Journal of modern optics,* vol. 48, no. 13, pp. 1967-1981, 2001.

[21] B. Korzh, T. Lunghi, K. Kuzmenko, G. Boso, and H. Zbinden, "Afterpulsing studies of low-noise InGaAs/InP single-photon negative-feedback avalanche diodes," *Journal of Modern Optics,* vol. 62, no. 14, pp. 1151-1157, 2015.

[22] X. Jiang, M. A. Itzler, K. O'Donnell, M. Entwistle, and K. Slomkowski, "Shortwave infrared negative feedback avalanche diodes and solid-state photomultipliers," *Optical Engineering,* vol. 53, no. 8, pp. 081908-081908, 2014.

[23] C. Hu, X. Zheng, J. C. Campbell, B. M. Onat, X. Jiang, and M. A. Itzler, "Characterization of an InGaAs/InP-based single-photon avalanche diode with

gated-passive quenching with active reset circuit," *Journal of Modern Optics,* vol. 58, no. 3-4, pp. 201-209, 2011.

[24] S. Cova, M. Ghioni, A. Lacaita, C. Samori, and F. Zappa, "Avalanche photodiodes and quenching circuits for single-photon detection," *Applied optics,* vol. 35, no. 12, pp. 1956-1976, 1996.

[25] R. G. Brown, R. Jones, J. G. Rarity, and K. D. Ridley, "Characterization of silicon avalanche photodiodes for photon correlation measurements. 2: Active quenching," *Applied Optics,* vol. 26, no. 12, pp. 2383-2389, 1987.

[26] Z. Yuan, B. Kardynal, A. Sharpe, and A. Shields, "High speed single photon detection in the near infrared," *Applied Physics Letters,* vol. 91, no. 4, p. 041114, 2007.

[27] M. A. Itzler, X. Jiang, B. Nyman, and K. Slomkowski, "InP-based negative feedback avalanche diodes," in *Proc. SPIE*, 2009, vol. 7222, p. 72221K.

[28] M. A. Itzler, "Negative feedback avalanche diode," ed: Google Patents, 2010.

[29] P. Lightwave. (2017). *PGQ Series Negative Feedback Avalanche Diodes (NFADs)*. Available: https://www.princetonlightwave.com/wp-content/uploads/2017/01/PGQ.pdf

[30] J. Zhang, M. A. Itzler, H. Zbinden, and J.-W. Pan, "Advances in InGaAs/InP single-photon detector systems for quantum communication," *Light: Science & Applications,* vol. 4, no. 5, p. e286, 2015.

[31] D. Hall, Y.-H. Liu, L. Yan, Y. Yu, and Y.-H. Lo, "Approaching the Quantum Limit of Photodetection in Solid-State Photodetectors," *IEEE Transactions on Electron Devices,* 2017.

[32] E. Amri, G. Boso, B. Korzh, and H. Zbinden, "Temporal jitter in free-running InGaAs/InP single-photon avalanche detectors," *Optics letters,* vol. 41, no. 24, pp. 5728-5731, 2016.

[33] B. Korzh, N. Walenta, T. Lunghi, N. Gisin, and H. Zbinden, "Free-running InGaAs single photon detector with 1 dark count per second at 10% efficiency," *Applied Physics Letters,* vol. 104, no. 8, p. 081108, 2014.

[34] S. Nauerth *et al.*, "Air-to-ground quantum communication," *Nature Photonics,* vol. 7, no. 5, pp. 382-386, 2013.

[35] B. Korzh *et al.*, "Provably secure and practical quantum key distribution over 307 km of optical fibre," *Nature Photonics,* vol. 9, no. 3, pp. 163-168, 2015.

[36] I. Quantique. (2017, 2017). *Quantum Safe Security*. Available: https://www.idquantique.com/quantum-safe-security/products/

[37] T. Europe. (2017). *Toshiba QKD system*. Available: https://www.toshiba.eu/eu/Cambridge-Research-Laboratory/Quantum-Information/Quantum-Key-Distribution/Toshiba-QKD-system/

[38] L. Comandar *et al.*, "Room temperature single-photon detectors for high bit rate quantum key distribution," *Applied Physics Letters,* vol. 104, no. 2, p. 021101, 2014.

[39] T. Müller *et al.*, "A quantum light-emitting diode for the standard telecom window around 1,550 nm," *Nature communications,* vol. 9, no. 1, p. 862, 2018.

[40] I. Quantique. (2017, 13-Sep-2017). *ID210 Infrared Single photon Detector*. Available: https://marketing.idquantique.com/acton/attachment/11868/f-0239/1/-/-/-/-/ID210_Brochure.pdf

[41] I. Quantique. (2017, 13-sep-2017). *ID230 Infrared Single-photon detector*. Available: https://marketing.idquantique.com/acton/attachment/11868/f-0234/1/-/-/-/-/ID230_Brochure.pdf

[42] L. C. Comandar *et al.*, "Gigahertz-gated InGaAs/InP single-photon detector with detection efficiency exceeding 55% at 1550 nm," *Journal of Applied Physics,* vol. 117, no. 8, p. 083109, 2015.

[43] M. Peev *et al.*, "The SECOQC quantum key distribution network in Vienna," *New Journal of Physics,* vol. 11, no. 7, p. 075001, 2009.

[44] W. Buttler *et al.*, "Practical free-space quantum key distribution over 1 km," *Physical Review Letters,* vol. 81, no. 15, p. 3283, 1998.

[45] Thorlabs. (2014). *Laser diode L635P5*. Available: https://www.thorlabs.com/drawings/80c6688b37a45cd2-84085345-5056-2306-D9C96EC183383DD5/L637P5-SpecSheet.pdf

[46] Multicomp. (2012). *MCL053HPD/5 LED*. Available: http://www.farnell.com/datasheets/1671507.pdf?_ga=2.19551615.657338610.1494263576-1398896301.1403011677

[47] J. Duligall, "Compact and Low Cost Quantum Cryptography " Ph.D., Electrical and Electronic Department, University of Bristol, Bristol United Kingdom, 2017.

[48] Q. Feng, B. Zhang, and C. Kuang, "A straightness measurement system using a single-mode fiber-coupled laser module," *Optics & Laser Technology,* vol. 36, no. 4, pp. 279-283, 2004.

[49] J. Rarity, P. Tapster, P. Gorman, and P. Knight, "Ground to satellite secure key exchange using quantum cryptography," *New Journal of Physics,* vol. 4, no. 1, p. 82, 2002.

[50] T. Instruments. (2008, 2008). *11.3 Gbps Laser Diode Driver*. Available: http://www.ti.com/lit/ds/symlink/onet1101l.pdf

[51] B. S. Ismael, *Teoria de los Circuitos* (Teoria de los Circuitos). ICE-ESIME Zacatenco Mexico: Academia de circuitos, 2003, p. 167.

[52] R. Ho, "Programmable LED driver," ed: Google Patents, 2000.

[53] H. Le Minh *et al.*, "High-speed visible light communications using multiple-resonant equalization," *IEEE Photonics Technology Letters,* vol. 20, no. 14, pp. 1243-1245, 2008.

[54] H. Tanaka, Y. Umeda, and O. Takyu, "High-speed LED driver for visible light communications with drawing-out of remaining carrier," in *Radio and Wireless Symposium (RWS), 2011 IEEE*, 2011, pp. 295-298: IEEE.

[55] N. semiconductors. (1995). *BFG198, NPN 8 GHz wideband transistor*. Available: http://www.nxp.com/docs/en/data-sheet/BFG198.pdf

[56] T. Instruments. (2010). *THS3202, 2GHz Low Distortion, Dual Current-Feedback Amplifiers*. Available: http://www.ti.com/lit/ds/slos242f/slos242f.pdf

[57] M. H. Rashid, *Power electronics handbook: devices, circuits and applications*. Academic press, 2010.

[58] T. Instruments. (2002). *THS3202EVM*. Available: http://www.ti.com/lit/ug/slou148/slou148.pdf

[59] PicoQuant. (2015, Octuber 2015). *PicoHarp 300, Picosecond Histogram Accumulating Real-time Processor Manual user*. Available: https://www.picoquant.com/dl_manuals/PicoHarp300_V3_0_DLL_manual.pdf

[60] Z. Yan, D. R. Hamel, A. K. Heinrichs, X. Jiang, M. A. Itzler, and T. Jennewein, "An ultra low noise telecom wavelength free running single photon detector using negative feedback avalanche diode," *Review of Scientific Instruments,* vol. 83, no. 7, p. 073105, 2012.

[61] D. J. Rogers, J. C. Bienfang, A. Nakassis, H. Xu, and C. W. Clark, "Detector dead-time effects and paralyzability in high-speed quantum key distribution," *New Journal of Physics,* vol. 9, no. 9, p. 319, 2007.

[62] A. Pérez-Serrano *et al.*, "Atmospheric CO 2 remote sensing system based on high brightness semiconductor lasers and single photon counting detection," in *Lidar*

Technologies, Techniques, and Measurements for Atmospheric Remote Sensing XI, 2015, vol. 9645, p. 964503: International Society for Optics and Photonics.

[63] S. Afanasiev *et al.*, "MRS silicon avalanche detectors with negative feedback for time-of-flight systems," *КРАТКИЕ СООБЩЕНИЯ ОИЯИ JINR RAPID COMMUNICATIONS,* p. 5, 1995.

[64] A. Khodin, V. Kovalevsky, T. Leonova, D. Shvarkov, and V. Zalessky, "Localised feedback in silicon-based avalanche photodiodes," *Nuclear Instruments and Methods in Physics Research Section A: Accelerators, Spectrometers, Detectors and Associated Equipment,* vol. 513, no. 1-2, pp. 178-182, 2003.

[65] P. Lightwave. (2010, 2010). *PNA-20x Negative Feedback Avalanche Diode*. Available: http://www.amstechnologies.com/fileadmin/amsmedia/downloads/3679_PNA-20X_NFADs.pdf

[66] J. Ma *et al.*, "Design considerations of high-performance InGaAs/InP single-photon avalanche diodes for quantum key distribution," *Applied optics,* vol. 55, no. 27, pp. 7497-7502, 2016.

[67] M. Covi *et al.*, "Liquid-nitrogen cooled, free-running single-photon sensitive detector at telecommunication wavelengths," *Applied Physics B,* vol. 118, no. 3, pp. 489-495, 2015.

[68] R. H. Hadfield, "Single-photon detectors for optical quantum information applications," *Nature photonics,* vol. 3, no. 12, p. 696, 2009.

[69] R. H. Brown and R. Q. Twiss, "Correlation between photons in two coherent beams of light," *Nature,* vol. 177, no. 4497, pp. 27-29, 1956.

[70] J. F. Clauser, "Experimental distinction between the quantum and classical field-theoretic predictions for the photoelectric effect," *Physical Review D,* vol. 9, no. 4, p. 853, 1974.

[71] PicoQuant. (2009). *Time-Correlated Single Photon Counting*. Available: http://ridl.cfd.rit.edu/products/manuals/PicoQuant/technote_tcspc.pdf

[72] K. Jensen *et al.*, "Afterpulsing in Geiger-mode avalanche photodiodes for 1.06 μ m wavelength," *Applied Physics Letters,* vol. 88, no. 13, p. 133503, 2006.

[73] Y. Zhao, Z. Dong, S. Miao, A. Deng, J. Yang, and B. Wang, "Origin of deep level defect related photoluminescence in annealed InP," *Journal of applied physics,* vol. 100, no. 12, p. 123519, 2006.

[74] K. Technologies. (2017, 2015). *53310A Modulation Domain Analyzer*. Available: http://literature.cdn.keysight.com/litweb/pdf/5966-4092E.pdf?id=1000032396:epsg:dow

[75] T. Lunghi *et al.*, "Free-running single-photon detection based on a negative feedback InGaAs APD," *Journal of Modern Optics,* vol. 59, no. 17, pp. 1481-1488, 2012.

[76] H. Lu, C.-H. F. Fung, X. Ma, and Q.-y. Cai, "Unconditional security proof of a deterministic quantum key distribution with a two-way quantum channel," *Physical Review A,* vol. 84, no. 4, p. 042344, 2011.

[77] N. Namekata, S. Sasamori, and S. Inoue, "800 MHz single-photon detection at 1550-nm using an InGaAs/InP avalanche photodiode operated with a sine wave gating," *Optics Express,* vol. 14, no. 21, pp. 10043-10049, 2006.

[78] J. Zhang, P. Eraerds, N. Walenta, C. Barreiro, R. Thew, and H. Zbinden, "2.23 GHz gating InGaAs/InP single-photon avalanche diode for quantum key distribution," *arXiv preprint arXiv:1002.3240,* 2010.

[79] M. Ren *et al.*, "Laser ranging at 1550 nm with 1-GHz sine-wave gated InGaAs/InP APD single-photon detector," *Optics express,* vol. 19, no. 14, pp. 13497-13502, 2011.

[80] W.-H. Jiang, J.-H. Liu, Y. Liu, G. Jin, J. Zhang, and J.-W. Pan, "1.25 GHz sine wave gating InGaAs/InP single-photon detector with monolithically integrated readout circuit," *arXiv preprint arXiv:1711.02796,* 2017.

[81] A. Restelli, J. C. Bienfang, and A. L. Migdall, "Single-photon detection efficiency up to 50% at 1310 nm with an InGaAs/InP avalanche diode gated at 1.25 GHz," *Applied Physics Letters,* vol. 102, no. 14, p. 141104, 2013.

[82] D.-Y. He *et al.*, "Sine-wave gating InGaAs/InP single photon detector with ultralow afterpulse," *Applied Physics Letters,* vol. 110, no. 11, p. 111104, 2017.

[83] N. Zhou *et al.*, "Sine wave gating silicon single-photon detectors for multiphoton entanglement experiments," *Review of Scientific Instruments,* vol. 88, no. 8, p. 083102, 2017.

[84] P. Sibson, J. E. Kennard, S. Stanisic, C. Erven, J. L. O'Brien, and M. G. Thompson, "Integrated silicon photonics for high-speed quantum key distribution," *Optica,* vol. 4, no. 2, pp. 172-177, 2017.

[85] K. J. Gordon, V. Fernandez, G. S. Buller, I. Rech, S. D. Cova, and P. D. Townsend, "Quantum key distribution system clocked at 2 GHz," *Optics Express,* vol. 13, no. 8, pp. 3015-3020, 2005.

[86] B. C. a. J. Forshaw, *The quantum universe: Everything that can happen does happen*. Penguin Books, 2012.

[87] F. J. K. a. M. J. S. W. Edward Gettis, *Physics: Classical and Modern*. McGraw-Hill, 1989.

[88] E. Collett, "Field guide to polarization," 2005.

[89] U. Titulaer and R. Glauber, "Correlation functions for coherent fields," *Physical Review,* vol. 140, no. 3B, p. B676, 1965.

[90] S. Gasiorowicz, *Quantum physics*. John Wiley & Sons, 2007.

[91] N. J. Krichel, A. McCarthy, and G. S. Buller, "Resolving range ambiguity in a photon counting depth imager operating at kilometer distances," *Optics express,* vol. 18, no. 9, pp. 9192-9206, 2010.

[92] J. A. Smolin, "The early days of experimental quantum cryptography," *IBM Journal of Research and Development,* vol. 48, no. 1, pp. 47-52, 2004.

[93] R. Alléaume *et al.*, "Quantum key distribution and cryptography: a survey," in *Dagstuhl Seminar Proceedings*, 2010: Schloss Dagstuhl-Leibniz-Zentrum für Informatik.

[94] V. Scarani, H. Bechmann-Pasquinucci, N. J. Cerf, M. Dušek, N. Lütkenhaus, and M. Peev, "The security of practical quantum key distribution," *Reviews of modern physics,* vol. 81, no. 3, p. 1301, 2009.

[95] D. Stebila, M. Mosca, and N. Lütkenhaus, "The case for quantum key distribution," in *International Conference on Quantum Comunication and Quantum Networking*, 2009, pp. 283-296: Springer.

[96] C. Timothy, "An emprical analysis of the Cascade secret key reconciliation protocol for quantum key distribution," Master thesis, Air Force Institute of Technology, Air University, 2011.

[97] C. H. Bennett and G. Brassard, "QUANTUM CRYPTOGRAPHY: PUBLIC KEY DISTRIBUTION AND CON Tos5," 1984.

[98] A. Mink and A. Nakassis, "LDPC for QKD reconciliation," *arXiv preprint arXiv:1205.4977,* 2012.

[99] C. Paar and J. Pelzl, *Understanding cryptography: a textbook for students and practitioners*. Springer Science & Business Media, 2009.

[100] R. Nock, N. Dahnoun, and J. Rarity, "Low cost timing interval analyzers for quantum key distribution," in *Instrumentation and Measurement Technology Conference (I2MTC), 2011 IEEE*, 2011, pp. 1-5: IEEE.

[101] A. Einstein, "The photoelectric effect," *Ann. Phys,* vol. 17, no. 132, p. 4, 1905.

[102] E. L. Dereniak and G. D. Boreman, *Infrared detectors and systems*. Wiley, 1996.

[103] W. D. Cooper, *Electronic instrumentation and measurement techniques*. Prentice Hall, 1970.